

NOTE TO USERS

This reproduction is the best copy available.

UMI[®]

FABRICATION AND ANALYSIS OF FERROMAGNETIC METALLIC
FILMS GROWN ONTO SEMICONDUCTOR SUBSTRATES
BY ELECTROCHEMICAL DEPOSITION

by

CHRISTIAN SCHECK

A DISSERTATION

Submitted in partial fulfillment of the requirements
for the degree of Doctor of Philosophy
in the Department of Physics
in the Graduate School of
The University of Alabama

TUSCALOOSA, ALABAMA

2004

UMI Number: 3163572

INFORMATION TO USERS

The quality of this reproduction is dependent upon the quality of the copy submitted. Broken or indistinct print, colored or poor quality illustrations and photographs, print bleed-through, substandard margins, and improper alignment can adversely affect reproduction.

In the unlikely event that the author did not send a complete manuscript and there are missing pages, these will be noted. Also, if unauthorized copyright material had to be removed, a note will indicate the deletion.

UMI[®]

UMI Microform 3163572

Copyright 2005 by ProQuest Information and Learning Company.


All rights reserved. This microform edition is protected against unauthorized copying under Title 17, United States Code.


ProQuest Information and Learning Company
300 North Zeeb Road
P.O. Box 1346
Ann Arbor, MI 48106-1346


Submitted by Christian Scheck in partial fulfillment of the requirements for the degree of Doctor of Philosophy specializing in Physics.


Accepted on behalf of the Faculty of the Graduate School by the dissertation committee:



James W. Harrell, Ph.D.


Benjamin C. Harms, Ph.D.


Raghvendra K. Pandey, Ph.D.



Pieter B. Visscher, Ph.D.


Rainer Schad, Ph.D.
Chairperson


Stanley Jones, Ph.D.
Department Chairperson

10-28-2004
Date

11/30/04
Date


Ronald W. Rogers, Ph.D.
Dean of the Graduate School

LIST OF ABBREVIATIONS AND SYMBOLS

d	Lattice spacing or metal density
e	Electron charge
f	Factor which is a function only of the ratio $R_{AB,CD}/R_{BC,DA}$
$g(L)$	Surface width function
h	Plank constant
k_B	Boltzmann's constant
l	Charge carrier diffusion length
mfp	Mean free path
$z(r)$	Surface height at distance r
A^{**}	Richardson constant
D	Diffusion coefficient
D_o	Outer diameter
D_i	Inner diameter
E	Free energy
E_p	Photon energy
H	Hurst exponent
H_c	Coercivity field
H_k	Anisotropy field
H_r	Ferromagnetic resonance field
I	Current

J	Current density
K	Bulk crystalline anisotropy constants
K_p	Perpendicular anisotropy
K_u	In plane uniaxial constant
L	Torque
M	Magnetic moment
M_r	Remanence magnetization
M_s	Saturation magnetization
R	Specular reflection
$R_{AB,CD}$	Resistance
R_0	Fresnel reflection coefficient
T	Temperature or thickness
T_M	Magnetic thickness
T_N	Nominal thickness
T_{Ox}	Thickness of hydroxide layer
T_{RBS}	RBS thickness
T_{XRR}	X-ray reflectivity thickness
V	Voltage
V_{th}	Threshold voltage
α	Absorption coefficient
ϕ	Rotation angle of the sample around the film plane normal (XRD experiment)
λ	Wavelength
μ	Charge-carrier mobility

ρ	Resistivity
σ_{∞}	Root-mean-square roughness
τ	Minority carrier lifetime in the semiconductor
ω	Angle between the incident x rays and the diffracting lattice planes (XRD experiment)
ω_c	Critical incident angle (XRD experiment)
ξ	Correlation length
Φ	Photon flux
ψ	Angle between the film plane normal and the diffraction plane (XRD experiment)
2θ	Angle between incident and diffracted beam (XRD experiment)

ACKNOWLEDGMENTS

I would like to express my sincere appreciation to my advisor Dr. Rainer Schad who brought me into the science of magnetism and electrodeposition, for his guidance, strong support and continuous encouragement throughout this research project.

I wish to thank Dr. Paul Evans and Dr. Yi-Kuang Liu for their help and strong support in this project.

I wish to thank Dr. Giovanni Zangari for his help and advice in this project.

I wish to thank Professor Chester Alexander and Dr. Yunfei Ding for their help in ferromagnetic magnetic resonance measurements.

I wish to thank Professor John R. Williams and Dr. T. F. Isaacs-Smith of Auburn University for their help in Rutherford backscattering spectroscopy and ion implantation measurements.

I wish to thank in particular Dr. James Weston for his technical support in this project.

I also wish to thank Mr. Tom Hunter, Mr. Mel Buchannan, and Mr. Danny Whitcomb of the machine and electronics shop of the Department of Physics and Astronomy for their assistance in this project.

I wish to thank all the members of the MINT center (professors, graduate students, technicians, and secretaries) for their special help and for providing such a convivial work ambiance.

Finally, I wish to thank my wife Vanessa and my family for their continuous love and support. I dedicate particularly this work to my father Gilbert Scheck.

This work was supported by the National Science Foundation under Grant No. ECS-0070236 and NSF MRSEC Shared Facilities Grant No. DMR-98-09423 and No. DMR-02-13985.

CONTENTS

LIST OF ABBREVIATIONS AND SYMBOLS.....	iii
ACKNOWLEDGMENTS.....	vi
LIST OF TABLES.....	xi
LIST OF FIGURES.....	xii
ABSTRACT.....	xxi
I. INTRODUCTION.....	1
A. Motivation.....	1
B. Overview.....	6
C. Experimental work and facilities.....	7
D. Experimental techniques.....	8
1. X-ray diffraction (XRD).....	8
<u>a. High incidence angle ω-2θ diffraction. Bragg diffraction.....</u>	8
<u>b. Grazing incidence angle ω-2θ diffraction.....</u>	11
<u>c. Grazing incidence angle x-ray diffraction reflectivity.....</u>	13
2. Rutherford backscattering spectroscopy (RBS).....	14
3. X-ray photoelectron spectroscopy (XPS).....	17
4. Vibrating sample magnetometer (VSM).....	21
5. Surface morphology characterization.....	22

II.	FABRICATION AND ANALYSIS OF NI, FE AND CO FILMS GROWN ONTO n-GAAS SUBSTRATES.....	24
A.	Sample preparation.....	24
B.	Thickness calibration.....	28
1.	Film.....	28
2.	Surface oxide layer.....	34
C.	Results and discussion.....	37
1.	Structure.....	37
	<u>a. GaAs(001)</u>	37
	<u>b. GaAs(011)</u>	69
2.	Magnetic properties.....	92
	<u>a. GaAs(001)</u>	92
	<u>b. GaAs(011)</u>	122
3.	Intermixing/Interface properties of Ni on GaAs(001).....	157
	<u>a. XPS analysis</u>	157
	<u>b. Resistivity and magnetic analysis</u>	160
	<u>c. I-V Schottky characterization</u>	167
D.	Conclusion.....	172
III.	SELECTIVE DEPOSITION OF METALLIC FILMS ONTO SEMICONDUCTOR SUBSTRATES.....	176
A.	Photoinduced electrochemical deposition of Cu on p-type Si substrates.....	176
1.	Experiment.....	176
2.	Results and discussion.....	181
	<u>a. Open circuit potential of Si in the electrolyte</u>	181

	<u>b. Morphological features of the dots</u>	181
	<u>c. Structure dimensions</u>	184
	<u>d. Surface roughness</u>	189
	<u>e. Significance of the electrolyte chemical composition</u>	193
	<u>f. Selective plating through an optical mask</u>	199
B.	Selective metal electrodeposition of FM materials through doping modulation of SC surfaces.....	204
1.	Co on etched n-p-GaAs.....	206
	<u>a. Experiment</u>	206
	<u>b. Results and discussion</u>	207
2.	(Co, Ni) on ion implanted n-p-Si.....	210
	<u>a. Experiment</u>	210
	<u>b. Results and discussion</u>	213
3.	“Side-plating” ECD of Co nanowires on n-p-Si.....	218
	<u>a. Experiment</u>	220
	<u>b. Results and discussion</u>	220
C.	Conclusion.....	224
IV.	CONCLUSION.....	228
	REFERENCES.....	230

LIST OF TABLES

I.	Fractal analysis of 400 nm thick Fe films grown on GaAs(001) from FeSO ₄ and FeCl ₂ solutions.....	69
II.	Fractal analysis of 400 nm thick Fe films grown on GaAs(011) from FeSO ₄ and FeCl ₂ solutions.....	84
III.	Effect of boric acid (H ₃ BO ₃) and current density on film growth and appearance.....	85
IV.	Effect of ammonium sulfate [(NH ₄) ₂ SO ₄], boric acid (H ₃ BO ₃) and current density, and pH on film growth and appearance.....	86
V.	Effect of pulsed plating on Fe film growth and appearance.....	86
VI.	Effect of pulsed plating and current density on Fe film growth and appearance. Increase of the current density leads to thicker films uniform to the naked eye however, reducing the deposition time reveals its non-uniformity and non covered area.....	88
VII.	Magnetic properties obtained from FMR spectra for two 400 nm Fe films electrodeposited on <i>n</i> -GaAs(001) from FeSO ₄ and FeCl ₂ solutions. K_p is the perpendicular anisotropy.....	121
VIII.	Coercivity H_c of 400 nm Fe films grown on GaAs(001) from FeSO ₄ and FeCl ₂ electrolyte solutions.....	122
IX.	Description of Co layers grown on GaAs(011) under different growth conditions as indicated in the table.....	146
X.	Magnetic properties obtained from FMR spectra for two 400 nm Fe films electrodeposited on <i>n</i> -GaAs(011) from FeSO ₄ and FeCl ₂ solutions. K_p is the perpendicular anisotropy	147
XI.	Coercivity H_c of 400 nm Fe films grown on GaAs(011) from FeSO ₄ and FeCl ₂ electrolyte solutions.....	148
XII.	Surface roughness analysis in the apparent shiny and dark areas.....	193
XIII.	Effect of solution on Cu background plating.....	194

LIST OF FIGURES

1.	Diffraction of x-ray by crystal lattice planes with lattice constant d	9
2.	Geometrical aspects of diffraction. ψ is the angle between the film plane normal and the diffraction plane which contains the incident and diffracted x-ray. ϕ is the rotation angle around the film plane normal axis. The angle ω and 2θ are both in the diffraction plane. The thick and thin arrows denote respectively the x-ray and the directions.	10
3.	Geometry of x-ray grazing incidence diffraction, the angle 2θ is between the projection of incident and diffracted x-ray in the film plane.....	12
4.	Principal of Rutherford backscattering spectroscopy (RBS). In (b), the sample is tilted (30°) in order to avoid any particular crystalline direction and thus channeling. The angle detector was set at 170° with respect to the incoming He^{2+} ions beam.....	15
5.	RBS analysis of a MoSiN film on carbon (C) substrate. The peak intensities corresponding to each element constituting the sample are well separated due to the difference of mass of the respective elements. The height of the peak indicates the density of atoms and the ion energy identifies the species and the depth below the surface.....	16
6.	Kinematics of x-ray photoelectron spectroscopy (XPS).....	19
7.	Energy-level diagram of states of an atom before (a) and after (b) x-ray photoelectron irradiation. In (b), the holes are numbered in the order of creation. The energy lost by the electron falling from 2 to 1 ejects the electron from 3 (Auger electron) or is converted to x-ray fluorescence.....	20
8.	Principal of a vibrating sample magnetometer.....	23
9.	Schema of the experimental set up for electrodeposition.....	25
10.	Cyclic voltammograms in 0.1 M NiSO_4 pH 2.3 solution using $n\text{-GaAs}(001)$ and (011) substrates. Scan rate = 50 mv/s.....	27
11.	Rutherford backscattering spectroscopy (RBS) energy spectrum of 2.4 MeV incident He^{2+} ions irradiating a 10 nm Ni film grown on $\text{GaAs}(001)$	30

12. X-ray reflectivity (XRR) data of a smooth 25 nm Ni film grown on GaAs(001). 32
13. Thickness of electrodeposited Ni layers on GaAs(001) (nominal T_N , magnetic T_M , estimated by RBS T_{RBS} and by XRR T_{XRR}) as a function of deposition time. The dotted line is a linear fit of T_{XRR} data. For definition of those four thickness values see text..... 33
14. High-resolution XPS spectra in the energy range of the Ni $2p$ peak The data points and the full line are the spectra measured, respectively, on a 51 nm thick Ni layer which was exposed to air (a) and a Ni film after sputter removal of the hydroxide layer (b). The dashed line is the difference [(a)-(b)] of the two spectra, representative of the Ni(OH)₂ layer which forms on Ni upon exposure to air..... 36
15. High angle ω - 2θ x-ray measurement of a 180 nm thick Ni layer on GaAs(001). The vertical dashed lines indicate the 2θ peak positions of Ni(111), Ni(002) and Ni(022). The measurements were made with an ω -offset of 0.5°..... 38
16. High angle ω - 2θ XRD rocking curve of Ni grown on GaAs(001) for Ni(200) and (220) peaks.....39
17. Grazing incidence x-ray diffraction measurements of a 31 nm thick Ni layer on GaAs(001) with the scattering vector oriented at $\psi = 88^\circ$ from the sample normal. The detector angle was set to the position of respectively the Ni(200), Ni(220) and Ni (111) peaks for the three scans shown. The sample was rotated around the sample normal (ϕ rotation). $\phi = 0^\circ$ corresponds to the GaAs[110] in-plane direction..... 41
18. Three of the four possible alignments of the Ni (011) unit mesh on the GaAs(001) substrate Only one of the Ni{111} directions can align with a GaAs{110} direction at a time.....42
19. In plane XRD spectra for 71 nm thick Ni film grown on *n*-GaAs(001)). (a) Beam is at a $\psi = 5^\circ$ grazing angle of incidence. (b) Beam is at a $\psi = 2^\circ$ grazing angle of incidence. Detector-beam angle satisfies Ni(111) Bragg condition. The GaAs[110] direction is along $\phi = 0^\circ$ (N.B. This effect is also seen with the 36 nm thick film but the increased signal with thickness makes it easier to see in this film).....44
20. High angle ω - 2θ x-ray measurement of a 180 nm thick Ni layers grown on GaAs(001) at different pH. The vertical dashed lines indicate the 2θ peak positions of Ni(111), Ni(002), and Ni(022).....46
21. Atomic force microscope (AFM) picture of a 6 nm thick Ni layer grown on GaAs(001).....47

22.	Atomic force microscope (AFM) picture of a 36 nm thick Ni layer grown on GaAs(001).....	48
23.	Three dimensions atomic force microscope (AFM) picture of a 6 nm thick Ni layer grown on GaAs(001).....	49
24.	Three dimensions atomic force microscope (AFM) picture of a 36 nm thick Ni layer grown on GaAs(001).....	50
25.	RMS roughness of Ni films grown on GaAs(001).The line is a guide to the eye.....	51
26.	A drawing showing some important low index planes in hexagonally close packed cobalt.....	53
27.	High angle ω - 2θ x-ray measurement of a 106 nm thick Co layer grown on GaAs(001). S are the satellites originated from the Cu K_{α} and K_{β} and Tungsten (W) filament from the x-ray diffractometer source.....	54
28.	High angle ω - 2θ x-ray measurement of a 106 nm thick Co layer on GaAs(001). The vertical dashed lines indicate the 2θ peak positions of fcc Co(022) / hcp Co(11 $\bar{2}$ 0) and hcp Co(10 $\bar{1}$ 3).....	55
29.	High angle ω - 2θ x-ray measurement of a 106 nm thick Co layer on GaAs(001). The vertical dashed lines indicate the 2θ peak positions of fcc Co(10 $\bar{1}$ 0), fcc Co(111), hcp Co(0002), hcp Co(10 $\bar{1}$ 1), and fcc Co(002).....	56
30.	Grazing incidence x-ray diffraction measurements of a 106 nm thick Co layer on GaAs(001) with the scattering vector oriented at $\psi = 88^{\circ}$ from the sample normal. The detector angle was set to the position of the Co fcc and hcp phases as defined in the graph. The sample was rotated around the sample normal (ϕ rotation). $\phi = 0^{\circ}$ corresponds to the GaAs[110] in-plane direction.....	58
31.	Nuclear magnetic resonance (NMR) data of a 36 nm thick Co film grown on GaAs(001).....	60
32.	High angle ω - 2θ XRD spectra of 400 nm Fe layers grown on GaAs(001) from: (a) a FeSO ₄ solution and (b) a FeCl ₂ solution. The vertical dashed lines indicate the 2θ positions of bcc Fe(011), Fe(002), and Fe(112) peak. In order to suppress the intense substrate peaks, the measurements were taken with a ω -offset of 0.2 $^{\circ}$ –0.4 $^{\circ}$	61
33.	Zoom in of a high angle ω - 2θ XRD spectra of 400 nm Fe layers grown on GaAs(001) from: (a) a FeSO ₄ solution and (b) a FeCl ₂ solution. The vertical dashed line indicates the 2θ positions of bcc Fe(002) peak. In order to suppress	

	the intense substrate peaks, the measurements were taken with a ω -offset of 0.2° – 0.4°	63
34.	ϕ -scans at grazing incidence ($\psi = 86^\circ$ from the film normal) of 400 nm Fe films grown on GaAs(001) showing the major Fe epitaxial relations with the GaAs substrate. ϕ is the angle enclosed between scattering vector and the GaAs[110] direction. Shown are spectra for Fe grown from: (a) a FeSO ₄ solution and (b) a FeCl ₂ solution. For each sample, the upper (lower) spectrum was obtained at $2\theta = 44.6^\circ$ (65.1°), corresponding to Fe{110} (Fe{100}) in-plane peaks. The spectra are vertically offset for clarity. The insert provides schematic visualization of the GaAs (circles) and Fe (squares) surface unit mesh.....	64
35.	Atomic force microscope (AFM) picture of a 400 nm thick Fe film grown on GaAs(001) from a FeSO ₄ solution at $pH = 2.5$ and 3.5 mA/cm^2	65
36.	SEM surface morphology of a 300 sec electrodeposited Fe film grown on GaAs(001) from a FeSO ₄ electrolyte solution.....	66
37.	SEM surface morphology of a 300 sec electrodeposited Fe film grown on GaAs(001) from a FeCl ₂ electrolyte solution.....	67
38.	RMS roughness of Fe films grown on GaAs(001) from FeSO ₄ and FeCl ₂ electrolytes.....	68
39.	High angle ω - 2θ x-ray measurement of a 21 nm thick Ni layer on GaAs(011). The measurements were made with an ω -offset of 0.5°	70
40.	Grazing incidence x-ray diffraction measurements of a 21 nm thick Ni layer on GaAs(011) with the scattering vector oriented at $\psi = 88^\circ$ from the sample normal. The detector angle was set to the position of respectively the Ni(200), Ni(220) and Ni(111) peaks for the three scans shown. The sample was rotated around the sample normal (ϕ rotation). $\phi = 0^\circ$ corresponds to the GaAs[100] in-plane direction.....	71
41.	High angle ω - 2θ x-ray measurement of a 180 nm thick Co layer on GaAs(011). The vertical dashed lines indicate the 2θ positions of hexagonal Co($10\bar{1}0$) and Co($10\bar{1}1$) peak. The measurements were made with an ω offset of 0.3°	73
42.	ω -rocking x-ray measurement of a 180 nm thick Co layer on GaAs(011) at high angle ω - 2θ corresponding to hcp Co ($10\bar{1}1$)	74
43.	Grazing incidence x-ray diffraction measurements of a 280 nm thick Co layer on GaAs(011) with the scattering vector oriented at $\psi = 88^\circ$ from the sample normal. The detector angle was set to the position of the fcc Co(220) / hexagonal	

	Co (11 $\bar{2}$ 0) and fcc Co(111) / hexagonal Co (20 $\bar{2}$ 0) peaks. The sample was rotated around the sample normal (ϕ rotation). $\phi = 0^\circ$ corresponds to the GaAs[100] in-plane direction.....	75
44.	TEM image of a 25 nm Co layer on GaAs(011). The dots are assigned to GaAs diffraction patterns.....	77
45.	Nuclear magnetic resonance (NMR) data of a 36 nm thick Co film grown on GaAs(011).....	78
46.	Nuclear magnetic resonance (NMR) data of a 36 nm thick Co films grown on GaAs(011) at different pH and current densities as indicated in the graph.....	79
47.	High angle ω - 2θ XRD spectra of 400 nm Fe layers grown on GaAs(011) from: (a) a FeSO ₄ solution and (b) a FeCl ₂ solution. The vertical dashed lines indicate the 2θ positions of bcc Fe(011), Fe(002), and Fe(112) peak. In order to suppress the intense substrate peaks, the measurements were taken with an ω -offset of 0.2°–0.4°	81
48.	Zoom in of high angle ω - 2θ XRD spectra showing the out-of-plane orientation of 400 nm Fe layers grown on GaAs(011) from: (a) a FeSO ₄ solution and (b) a FeCl ₂ solution. The vertical dashed lines indicate the 2θ positions of bcc Fe(011) peak. In order to suppress the intense substrate peaks, the measurements were taken with a ω -offset of 0.2°–0.4°	82
49.	ϕ -scans at grazing incidence ($\psi = 86^\circ$ from the film normal) of 400 nm Fe films grown on GaAs(011) showing the major Fe epitaxial relations with the GaAs substrates. ϕ is the angle enclosed between scattering vector and the GaAs[110] direction. Shown are spectra for Fe grown from: (a) a FeSO ₄ solution and (b) a FeCl ₂ solution. For each sample, the upper (lower) spectrum was obtained at $2\theta = 44.6^\circ$ (65.1°), corresponding to Fe{100} (Fe{110}) in-plane peaks. The spectra are vertically offset for clarity. The insert provides schematic visualization of the GaAs (circles) and Fe (squares) surface unit mesh.....	83
50.	High angle ω - 2θ x-ray measurement of a 46 nm thick FeNi layer on GaAs(011). The measurements were made without any ω -offset.....	89
51.	Zoom in of a high angle ω - 2θ x-ray measurement of a 46 nm thick FeNi layer on GaAs(011). The measurements were made with an ω -offset of 0.5°.....	90
52.	Grazing incidence x-ray diffraction measurements of a 46 nm thick FeNi layer on GaAs(011) with the scattering vector oriented at $\psi = 88^\circ$ from the sample normal. The detector angle was set to the position of respectively the Fe(211), Fe(220) and Fe(110) peaks for the three scans shown. The sample was rotated around the	

- sample normal (ϕ rotation). $\phi = 0^\circ$ corresponds to the GaAs[100] in-plane direction..... 91
53. Angular dependence of the remanence for Ni films grown on GaAs(001) with thicknesses indicated in the graph. A value of the sample rotation angle ϕ equal to zero corresponds to a magnetic field direction parallel to GaAs[110]..... 94
54. Free anisotropy energy and expected remanence for: (a) uniaxial, (b) (001), and (c) (011) anisotropy as a function of in-plane angle using Eqs. (10)–(12) assuming $K_1 = -0.5 \times 10^5$ erg/cm³ and $K_2 = -0.2 \times 10^5$ erg/cm³. The (001) and (011) anisotropy are plotted following the epitaxial relationship Ni[100](001)//GaAs[110](011) and Ni[111](011)//GaAs[110](001) respectively. The zero degree angle corresponds to the hard axis of the system which is along the GaAs[110] direction.....95
55. Remanence simulation of respectively (001), (011), and uniaxial anisotropy expected from its respective free energy using Eqs. (10)–(12). The bold curve represents the sum of the three anisotropy affected with the same weight of 0.33. The (001) and (011) anisotropy are plotted following the epitaxial relationship Ni[100](001)//GaAs[110](011) and Ni[111](011)//GaAs[110](001) respectively. The zero degree angle corresponds to the GaAs[110] direction.97
56. Angular dependence of the remanence for a 48 nm and a 19 nm thick Ni film on GaAs(001). A value of the sample rotation angle ϕ equal to zero corresponds to a magnetic field direction parallel to GaAs[110]. The three arrows point to the characteristic positions of the remanence loops (hard axis, easy axis and 'almost-easy axis) for which individual hysteresis loops are shown in Fig. 58. The lines correspond to a fit by simulation of a mixture of a four-fold and a uniaxial anisotropy components. The amount of (011), (001) and uniaxial component in 19 nm and 48 nm thick Ni film is respectively 1.6%, 38.4%, 60% and 1%, 19%, 80%..... 98
57. Angular dependence of the remanence for a 48 nm thick Ni film on GaAs(001). A value of the sample rotation angle ϕ equal to zero corresponds to a magnetic field direction parallel to GaAs[110]. The lines correspond to a fit by simulation of a mixture of a four-fold and a uniaxial anisotropy components taking into account the azimuthal mosaic spread present in XRD data. The amount of (011), (001) and uniaxial component in the 48 nm thick Ni film is 1%, 19%, 80% respectively.. 100
58. Hysteresis loops of four different Ni layers grown on GaAs(001) with the thicknesses indicated in the graph. The measurements actually were extended to 10 kOe to ensure saturation of the films. Shown are only parts of those loops. Each graphs does show three loops for each of which the orientation of the magnetic field with respect to the GaAs[110] direction is mentioned.....101

59. The effect of film thickness on magnetic anisotropy for Ni films grown on GaAs(001) from a solution with $pH = 2.5$, squareness (M_r/M_s , normalized by M_s) as a function of film thickness..... 103
60. Coercivity H_c as a function of Ni layer thickness for three different orientations of the magnetic field as described in the text. The lines are guides to the eye..... 104
61. Angular dependence of the remanence for 36 nm thick Ni films grown on GaAs(001) at different pH with their values indicated in the graph. A value of the sample rotation angle ϕ equal to zero corresponds to a magnetic field direction parallel to GaAs[110].....106
62. Free anisotropy energy and expected torque for: (a) uniaxial, (b) (001), and (c) (011) anisotropy as a function of in-plane angle using Eqs. (10)–(12) and (14)–(16) assuming $K_1 = -0.5 \times 10^5 \text{ erg/cm}^3$ and $K_2 = -0.2 \times 10^5 \text{ erg/cm}^3$. The (001) and (011) anisotropy are plotted following the epitaxial relationship Ni[100](001)//GaAs[110](011) and Ni[111](011)//GaAs[110](001) respectively. The zero degree angle corresponds to the hard axis of the system which is along the GaAs[110] direction.....108
63. Torque simulation of respectively (001), (011), and uniaxial anisotropy expected from its respective free energy using Eqs. (14)–(16) assuming $K_1 = -0.5 \times 10^5 \text{ erg/cm}^3$ and $K_2 = -0.2 \times 10^5 \text{ erg/cm}^3$. The bold curve represents the sum of the three torques $L_{(001)}$, $L_{(011)}$, and $L_{(uni)}$ affected with the same weight of 0.33. The (001) and (011) anisotropy are plotted following the epitaxial relationship Ni[100](001)//GaAs[110](011) and Ni[111](011)//GaAs[110](001) respectively. The zero degree angle corresponds to the GaAs[110] direction. 109
64. Torque curves for a 36 nm thick Ni film on GaAs(001). A value of the sample rotation angle ϕ equal to zero corresponds to a random position for the magnetic field with respect to GaAs[110]. The external applied field had a value of 2000 Oe..... 110
65. In-plane dispersion of the Damon-Eshbach spin wave mode from Brillouin light scattering (BLS) on the in-plane direction of the applied magnetic field for 7, 15, 30 and 35 nm thick Ni films grown on GaAs(001) surfaces..... 112
66. Dependence of the in-plane uniaxial anisotropy constant K_u^2 from BLS on the inverse Ni film thickness grown on GaAs(001) surfaces..... 113
67. Angular dependence of the remanence for Co films grown on GaAs(001) with thicknesses indicated in the graph. A value of the sample rotation angle ϕ equal to zero corresponds to a magnetic field direction parallel to GaAs[110]. The three arrows point to the characteristic positions of the remanence loops (easy axis and hard axis) of a 36 nm thick Co film for which individual hysteresis loops are shown in Fig 68.....115

68. Hysteresis loops of the three different Co layers grown on GaAs(001) with thicknesses indicated in the graph. The measurements actually were extended to 2 kOe to ensure saturation of the films. Shown are only parts of those loops. Each graphs does show loops for each of which the orientation of the magnetic field with respect to the GaAs[110] direction is mentioned.....116
69. Angular dependence of the remanence for Co films grown on GaAs(001) with pH and thicknesses indicated in the graph. A value of the sample rotation angle ϕ equal to zero corresponds to a magnetic field direction parallel to GaAs[110]...118
70. Angular dependence of the remanence for 400 nm Fe films grown on GaAs(001) from: (a) a $FeSO_4$ solution and (b) a $FeCl_2$ solution. Dominant is a four-fold anisotropy.....119
71. (a) Angular dependence of the remanence (M_r/M_s , normalized by M_s). (b) FMR resonance field (H_r), showing the in-plane magnetic anisotropy symmetry for 400 nm Fe films deposited using $FeSO_4$ solutions on GaAs(001). Similar results were also observed for Fe films deposited using $FeCl_2$ solution. The line in (b) is a fit to the data to extract the anisotropy values. A value of the sample rotation angle ϕ equal to zero corresponds to a magnetic field direction parallel to GaAs[110]...120
72. Hysteresis loops for 400 nm Fe films grown on GaAs(001) from: (a) a $FeSO_4$ solution and (b) a $FeCl_2$ solution. The field is applied along the [001] (solid line) and the $[\bar{1}\bar{1}0]$ (dashed line) directions for (a) and (b). Shown are only the low field parts of the hysteresis loops which were measured between ± 10 kOe..... 123
73. Angular dependence of the remanence for a 21 nm and 85 nm thick Ni films grown on GaAs(011). A value of the sample rotation angle ϕ equal to zero corresponds to a magnetic field direction parallel to GaAs[110]..... 125
74. Squareness (M_r/M_s , normalized by M_s) of Ni films grown on GaAs(011) as a function of the film thickness for orientation of the magnetic field along easy and hard axis of the films.....126
75. Squareness (M_r/M_s , normalized by M_s) of Ni films grown on GaAs(011) as a function of the pH of the electrolyte solution for orientation of the magnetic field along easy and hard axis of the films.....127
76. Hysteresis loops of Ni films grown on GaAs(011) with thicknesses indicated in the graph. The graph does show two loops for each of which the orientation of the magnetic field with respect to the GaAs directions is mentioned. The dotted line in (b) shows the hard axis loop located at 83° away from GaAs[110]..... 129
77. Anisotropy field (H_k) versus thickness for Ni films grown on GaAs(011). The line is a guide to the eye.....130

78. Coercivity H_c as a function of Ni layer thickness for two different orientations of the magnetic field as described in the text. The lines are guides to the eye..... 131
79. In-plane dispersion of the Damon-Eshbach spin wave mode from Brillouin light scattering (BLS) on the in-plane direction of the applied magnetic field for 15, 20 and 30 nm thick Ni films grown on GaAs(011) surfaces..... 132
80. Dependence of the in-plane uniaxial anisotropy constant K_u^2 from Brillouin light scattering (BLS) on the inverse Ni film thickness grown on GaAs(011) surfaces..... 133
81. Torque data of a 36 nm thick Ni layer grown on GaAs(011) with thicknesses indicated in the graph. The measurements were performed under an external magnetic field of 2000 Oe. The orientation of the magnetic field with respect to the GaAs[100] direction is random..... 135
82. Free anisotropy energy and expected torque for (111) surface as a function of in-plane angle using Eqs. (17)–(18) assuming $K_1 = -0.5 \times 10^5$ erg/cm³ and $K_2 = -0.2 \times 10^5$ erg/cm³ and the epitaxial relationship Ni(111)[110]//GaAs(011)[110]. The zero degree angle corresponds to the hard axis of the system which is along the GaAs[110] direction..... 136
83. Angular dependence of the remanence for Co films grown on GaAs(011) with thicknesses indicated in the graph. A value of the sample rotation angle ϕ equal to zero corresponds to a magnetic field direction parallel to GaAs[100]. The two arrows point to the characteristic positions of the remanence loop (easy axis and hard axis) of a 18 nm thick Co film for which individual hysteresis loops are shown in Fig. 84..... 138
84. Hysteresis loops of four different Co layers grown on GaAs(011) with thicknesses indicated in the graph. The measurements actually were extended to 2 kOe to ensure saturation of the films. Shown are only parts of those loops. Each graph does show two loops for each of which the orientation of the magnetic field with respect to the GaAs direction is mentioned..... 139
85. Squareness (M_r/M_s , normalized by M_s) of Co films grown on GaAs(011) as a function of the film thickness for orientation of the magnetic field along easy and hard axis of the films..... 141
86. Anisotropy field (H_k) versus thickness for Co films on GaAs(011). The line is a guide to the eye..... 142
87. Coercivity H_c as a function of Co layer thickness for two different orientations of the magnetic field as described in the text. The lines are guides to the eye..... 143

88. Remanence curve of a 36 nm thick Co layer grown on GaAs(011) with a current density of 11 mA/cm² and a pH of 3.35. A value of the sample rotation angle ϕ equal to zero corresponds to a magnetic field direction parallel to GaAs[001]. The three arrows point to the characteristic positions of the remanence loop (easy axis and hard axis) for which individual hysteresis loops are shown in Fig. 89..... 144
89. Hysteresis loop of a 36 nm thick Co layer grown on GaAs(011) at a current density of 11 mA/cm² and a pH of 3.35. The measurements actually were extended to 2 kOe to ensure saturation of the films. Shown are only parts of those loops. The graph does show three loops for each of which the orientation of the magnetic field with respect to the GaAs[001] direction is mentioned..... 145
90. Angular dependence of the remanence for 400 nm Fe films grown on GaAs(011) from: (a) a FeSO₄ solution and (b) a FeCl₂ solution. Dominant is a uniaxial anisotropy..... 149
91. (a) Angular dependence of the remanence (M_r/M_s , normalized by M_s) and (b) FMR resonance field (H_r), showing the in-plane magnetic anisotropy symmetry for 400 nm Fe films deposited using FeSO₄ solutions on GaAs(011). Similar results were also observed for Fe films deposited using FeCl₂ solution. The line in (b) is a fit to the data to extract the anisotropy values..... 150
92. Hysteresis loops for 400 nm Fe films grown on GaAs(011) from: (a) a FeSO₄ solution and (b) a FeCl₂ solution. The field is applied along the [011] (solid line) and the [100] (dashed line) directions for (a) and (b). Shown are only the low field parts of the hysteresis loops which were measured between ± 10 kOe..... 151
93. Angular dependence of the remanence for FeNi films grown on GaAs(011) with thicknesses indicated in the graph. A value of the sample rotation angle ϕ equal to zero corresponds to a magnetic field direction parallel to GaAs[100]. The two arrows point to the characteristic positions of the remanence loops (easy axis and hard axis) for which individual hysteresis loops are shown in Fig. 94..... 153
94. Hysteresis loops of FeNi films grown on GaAs(011) with thicknesses indicated in the graph. The measurements actually were extended up to 5 kOe to ensure saturation of the films. Shown are only parts of those loops. The graph does show two loops for each of which the orientation of the magnetic field with respect to the GaAs directions is mentioned..... 154
95. Squareness (M_r/M_s , normalized by M_s) of FeNi films grown on GaAs(011) as a function of the film thickness for orientation of the magnetic field along easy and hard axis of the films..... 155
96. Anisotropy field (H_k) versus thickness for FeNi films on GaAs(011). The line is a guide to the eye..... 156

97. Coercivity H_c as a function of FeNi layer thickness for two different orientations of the magnetic field as described in the text. The lines are guides to the eye... 158
98. (a) XPS spectra in the energy range of the Ga $2p$ peak measured on a 6 nm thick Ni layer. No Ga peak is observed. (b) XPS spectra in the energy range of the As $3d$ peak. The three spectra shown were measured on a 6 nm thick Ni layer and a 14 nm thick Ni layer, respectively. The two spectra of the 6 nm thick layer were measured at different detector angles as indicated..... 159
99. Van der Pauw configuration for resistivity measurements. The first resistance is defined as $R_{AB,CD} = (V_D - V_C)/i_{AB}$, when a current i_{AB} is applied to contact A and take off at contact B while the potential difference is measured between contacts C and D. Analogously, the second resistance is defined as $R_{BC,DA} = (V_A - V_D)/i_{BC}$. The resistivity is then calculated from Eq. (20) as

$$\rho = \frac{\pi T}{\ln 2} \frac{R_{AB,CD} + R_{BC,DA}}{2} \cdot f \dots\dots\dots 161$$
100. Plot of the factor f from Eq. (21) which is a function only of the ratio $R_{AB,CD}/R_{BC,DA}$. The relation between f and the ratio is given by

$$\cosh\left[\frac{(R_{AB,CD}/R_{BC,DA}) - 1 \ln 2}{(R_{AB,CD}/R_{BC,DA}) + 1} \frac{1}{f}\right] = \frac{1}{2} \exp\left(\frac{\ln 2}{f}\right) \dots\dots\dots 162$$
101. (a) Saturation magnetization per unit area $M_s \times T$ of Ni films as a function of layer thickness (data points). The dashed line corresponds to the values expected for bulk Ni. The insert shows the saturation magnetization M_s , which reveals a small deviation from the bulk properties (dashed line) for the thinnest films. (b) Room-temperature resistivity times layer thickness as a function of Ni layer thickness (data points). The straight line is a linear fit to the experimental data according to Fuchs' model. The insert shows a magnification of (b) in the thickness range 0–20 nm..... 165
102. Transmission electron microscope (TEM) cross section picture of a Ni film grown on GaAs(001)..... 166
103. Graph allowing the extraction of both ideality factor and barrier height according to Eq. (24). The insert shows the current versus bias voltage characteristics for different annealing temperatures as indicated in the graph..... 169
104. Barrier height (determined from Schottky barrier $I-V$ measurements) of a 200 nm Ni film on GaAs(001) and corresponding XPS As $3d$ peak intensity (for a 9.5 nm thick Ni film) for different annealing temperatures..... 170
105. Temperature dependence of the RMS roughness of a 200 nm Ni film grown on GaAs(001). For each temperature, roughness analysis was made at different area

- of the surface of the film using a AFM scanning probe. The dashed line is a guide to the eye..... 171
106. Sketch of (a) the principle of photoinduced deposition on a *p*-type semiconductor and (b) schematic band diagram of *p*-Si in aqueous solution before contact..... 177
107. Experimental set up for photoinduced electrodeposition of Cu on *p*-Si substrate..... 180
108. The open cell potential, measured against a SCE of *n*-Si and *p*-Si in the CuSO₄ solution used for deposition. Electrical contact is made to the back of the Si substrate using Ga-In eutectic. The laser is switched on after 100 s and it illuminates an area ~ 4 mm². These are the original data without any shifting of the curves and show the qualitative trend of the opposite OCP signs of *n*- and *p*-type Si upon illumination..... 182
109. Optical images (100×100 μm² area) and AFM cross-section profiles of two typical Cu dots formed by illuminating *p*-Si with a ~ 1–2 μm diameter laser spot. (a) An optical image for the dot formed after 60 s of red laser illumination. (b) An optical image for the dot formed after 5 s of red laser illumination. (c) AFM cross-section profile for the dot in (a). (d) AFM cross-section profile for the dot in (b). There is a dark ring surrounding the inner shiny area as shown (c). Inside the dark ring, islands of Cu clusters with Cu metallic color are identified using both a high magnification lens and an AFM. For the dark Cu spot, no distinct inner area can be differentiated and the diameter is represented by D_o only, as shown in (d)... 183
110. Average outer diameter D_o of a time dependence series (0–60 s) of Cu dots formed by laser illuminating of *p*-Si substrates, indicating the effects of wavelength, beam intensity and substrate surface defect density [(a) undamaged Si; (b) ion irradiated Si]. Small and large circles (squares) indicate illumination with low and high intensity red (green) laser light, respectively..... 187
111. Surface roughness σ_∞ and correlation length ξ for four Cu dots inside D_i using surface fractal analysis, showing the effect of intermittent illumination and the method used in the surface analysis. Both the vertical and horizontal axes are in logarithmic bases. All have total 10 s of illumination. Curve *A* is made by green laser beam with no interruption, curve *B* is made by green beam also with a 1 s of no illumination between ten 1 s of illumination. Curves *C* and *D* are the counterparts of curves *A* and *B* by red laser beam, respectively. Cross-wavelength comparison is not intended due to the complication of the wavelength effect on the growth of Cu features..... 190
112. Roughness σ_∞ and correlation length ξ inside D_i of Cu dots formed by illuminating the *p*-Si substrate using a red laser beam for 5–60 s. The open and closed circles indicate data points for the Cu dots generated by the red laser

- illumination at high and low intensities, respectively. The open and closed squares are for the counterparts in the case of green laser illumination..... 191
113. Optical images ($150 \times 150 \mu\text{m}^2$) of Cu dots formed by illuminating *p*-Si using a red laser beam of $\sim 1\text{--}2 \mu\text{m}$ focused spot size for 60 s with (a) no additives, (b) 0.01 mol/L ascorbic acid and 0.005 mol/L SPT but no NH_4F , (c) 0.01 mol/L ascorbic acid, 0.005 mol/L SPT, and 0.0025 mol/L NH_4F , (d) 0.01 mol/L ascorbic acid, 0.005 mol/L SPT, and 0.02 mol/L NH_4F , in the CuSO_4 + DW solution..... 195
114. XPS spectra measured in the background region away from any visible Cu dots for solutions containing (a) no additives, (b) all additives but no NH_4F , (c) all additives, 0.0025 mol/L NH_4F , (d) all additives, 0.01 mol/L NH_4F , and (e) all additives, 0.02 mol/L NH_4F . Only (a) has no XPS signal for Cu. Table XIII lists the additives and their concentrations in these solutions..... 197
115. (a) Optical and (b) AFM images ($10 \mu\text{m} \times 10 \mu\text{m}$ area) of part of a Cu dot formed by illuminating undamaged *p*-Si with a $1\text{--}2 \mu\text{m}$ diameter red laser spot using solution (e). The scratches result from profilometry..... 198
116. Experimental set up for photoinduced deposition of Cu features onto *p*-Si substrate through an optical mask..... 200
117. Optical picture of photoinduced electrodeposition of Cu on *p*-Si substrate through a mask using 150 mW green laser beam..... 201
118. Experimental set up for photoinduced electrodeposition of Ni onto *p*-Si and *p*-GaAs substrates..... 203
119. Current-voltage characteristic for electrodeposition on *p*- and *n*-type GaAs. Applying an increasing cathodic potential to the *n*- or *p*-type GaAs substrate while monitoring the current flow allows to identify the onset of the electrochemical deposition of Co. Deposition starts at -0.9 V (vs. standard calomel electrode) for *n*-type GaAs ($7 \times 10^{17} \text{ cm}^{-3}$ carrier concentration) substrates and -1.6 V for *p*-type GaAs ($8 \times 10^{17} \text{ cm}^{-3}$ carrier concentration). In the corresponding intermediate potential range with width $\Delta V = 0.7 \text{ V}$ Co deposition would occur selectively, being enabled on *n*-doped surfaces and inhibited on *p*-type areas..... 205
120. Sample preparation for selective ECD of Co/Ni on patterned etched *n-p*-GaAs. A 500 nm thick *n*-doped GaAs layer is grown by Molecular Beam Epitaxy on a *p*-type GaAs substrate (a). Subsequently, through masking and a chemical etch, pits are formed with their depth extending into the *p*-doped substrate (b). This way both *n*-doped and *p*-doped regions are exposed at the sample surface. Samples were prepared with structure sizes ranging from mm to a few μm 208
121. Demonstration of selective Co growth on patterned *n-p*-GaAs. Optical micrographs showing three examples of selective electrodeposition of Co on *n*-

	doped surface areas of GaAs while leaving <i>p</i> -doped areas uncovered. The deposition was done at a cathodic potential corresponding to the voltage range between the onset of deposition on <i>n</i> -type GaAs and that of <i>p</i> -type GaAs (Fig. 119). The bars in the lower left corner of each panel correspond to a length of 10 μm	209
122.	Optical picture of a Co film selectively plated on (500 nm) <i>n-p</i> -GaAs etched substrate. The deposition of small Co pits in the center of the picture coincides with the dislocation of the substrate (500 nm) <i>n-p</i> -GaAs.....	211
123.	AFM micrograph of defect plating. On larger areas of <i>p</i> -doped GaAs surfaces small defects in form of conical protrusions are found. The defects are small Co deposits on the surface regions which inhibit Co deposition. The dimensions in this example are about 200 nm height with a 10 μm diameter. The area density of these defects corresponds to the density of screw dislocations ending at the surface. We believe that these Co deposits are formed through nucleation enabled through electronic defect states in the vicinity of screw dislocations.....	212
124.	Substrate preparation for selective electrodeposition of Co on ion implanted <i>p</i> -Si substrate.....	214
125.	(a) Optical pictures of a Ta pattern sputter deposited on <i>p</i> -Si substrate. A white light is shining from the left in order to reveal the topography of the mask features. The reflection of the lights (bright lines) indicates higher features on the Ta surface. (b) Optical pictures of Ni film selectively electroplated on the <i>n</i> -Si features on the corresponding ion implanted <i>p</i> -Si wafer under -1.5 V for 220 s. It is to notice the unusual progressive deposition of material.....	215
126.	Implantation profile of P ions irradiated on a pattern Ta/ <i>p</i> -Si substrate.....	217
127.	Drawing of the side plating sample preparation and experimental set up.....	219
128.	SEM picture of a ~ 1.3 μm and a ~ 800 nm wide Co wire “electro-sideplated” on (50 nm)SiO ₂ /(500 nm)Cr/(50 nm)SiO ₂ /(500 nm)Cr/ <i>p</i> -Si and (200 nm)SiO ₂ /(800 nm) <i>n</i> -Si/ <i>p</i> -Si substrate respectively.....	222
129.	SEM picture of a ~ 1.5 μm and a ~ 800 nm wide Co wire “electro-sideplated” on a (200 nm)SiO ₂ /(800 nm) <i>n</i> -Si/ <i>p</i> -Si substrate. The sample was tilted by 40° with respect to the normal of the wire surface.....	223

ABSTRACT

The discovery of spin-dependent transport phenomena has spurred investigations of various material combinations involving ferromagnetic (FM) materials. The proposal of creating active spin-electronic three-terminal devices with transistor-like characteristics caused a wide interest in combinations of ferromagnetic materials with semiconductors (SC). Such devices would require the growth of epitaxial ferromagnetic layers with well-defined crystallographic magnetic and interface properties.

In this respect, electrochemical deposition (ECD) is a low-energy, room temperature deposition process, which is capable of growing high quality epitaxial layers.

In the present work, the author presents the structural and magnetic properties of Ni, Co, Fe and iron-rich FeNi films grown by ECD directly onto *n*-GaAs(001) and (011). In particular, the conditions upon which high quality, continuous films with defined magnetic properties at low thickness have been determined. For instance, epitaxial Ni films grown on GaAs(001) exhibited a sharp FM/SC interface after annealing at temperatures up to 250 °C. In addition, successful electrodeposition of epitaxial Fe films on *n*-GaAs(001) and (011) has been achieved where the structural quality of the films depends on the composition of the plating solution.

Another attractive aspect of ECD is its capability to achieve selective growth of FM metallic features directly onto SC substrates without the need for mask fabrication. For instance, focused light beam illumination of SC substrates can induce metal film deposition at the illuminated regions. Similarly, upon application of a cathodic potential,

the Schottky barrier formed at the SC substrate/electrolyte interface can be biased in the forward (reverse) direction for *n*-type SC (*p*-type SC), leading to selective electron transfer from a *n*-type SC while breakdown of the Schottky barrier would be necessary for deposition on a *p*-type substrate. The process will thus be spatially selective on a lateral modulation of the substrate doping.

In this respect, the author presents experimental results to elucidate the electroless growth of Cu structures from CuSO₄ based solutions on *p*-Si upon laser illumination.

Additionally, the author demonstrates the selective electrodeposition of ferromagnetic Co on *p/n* doping patterns in a GaAs and a Si surface where patterns were created by chemical etching (GaAs) and ion-implantation (*p*-Si).

I. INTRODUCTION

A. Motivation

The discovery of spin-dependent transport phenomena^{1,2,3} has spurred investigations on the spin-dependent transport properties of various material combinations involving ferromagnetic (FM) materials. The proposal of creating active spin-electronics three-terminal devices with transistor-like characteristics⁴ caused a still increasing interest in the integration of ferromagnetic materials with semiconductors. Such devices would require that electrons could be transferred between the FM and the semiconductor under conservation of the spin polarisation.⁵ Although diffusive transport with spin conservation appears unfeasible,^{6,7} ballistic transport or tunnelling could conserve the electron spin. These effects might be achieved by forming a Schottky barrier at the FM/semiconductor. This interface would have to be chemically sharp at the atomic level and exhibit the least possible concentration of defects, features that are very difficult to achieve. Most transition elements (including Ni, Fe and Co) react with silicon and form silicides even at room temperature.^{8,9} FM materials deposited on GaAs by evaporation or sputtering often show interdiffusion of Ga and/or As into the FM layer, which results in reduced magnetization values and increased resistivities.¹⁰⁻¹³ More recent work showed that Fe intermixing with GaAs(001) substrates can be avoided by room temperature deposition with suitable prior surface preparation while still obtaining good epitaxial growth.^{14,15} Spin-injection experiments using Fe layers on AlGaAs¹⁶ also showed encouraging results.

A promising route to overcoming the problem of interface intermixing might be the use of a deposition technique wherein the atoms to be deposited reach the substrate with very low energy. Electrodeposition is of interest in this respect, as it is a room temperature process which, as shown previously,¹⁷⁻²⁰ can yield high quality epitaxial layers. Electrodeposition of Fe however is complicated by the sensitivity to the oxidation state of the Fe ions and so far has eluded successful deposition on semiconductor materials.

In this present study, the structural and magnetic properties of Ni, Co, and Fe films grown by electrodeposition from respectively NiSO₄, CoSO₄ and FeSO₄/FeCl₂ solutions directly onto the (001)/(011) surfaces of *n*-GaAs are presented.²¹⁻²⁷ In particular, the conditions upon which high quality, continuous films are obtained at low thickness are discussed. Subsequently, the author shows how Ni films can be grown by electrodeposition directly onto GaAs(001) without interdiffusion^{28,29} or surface segregation of As or Ga. The resulting electrical and magnetic properties confirm the good quality of the ferromagnetic film and of the interface. The effect of annealing on the chemical interface intermixing and resulting changes in the Schottky barrier properties of electrodeposited epitaxial Ni/GaAs(001) contacts is also reported.²⁹

Another attractive aspect of the ECD technique is its potential to grow patterned FM materials on semiconductor either by selective photoinduced deposition on *p*-doped SC substrate or selective ECD through doping modulation of SC surfaces.

Current methods for selective metal deposition require lithographic methods for the definition of a pattern by a resist mask, followed by blanket deposition and consequent mask removal. ECD on the other hand is a suitable technique to achieve

selective growth *directly*, without the need for mask fabrication. Metallic film growth by ECD in fact takes place through electron transfer from the substrate to the metal ion in solution, and consequently depends on the redox potential (E_{redox}) of the metal ion and on the distribution of electronic states at the solid surface.³⁰ The latter is a function of the electronic band structure of the substrate, as well as of surface structure and defects; these characteristics can all be locally manipulated to achieve spatially selective deposition of thin-film features. For example, by selective generation of surface scratches/defects using either a focused ion beam or atomic force microscope (AFM) scratching of a native oxide layer, selective deposition of Cu and Au on *p*-Si and *n*-Si substrates (the latter biased with negative voltages) was achieved.^{31,32}

Focused light beam illumination of SC substrates (Si, Ge, GaAs, SiC, InP, InSe, TiO₂, etc.) immersed in electrolytic solutions containing metal ions (Cu, Ni, Au, Pt, Pd, W, Cd, etc.)³³⁻³⁸ was reported to induce metal film deposition at the illuminated regions. In these instances, metal reduction is activated by electrons that become available at the semiconductor surface, either through a complementary oxidation reaction at the nonilluminated³⁹ region or through the production of electron-hole pairs in the semiconductor, followed by separation of the charge carriers.

With Si substrates, the oxidation reaction is often Si dissolution, which can be induced by the presence of fluorine ions, for example through the following reaction:



Electron-hole separation could be induced by the band bending at the interfaces or by the application of a bias voltage to the substrate. Spontaneous precipitation of copper from electrolytes containing Cu²⁺ ions and F⁻ was reported to take place on *n*-type Si (*n*-Si), *p*-

type Si (*p*-Si), and polycrystalline Si (poly-Si) substrates with or without laser illumination.⁴⁰⁻⁴³ In microelectronic circuit microfabrication, this process can lead to unwanted contamination and device failure; consequently, modeling⁴³ and experimental activities were performed with the objective to avoid it. The addition of suitable surfactants⁴⁰ or substrate biasing during HF etching⁴³ was found to reduce Cu contamination. On the other hand, this phenomenon can be exploited for metallization of Si substrates. In this respect, addition of ammonium fluoride (NH₄F) in CuSO₄ solutions produced uniform and adhesive Cu films on Si substrates with or without illumination after the Si (*n*-, *p*-, or poly-Si) substrates were immersed in the solution for 10 s to several hours.⁴² Under optimum conditions, the deposition rate was around 100 nm/h and the surface roughness was 10–20 nm 2 h after the immersion of the substrate in the electrolyte. Except for illumination using near field optics, which resulted in Ni (Ref. 37) or Co (Ref. 44)⁴⁴ structures as small as 250 nm on *p*-Si, the sizes of the deposited features were reported to be much larger than the laser beam diameter. Light-induced charge-carrier diffusion,⁴⁵ localized thermal profile,^{36,46} and laser beam intensity profile⁴⁵ are the main possible factors limiting the miniaturization of these structures. The structure sizes obtained by far field laser-induced Cu deposition were reported to be as small as 1 μm with dilute HF present in the solution on *n*-GaAs substrates but they were not as small on *p*-Si or *p*-GaAs using a relative motion between the substrate and the laser beam.³⁸ Larger structure sizes were reported if the relative motion was slowed down or stopped. In addition, background Cu precipitation was observed everywhere on the substrates.³⁸

In the present work, experimental results to elucidate the electroless growth of Cu structures from CuSO_4 based solutions on p -Si upon laser illumination are presented.^{47,48} The dependence of the structure dimensions on duration, intensity, and wavelength of the illumination and on the carrier lifetime in the p -Si semiconductor substrate is demonstrated. The effect of spontaneous background plating is studied as a function of the composition of the plating solution. In addition, electroless photoinduced metal pattern deposition through optical masks is investigated.

Alternatively, selective metal ECD through doping modulation of SC surfaces is of growing interest. Indeed, electrodeposition is a method widely used in industrial production, which has been proven capable to produce high quality – in some cases even epitaxial – metallic layers.²⁷ On one hand, the nature of the deposition process allows deposition into cavities, like pores in polycarbonates^{49,50} or alumite,⁵¹ which otherwise would be inaccessible by molecular beam epitaxy or sputtering. On the other hand, the process requires a constant charge transfer between substrate and solution and is consequently limited to deposition onto conducting substrates. This charge transfer can, in the simplest case, be inhibited by an insulating layer. Alternatively, the charge transport can be funneled through a quantum well structure surrounded by low carrier concentration semiconductor material.⁵² The work presented here was motivated by the observation of the different electrochemical response of p - or n -doped GaAs surfaces in electrolytic solutions. During the ECD process, the semiconductor substrate serves as cathode and therefore is negatively biased against the plating solution. The semiconductor/electrolyte interface essentially forms a diode, the forward or reverse bias direction of which depends on the doping polarity. Electron transfer from a n -type

semiconductor is thus possible, while breakdown of the Schottky barrier would be necessary for deposition on a *p*-type substrate. The process will thus be spatially selective on a lateral modulation of the substrate doping. The ability to perform selective deposition of ferromagnetic films on semiconductors could enable the maskless fabrication of devices based on spin-dependent transport⁵³ such as MRAMs and spin transistors.^{4,54} Here, the selective electrodeposition of ferromagnetic Co (Ni) on a *n/p* doping pattern in a GaAs (Si) surface along with ECD of Co nanowires on *n/p* doping longitudinal pattern in a Si cleaved edge substrate are demonstrated.⁵⁵

B. Overview

This work is divided into three parts: Sec. I describes the experimental techniques used by the author in his present work, Sec. II describes the structural and magnetic properties of ferromagnetic metallic thin films (Ni, Fe, Co) grown onto GaAs substrates using electrochemical deposition (ECD) and Sec. III describes the selective self-assembled property of electrodeposition technique for metallic films (Cu, Co) onto semiconductor substrates (Si, GaAs). In detail, Sec. I D describes, by order of appearance, the principles of x-ray diffraction (XRD), Rutherford backscattering spectroscopy (RBS), x-ray photoelectron spectroscopy (XPS), and vibrating sample magnetometry (VSM). Section II A describes the sample preparation, Sec. II B the thickness calibration, and Sec. II C the results and discussion of the structure and magnetic properties of Ni, Co, and Fe thin films grown on GaAs(001) and (011) substrates. More specifically, Sec. II C 3 describes the intermixing/interface properties of Ni films on GaAs(001), Sect. III A the photoinduced electrochemical deposition of Cu on

p-type Si substrates while Sec. III B describes the selective metal electrodeposition of FM materials through doping modulation of SC surfaces for Co on etched *n/p*-GaAs, Ni on ion implanted *n/p*-Si and “side-plating” ECD of Co nanowires on cleaved *n/p*-Si substrate.

C. Experimental work and facilities

Except as stated below, the experimental work was done by the author using the facilities at the center for materials for information technology (MINT) at the University of Alabama, Tuscaloosa, AL, USA. The ferromagnetic resonance (FMR) measurements were performed by Dr. Y. Ding and Prof. C. Alexander at the MINT center. The nuclear magnetic resonance (NMR) measurements were done by Jürgen Kohlhepp at the University of Technology, Eindhoven, Netherlands. The Rutherford backscattering spectroscopy (RBS) measurements were performed by Dr. T.F. Isaacs-Smith of Auburn University using the facilities at the Space Research Institute, 231 Leach Science Center, Auburn University, Auburn, AL, USA. The RBS spectra were analyzed by Dr. T.F. Isaacs-Smith and the author using the RUMP code. The transmission electron microscope (TEM) analysis on Ni/GaAs(001) interface was performed by Prof. Jim Howe at the department of materials science and engineering and center for electrochemical science and engineering, University of Virginia, Charlottesville, VA, USA. The Brillouin light scattering (BLS) analysis was performed by the group of Dr. G. Gubbiotti at INFN, Dipartimento di Fisica, Unità di Perugia, Via A. Pascoli, 06123 Perugia, Italy.

D. Experimental techniques

1. X-ray diffraction (XRD)

X-ray diffraction provides a convenient way to determine the crystal orientation, the lattice spacing and other structural properties such as grain size and film thickness.⁵⁶ The out-of-plane crystal orientation is measured by using conventional Bragg diffraction while in-plane orientation is measured using grazing incidence diffraction. The apparatus used is an XRD Philips MRD X'Pert system which provides x rays from a Cu K_{α} radiation source with a wavelength $\lambda = 1.542 \text{ \AA}$.

a. High incidence angle ω - 2θ diffraction. Bragg diffraction. As shown in Fig. 1, when an x-ray beam is incident onto a crystal at a certain angle, a portion of it will be diffracted. This is called the Bragg diffraction and the condition can be written as⁵⁶

$$2d \sin \omega = n\lambda, \quad (2)$$

with the lattice spacing d of the reflection planes, the wavelength λ and the angle between the incident x rays and the diffracting lattice planes ω . The geometry of the x-ray diffractometer is shown in Fig. 2 with the angle between the incident beam and the film plane ω , the angle between incident and diffracted beam 2θ , the angle between the film plane normal and the diffraction plane (i.e. plane containing the incident and diffracted beam) ψ , and the rotation angle of the sample around the film plane normal ϕ . Figure 1 shows the simplest case in which the diffracting lattice plane is parallel to the film plane so that $\psi = 0^{\circ}$ and $\omega = \theta$ and there is no dependence on ϕ . In the present investigation, due to the geometry of the apparatus and the expected epitaxial properties of the films, out of plane crystal orientation is characterized by setting $\psi = 0^{\circ}$ and allowing 2θ to vary

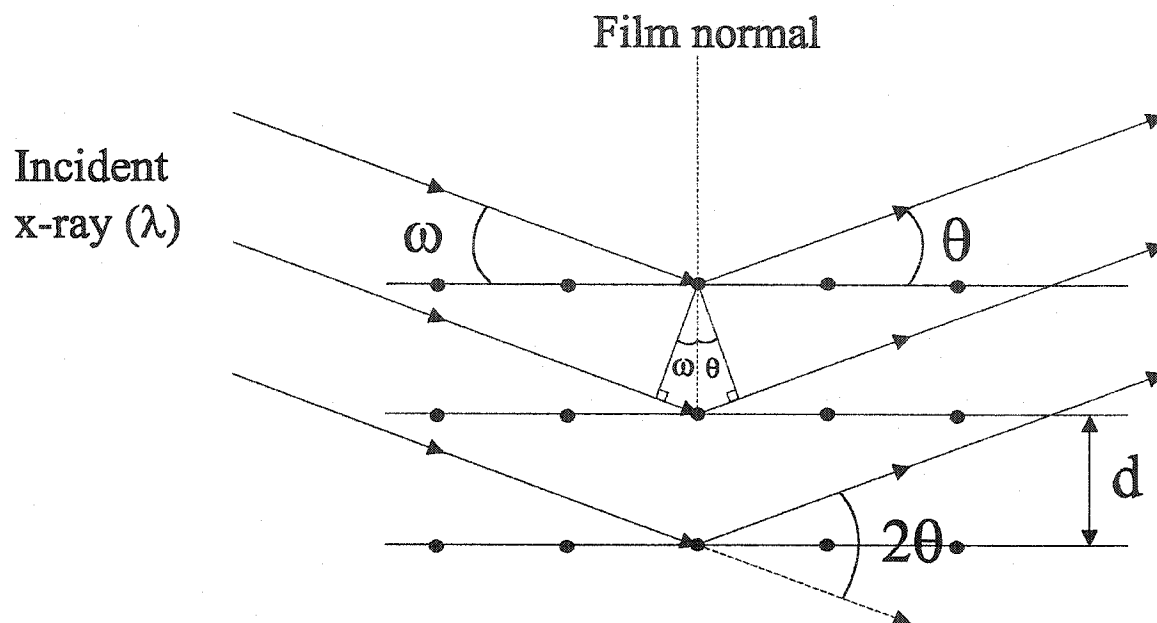


FIG. 1. Diffraction of x-ray by crystal lattice planes with lattice constant d .

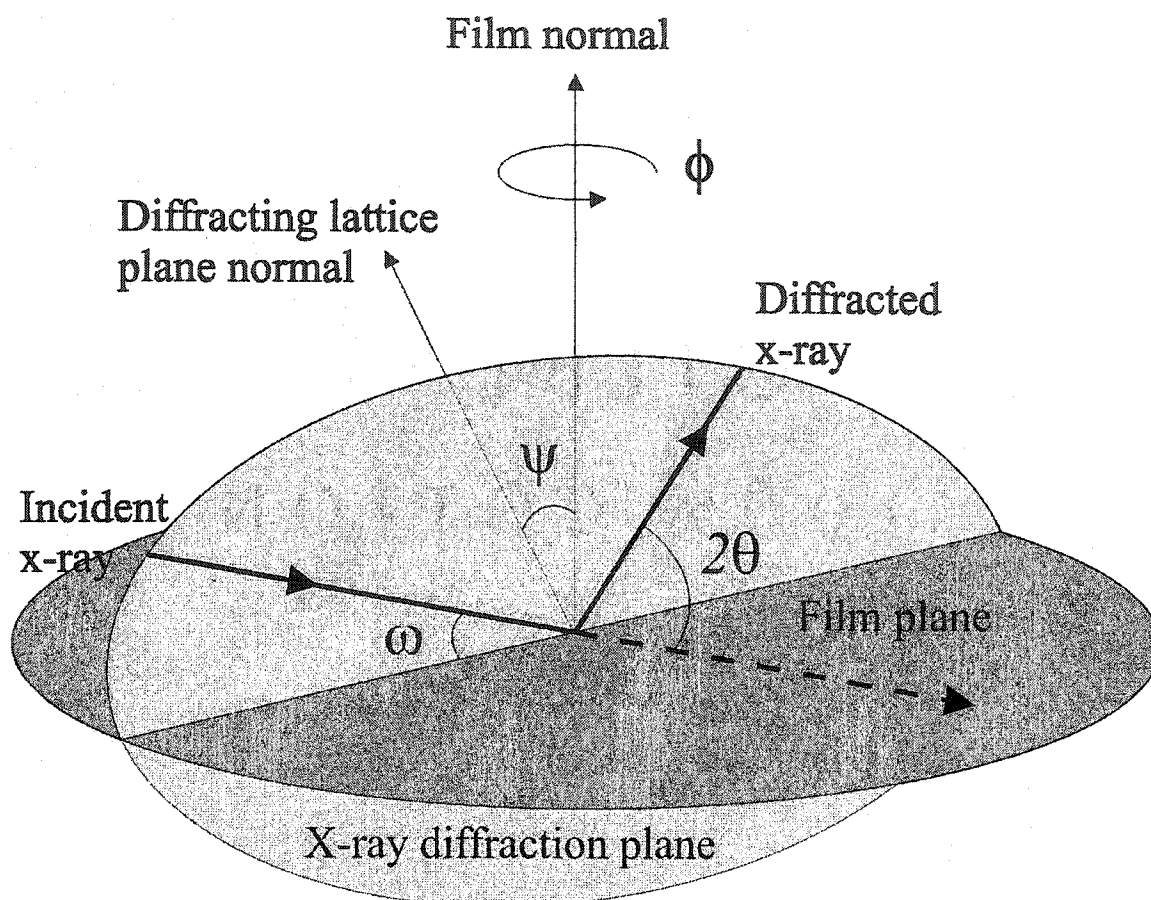


FIG. 2. Geometrical aspects of diffraction. ψ is the angle between the film plane normal and the diffraction plane which contains the incident and diffracted x-ray. ϕ is the rotation angle around the film plane normal axis. The angle ω and 2θ are both in the diffraction plane. The thick and thin arrows denote respectively the x-ray and the directions.

from 0° to 90° to satisfy the Bragg condition from diffraction planes parallel to the film plane.

In the case of a polycrystalline sample (not applicable in the present work), it is necessary to use the diffraction from a plane with an angle α to the film plane, which is achieved by setting $\psi = \alpha$ and 2θ and ω for the Bragg condition of that plane and do a conventional ω - 2θ scan.

Eq. (2) allows calculating details about the crystal structure. The value of d is determined by the Miller indices (h, k, l) of the family of planes. For cubic crystal with lattice constant a , the distance is:

$$d = \frac{a}{\sqrt{h^2 + k^2 + l^2}}. \quad (3)$$

b. Grazing incidence angle ω - 2θ diffraction. The conventional high incidence angle x-ray ω - 2θ diffraction can reveal some information about the orientation of the film, but in an epitaxial film only peaks from lattice planes parallel to the film plane will appear. Hence, using grazing incidence ω - 2θ diffraction gives information about planes perpendicular to the surface as shown in Fig. 3. In practice, in order for the x-ray beam not to miss the sample, the typical grazing angles γ are set in the range between 1° to 5° (i.e. ψ is set near 90° , generally 85° to 89°) then by setting ω - 2θ to the diffraction condition for a plane perpendicular to the film plane and doing a ϕ scan from 0° to 360° the crystal orientation of the film can be determined. In a polycrystalline sample (not applicable in the present work), to completely determine the texture of the film, a pole figure scan is needed which is achieved by simultaneously setting ω - 2θ to the diffraction condition of a specific plane, rotating ϕ from 0° to 360° and ψ from 0° to 90° .

c. Grazing incidence angle x-ray diffraction reflectivity. X-ray diffraction reflectivity (XRR) is a non-destructive and non-contact technique for thickness determination between 2–200 nm (smooth films) with a precision of about 1–3 Å. In addition to thickness determination, this technique is also employed for the determination of density and roughness of films and also multilayers with a high precision.

The XRR method involves monitoring the intensity of the x-ray beam reflected by the sample at grazing angles. The diffraction condition is satisfied when the incident angle ω is always half of the angle of diffraction 2θ , (i.e. $\omega = \theta$). For incident angle ω below the critical angle ω_c , total external reflection occurs (less than 0.3° for most materials). Above ω_c , the x-ray beam penetrates inside the film and the reflection therefore occurs at the top and the bottom surfaces of the film. The interference between the rays reflected from the top and the bottom of the film surfaces results in interference fringes, whose period and fall in the intensity are related to the thickness and the roughness of the film. In addition, the surface- and interface-roughness give rise to diffuse scattering, decreasing the intensity of the reflected beam. This is characteristic of the vanishing of the interference peak intensity at higher angle diffraction. The reflection can be analyzed using the classical theory (Fresnel equation), thus for small angle, $\sin\theta \sim \theta$ in Eq. (2), and the thickness determined given by

$$d \approx \frac{\lambda}{2(\omega_{m+1} - \omega_m)}, \quad (4)$$

with the angles corresponding to two consecutive interference maximum ω_{m+1} and ω_m .

2. Rutherford backscattering spectroscopy (RBS)

Rutherford backscattering spectroscopy is a suitable non-destructive method to identify elements, quantitatively evaluate their crystallinity and measure the thickness of the layers constituting a sample. If a sample is bombarded with a high energy ion beam, usually He^{2+} ions (~ 2 MeV), most of the ions pass through the sample. However, as was found by Rutherford in 1911, a fraction of these ions are scattered backwards due to collisions on the nuclei of the atoms in the crystal as shown in Fig. 4. The energy of a reflected He^{2+} ion depends on the mass of the nucleus with which it collide, and the angle at which the ions are detected. In the energy spectrum of the backscattered ions, peaks occur at certain energies, which are related to the mass of the nuclei of the sample as shown⁵⁷ in Fig. 5. If the masses of the nuclei are too similar, then their corresponding peaks in the energy spectrum could overlap. In the case of a simple-element film (one type of nucleus), only two peaks appear, one originating from the film and one from the substrate. Due to the interaction of the He^{2+} ions with the orbital electrons around the nuclei in the film and due to grazing collisions with nuclei, the ions lose energy when they traverse the sample before and after the collision. The result is that scattering at the top surface [Fig. 4 (a) event *A*] leads to an energy loss that is determined by the mass of the nuclei only, but scattering at deeper lying atoms [Fig. 4 (a) events *B* and *C*] leads to a larger energy loss. This energy loss is proportional to the path length through the film and consequently is proportional to the film thickness, which determines the width of the energy spectrum peak as shown in Fig. 5. The energy loss due to multiple bounces of the reflected ions adds to the background signal of the energy spectrum. By enlarging the angle at which the particles are detected, the peak also broadens because of the longer

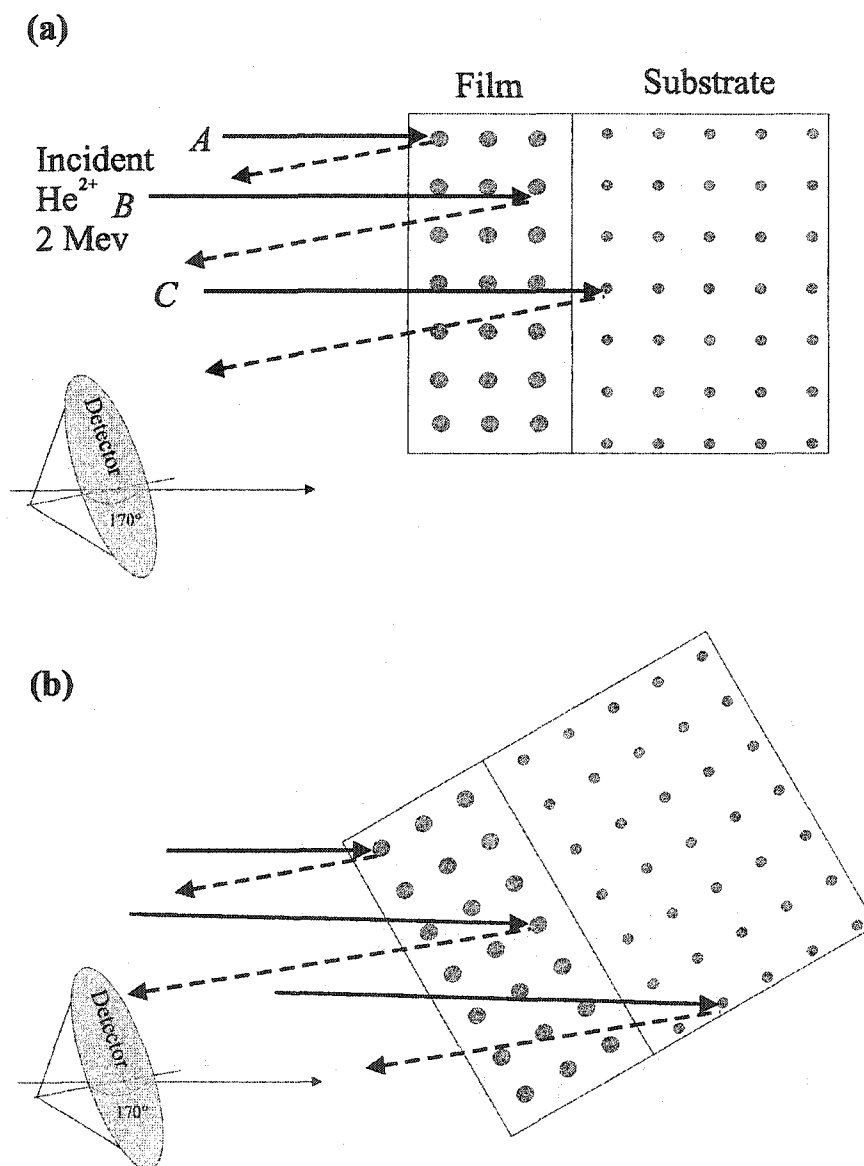


FIG. 4. Principle of Rutherford backscattering spectroscopy (RBS). In (b), the sample is tilted (30°) in order to avoid any particular crystalline direction and thus channeling. The angle detector was set at 170° with respect to the incoming He^{2+} ions beam.

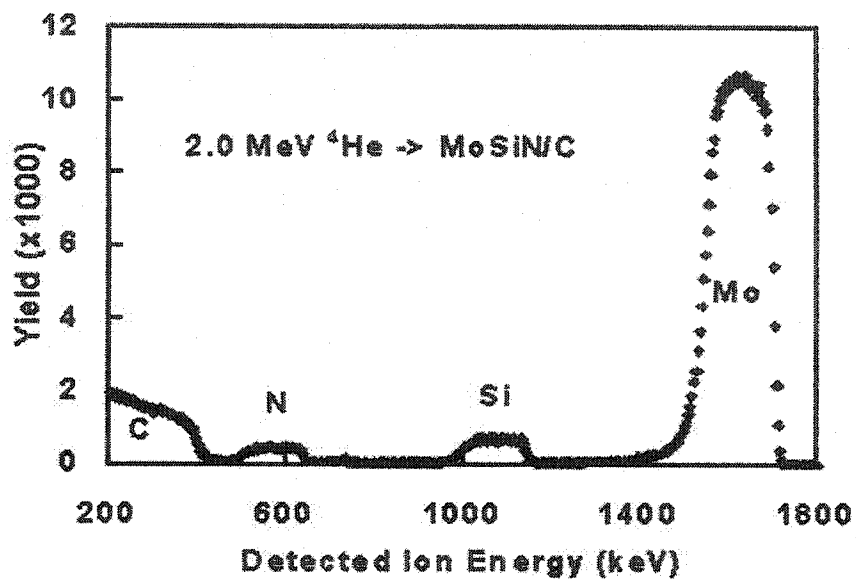


FIG. 5. RBS analysis of a sample of MoSiN film on a carbon (C) substrate. The peak intensities corresponding to each element constituting the sample are well separated due to the difference of mass of the respective elements. The height of the peak indicates the density of atoms and the ion energy identifies the species and the depth below the surface.

path the He^{2+} ions travel before reaching the detector. In practice, for thickness determination, the incident beam is set at a desired angle for the He^{2+} ions to collide with the sample atoms in order to avoid any particular crystalline direction as shown in Fig. 4 (b), and therefore avoiding any channeling effect. Indeed, it is obvious that as shown in Fig. 4 (a), an incoming ion beam hitting the surface in the direction of a crystalline direction will be sensitive only to the first layer of atoms, thus preventing any deeper nuclei to interact with the incoming ions and thus get any thickness information from the film.

In the present work, the RBS measurements were performed on a tandem accelerator (6SDH-2 Pelletron) built by National Electrostatics Corporation. A RF exchange ion source was used in this experiment to produce a collimated beam of He^{2+} ions. The 30° incident 2 mm diameter beam had an energy of 2.4 MeV and the backscattering angle was 170° . The RBS spectra were analyzed using the RUMP code in order to determine the thickness of the films.

3. X-ray photoelectron spectroscopy (XPS)

X-ray photoelectron spectroscopy is known as a weakly (usually non-) destructive method to determine the chemical composition of surface materials. In XPS, the photoemission consists of the ejection of an electron from a core level by an x-ray photon of energy $h\nu$.

Considering a single atom with just one x-ray photon on the way as shown in Fig. 6, the total energy is

$$E_T = h\nu + E_i, \quad (5)$$

where E_i is the energy of the atom in its initial state. Following the absorption of the photon and the emission of the photoelectron, the total energy is now

$$E_T = E_k + E_f, \quad (6)$$

where E_k is the electron kinetic energy and E_f the final state energy of the atom (now an ion). Because total energy is conserved

$$h\nu + E_i = E_k + E_f$$

or

$$h\nu - E_k = E_f - E_i = E_B, \quad (7)$$

where E_B , the difference between the photon energy (known) and the electron energy (measured), is the binding energy of the orbital from which the electron was expelled. E_B is roughly equal to the Hartree-Fock⁵⁸ energy of the electron orbital and so peaks in the photoelectron spectrum can be identified with specific atoms and hence, a surface compositional analysis performed.

The energy of the emitted photoelectrons is analyzed by the electron spectrometer and the data presented as a graph of intensity binding or kinetic energy. Those electrons which are excited and escape without energy loss, contribute to the characteristic peaks in the spectrum; those, which undergo inelastic scattering and suffer energy loss, contribute to the background of the spectrum. Once a photoelectron has been emitted, the ionized atom must relax in some way. This can be achieved by the emission of an x-ray photon, known as x-ray fluorescence, or the ejection of an Auger electron (Fig. 7). The depth of analysis in XPS varies with the kinetic energy of the electrons under consideration. It is determined by a quantity known as the attenuation length of the electrons, which is related to the inelastic mean free path (imfp). In addition to the characteristic peaks in the

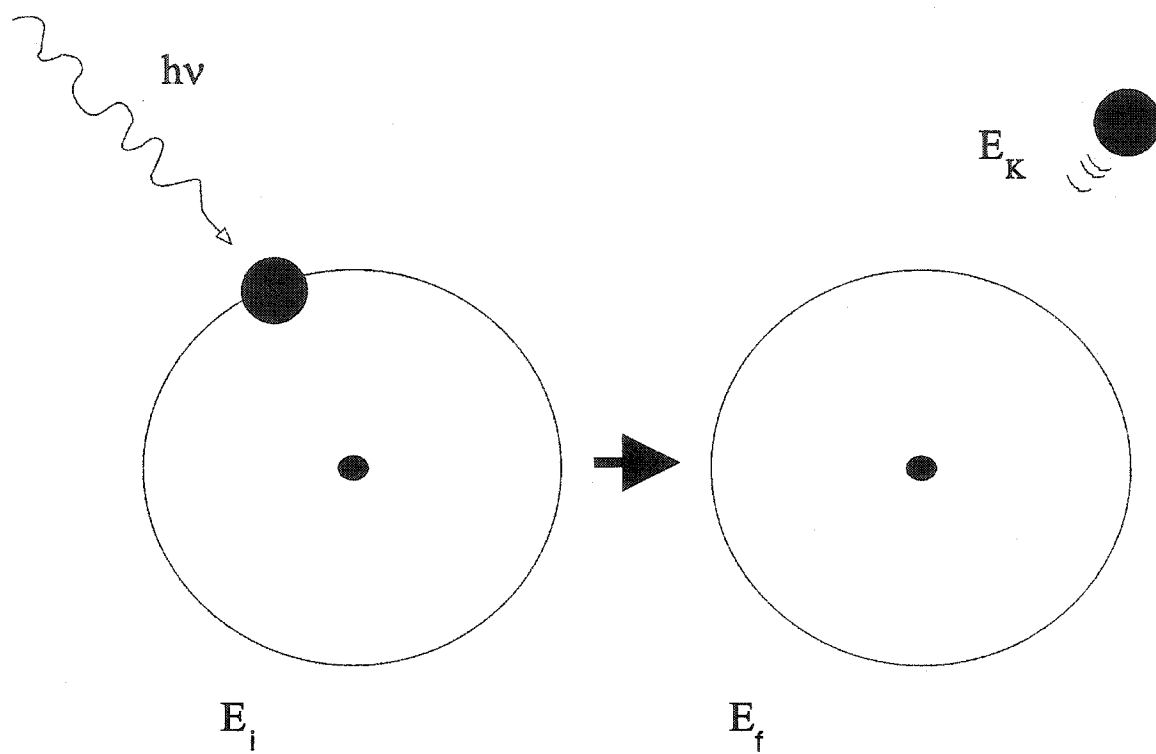


FIG. 6. Kinematics of x-ray photoelectron spectroscopy (XPS).

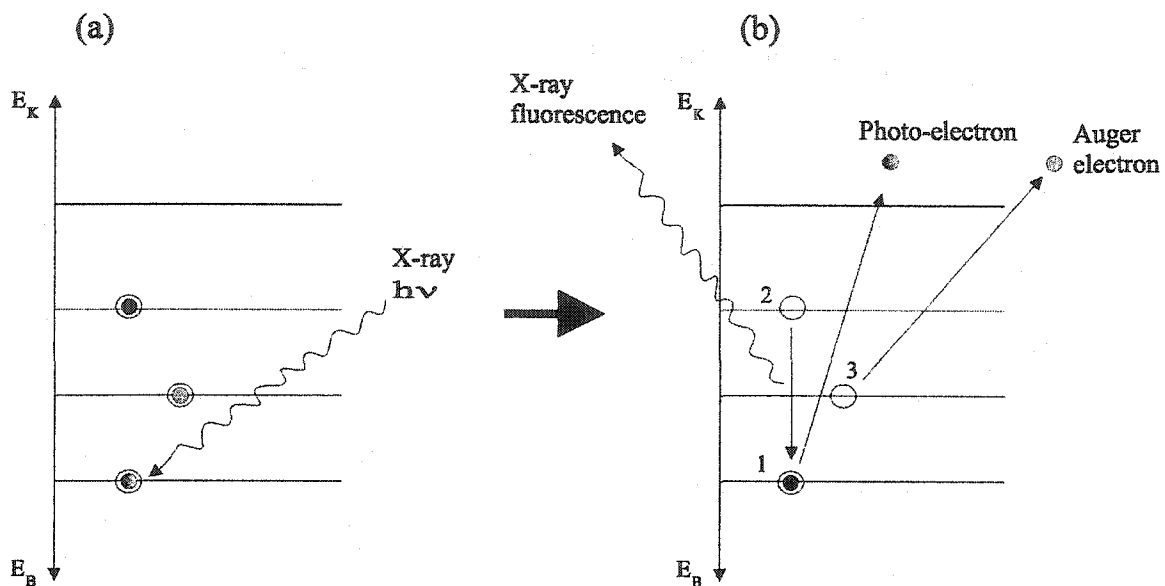


FIG. 7. Energy-level diagram of states of an atom before (a) and after (b) x-ray photoelectron irradiation. In (b), the holes are numbered in the order of creation. The energy lost by the electron falling from 2 to 1 ejects the electron from 3 (Auger electron) or is converted to x-ray fluorescence.

XPS spectrum, two phenomena are often present in the XPS analysis. First of all, the so called “shake-up” effect may occur when the outgoing photoelectron simultaneously interacts with a valence electron and excites it (shakes it up) to a higher-energy level; the energy of the core electron is then reduced slightly giving a peak a few electron volts below (on a kinetic-energy scale) the core level position. On the second hand, the presence of chemical bonding (such as atomic oxidation state) clearly have an effect on both the initial state energy of the atom and the final state energy of the ion created by emission of the photoelectron causing binding energy shifts in the spectrum known as “chemical shift”.

In order to quantify spectra from XPS, the intensity is usually taken as the integrated area under the peak following the subtraction of a linear background. The Beer-Lambert law of exponential intensity attenuation can be used along with the imfp to quantify the analyzed area. In the present work, chemical analysis was performed using X-ray photoelectron spectroscopy (XPS) with a monochromatic beam from an Al target (1486 eV, Kratos Axis 165 system).

4. Vibrating sample magnetometer (VSM)

The magnetic characterization (magnetic moment, hysteresis, remanence) of the various metallic films grown in this work was performed on a vibrating sample magnetometer (VSM DMS model 990 Magnetometer) which uses an induction technique. In a VSM, the sample is mounted at the end of a rigid rod attached to a mechanical resonator that oscillates the sample in the vertical direction (Fig. 8). Surrounding the sample nearby is a set of pick-up coils. As the sample moves, its

magnetic field, which is proportional to its magnetic moment M , alters the magnetic flux through the coils, dM/dt . This induces a current directly proportional to dM/dt , which can be amplified and detected using lock-in amplifiers. The sample is subjected to an in-plane external magnetizing field provided by a horizontal electromagnet that can provide fields up to 11 kOe in the present case. The change in M with respect to the applied external field gives rise to the well-known hysteresis loop.

In order to measure the in-plane remanent states of the magnetization at a different angle ϕ away from a reference crystallographic direction of the substrate, the sample is first saturated under the external magnetizing field. Then, the external field is removed allowing the magnetization to relax (for approximately two seconds) and the remaining sample magnetization at zero field recorded. This procedure is then repeated at different angles ϕ varying from 0° to 360° , where $\phi = 0$ is the easy direction.

5. Surface morphology characterization

The surface roughness of all films was analyzed using tapping mode atomic force microscopy (AFM) on a Veeco/Digital Instruments Nanoscope IV scanning probe microscope. Root mean square (RMS) roughness (σ_∞) and correlation length (ξ) of the surfaces of the films were extracted using fractal analysis.^{59,60}

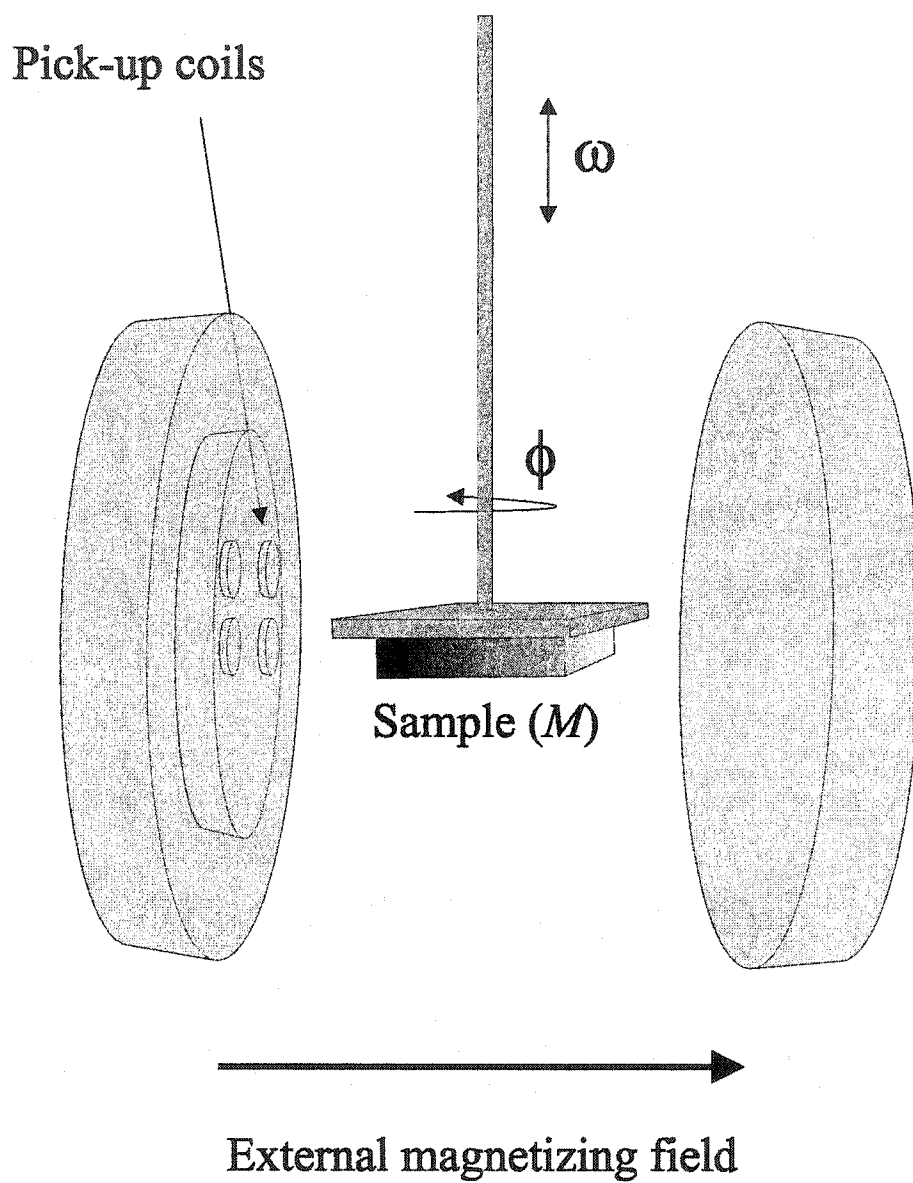


FIG. 8. Principle of a vibrating sample magnetometer.

II. FABRICATION AND ANALYSIS OF NI, FE AND CO FILMS GROWN ONTO *n*-GAAS SUBSTRATES

A. Sample preparation

The substrates were single crystalline GaAs(001) or GaAs(011) oriented wafers (El-Cat, Inc.), "epi-ready," Te-doped *n*-type with a donor density of $2 \times 10^{17} \text{ cm}^{-3}$ [GaAs(001)] or $1.2 \times 10^{18} \text{ cm}^{-3}$ [GaAs(011)]. The substrates were mounted on a copper plate electrode whose areas exposed to the electrolyte solution were covered with rubber paint to avoid any leakage current. The electrical back contact to the GaAs was made using a Ga (75%) - In (25%) eutectic, which is liquid at room temperature. Initially, the area of deposition on the substrate for each sample was defined by covering the surface with an adhesive tape with a hole, which exposed a surface area of 28.3 mm^2 . Later, the area of deposition was defined as a 1 cm^2 square area in order to allow XRR thickness calibration (see Sec. II. B 1). Immediately prior to deposition, the substrates were etched for 2 minutes with a 10% ammonium hydroxide solution (NH_4OH) and subsequently rinsed in de-ionized water (DW) for 30 seconds. Electrodeposition was carried out under galvanostatic control at room temperature (RT) in a prismatic cell with vertical parallel electrodes using a galvanostat/potentiostat EG&G Model 273A (Fig. 9). In order to reduce the effect of any resistance variation of the back contact to the substrate, galvanostatic deposition was preferred rather than potentiostatic. Graphite was used as the counter electrode. Ni and Co were deposited from a 0.1 mol/L sulfate solution (NiSO_4 , CoSO_4) at $\text{pH} = 2.5$ and grown at a current density $J = 3.5 \text{ mA/cm}^2$ without

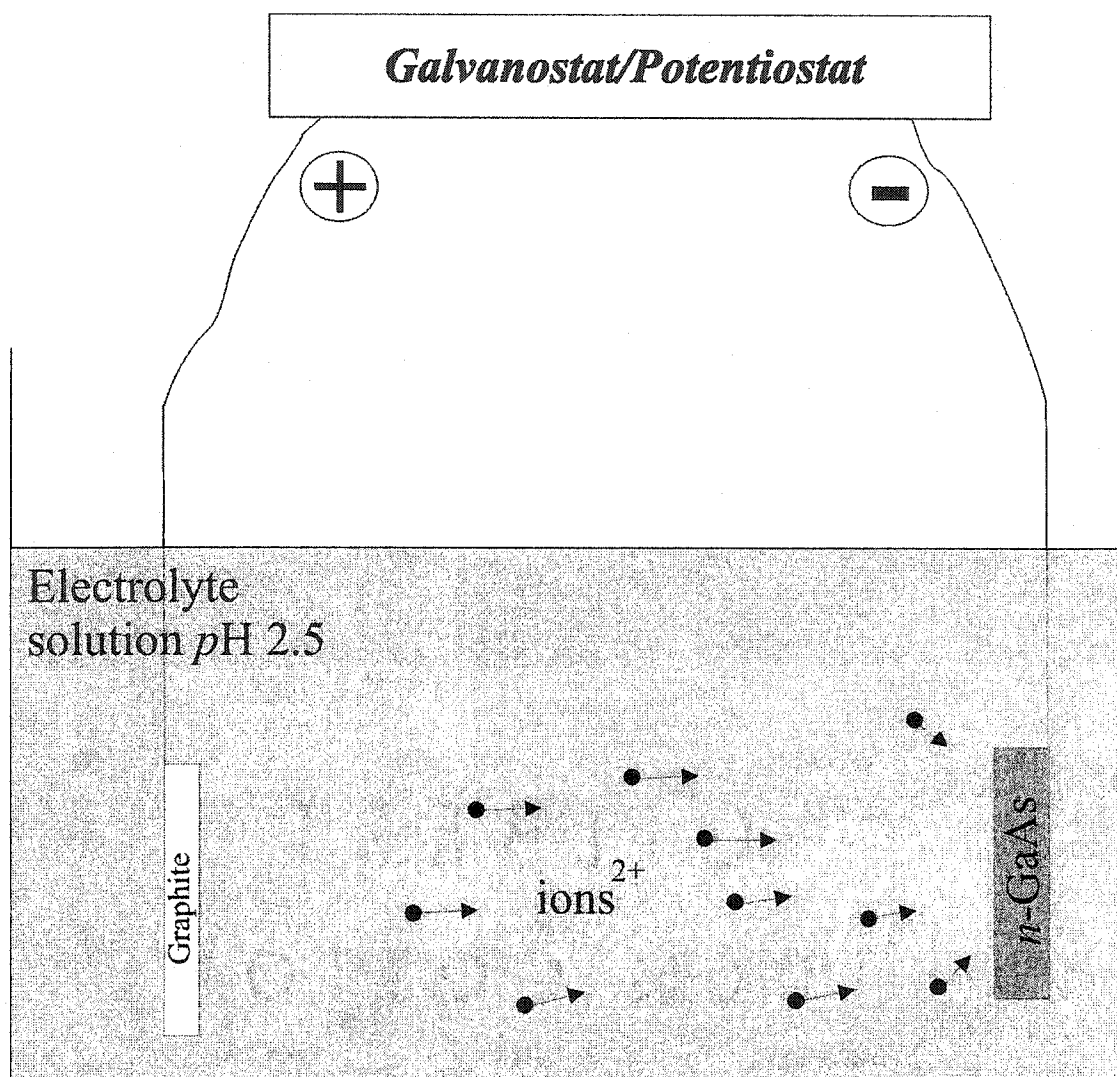


FIG. 9. Schema of the experimental set up for electrodeposition.

agitating the solution during deposition. Fe was deposited from a 0.1 mol/L sulfate solution (FeSO_4) with 0.5 mol/L of boric acid (H_3BO_3) at $\text{pH} = 2.5$ and grown at $J = 2.5$ mA/cm^2 . It is noted that without boric acid, the Fe films appear dull. Addition of acetic acid as a possible complexing agent for Fe or of a reducing agent (ascorbic acid) deteriorates the structural quality of the films. In the case of FeNi films, the solution was composed of 0.18 mol/L FeSO_4 and 0.019 mol/L NiSO_4 with 0.028 mol/L of ascorbic acid and 0.4 mol/L of boric acid as a “stabilizer” and the $\text{pH} = 2.5$. Energy dispersive x-ray (EDX) analysis on the resulting $\text{Fe}_x\text{Ni}_{1-x}$ films confirmed a composition of $x \geq 0.9$. The pH of the solutions was adjusted to 2.5 by addition of diluted sulfuric (H_2SO_4) or hydrochloric (HCl). After deposition, the samples were rinsed with DW and blown dry.

Figure 10 shows a cyclic voltammogram for Ni deposition on (001) and (011) oriented GaAs. The Ni starts to deposit at a less negative potential (-0.9 V vs a saturated calomel electrode SCE) on the (011) wafer than for the (001) wafer and the current in general is higher for a given potential on the (011) wafer. This is most probably caused by the lower doping density, and hence higher resistivity, of the (001) wafers leading to a larger voltage drop across the thickness of the substrate. No dissolution is seen of the Ni films during the anodic part of the scan for the (001) wafer, owing to the formation of a Schottky barrier which is reverse biased when the voltage is positive. A small anodic current is seen for the (011) wafers but still smaller than would be expected for a metallic substrate. Hence, the Ni/GaAs interface forms a Schottky barrier with a typical ideality factor 1.1 and barrier height 0.765 eV at RT (see Sec. I C 3).

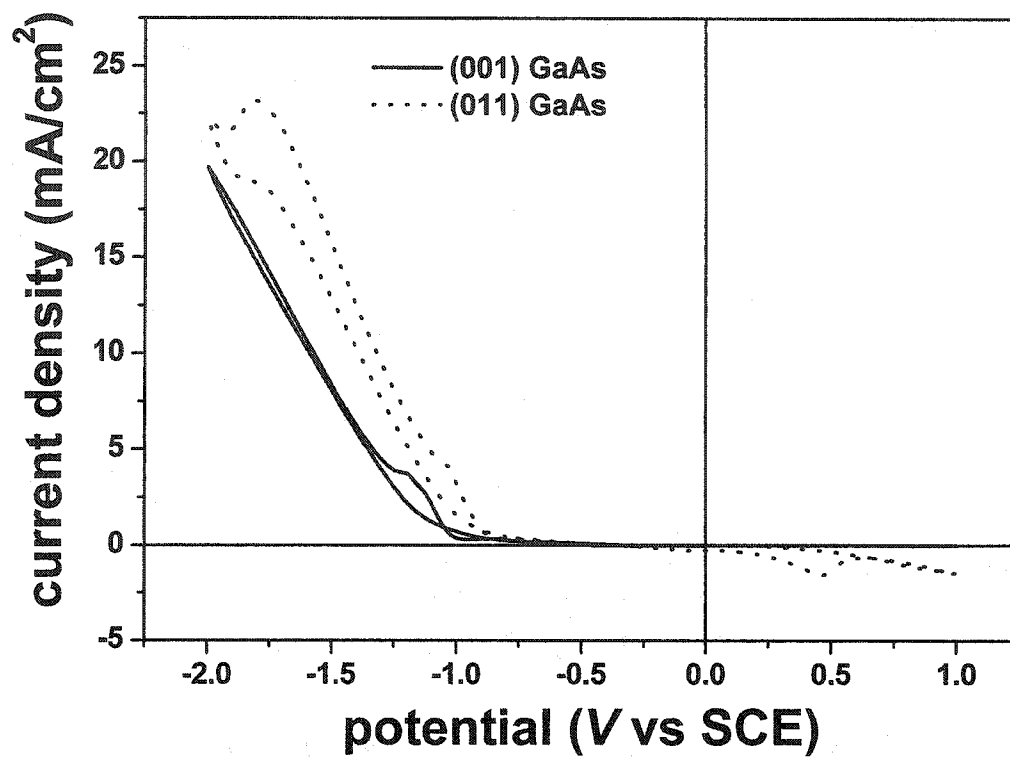


FIG. 10. Cyclic Voltammograms in 0.1 M NiSO₄ pH 2.3 solution using *n*-GaAs (001) and (011) substrates. Scan rate = 50 mv/s.

B. Thickness calibration

1. Film

The thickness of the films, initially Ni films, was measured or calculated using four different methods: the nominal thickness (T_N) was obtained from Faraday's law, assuming 100% efficiency of the electrochemical reduction process; the magnetic thickness (T_M) was calculated from the total magnetic moment of the sample, the thickness at the center of the sample was measured through RBS (T_{RBS}) and XRR (T_{XRR}).

T_N was determined using the formula

$$T_N = \frac{I \times t \times M}{N_A \times 2e \times d \times A}, \quad (8)$$

with plating current I , deposition time t , atomic mass M_a , Avogadro's constant N_A , elementary charge e , metal density d and film area A . For example, according to the electrodeposition process using Ni^{2+} ions, two electrons are necessary to reduce one Ni ion to its elementary form as Ni atom in the film. This assumes a current efficiency of 100%, a condition that typically is not fulfilled. Hence, T_N gives an upper limit for the true film thickness.

The measurement of the saturation magnetisation (M_s) allows an estimation of the actual thickness under the assumption that the deposited films show bulk properties with respect to both density ($d_{\text{Ni}} = 8.908 \text{ g/cm}^3$) and magnetic moment ($M_{\text{Ni}} = 54.4 \text{ emu/cm}^3$) and no oxidation of the Ni surface so that

$$T_M = \frac{M_s}{M_{\text{Ni}} \times d_{\text{Ni}} \times A}. \quad (9)$$

The assumption of bulk properties should be asymptotically justified for large enough values of the film thickness. Both surface oxidation and interdiffusion at the

interface to the substrate would reduce M_s . This effect would cause the strongest deviations for thin films. Surface oxidation cannot be easily avoided by adding a protective cap layer when using electrodeposition since a change of the material being deposited is far less trivial by electrodeposition than it is for evaporation or sputtering. Some attempts have been made to deposit a top layer of platinum (Pt) from a 0.1 mol/L NiSO_4 solution with 0.002 mol/L of platinum chloride (H_2PtCl_6) by changing the applied voltage in order to selectively deposit the Ni film first followed by a protective Pt layer; however the presents were unsuccessful. Therefore, our films were exposed to air and necessarily oxidized. Often it is observed that thin films of $3d$ metals with a good crystalline order show a limited amount of oxidation (around 1–2 nm of the metal film being oxidized) which effectively prevents further oxidation over long time periods.⁶¹⁻⁶⁵ Ni films are known to form, upon exposure to oxygen/air, NiO which is antiferromagnetic and insulating⁶⁴ or Ni(OH)_2 .⁶⁶ The thickness of the oxide layer formed saturates at a couple of monolayers.^{63,65} In the present work, the oxide layer was identified as Ni(OH)_2 and its thickness estimated at 1.9 nm from XPS analysis²⁸ (see Sec. I. B 2 for further details). It appeared that the magnetic moments measured did not change over time, suggesting that the oxidation product indeed forms a stable cover layer which should reduce the moments systematically by a fixed amount. Interface intermixing can potentially also lead to a reduction of M_s ¹⁰⁻¹³ though interface analysis demonstrated no or little intermixing^{28,29} (see Sec. I C 3).

T_{RBS} was evaluated from RBS spectra as shown in Fig. 11 by simulation of the experimental data using the RUMP code. Since the film (Ni) and the substrate (GaAs) have similar masses, the peak originating from He^{2+} ions colliding with the Ni atoms is

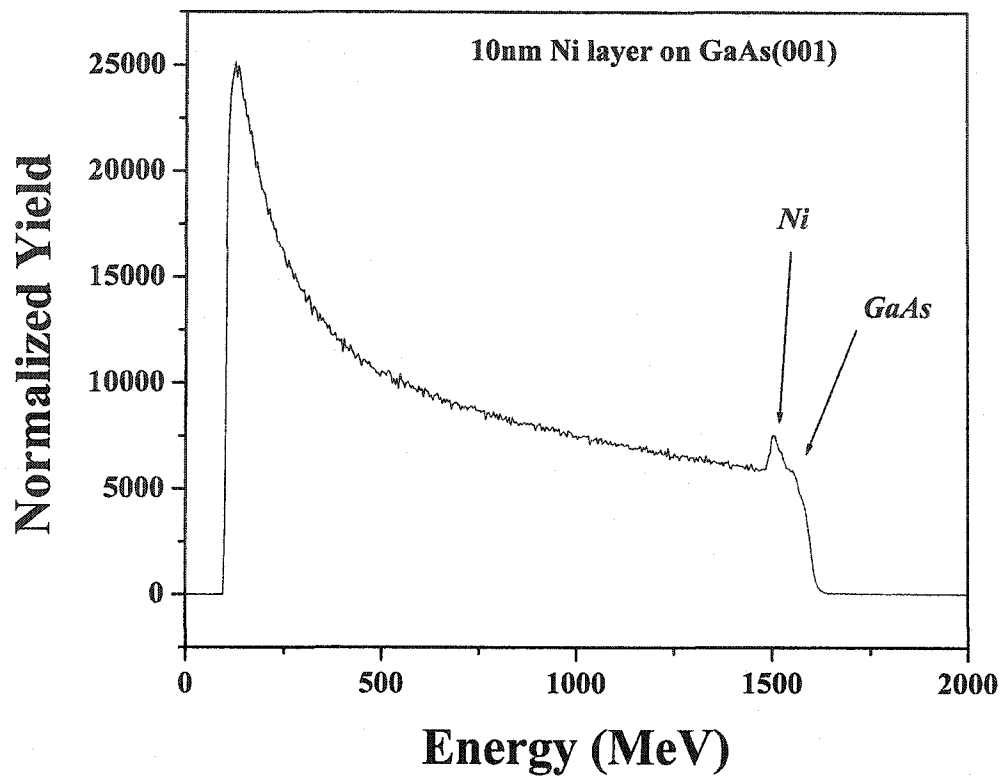


FIG. 11. Rutherford backscattering spectroscopy (RBS) energy spectrum of 2.4 MeV incident He^{2+} ions irradiating a 10 nm Ni film grown on GaAs (001).

not well separated from the one originating from the substrate. Nevertheless, this does not prevent one from estimating the film thickness from the width of the simulated peak. T_{XRR} was extracted from XRR intensity plot (Fig. 12) where the period of the intensity oscillation is characteristic of the total thickness of the deposited layer. Simulation of the experimental data using WinGixia software version V1.102 for Philips diffractometers along with Eq. (4) as a first estimation tool, led to the determination of the film thickness. The XRR data in Fig. 12 indicate the growth of very smooth layers.

Figure 13 shows film thickness obtained from the four methods as a function of electrodeposition time. T_M , T_{RBS} , and T_{XRR} linearly increase with deposition time but show thickness values clearly below T_N . The linear increase of both T_{RBS} and T_{XRR} indicates a constant growth rate. T_M also increases linearly in time. Under the assumption that for larger thickness values the Ni film magnetization assumes bulk properties this would indicate that also for the thinner samples no strong deviation from bulk properties is observed, as one would expect for significant intermixing¹⁰ or oxidation. This point needed further verification^{28,29} (see Sec. III C 1) and a quantification of the degree of surface oxidation is evaluated in Sec. I C.

The surprising difference in slope between T_M and both T_{RBS} and T_{XRR} is caused by a small non-uniformity of the sample thickness. This is because during electrodeposition, the current density at the sample edges is higher than at the sample center, causing the edges to grow at a slightly faster rate. Since the 2 mm diameter He^{2+} beam used in the RBS measurements was aimed at the sample center, this technique effectively measured the thinner part of the sample. In the case of XRR, in order to ensure a homogeneous sample thickness throughout the entire sample surface, the outer edges (2 mm width)

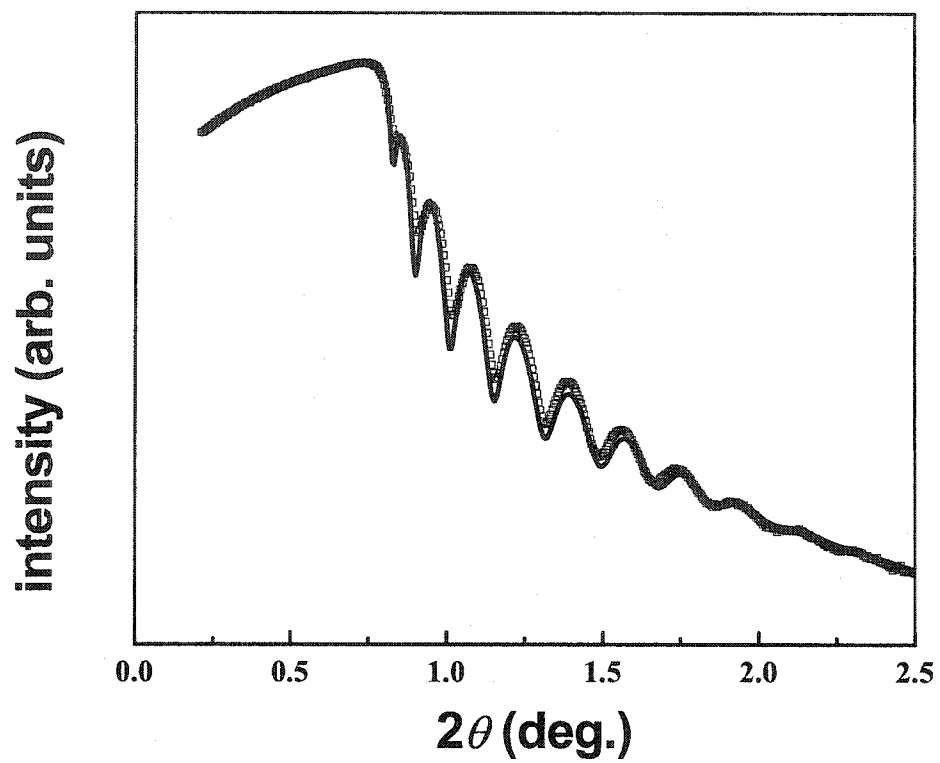


FIG. 12. X-ray reflectivity (XRR) data of a smooth 25 nm Ni film grown on GaAs(001).

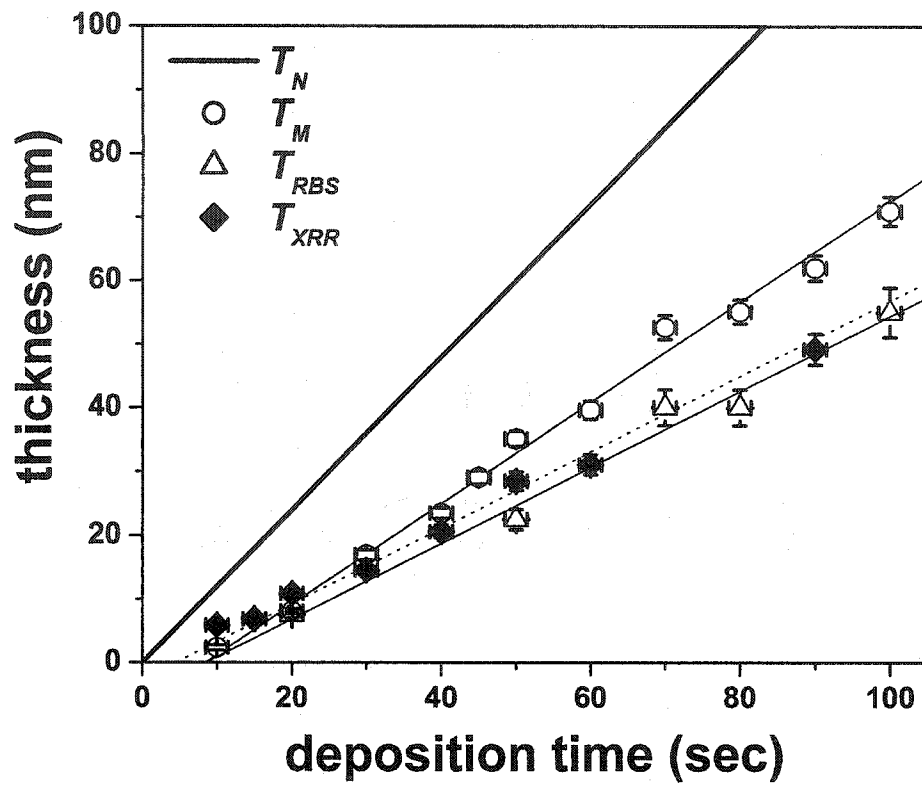


FIG. 13. Thickness of electrodeposited Ni layers on GaAs (001) (nominal T_N , magnetic T_M , estimated by RBS T_{RBS} and by XRR T_{XRR}) as a function of deposition time. The dotted line is a linear fit of T_{XRR} data. For definition of those four thickness values see text.

were cleaved off the initial 1 cm² sample area leaving the center part for thickness characterization. The magnetic measurements, however, integrate over the entire sample area leading to the consistently higher values of T_M as compared with T_{RBS} and T_{XRR} . Profilometer (Dektak IIA) measurements performed on various samples for different thicknesses confirmed that all films appeared to be thicker at the edges than at their center.

Comparing the nominal thickness T_N with T_{XRR} , a current efficiency (for long deposition times > 90 s) of $T_{XRR}/T_N = 49$ %. All thicknesses quoted in the following are based on the XRR calibration after subtraction of the magnetically and electrically inactive 1.9 nm Ni(OH)₂ oxide layer thickness²⁸. The growth rate is 0.59 nm/s and the linear extrapolations of both T_M and T_{RBS} intersect the x-axis (Fig. 13) at about 10 seconds as compared to 5 seconds for T_{XRR} . This delay in the deposition process is not atypical for electrodeposition and is ascribed to a capacitive charging current in the system electrolyte/electrodes. Measurements done on Fe_xNi_{1-x} films showed a deposition rate of 0.45 nm/s.

Fe films thickness was estimated using a profilometer due to the non-homogeneity and important surface roughness of the deposited films (see Sec. II).

2. Surface oxide layer

The thickness and chemical nature of the oxidation products of the Ni layers were determined using XPS. The carbon contamination of the Ni layers is below the detection limit of the XPS system which, as compared to the Ni peak intensities, indicates carbon contamination levels below 0.1%. Figure 14 shows the Ni 2*p* XPS spectrum of a Ni film

covered by its native oxide [spectrum (a)] after subtraction of a linear background. The main peak at binding energy (BE) 853 eV corresponds to elemental Ni. The peak at BE 856 eV corresponds to the Ni(OH)₂ rather than to NiO because on one hand hydroxide formation is expected upon wet oxidation (air)⁶⁶ while on the other hand the chemical shift of $\Delta E = 3.2$ eV is characteristic for Ni(OH)₂. The shoulder present around BE 860 eV is due to shake-up effects.

For comparison, the spectrum of a clean Ni film was obtained by sputter cleaning a Ni layer and is reported as spectrum (b) in Fig. 14. The intensity of the latter spectrum was normalized to match the peak intensity of elementary Ni in spectrum (a) of the oxidized film. The difference between the two spectra [spectrum (c)] hence corresponds to the spectrum of the hydroxide layer showing the 3.2 eV chemical shift. By applying the Beer-Lambert law of exponential intensity attenuation, the ratio of the areas under the curves allows to estimate the thickness of the hydroxide layer at $T_{Ox} = 1.9$ nm. XPS analysis of other samples and at different analyzer angles verified this result, which was used for the Ni layer thickness estimation through XRR. Figure 12 shows a XRR plot of a smooth Ni layer and its simulation fit taking into account the oxide layer thickness in the simulation parameters.

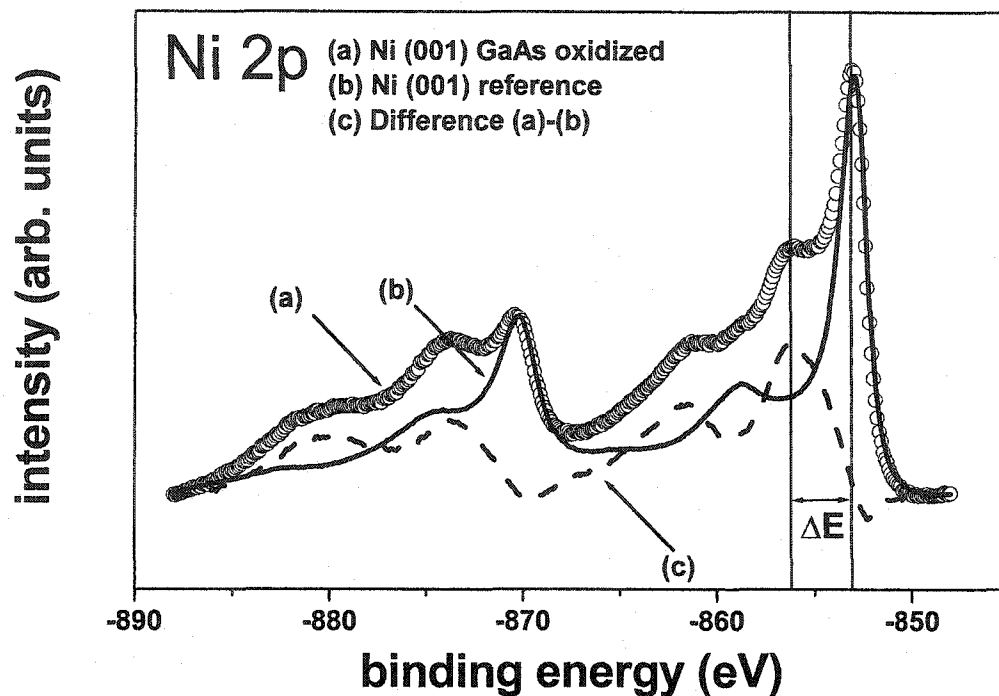


FIG. 14. High-resolution XPS spectra in the energy range of the Ni 2p peak. The data points and the full line are the spectra measured, respectively, on a 51 nm thick Ni layer which was exposed to air (a) and a Ni film after sputter removal of the hydroxide layer (b). The dashed line is the difference [(a)-(b)] of the two spectra, representative of the $\text{Ni}(\text{OH})_2$ layer which forms on Ni upon exposure to air.

C. Results and discussion

1. Structure

a. GaAs(001). (1) Figure 15 shows the high angle ω - 2θ XRD scan for a 90 nm thick Ni film.²³ In order to suppress the dominant GaAs(004) peak and its K_β satellite the sample angle ω was intentionally offset by 0.5° . Due to the narrow rocking curve widths of the substrate, this offset reduces the GaAs peak intensities considerably without substantially weakening the Ni peaks. A clear Ni(002) peak and a weaker (022) peak can be seen. The low signal levels are caused by a rather wide polar angular distribution of the crystal orientation with rocking curve widths of respectively 22° (002) and 8° (022). We find that the intensity ratios of (002) and (022) vary from sample to sample but with (002) always dominating. However, the most interesting point to note is the absence of the Ni(111) peak ($2\theta = 44.49^\circ$), which would be the most intense peak for a completely untextured film and would also be expected as the texture of a non-epitaxial fcc film.

As shown in Fig. 16, ω -rocking curves were measured for these two peaks and it was found that the Ni (200) peak had a large angular dispersion of $\sim 20^\circ$ about the GaAs(001) direction, whilst the Ni(220) peak had a narrower angular dispersion of 8° . This means that the ω - 2θ measurement is more sensitive to the Ni(220) peak, and it is not possible to estimate the relative amounts of each epitaxy simply by comparing the intensity of the peaks. Large angular dispersions with respect to the substrates have also previously been observed for electrodeposited Cu on GaAs(001).^{67,68}

This suggests that the films grow either with a texture unusual for fcc materials or that Ni grows epitaxially on GaAs(001). This was confirmed by in-plane XRD, where

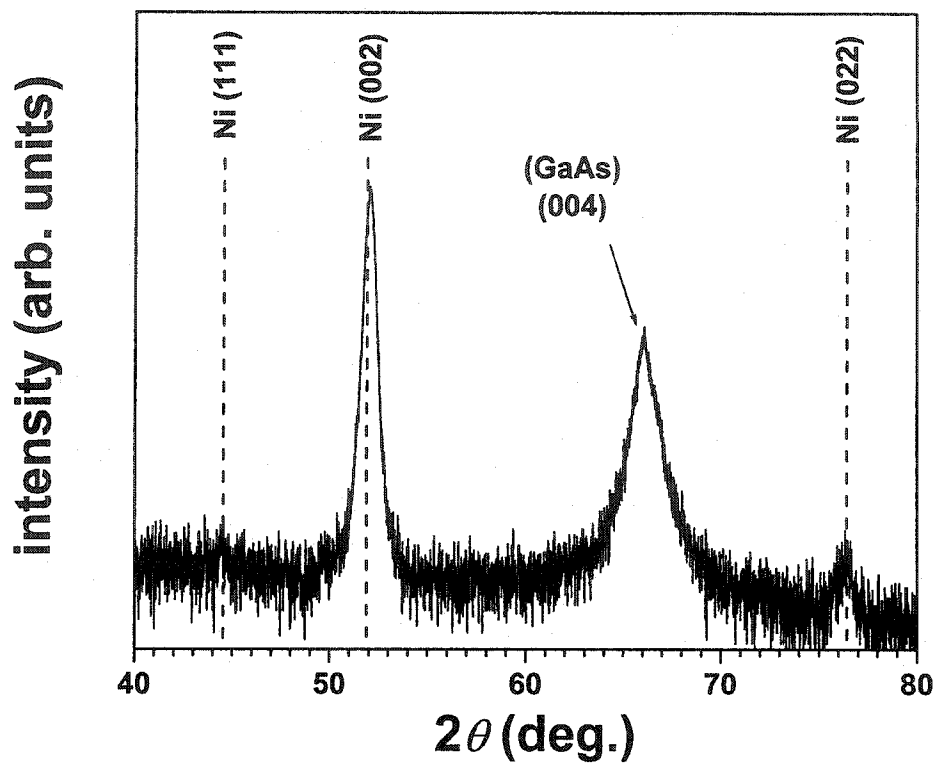


FIG. 15. High angle ω - 2θ x-ray measurement of a 180 nm thick Ni layer on GaAs(001). The vertical dashed lines indicate the 2θ peak positions of Ni(111), Ni(002) and Ni(022). The measurements were made with an ω -offset of 0.5° .

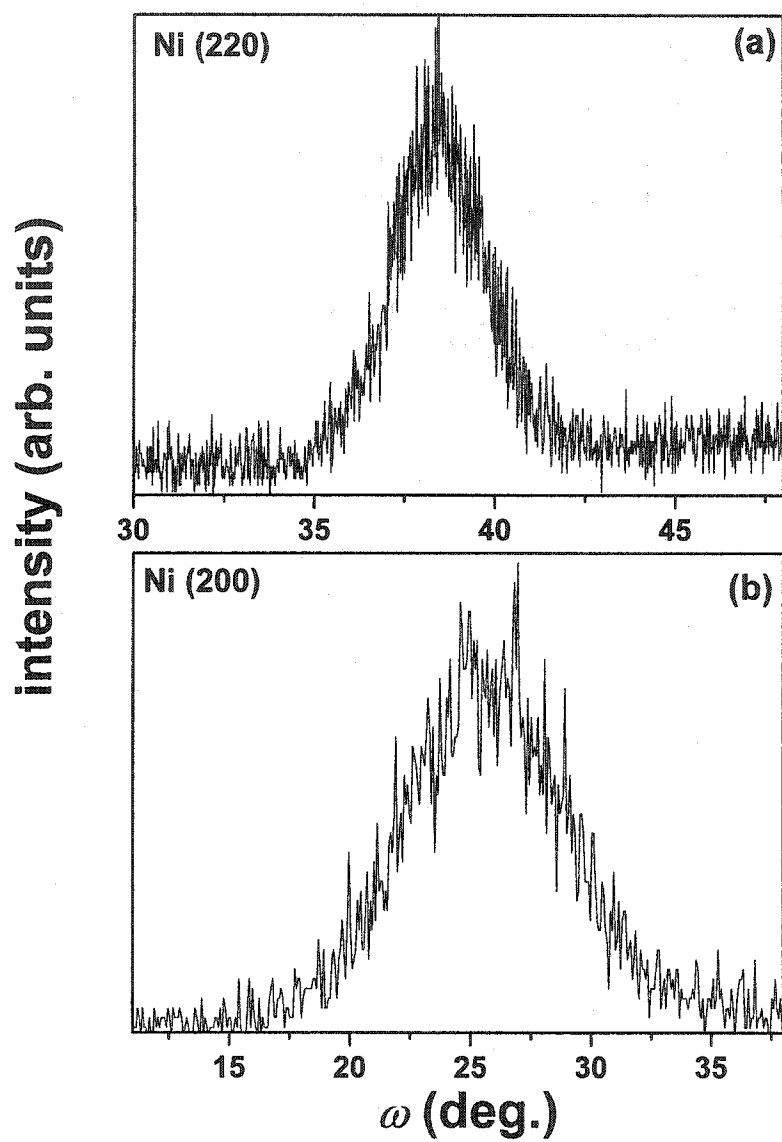


FIG. 16. High angle ω - 2θ XRD rocking curve of Ni grown on GaAs(001) for Ni(200) and (220) peaks.

two preferred epitaxial growth relationships were observed. Figure 17 shows three ϕ scans for the detector angle 2θ set at the Ni(200), Ni(220) and Ni(111) peak positions, respectively. The ϕ scan with 2θ corresponding to the Ni(200) position shows four peaks with the Ni $\langle 100 \rangle$ in-plane directions parallel to GaAs $\langle 110 \rangle$. The ϕ scan with 2θ corresponding to the position of Ni(220) shows the Ni $\langle 110 \rangle$ to be aligned along the GaAs $\langle 100 \rangle$ directions, i.e. enclosing an angle of 45° with the in-plane Ni $\langle 200 \rangle$ directions. Those two scans can be assigned to the first epitaxial relationship Ni(001)[100]//GaAs(001)[110]. This corresponds to a 45° rotation of the fcc Ni structure with respect to the substrate, which has been reported previously for electrodeposited NiCu^{17,18} and Cu⁶⁸ on GaAs(001). It should be noted that the Ni(001) orientation does not have any [111] in-plane direction, however, the (022) orientation does. The second epitaxial growth relationship is related to the Ni(022) peak seen in the ω - 2θ scan (Fig. 15) combined with the Ni $\langle 111 \rangle$ directions oriented along the GaAs[110] directions in plane as showed in Fig. 17. The Ni(111) triplet peaks are characteristic of the four possible variants of having one of the in-plane Ni[111] direction aligned parallel to GaAs[110] or GaAs[$\bar{1}\bar{1}0$]. Indeed, in the Ni(011) surface, the $\langle 111 \rangle$ directions are at 109.5° to each other whereas in the GaAs (001) surface, the $\langle 110 \rangle$ direction are at 90° , which leads to the four possible configurations, three of which are shown in Fig. 18. In (A), the Ni atoms are aligned with the GaAs[$\bar{1}\bar{1}0$] direction whereas in (B) and (C) the Ni atoms are aligned along the GaAs[110]. Cases B and C lead to a misalignment of the Ni atoms along the GaAs[$\bar{1}\bar{1}0$] direction which gives rise to a triplet peak around GaAs[$\bar{1}\bar{1}0$] (Fig. 17). However, the experimentally observed angle between the peaks in a triplet

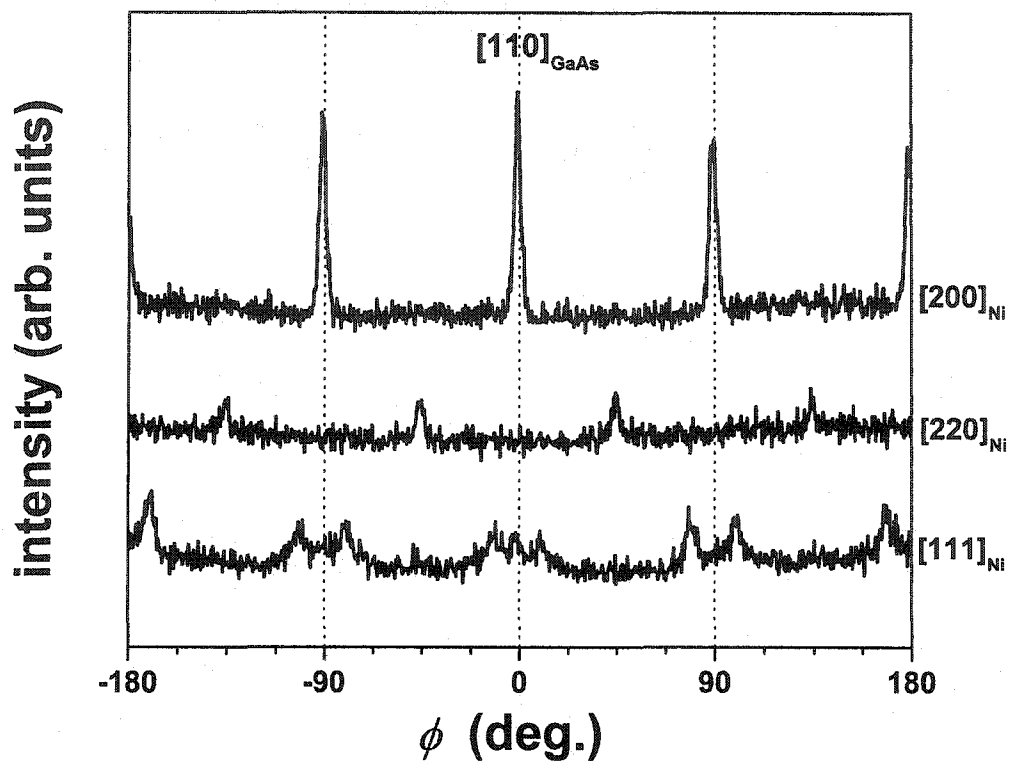


FIG. 17. Grazing incidence x-ray diffraction measurements of a 31 nm thick Ni layer on GaAs(001) with the scattering vector oriented at $\psi = 88^\circ$ from the sample normal. The detector angle was set to the position of respectively the Ni(200), Ni(220) and Ni (111) peaks for the three scans shown. The sample was rotated around the sample normal (ϕ rotation). $\phi = 0^\circ$ corresponds to the GaAs[110] in-plane direction.

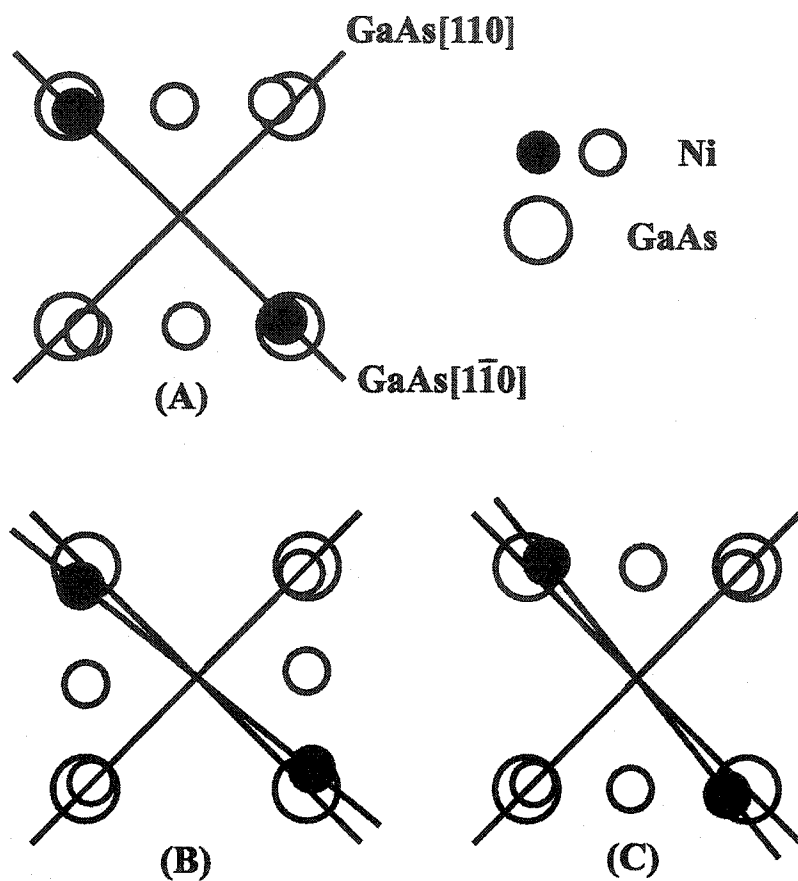


FIG. 18. Three of the four possible alignments of the Ni(011) unit mesh on the GaAs(001) substrate. Only one of the Ni{111} directions can align with a GaAs{110} direction at a time.

(10°) does not correspond with the theoretical angle between the Ni[111] and the GaAs [110] directions (19.5°). This might be due to some lattice deformation.

Detection of the three Ni(111) peaks is found to depend on the grazing angle of incidence.²⁴ Figure 19 (a) shows a ϕ scan with the grazing angle at $\psi = 85^\circ$ to the film surface, showing only two peaks along each GaAs[110] direction. However when the grazing angle of incidence is only at $\psi = 88^\circ$, the peak corresponding to the Ni[111] being exactly along the GaAs[110] is now seen [Fig. 19 (b)]. Hence it appears that the Ni[111] directions exactly parallel to the GaAs[011] directions show a smaller dispersion around the surface normal than the Ni[111] directions which lie close to the GaAs[110]. No obvious variation is seen in the structure with film thickness for the range investigated (10–100 nm). There have also been reports of another possible epitaxial relationship for fcc NiCoCu on GaAs(001)⁶⁹ with the Ni(211) direction along the GaAs(001), which would not be seen by a conventional ω - 2θ scan. To investigate this possibility, in plane measurements along (311) planes have been performed, but no peak was observed.

It is interesting to note that the azimuthal mosaic spread (3° in Fig. 17) of the (001) epitaxy is much narrower than the polar mosaic spread (22°). Hence, the Ni layers have a rather well defined in-plane registry with the substrate while showing a wide spread in canting angle.

The (011) orientation of Ni layers electrodeposited on GaAs(001) had been reported previously.^{17,20} Here we find a mixture of Ni(001) and Ni(011) with, considering the substantially larger rocking curve width for Ni(001), dominantly Ni(001). In a previous study of electrodeposition of Ni on GaAs(001) as a function of current density,²⁰

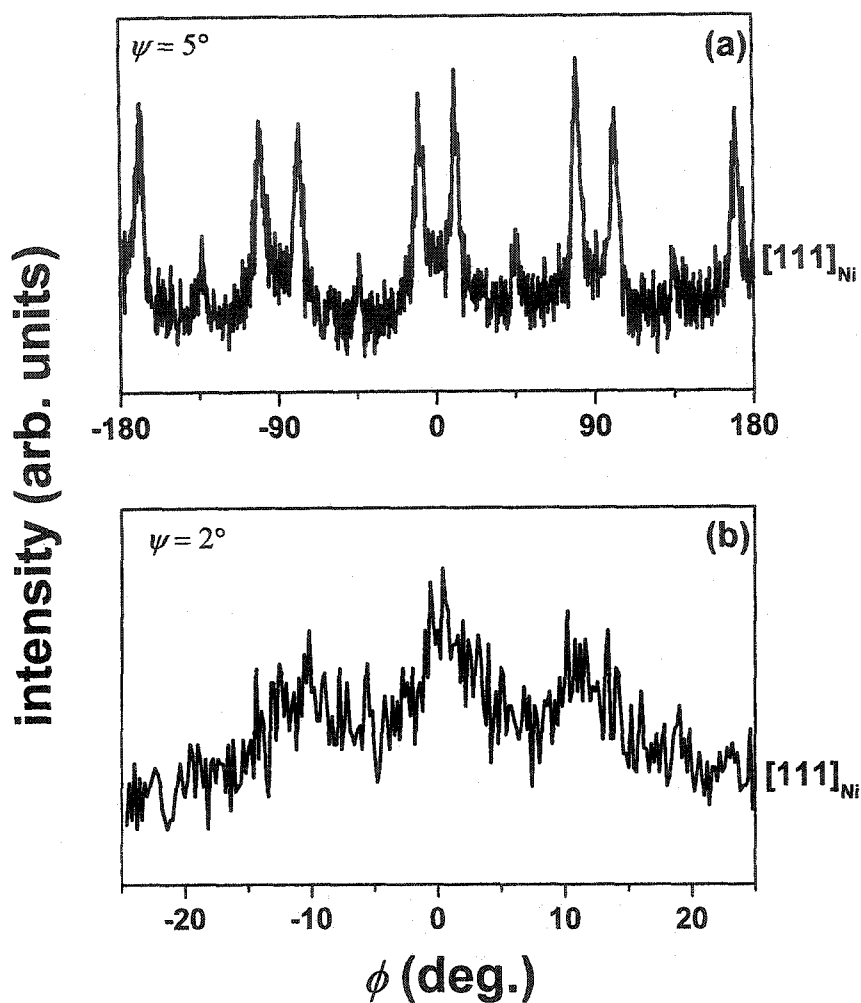


FIG. 19. In plane XRD spectra for 71 nm thick Ni film grown on *n*-GaAs(001). (a) Beam is at a $\psi = 5^\circ$ grazing angle of incidence. (b) Beam is at a $\psi = 2^\circ$ grazing angle of incidence. Detector-beam angle satisfies Ni(111) Bragg condition. The GaAs[110] direction is along $\phi = 0^\circ$ (N.B. This effect is also seen with the 36 nm thick film but the increased signal with thickness makes it easier to see in this film).

the authors report increasing peak intensities of (002) and (111) with decreasing current density. The current density used here (3.5 mA/cm^2) is lower than the range studied by Attenborough et al. but the intensity of the (002) peak we find is not in disagreement with Ref. 20, given the different compositions and pH of the deposition solutions. Obvious, however, is the absence of the (111) orientation in the present case (for all thicknesses), which might be due to the more complex plating solution composition used in Ref. 20. The present XRD data do not show evidence for formation of bcc Ni as it was reported in Ref. 70.⁷⁰

A short study of pH dependence on the growth of Ni films on GaAs(001) has also been performed.²² Figure 20 shows conventional ω - 2θ XRD spectra made on 180 nm thick Ni films grown respectively at $pH = 2.3$, $pH = 2.5$, and $pH = 2.7$. Ni (200) and (220) peaks were observed but no (111) peak. The ratio of the (200) to the (220) increases as the pH decreases. However, as mentioned earlier, rocking curves show that the (220) peak has a narrower angular distribution with respect to the surface normal than the (200), so it is difficult to determine the relative amount of the two orientations in the film by XRD alone. In-plane XRD spectra for films grown at $pH = 2.3$ and $pH = 2.7$ exhibit similar structure as for $pH = 2.5$ previously shown in Fig. 17.

In the following, in-plane directions will be stated with respect to the GaAs substrate axes because of the mixture of two crystalline orientations for the Ni films. The morphology of Ni films has been characterized using atomic force microscopy (AFM) analysis. Figures 21 and 22 show a two-dimension AFM picture of respectively 6 nm and 36 nm thick Ni film grown on GasAs(001). From Fig. 22, the grains size of the 36 nm thick film is estimated at ~ 37 nm. Three-dimension plots of the reconstituted AFM data

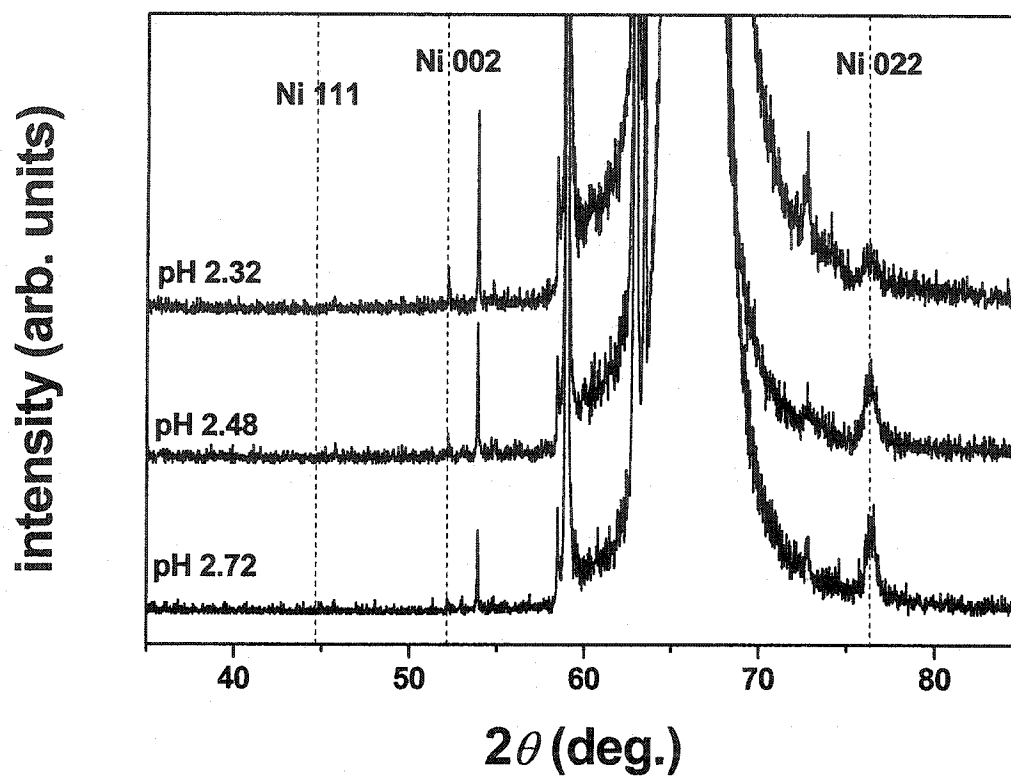


FIG. 20. High angle ω - 2θ x-ray measurement of 180 nm thick Ni layers grown on GaAs(001) at different pH. The vertical dashed lines indicate the 2θ peak positions of Ni(111), Ni(002), and Ni(022).

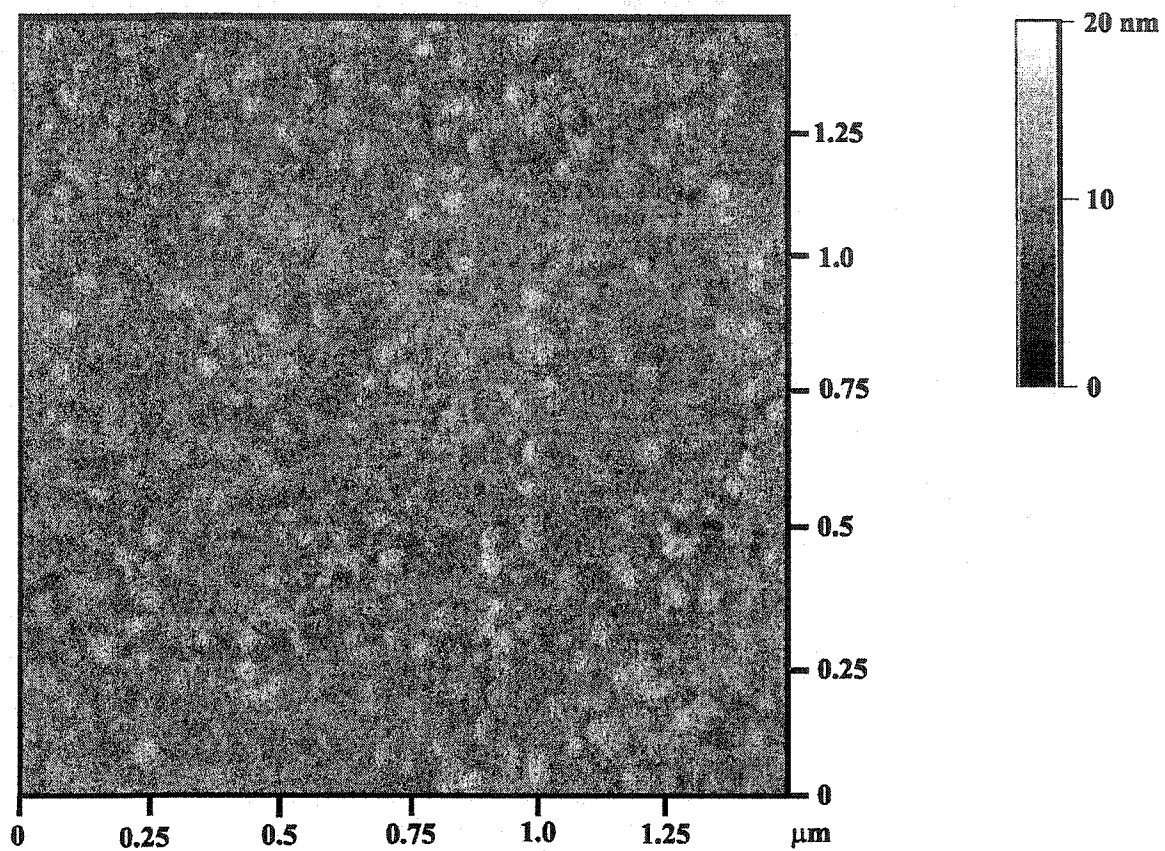


FIG. 21. Atomic force microscope (AFM) picture of a 6 nm thick Ni layer grown on GaAs(001).

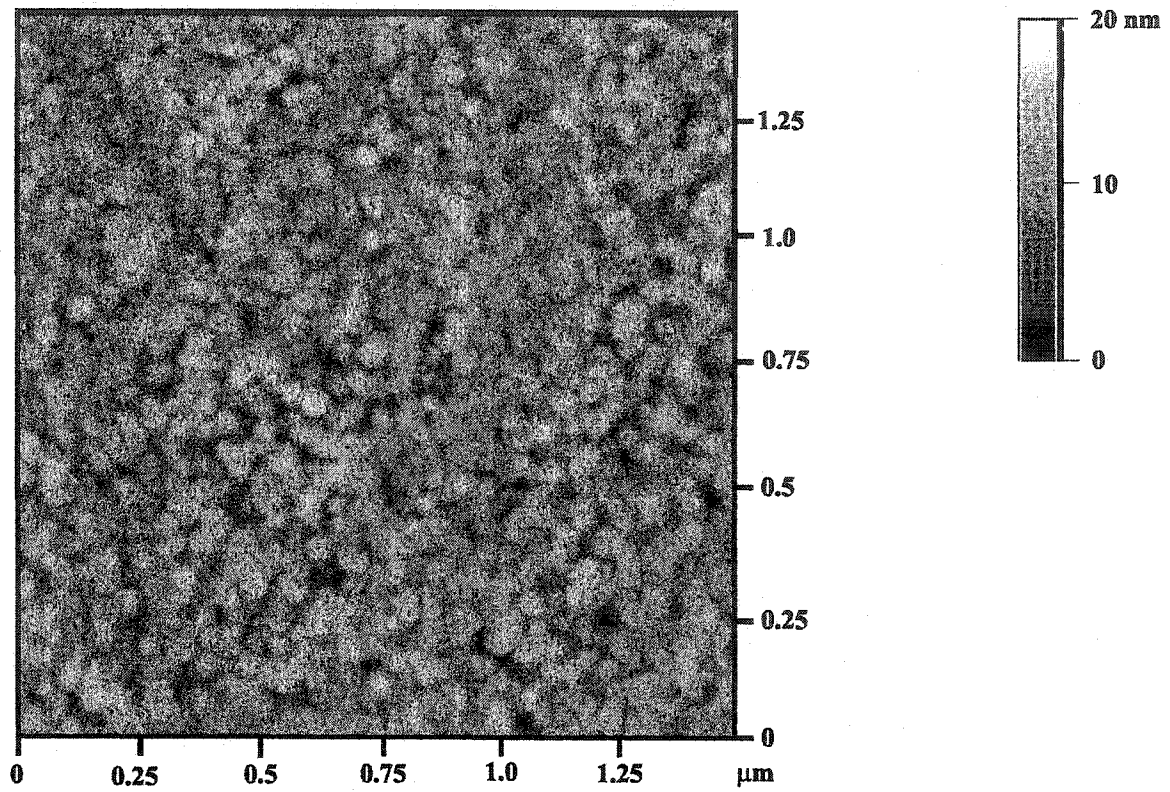


FIG. 22. Atomic force microscope (AFM) picture of a 36 nm thick Ni layer grown on GaAs(001).

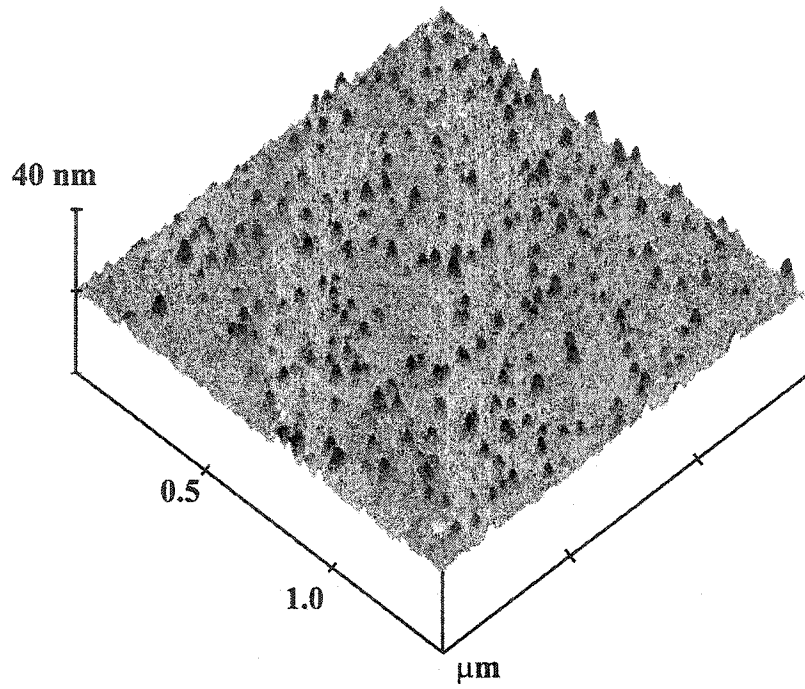


FIG. 23. Three dimensions atomic force microscope (AFM) picture of a 6 nm thick Ni layer grown on GaAs(001).

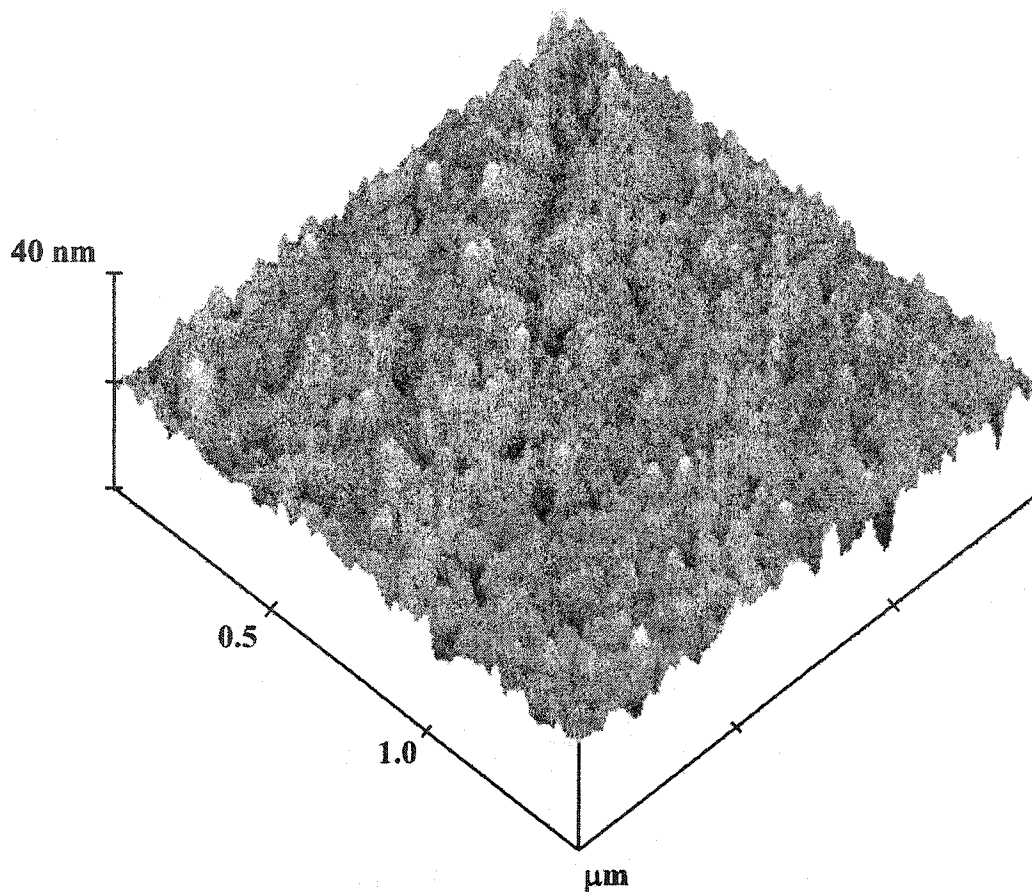


FIG. 24. Three dimensions atomic force microscope (AFM) picture of a 36 nm thick Ni layer grown on GaAs(001).

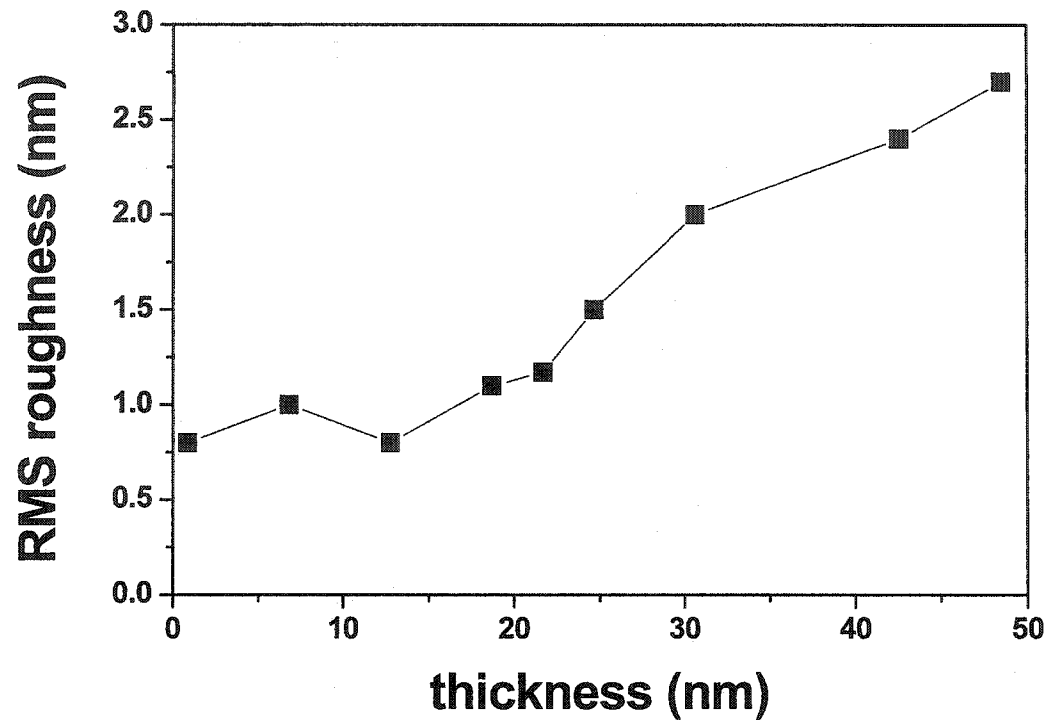


Fig. 25. RMS roughness of Ni films grown on GaAs(001). The line is a guide to the eye.

scans of these films are shown in Figs. 23 and 24. The thicker film (Fig. 24) looks particularly rougher on its surface compared to the thinner one (Fig. 23). Surface RMS roughness analysis with respect to the film thickness is shown in Fig. 25. An increase in the RMS roughness with increasing thickness is clearly seen, with a value starting at ~ 0.75 nm for thin film to 2.7 nm for 50 nm thick film. This is not surprising since the growth of thicker layers is influenced by the seed layers.

(2) Electrodeposited Co can grow with a fcc structure, hcp (see Fig. 26) or a mixture of both, depending on the deposition conditions.^{71,72} These phases are sometime difficult to discriminate by XRD. Figure 27 shows the conventional ω - 2θ XRD spectrum for a 106 nm thick Co film. Satellites originated by the x-ray source (W) and the substrate (GaAs K_α and K_β lines) are present along with a forbidden GaAs(002) peak which could be assigned to a lattice expansion.

A clear fcc Co(022) peak, with its corresponding lattice spacing $d = 1.2532$ Å, can be seen around $2\theta = 76^\circ$. However, since Co can also be present in its hexagonal structure, this peak could also be assigned to the hcp α -Co(11 $\bar{2}$ 0) which has a very close lattice spacing of $d = 1.252$ Å. In order to identify further hypothetic fcc or hcp peaks, a longer scan in the regions of interest have been performed. Figure 28 shows a zoom in of the previous spectrum for the region included between $2\theta = 73^\circ$ to $2\theta = 86^\circ$ where hcp α -Co(10 $\bar{1}$ 3) is expected around $2\theta = 84.15^\circ$ ($d = 1.149$ Å). The only peak present is the one previously assigned to fcc Co(022)/hcp α -Co(11 $\bar{2}$ 0). In the region included between $2\theta = 40^\circ$ to $2\theta = 52^\circ$, various peaks originated by either hcc phase [(111) and (002)] or hcp α -Co phase [(10 $\bar{1}$ 0), (0001), and (10 $\bar{1}$ 1)] are expected but no peaks were observed as shown

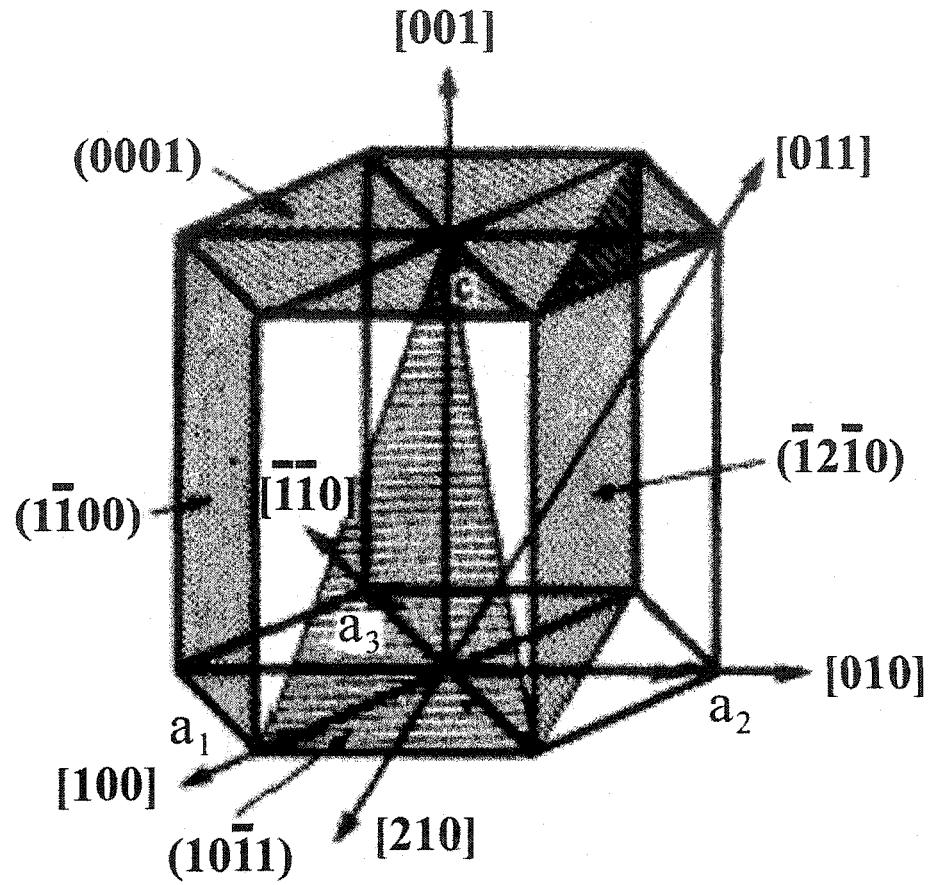


FIG. 26. A drawing showing some important low index planes in hexagonally close packed cobalt.

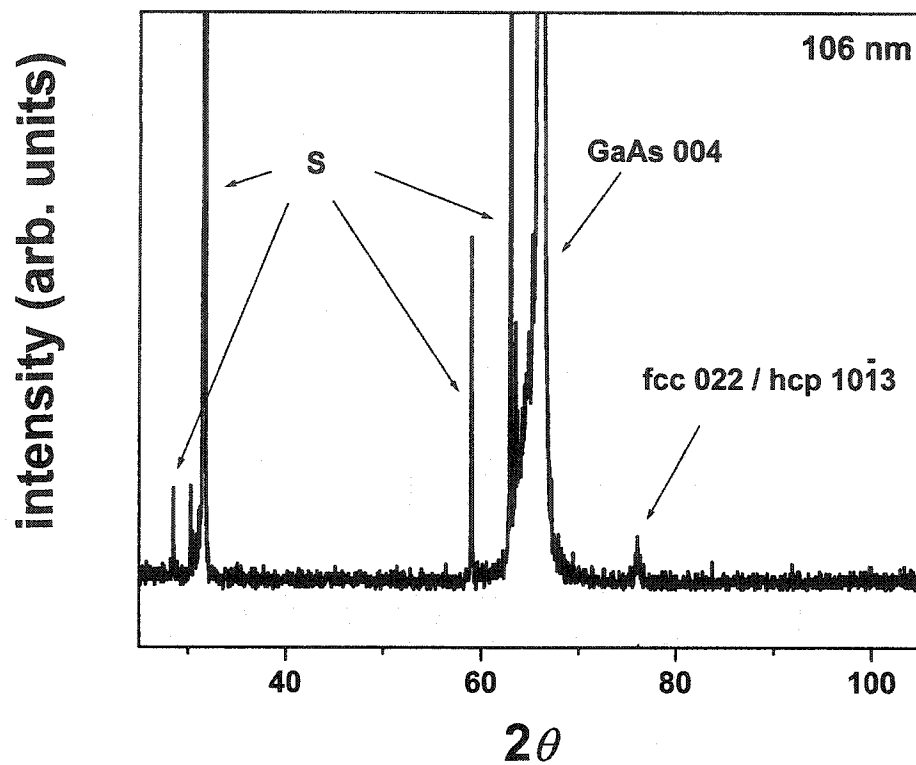


FIG. 27. High angle ω - 2θ x-ray measurement of a 106 nm thick Co layer grown on GaAs(001). *S* are the satellites originated from the Cu K_{α} and K_{β} and Tungsten (W) filament from the x-ray diffractometer source.

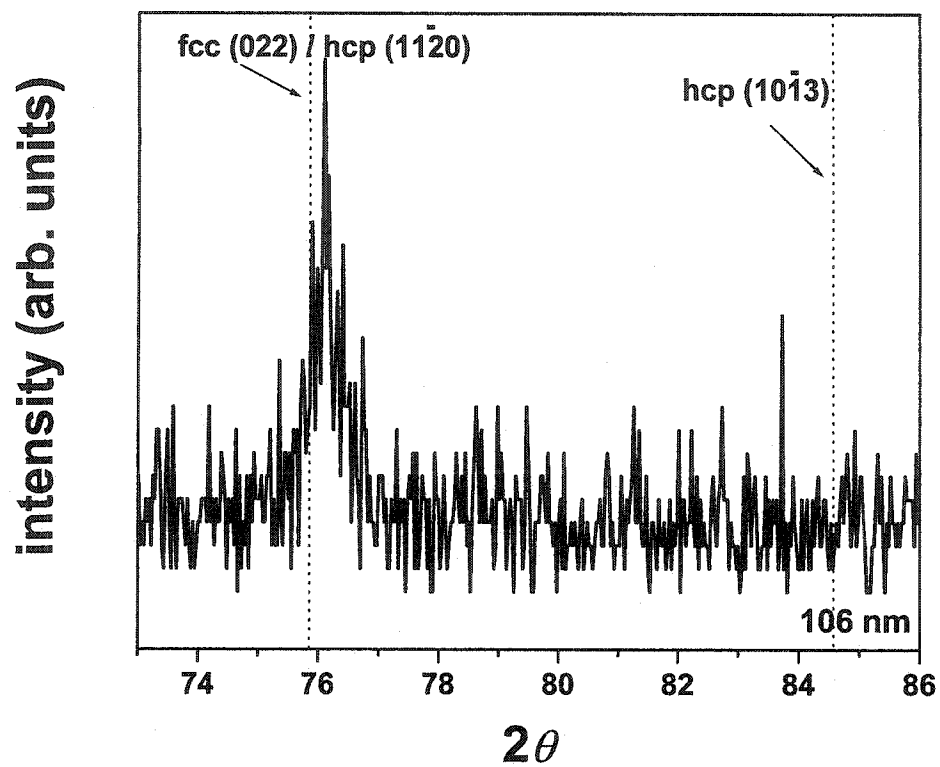


FIG. 28. High angle ω - 2θ x-ray measurement of a 106 nm thick Co layer on GaAs(001). The vertical dashed lines indicate the 2θ peak positions of fcc Co(022) / hcp Co(11 $\bar{2}$ 0) and hcp Co(10 $\bar{1}$ 3).

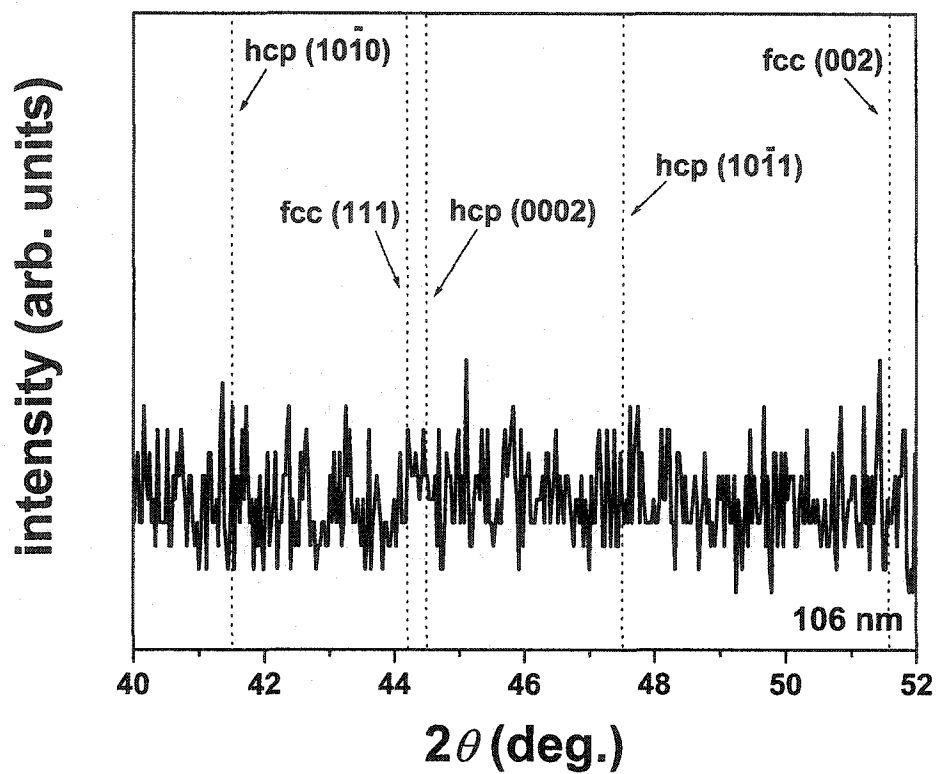


FIG. 29. High angle ω - 2θ x-ray measurement of a 106 nm thick Co layer on GaAs(001). The vertical dashed lines indicate the 2θ peak positions of hcp Co(1010), fcc Co(111), hcp Co(0002), hcp Co(1011), and fcc Co(002).

in Fig. 29. A strong hcp α -Co(11 $\bar{2}$ 0) texture has been seen in previous work⁷³ for a 32 nm thick Co film while for thicker films (~ 133 nm and up) significant diffraction from hcp α -Co(10 $\bar{1}$ 0) along with lesser contribution from (0002), and (1011) orientations were observed without the presence of fcc phase. However, it is important to mention that the electrodeposition growth conditions used in Ref. 73 were somewhat different from those used in the present work. Indeed, boric acid was added to the electrolyte while potentiostatic/galvanostatic was used with higher potential/current density ($V = -1.8$ V, $J = 10$ mA/cm²) and the solution was at pH = 3.45.

In plane XRD has been performed in order to clear the ambiguity pointed in the conventional ω - 2θ XRD scan. Figure 30 shows grazing incidence x-ray diffraction measurements with the scattering vector oriented at $\psi = 88^\circ$ from the sample normal. The detector angle was set to the position of the fcc Co [(220), (200), and (111)] and hcp α -Co phases [(10 $\bar{1}$ 3), (10 $\bar{1}$ 0), (10 $\bar{1}$ 1), and (0002)]. The sample was rotated around the sample normal (ϕ rotation). $\phi = 0^\circ$ corresponds to the GaAs[110] in-plane direction. A four-fold symmetry peak corresponding to either a hcp α -Co(0002) ($d = 2.023$ Å) or a fcc(111) ($d = 2.0467$ Å) is observed parallel to the GaAs[110]. However, according to the out of plane hcp α -Co(11 $\bar{2}$ 0) peak, the c -axis [0001] of the (11 $\bar{2}$ 0) hexagonal phase would lie down in plane and only a two-fold symmetry would therefore be expected from the hcp α -Co(0002) ruling out the possibility of assigning the out of plane peak to hcp α -Co(11 $\bar{2}$ 0) peak. Nevertheless, an even distribution between orthogonal in-plane hcp α -Co(11 $\bar{2}$ 0) [0001]//GaAs(001)[110] and Co(11 $\bar{2}$ 0) [0001]//GaAs(001)[$\bar{1}$ 10] variants [as well as the Co(1010)<0001>//GaAs(001)<110>] have been observed in Ref. 73 leading

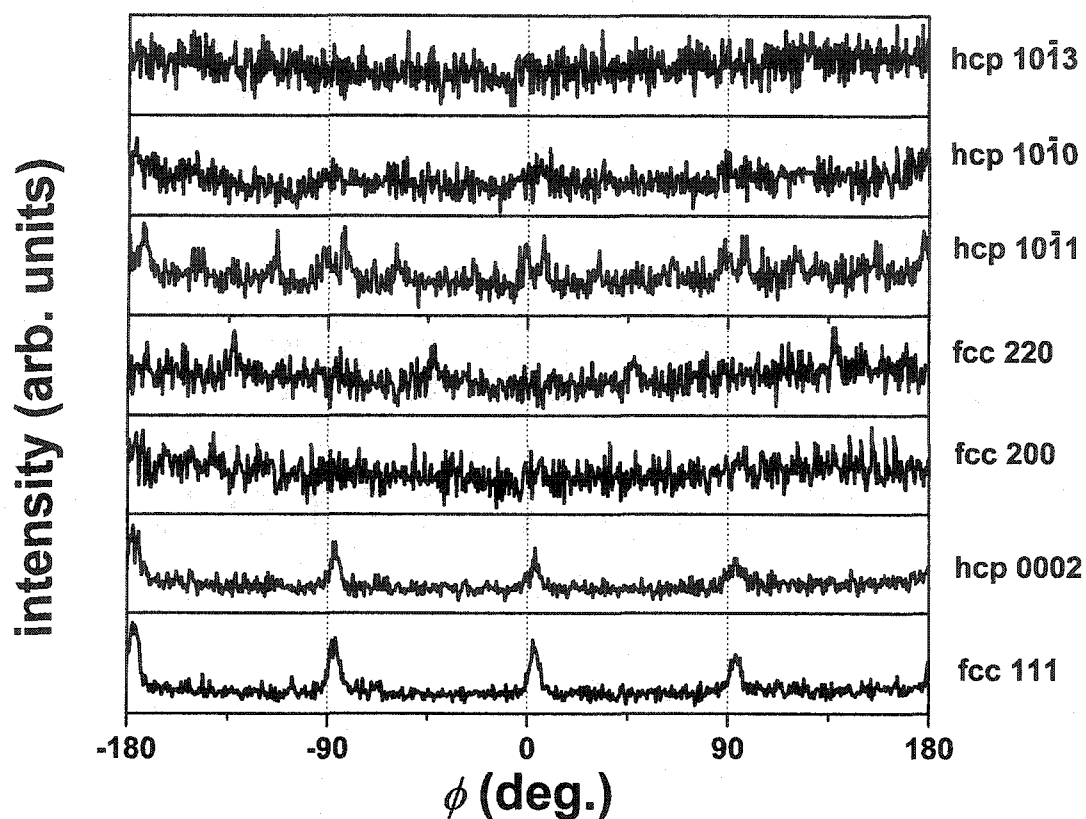


FIG. 30. Grazing incidence x-ray diffraction measurements of a 106 nm thick Co layer on GaAs(001) with the scattering vector oriented at $\psi = 88^\circ$ from the sample normal. The detector angle was set to the position of the Co fcc and hcp phases as defined in the graph. The sample was rotated around the sample normal (ϕ rotation). $\phi = 0^\circ$ corresponds to the GaAs[110] in-plane direction.

to a four fold symmetry in the XRD peak intensity. On the other hand, a fcc (111) peak in plane would result in a non-symmetric four-fold symmetry since the $\langle 111 \rangle$ directions in a cubic cell are not at 90° away to each other. Hence, this will rule out the possibility of having the fcc Co(022) peak out of plane. In addition, a very weak four-fold symmetry hcp α -Co(10 $\bar{1}$ 1) ($d = 1.91 \text{ \AA}$) or fcc (220) ($d = 1.2532 \text{ \AA}$) is seen in plane however a two-fold symmetry peak is expected for the fcc (220). As a result, the structure of Co grown on GaAs(001) can not be assigned unambiguously by this technique.²²

Nuclear magnetic resonance (NMR) peaks depend upon the chemical environment.^{74,75} By using this technique, it is thus possible to distinguish between fcc, bcc and hcp Co phases. The resonant frequencies associated with the fcc and hcp α -Co phases are expected at respectively 217.4 MHz and around 222 MHz.⁷⁴ Figure 31 shows a NMR spectrum for a 36 nm thick Co film grown on GaAs(001). A mixed fcc/hcp phase is observed with a predominant hcp component compared to the fcc while no evidence of bcc Co is observed which confirms the growth of a mixture of both fcc and hcp α -Co phase.²²

(3) The high-angle ω - 2θ XRD spectra shown in Fig. 32 reveal the out-of-plane orientation of the 400 nm thick Fe films grown on GaAs(001)^{26,27} from FeSO₄ and FeCl₂ electrolyte solutions. In order to suppress the dominant substrate peaks, which would otherwise obscure the superposing Fe peaks, the samples were offset in ω by 0.2° – 0.4° . Both spectra are dominated by the Fe peaks related to the preferential orientation Fe (001) on GaAs(001) regardless of the electrolyte used. The (001) oriented layers ($2\theta = 66^\circ$) show small peaks related to other orientations, mostly (011) around $2\theta = 45^\circ$ and

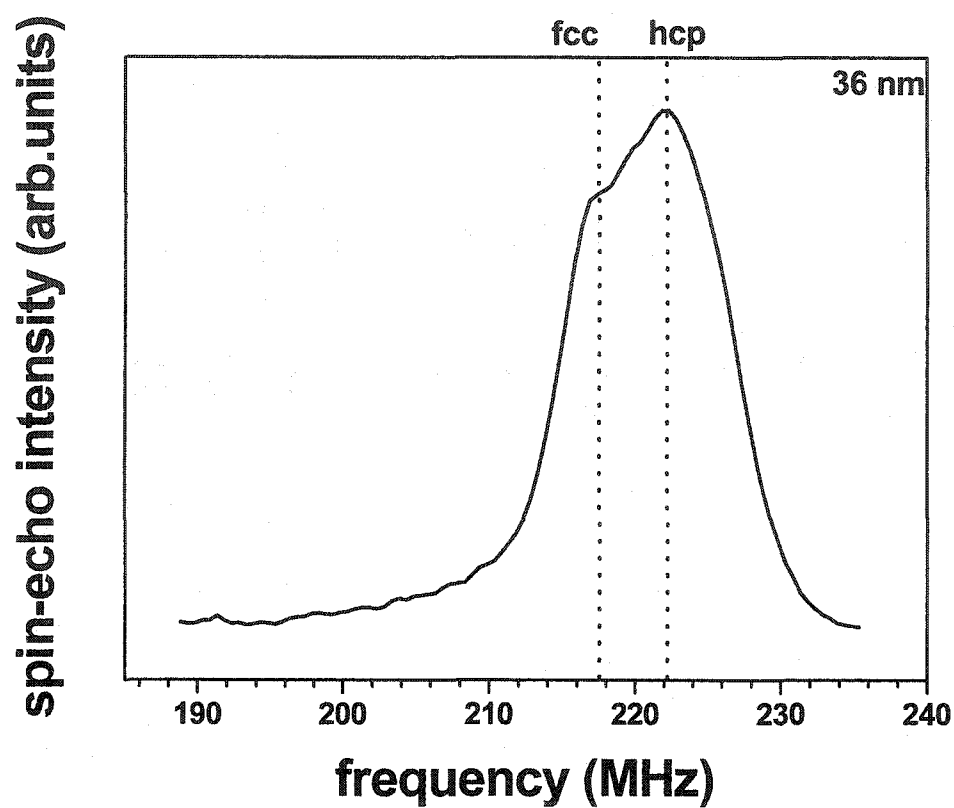


FIG. 31. Nuclear magnetic resonance (NMR) data of a 36 nm thick Co film grown on GaAs(001).

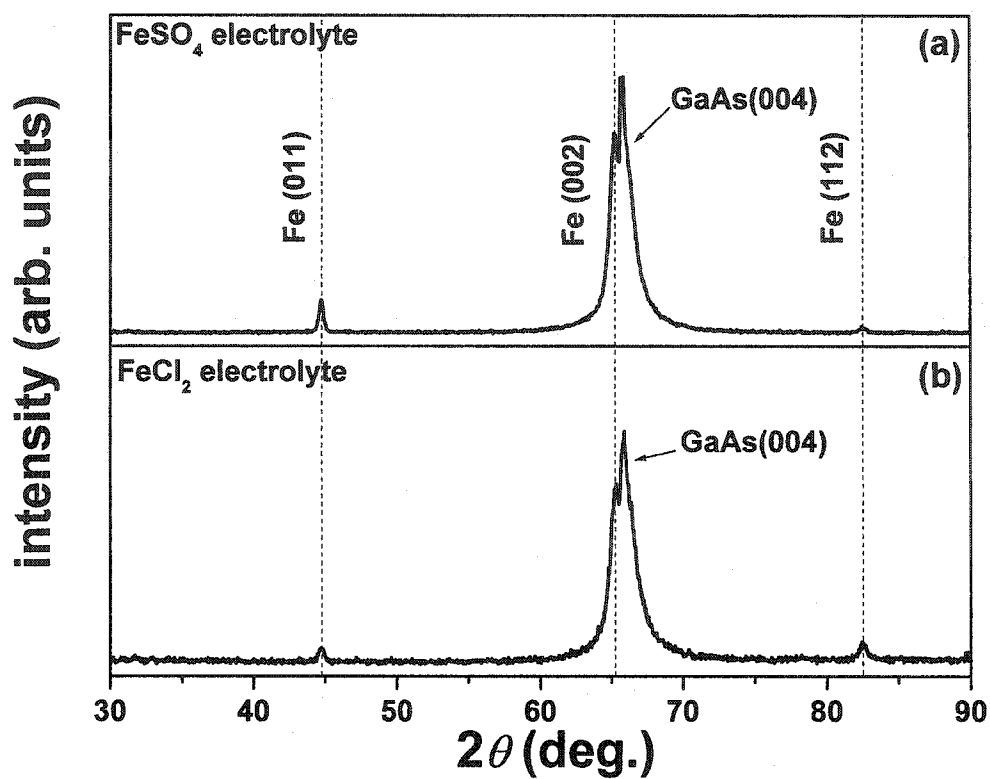


FIG. 32. High-angle ω - 2θ XRD spectra showing the out-of-plane orientation of 400 nm Fe layers grown on GaAs(001) from: (a) a FeSO₄ solution and (b) a FeCl₂ solution. The vertical dashed lines indicate the 2θ positions of bcc Fe(011), Fe(002), and Fe(112) peak. In order to suppress the intense substrate peaks, the measurements were taken with a ω -offset of 0.2°–0.4°.

very little (112) around $2\theta = 84^\circ$. From Fig. 33, the ω -rocking curve widths of the major peak Fe(002) is about 3.2° and 2.6° using respectively FeSO₄ and FeCl₂.

In order to verify the in-plane registry of the film with the substrate, glancing angle XRD intensities were measured with the scattering vector oriented at $\psi = 86^\circ$ from the sample normal (Fig. 34). The in plane XRD spectra for Fe films deposited on GaAs(001) using the FeSO₄ and FeCl₂ solutions are shown in Figs. 34 (a) and 34 (b) respectively, indicating a four-fold symmetry for Fe(110) and Fe(100) peaks. Thus the dominating epitaxial relation is Fe(001)[100]//GaAs(001)[100], which can be visualized by the schematic diagrams shown in the inset of the XRD spectra shown in Fig. 34. This is in agreement with the structure of epitaxial Fe layers grown by molecular beam epitaxy (MBE).⁷⁶ The azimuthal width of the peaks is around 7° (11° – 16°) for samples plated from the FeSO₄ (FeCl₂) solution.

Besides the dominating symmetries, one notices [most pronounced in Fig. 34 (b)] additional minor peaks with a 30° period in ϕ which indicate the presence of other orientational relationships at the interface and the imperfection of the epitaxial growth. These minor orientations are close to Fe(001)[210]//GaAs(001)[100]. On the basis of the glancing angle XRD spectra, the FeSO₄ solution clearly produces films with the best structural quality [Fig. 34 (a)].

The morphology of Fe films was characterized using AFM analysis. The surface RMS roughness as extracted from AFM images is about 20 nm for all Fe layers. Fractal analysis in Table I revealed that the lateral correlation length is larger for Fe layers grown from FeCl₂ (~ 1340 nm) than for those grown from FeSO₄ (~ 470 nm). A typical AFM image of a 400 nm thick Fe film grown on GaAs(001) is shown in Fig. 35. From

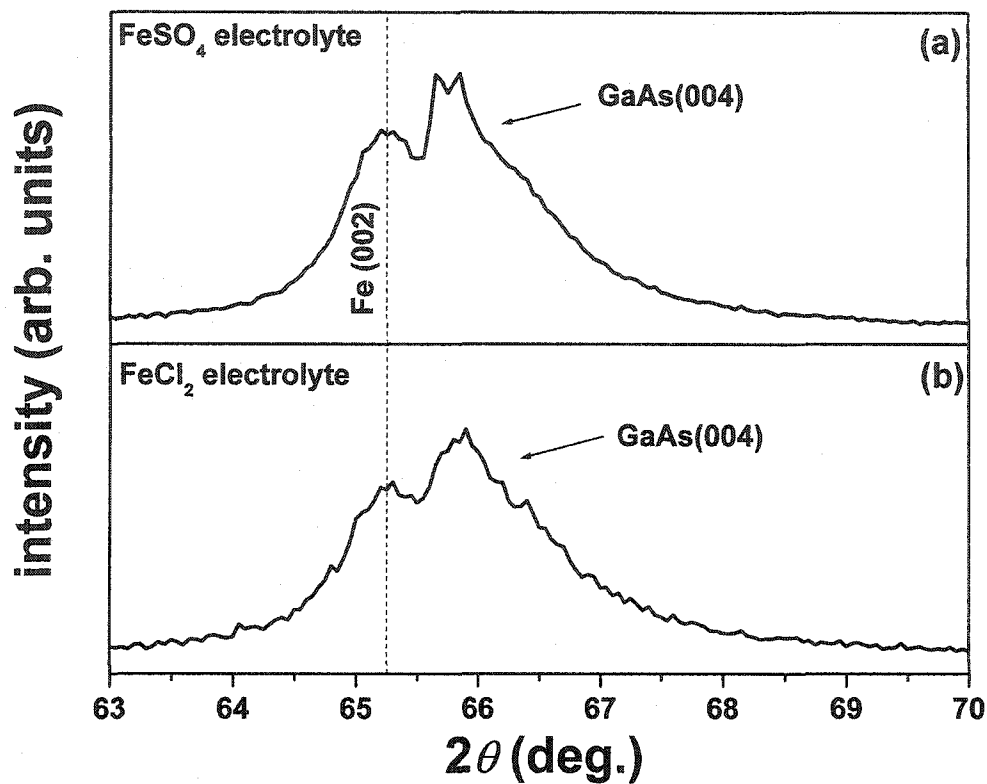


FIG. 33. Zoom in of high-angle ω - 2θ XRD spectra showing the out-of-plane orientation of 400 nm Fe layers grown on GaAs(001) from: (a) a FeSO₄ solution and (b) a FeCl₂ solution. The vertical dashed line indicates the 2θ positions of bcc Fe(002) peak. In order to suppress the intense substrate peaks, the measurements were taken with a ω -offset of 0.2°–0.4°.

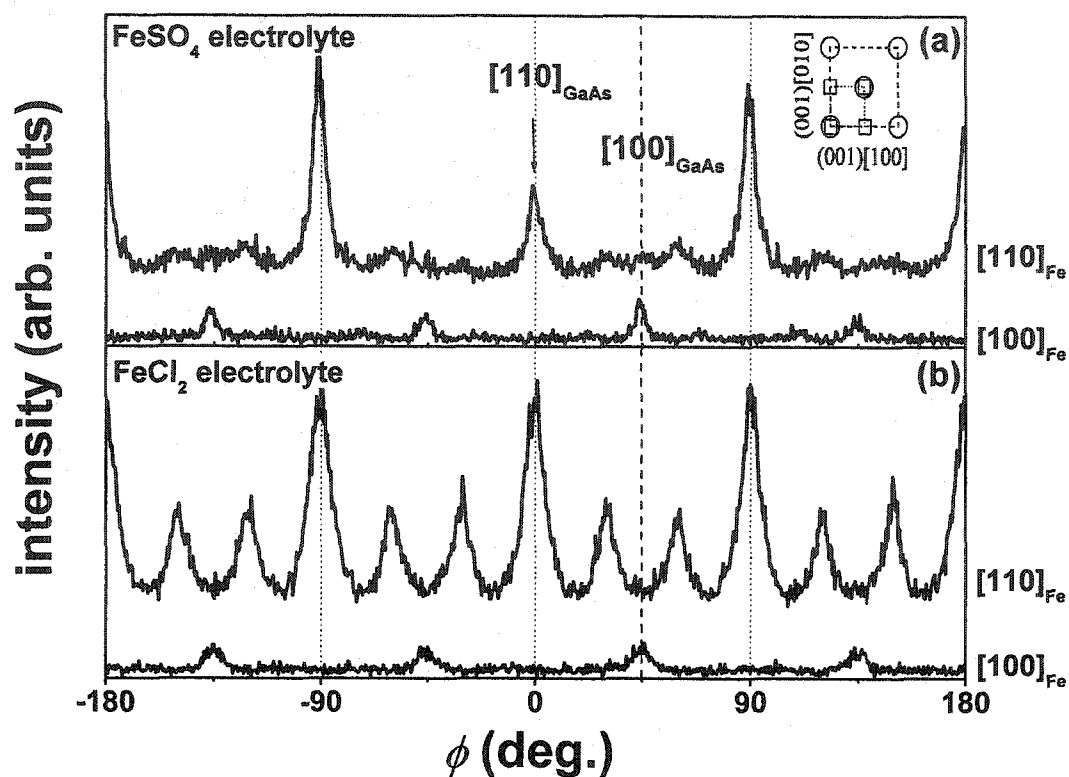


FIG. 34. ϕ -scans at grazing incidence ($\psi = 86^\circ$ from the film normal) of 400 nm Fe films grown on GaAs(001) showing the major Fe epitaxial relations with the GaAs substrate. ϕ is the angle enclosed between scattering vector and the GaAs[110] direction. Shown are spectra for Fe grown from: (a) a FeSO_4 solution and (b) a FeCl_2 solution. For each sample, the upper (lower) spectrum was obtained at $2\theta = 44.6^\circ$ (65.1°), corresponding to $\text{Fe}\{110\}$ ($\text{Fe}\{100\}$) in-plane peaks. The spectra are vertically offset for clarity. The insert provides schematic visualization of the GaAs (circles) and Fe (squares) surface unit mesh.

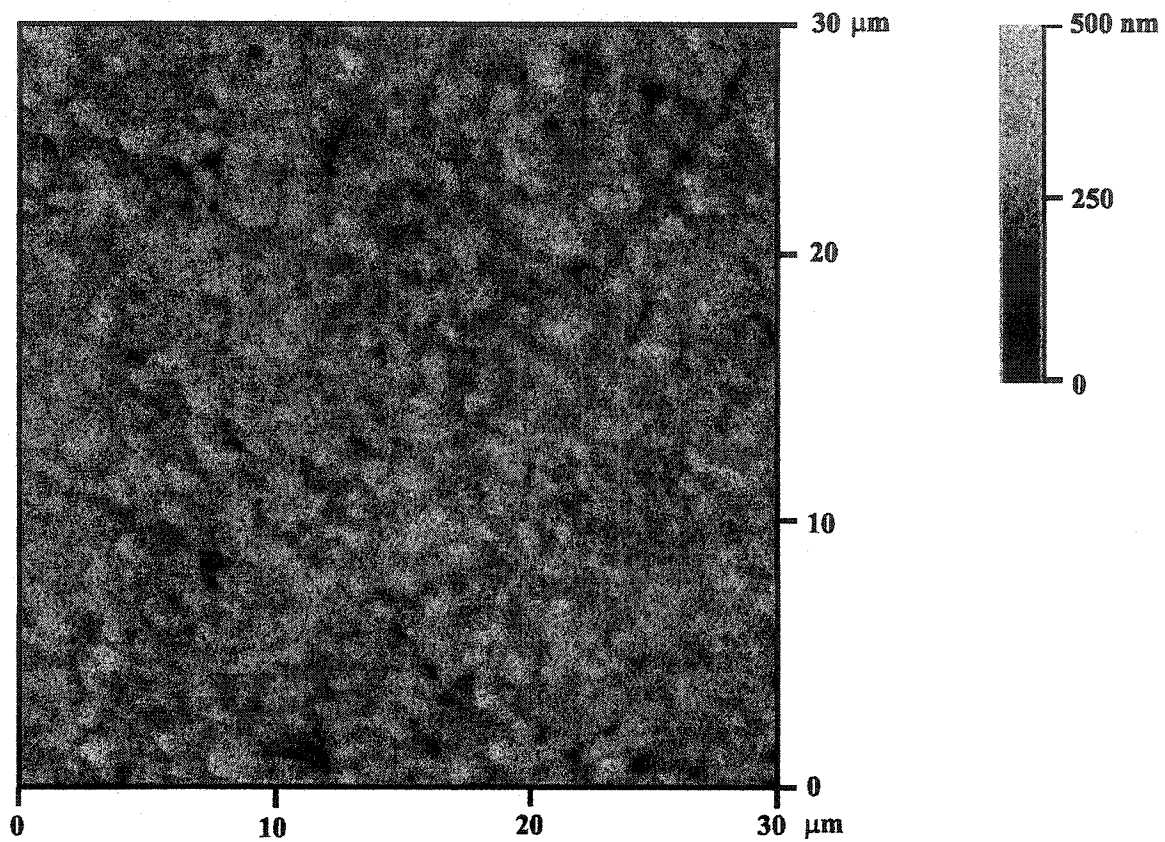


FIG. 35. Atomic force microscope (AFM) picture of a 400 nm thick Fe film grown on GaAs(001) from a FeSO_4 solution at $\text{pH} = 2.5$ and 3.5 mA/cm^2 .

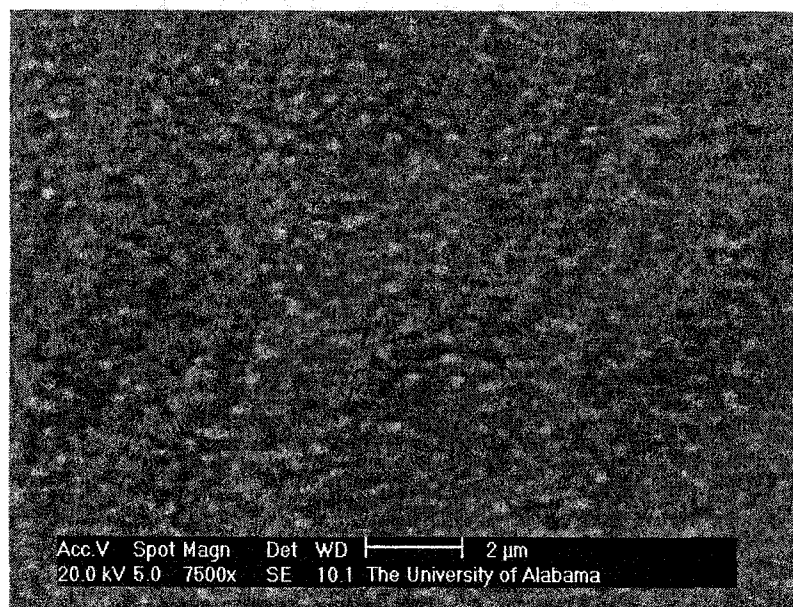


FIG. 36. SEM surface morphology of a 300 sec electrodeposited Fe film grown on GaAs(001) from a FeSO_4 electrolyte solution.

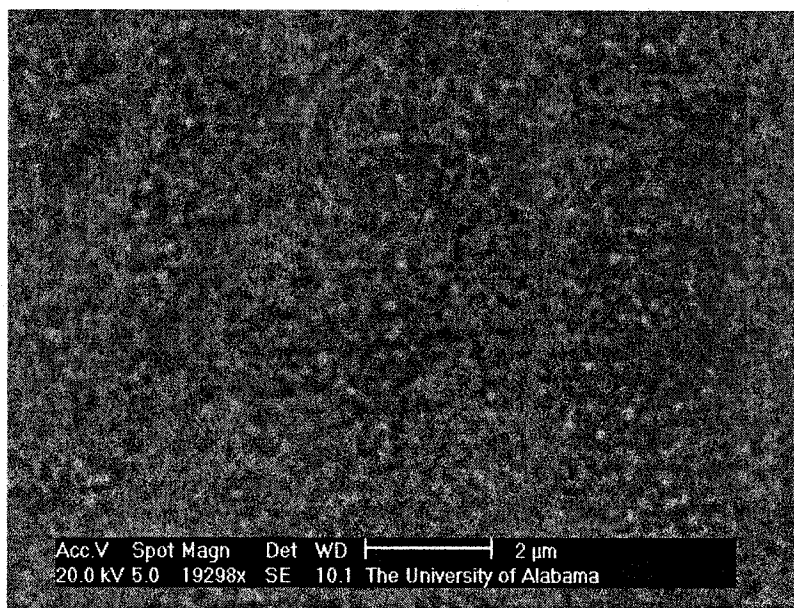


FIG. 37. SEM surface morphology of a 300 sec electrodeposited Fe film on GaAs(001) from a FeCl_2 electrolyte solution.

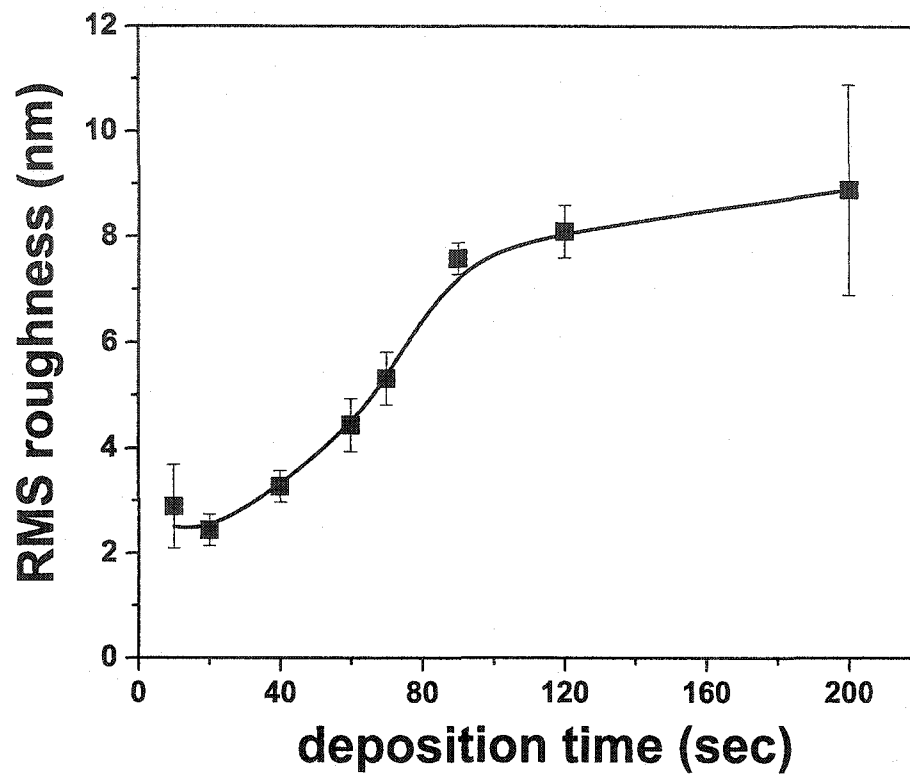


FIG. 38. RMS roughness of Fe films grown on GaAs(001) from FeSO_4 and FeCl_2 electrolytes.

TABLE I. Fractal analysis of 400 nm thick Fe films grown on GaAs(001) from FeSO₄ and FeCl₂ solutions.

	Fe on GaAs(001) FeSO ₄ solution	Fe on GaAs(001) FeCl ₂ solution
Correlation length (nm)	468	1336
Roughness (nm)	28	31

scanning electron microscope (SEM) images of a 150 nm thick Fe film grown from FeSO₄ (Fig. 36) and a 200 nm thick Fe film grown from FeCl₂ (Fig. 37), the grain sizes are smaller than 100 nm. It is also noted that after a few weeks of exposure to air, Fe films prepared using FeCl₂ solutions appeared less shiny than those prepared from FeSO₄ solutions. This is not surprising as the FeSO₄ grown layers are of better crystalline quality, which can prevent Fe layers from oxidizing.⁷⁷ AFM performed on a series of films indicated an increase in the RMS roughness from 2 to 9 nm as the deposition time increased from 10 to 200 seconds (Fig. 38).

(4) Before obtaining successful electrodeposited epitaxial Fe films onto GaAs(001), preliminary work was done on Fe_xNi_{1-x} films ($x \geq 0.9$) as a preferred as a first step to reproduce the epitaxial growth schema of Fe onto GaAs(001).⁷⁶ Unfortunately, no evidence of texture growth was seen either by using conventional ω - 2θ or glancing angle XRD.

b. GaAs(011). (1) High angle ω - 2θ XRD scan on a 21 nm thick Ni film is shown in Fig. 39. In order to suppress the dominant GaAs(022) peak and its K_{β} satellite the sample angle ω was intentionally offset by 0.5°. A clear fcc Ni(111) peak perpendicular to the GaAs(011) surface with a rocking curve width of $\Delta\omega = 4^\circ$ is observed.

In-plane XRD measurements at grazing incidence with the scattering vector

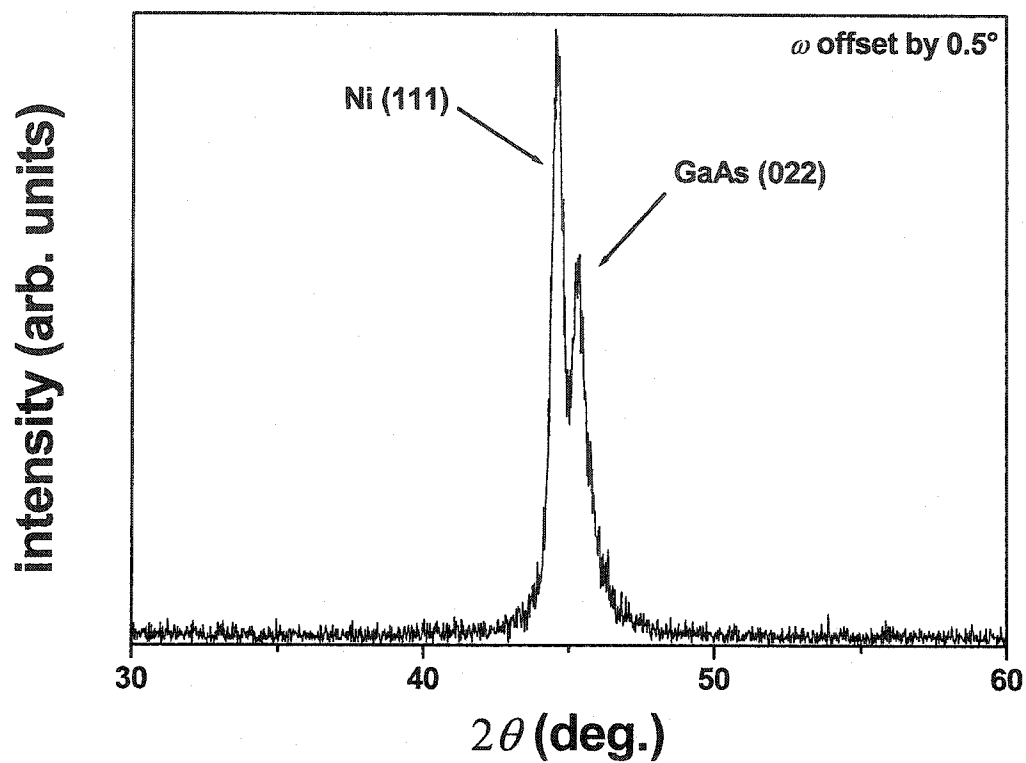


FIG. 39. High angle ω - 2θ x-ray measurement of a 21nm thick Ni layer on GaAs(011). The measurements were made with an ω -offset of 0.5°.

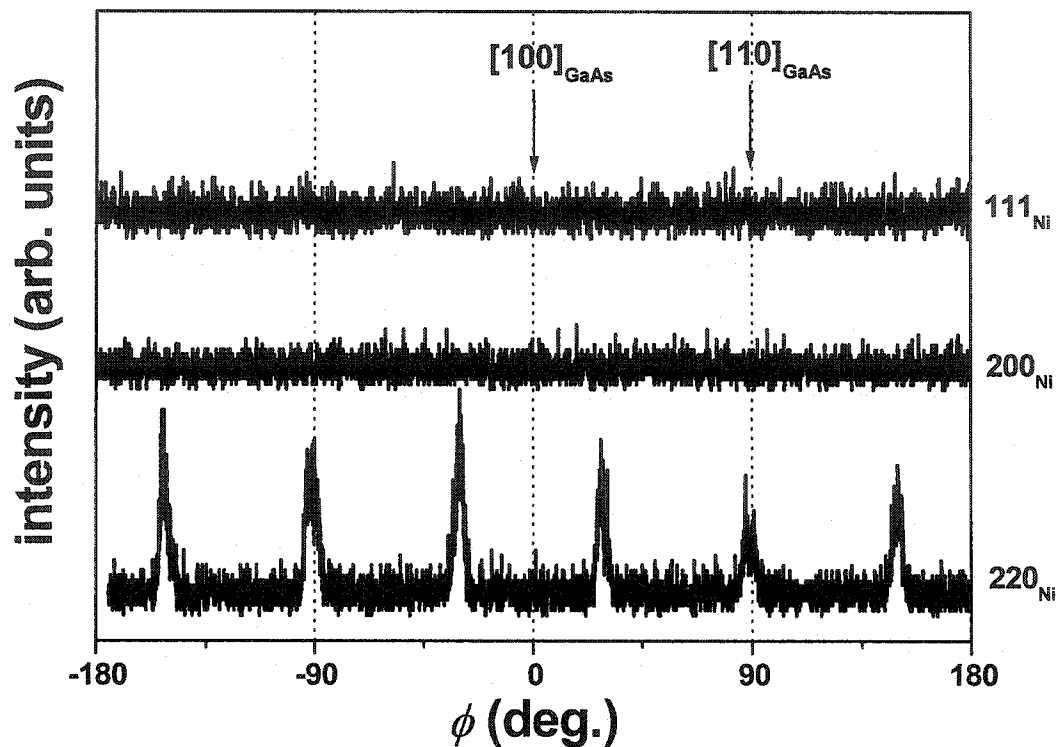


FIG. 40. Grazing incidence x-ray diffraction measurements of a 21 nm thick Ni layer on GaAs(011) with the scattering vector oriented at $\psi = 88^\circ$ from the sample normal. The detector angle was set to the position of respectively the Ni(200), Ni(220) and Ni(111) peaks for the three scans shown. The sample was rotated around the sample normal (ϕ rotation). $\phi = 0^\circ$ corresponds to the GaAs[100] in-plane direction.

oriented at $\psi = 88^\circ$ from the sample normal are shown in Fig. 40 for the position of the detector angle corresponding to Ni(200), Ni(220), and (111). Six fcc Ni(220) peaks with a full width at half maximum of $\Delta\phi = 5^\circ$ separated by 30° and with the $\langle 110 \rangle$ Ni direction parallel to the $\langle 110 \rangle$ GaAs direction are seen, giving the epitaxial relationship Ni(111)[110] // GaAs(011)[110].²⁵ However, the (220) peaks appear to be split along the $\langle 110 \rangle$ GaAs directions, probably indicating two variants of Ni[110] at a small angle with respect to GaAs[110]. No Ni(111) nor Ni(200) peaks were seen. It should be mentioned that for $pH = 2.3$ to $pH = 2.7$, the crystalline structure of Ni films grown on GaAs(011) remains unchanged too.²²

(2) High angle ω - 2θ XRD scans on a 90 nm thick Co film (Fig. 41) were measured with a deliberate sample misalignment of $\omega = 0.3^\circ$ in order to attenuate the GaAs (011) peak. The spectrum shows two peaks at $2\theta = 41.7^\circ$ and $2\theta = 47.5^\circ$. Those peaks match with the position of hcp α -Co($10\bar{1}0$) and hcp α -Co($10\bar{1}1$) respectively but have no correspondence with fcc Co peaks. However, this does not rule out the possibility of having a fcc structure since a fcc-Co(111) peak could be hidden at $2\theta = 44.2^\circ$ under the substrate peak. An ω -rocking curve at high angle ω - 2θ corresponding to the hcp α -Co ($10\bar{1}1$) peak is shown in Fig. 42. The resulting angle dispersion is $\sim 8^\circ$.

In order to reveal the in-plane registry of a 280 nm thick Co film with the substrate, glancing angle XRD intensities were measured with the scattering vector oriented at $\psi = 88^\circ$ from the sample normal (Fig. 43). Peaks for $2\theta = 75.6^\circ$ (either fcc Co(220) or hcp α -Co($11\bar{2}0$)) with a six-fold symmetry in ϕ and peaks for $2\theta = 44.2^\circ$

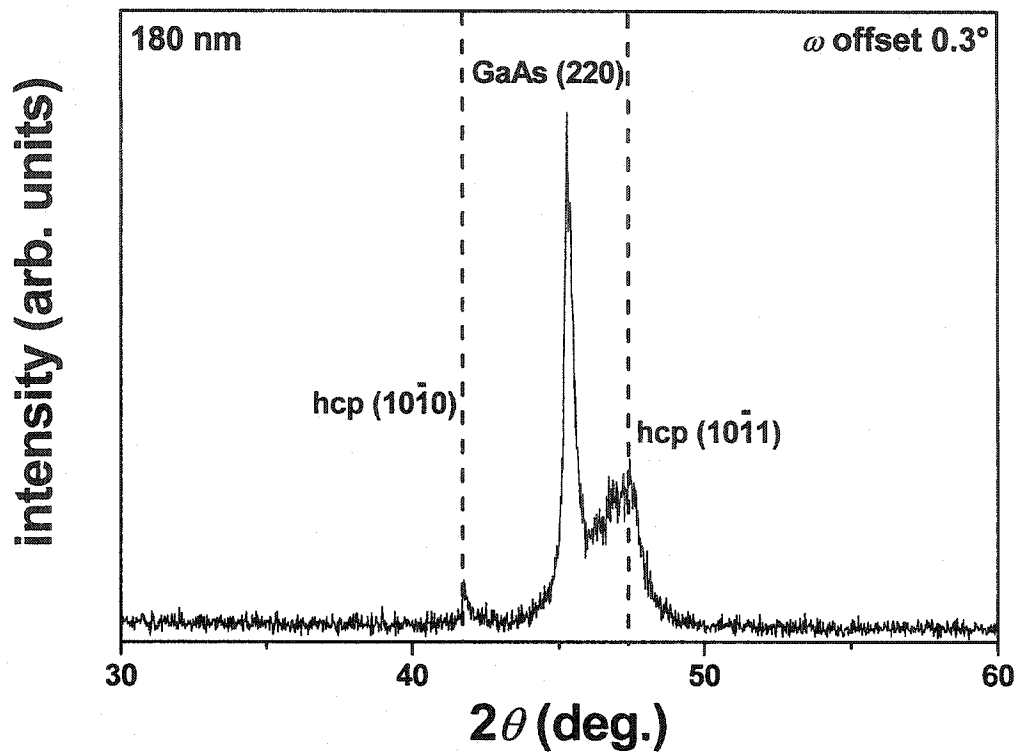


FIG. 41. High angle ω - 2θ x-ray measurement of a 180 nm thick Co layer on GaAs(011). The vertical dashed lines indicate the 2θ positions of hexagonal Co(10 $\bar{1}$ 0) and Co(10 $\bar{1}$ 1) peak. The measurements were made with an ω offset of 0.3°.

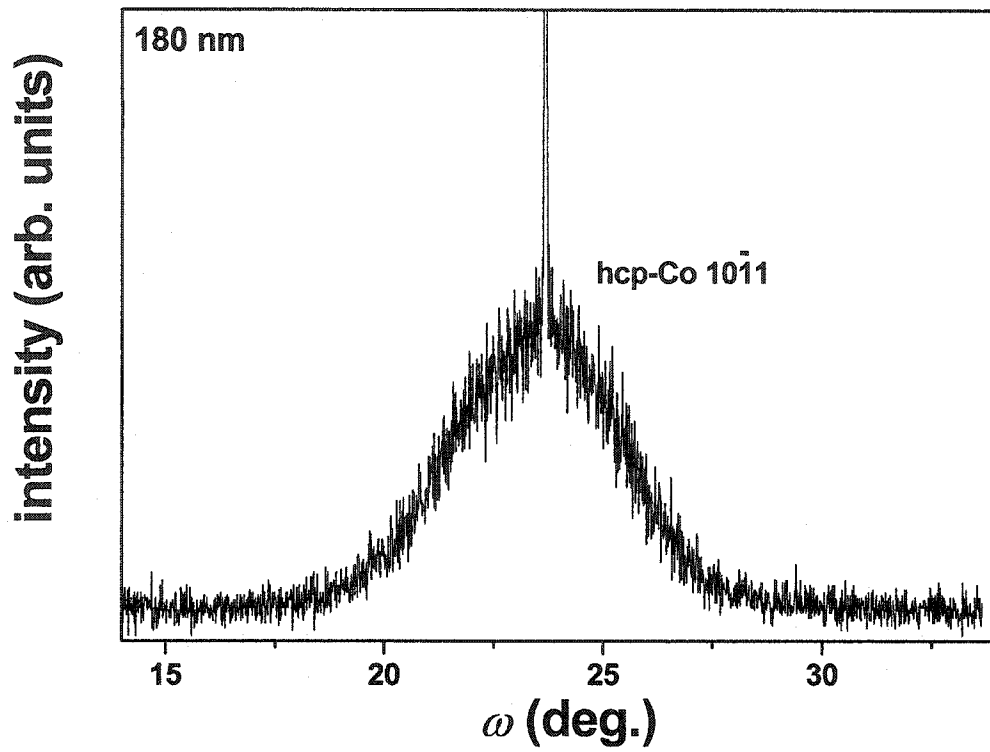


FIG. 42. ω -rocking x-ray measurement of a 180 nm thick Co layer on GaAs(011) at high angle ω - 2θ corresponding to hcp Co(10 $\bar{1}$ 1).

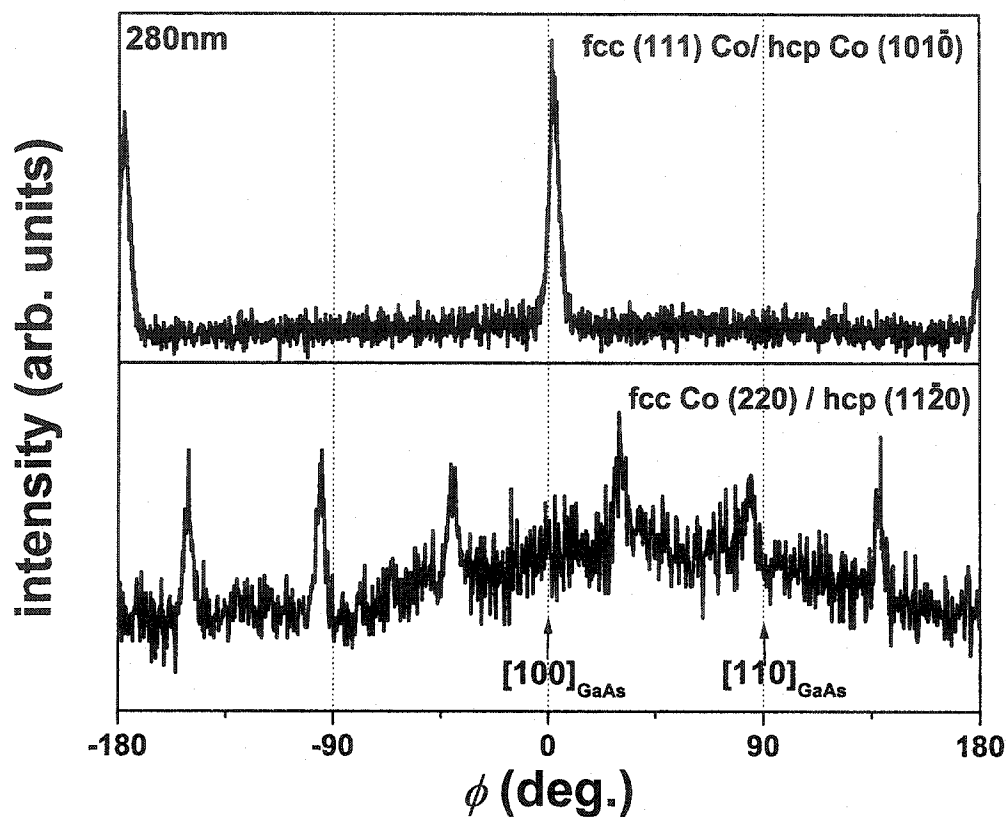


FIG. 43. Grazing incidence x-ray diffraction measurements of a 280 nm thick Co layer on GaAs(011) with the scattering vector oriented at $\psi = 88^\circ$ from the sample normal. The detector angle was set to the position of the fcc Co(220) / hexagonal Co(1120̄) and fcc Co(111) / hexagonal Co(2020̄) peaks. The sample was rotated around the sample normal (ϕ rotation). $\phi = 0^\circ$ corresponds to the GaAs[100] in-plane direction.

(either fcc Co(111) or hcp α -Co(0002)) with a two-fold symmetry in ϕ are observed. The hcp α -Co[0001] direction in plane would be expected for hcp α -Co grains with the $(10\bar{1}0)$ perpendicular orientation observed in Fig. 41.

These data suggest a mixed structure of hexagonal and fcc Co phases, which was confirmed by transmission electron microscopy (TEM) analysis on a 25 nm thick Co film grown on GaAs(011) as shown in Fig. 44. TEM images of a 25 nm Co film also showed a grain size of approximately 20 nm. Additional NMR measurements were performed on a 36 nm thick Co film grown on GaAs(011) in order to confirm the mixed fcc/hcp phase observed by XRD and TEM techniques. The fcc phase is here predominant compared to the hcp as opposed to the (001) substrate orientation while no evidence of bcc Co is observed (Fig. 45) which confirms the growth of a mixture of both fcc and hcp α -Co phase on GaAs(011).²²

It should be mentioned that modification of the growth conditions such as current density or pH can affect the film structure. NMR data of 36 nm thick Co films grown on GaAs(011) at pH varying from 2.5 to 3.3 and at current density of $J = 3.5 \text{ mA/cm}^2$ and $J = 11 \text{ mA/cm}^2$ are shown in Fig. 46. The predominance of fcc Co phase on hcp α -Co phase is seen on films grown at $pH = 3$. Increasing the pH for films grown at $J = 3.5 \text{ mA/cm}^2$ leads to an increase in the predominance of the fcc phase upon the hcp α -Co phase. The opposite is observed for films grown at $J = 11 \text{ mA/cm}^2$ (i.e. hcp α -Co phase is predominant).

(3) The high-angle ω - 2θ XRD spectra shown in Fig. 47 reveal the out-of-plane orientation of the 400 nm thick Fe films grown on GaAs(001) from FeSO_4 and FeCl_2 electrolyte solutions. In order to suppress the dominant substrate peaks, which would

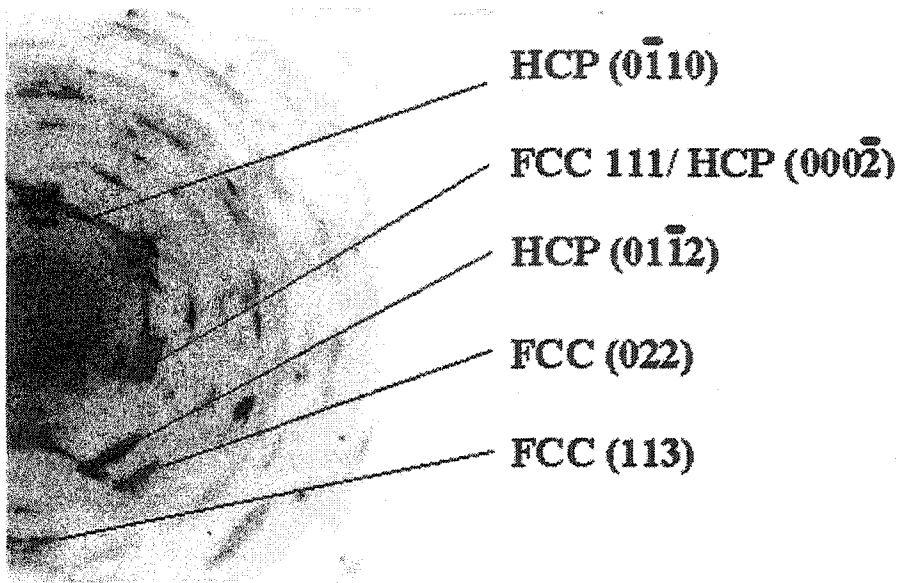


FIG. 44. TEM image of a 25 nm Co layer on GaAs(011). The dots are assigned to GaAs diffraction patterns.

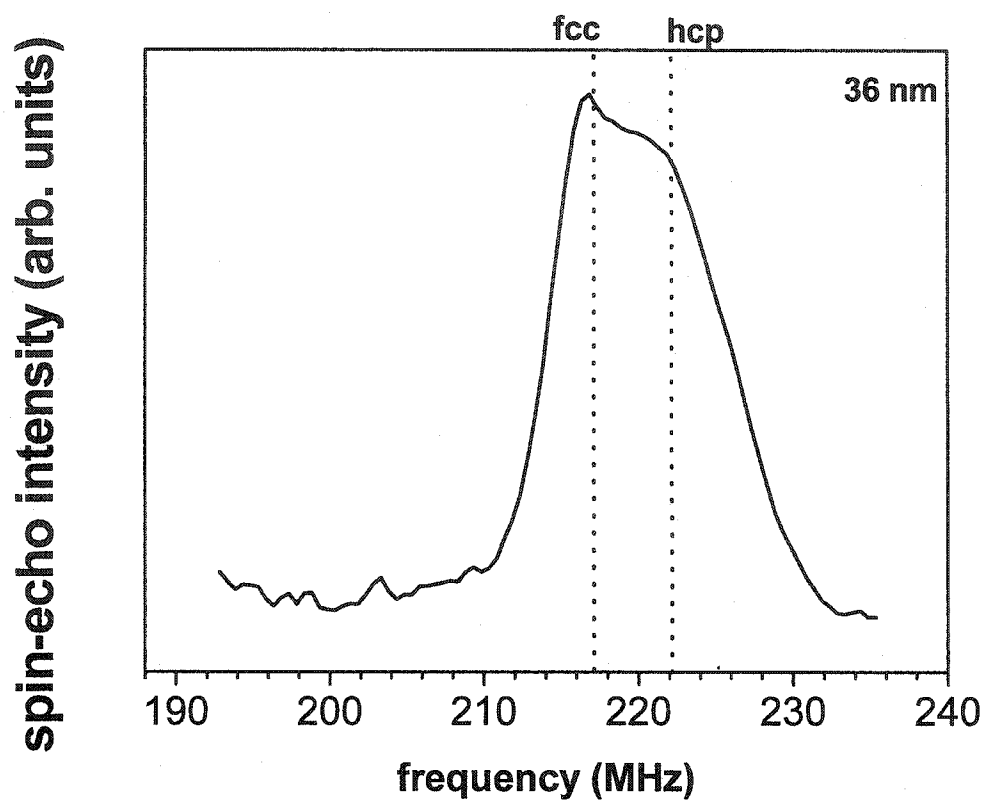


FIG. 45. Nuclear magnetic resonance (NMR) data of a 36 nm thick Co film grown on GaAs(011).

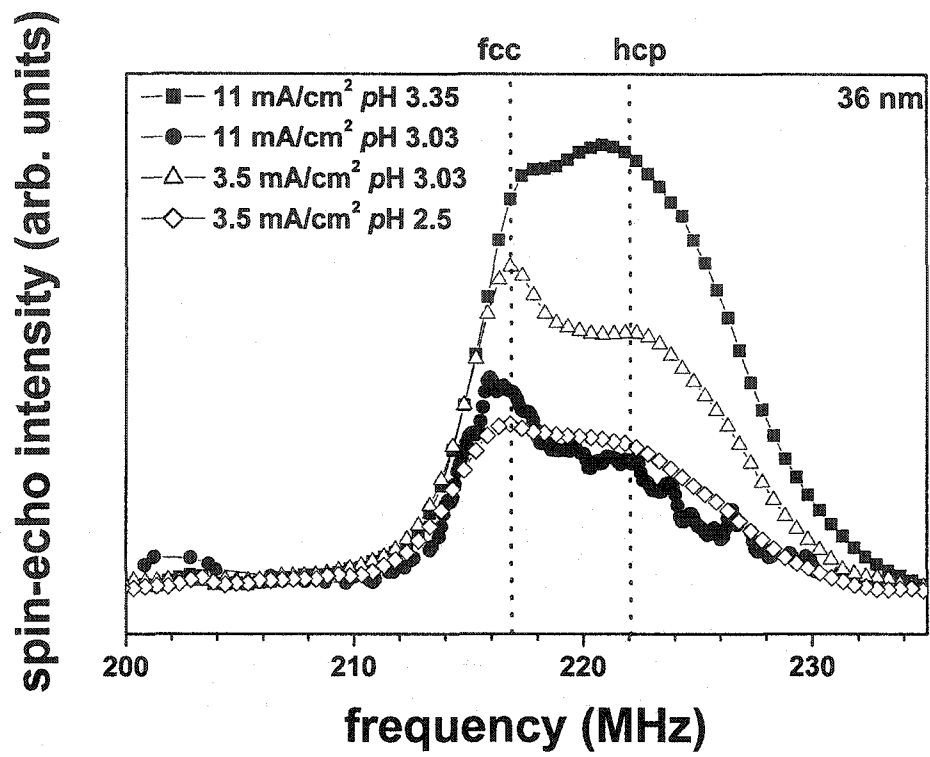


FIG. 46. Nuclear magnetic resonance (NMR) data of 36 nm thick Co films grown on GaAs(011) at different pH and current densities as indicated in the graph.

otherwise obscure the superposing Fe peaks, the samples were offset in ω by 0.2° – 0.4° . Both spectra are dominated by the Fe peaks related to the preferential orientation Fe(011) on GaAs(011) regardless of the electrolyte used. The (011) oriented layers are essentially mono-oriented as compared to Fe films on GaAs(001). From Fig. 48, the ω -rocking curve widths of the major peak Fe(011) is about 3.2° and 2.6° using respectively FeSO₄ and FeCl₂.

In order to verify the in-plane registry of the film with the substrate, glancing angle XRD intensities were measured with the scattering vector oriented at $\psi = 86^\circ$ from the sample normal (Fig. 49). The in plane XRD spectra for Fe films deposited on GaAs(011) using the FeSO₄ and FeCl₂ solutions are shown in Fig. 49 (a) and Fig. 49 (b) respectively, indicating a two-fold symmetry for Fe(110) and Fe(100) peaks. Thus the dominating epitaxial relation is Fe(001)[100]//GaAs(001)[100], which can be visualized by the schematic diagrams shown in the inset of the XRD spectra shown in Fig. 49. This is in agreement with the structure of epitaxial Fe layers grown by molecular beam epitaxy (MBE).⁷⁶ The azimuthal width of the peaks is around 7° (11° – 16°) for samples plated from the FeSO₄ (FeCl₂) solution. Besides the dominating symmetries, additional minor peaks (less pronounced than with the (001) substrate orientation) with a 30° period in ϕ are still present, which indicate the presence of other orientational relationships at the interface and the imperfection of the epitaxial growth. These minor orientations are close to Fe(011)[2 $\bar{1}1$]//GaAs(011)[100].

As for (001) oriented GaAs substrate, the surface RMS roughness as extracted from AFM images is about 20 nm for all Fe layers. Fractal analysis in Table II revealed that the lateral correlation length is larger for Fe layers grown from FeCl₂ (~ 1010 nm)

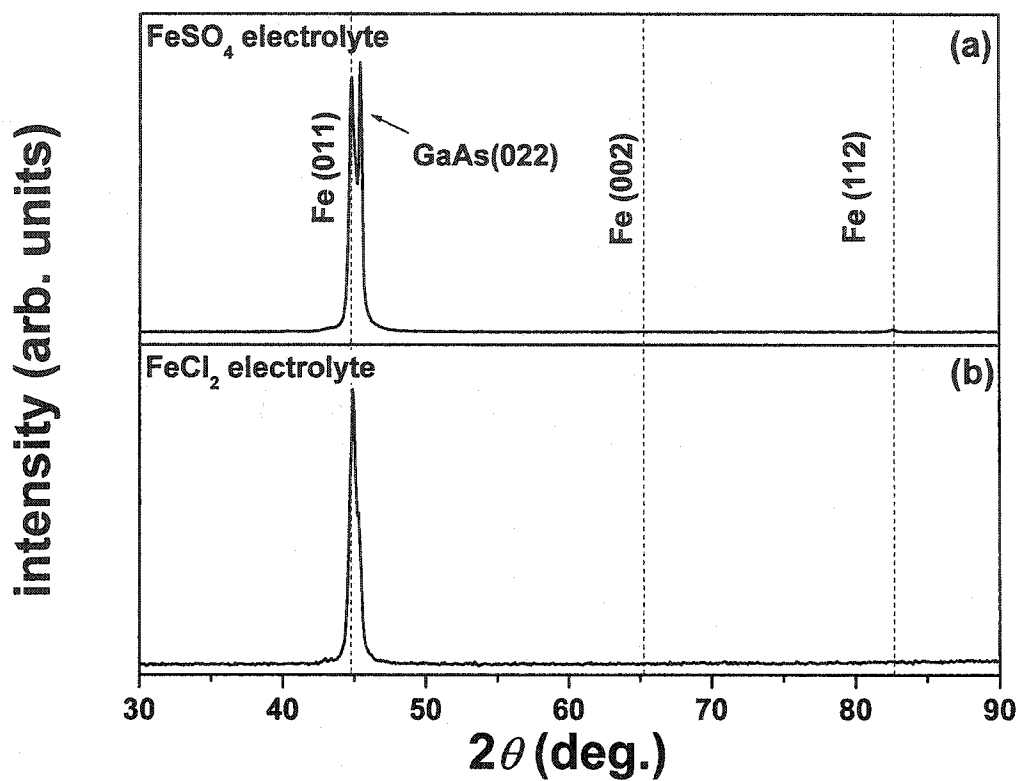


FIG. 47. High-angle ω - 2θ XRD spectra showing the out-of-plane orientation of 400 nm Fe layers grown on GaAs(011) from: (a) a FeSO₄ solution and (b) a FeCl₂ solution. The vertical dashed lines indicate the 2θ positions of bcc Fe(011), Fe(002), and Fe(112) peak. In order to suppress the intense substrate peaks, the measurements were taken with an ω -offset of 0.2°–0.4°.

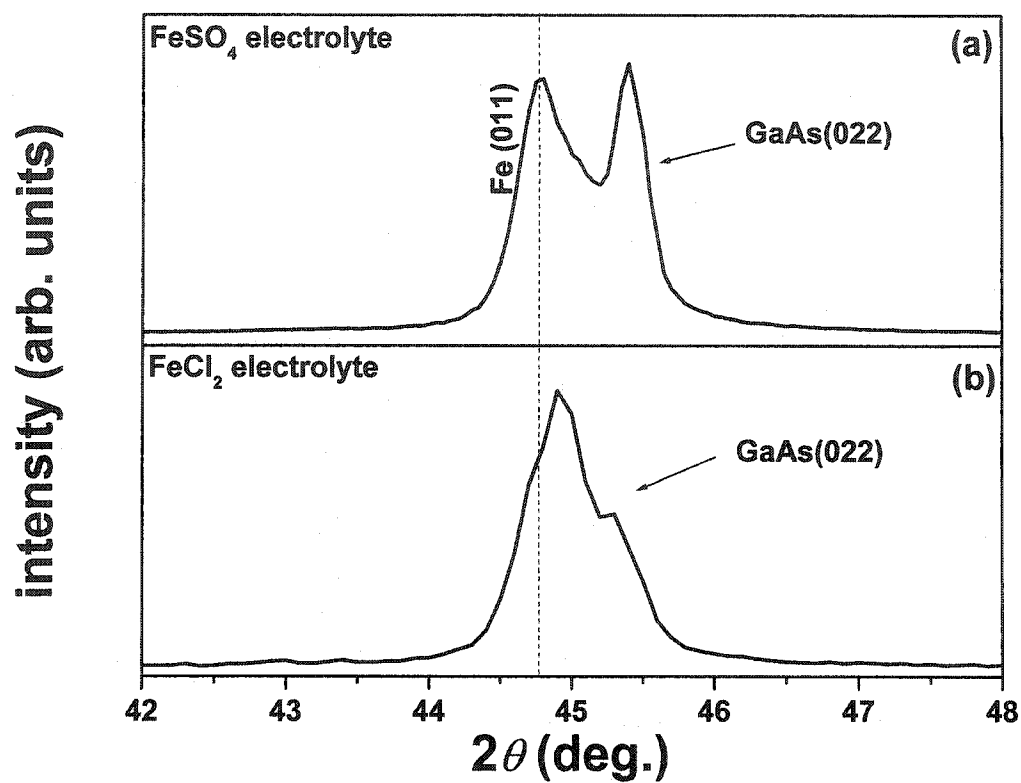


FIG. 48. Zoom in of high-angle ω - 2θ XRD spectra showing the out-of-plane orientation of 400 nm Fe layers grown on GaAs(011) from: (a) a FeSO₄ solution and (b) a FeCl₂ solution. The vertical dashed lines indicate the 2θ positions of bcc Fe(011) peak. In order to suppress the intense substrate peaks, the measurements were taken with a ω -offset of 0.2° – 0.4° .

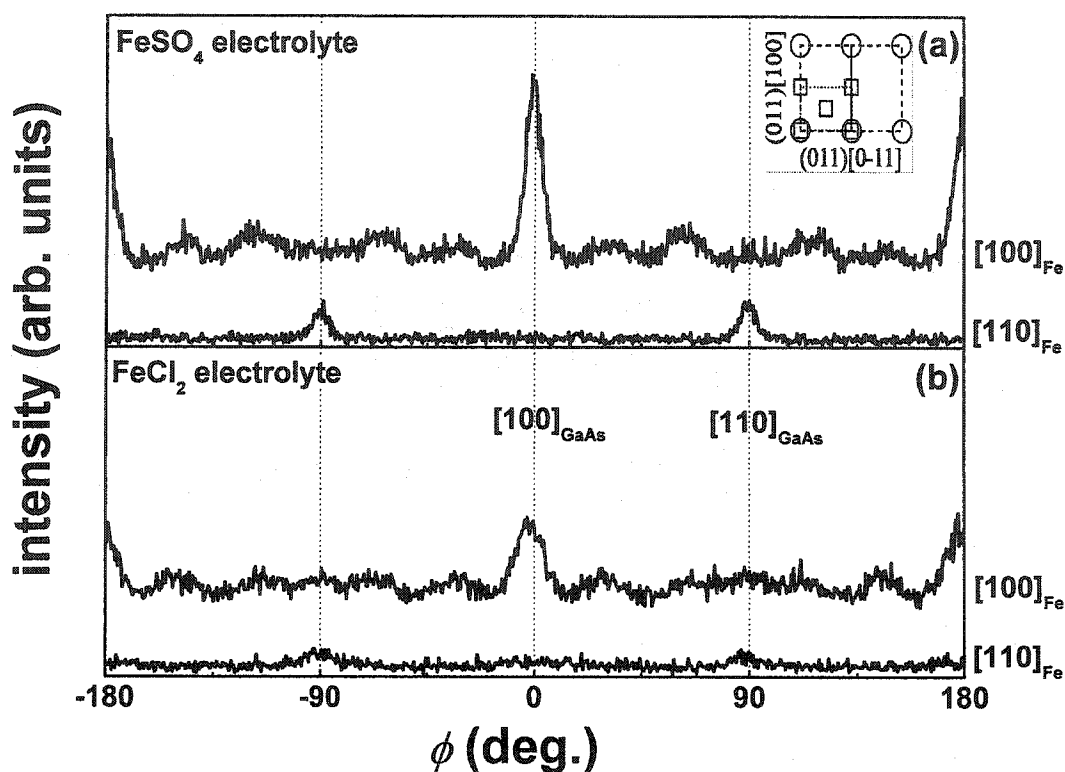


FIG. 49. ϕ -scans at grazing incidence ($\psi = 86^\circ$ from the film normal) of 400 nm Fe films grown on GaAs(011) showing the major Fe epitaxial relations with the GaAs substrates. ϕ is the angle enclosed between scattering vector and the GaAs[110] direction. Shown are spectra for Fe grown from: (a) a FeSO_4 solution and (b) a FeCl_2 solution. For each sample, the upper (lower) spectrum was obtained at $2\theta = 44.6^\circ$ (65.1°), corresponding to $\text{Fe}\{100\}$ ($\text{Fe}\{110\}$) in-plane peaks. The spectra are vertically offset for clarity. The insert provides schematic visualization of the GaAs (circles) and Fe (squares) surface unit mesh.

than for those grown from FeSO_4 (~ 330 nm). After a few weeks of exposure to air, Fe films on GaAs(011) prepared using FeCl_2 solutions appeared also less shiny than those prepared from FeSO_4 solutions. It is noted that the RMS roughness increases from 2 to 9 nm as the deposition time increased from 10 to 200 seconds.

TABLE II. Fractal analysis of 400 nm thick Fe films grown on GaAs(011) from FeSO_4 and FeCl_2 solutions.

	Fe on GaAs(011) FeSO_4 solution	Fe on GaAs(011) FeCl_2 solution
Correlation length (nm)	332	1013
Roughness (nm)	26	60

Improvement of Fe films grown on both GaAs(001) and (011) substrates are necessary in order to pursue the complete characterization of Fe films. Indeed, homogenous films are primordial in order to perform thickness calibration, interface analysis (XPS) and resistivity measurements. Several attempts have been made to meet those requirements by changing the growth conditions (electrolyte, pH, current density, additives, pulsed deposition, etc.).

Table III shows the description of Fe films grown on both GaAs orientation at pH = 2.9, at two different current densities ($J = 2.7 \text{ mA/cm}^2$ and $J = 5.4 \text{ mA/cm}^2$) in a 0.4 mol/L FeSO_4 solution for different boric acid (H_3BO_3) concentrations. The surface of the substrate is not entirely covered by the Fe film; some stripes are clearly visible. The addition of 0.5 mol/L of boric acid helps improving the metallic appearance and coverage of the film but the characteristic non-uniformity of the film remains.

TABLE III. Effect of boric acid (H_3BO_3) and current density on film growth and appearance.

I (mA)	Time (s)	Area (cm^2)	J (mA/cm^2)	pH	Solution (mol/L)	Film appearance
-20	30	3.68	5.43	2.9	FeSO_4 (0.1) H_3BO_3 (0)	Stripes
-10	30	3.68	2.71	2.9	FeSO_4 (0.1) H_3BO_3 (0)	Stripes
-20	30	3.68	5.43	2.9	FeSO_4 (0.1) H_3BO_3 (0.5)	Thicker film, looks better but still non-uniform
-10	30	3.68	2.71	2.9	FeSO_4 (0.1) H_3BO_3 (0.75)	Stripes

A modification of the pH to 4.6 or 5.16 and addition of 0.1 mol/L of ammonium sulfate $[(\text{NH}_4)_2\text{SO}_4]$ in the solution does not give significant improvements as shown in Table IV. As the concentration of H_3BO_3 is reduced to 0.25 mol/L, the films look oxidized (loss of metallic appearance). Increasing the current density to $J = 7.5 \text{ mA}/\text{cm}^2$ does not prevent the film from oxidizing.

Another possible way to reduce the roughness of the films is the use of pulsed deposition. Tables V and VI shows the appearance of series of films grown by pulsed technique in a 0.1 mol/L FeSO_4 solution with 0.5 mol/L of H_3BO_3 for different pH, pulse time and current densities.

The first attempt consisted in comparing a 30 seconds non-pulsed deposited Fe film (pH = 2.8 and $J = 2.5 \text{ mA}/\text{cm}^2$) with a 1 s pulsed 30 seconds deposited film as detailed in Table V. No improvement was noticed, the pulsed film looked still non-uniform with stripes on it. Reducing the pulse time down to 10 ms for a deposition

TABLE IV. Effect of ammonium sulfate $[(\text{NH}_4)_2\text{SO}_4]$, boric acid (H_3BO_3) and current density, and $p\text{H}$ on film growth and appearance.

Time (s)	J (mA/cm ²)	$p\text{H}$	Additives (mol/L)	Film appearance
30	5.43	2.9	none	Stripes
30	2.71	2.9	none	Stripes
30	5.43	2.9	H_3BO_3 (0.5)	Thicker film, looks better but still non-uniform
30	2.71	2.9	H_3BO_3 (0.75)	Stripes
30	2.5	5.2	H_3BO_3 (0.5) $(\text{NH}_4)_2\text{SO}_4$ (0.1)	Stripes
30	2.5	4.6	H_3BO_3 (0.25) $(\text{NH}_4)_2\text{SO}_4$ (0.1)	Oxidation
30	7.5	4.6	H_3BO_3 (0.25) $(\text{NH}_4)_2\text{SO}_4$ (0.1)	Oxidation

TABLE V. Effect of pulsed plating on Fe film growth and appearance.

Source	Pulse time (s)	Deposition time (s)	J	Solution (mol/L)	$p\text{H}$	Film appearance
DC	none	30	2.5	FeSO_4 (0.1) H_3BO_3 (0.5)	2.8	Stripes, non uniform
Pulsed	1	30	2.5	Same as above	2.8	No better
Pulsed	0.01	60	2.5	Same as above	2.8	Uniform around the edge but not at the center
Pulsed	0.005	90	2.5	Same as above	2.8	Overall more uniform but thicker film

time of 60 seconds tended to lead to a more uniform film around the edge but not at its center. Thicker films could be obtained with better initial uniformity by reducing the pulse time down to 500 ms for a deposition time of 90 seconds but the goal of growing uniform films down to at least 10 nm thick is still not reached.

As the current density increases, the films get thicker and completely covered (no stripes) however its non-uniformity is still visible to the naked eye except for very thick films (~ 300 nm). This pulse technique seemed to be promising but the initial pulsed deposited films were thicker than the ones grown in a constant way, therefore the results were misleading. As the deposition time was reduced to match the regular deposited film thickness (15–20 nm), the non-uniformity and roughness of the pulsed films appeared, leaving stripes and uncovered regions on the substrate.

Later, in order to provide a constant Fe^{2+} ions source during deposition, a Fe reference electrode was used in place of the graphite but no significant progress was observed. Furthermore, in order to attenuate any fluid dynamics effect at the plating electrode, which could influence the formation of stripes or the non-uniformity of thin films, the substrates were placed respectively on top and under a horizontal electrode while the solution was stirred. The films were plated at $\text{pH} = 2.5$, $J = 2.5 \text{ mA/cm}^2$, from a 0.1 mol/L FeSO_4 solution with 0.5 mol/L of H_3BO_3 . The resulting films appeared much less uniform than with the use of vertical electrode and no stirring of the solution during deposition. As a consequence, the achievement of smooth electrodeposited epitaxial Fe films grown on GaAs is still an issue.

TABLE VI. Effect of pulsed plating and current density on Fe film growth and appearance. Increase of the current density leads to thicker films uniform to the naked eye however, reducing the deposition time reveals its non-uniformity and non covered area.

Source	Pulse time (s)	Deposition time (s)	J	Solution (mol/L)	pH	Film appearance
DC	None	30	2.7	FeSO ₄ (0.1) H ₃ BO ₃ (0.5)	3.5	Stripes
DC	None	30	5	Same as above	3.5	Better coverage, but patches
Pulsed	200	60	5.3	Same as above	2.9	Edge uniform, center striped
Pulsed	200	60	7.9	Same as above	2.9	Center non uniform (film thicker)
Pulsed	200	60	2.6	Same as above	2.9	Film at the edge, but not at the center
Pulsed	200	20	7.9	Same as above	2.9	Same as above
Pulsed	200	60	2.6	Same as above	2.9	Same as above

(4) As mentioned earlier, Fe_xNi_{1-x} films ($x \geq 0.9$) growth have been preferred as a first step to reproduce the epitaxial growth schema of Fe onto GaAs(011).⁷⁶

Figure 50 shows the conventional ω - 2θ XRD spectrum for a 46 nm thick Fe_xNi_{1-x} film. Satellites originated by the x-ray source (W) and the substrate (GaAs K_α and K_β lines) are present but no clear peak could be assigned to either Fe or Ni. In Fig. 51, the sample angle ω was intentionally offset by 0.5° to reduce undesirable satellite and substrate peaks however still no clear peak was observed.

In-plane measurements shown in Fig. 52 did not reveal any accurate information

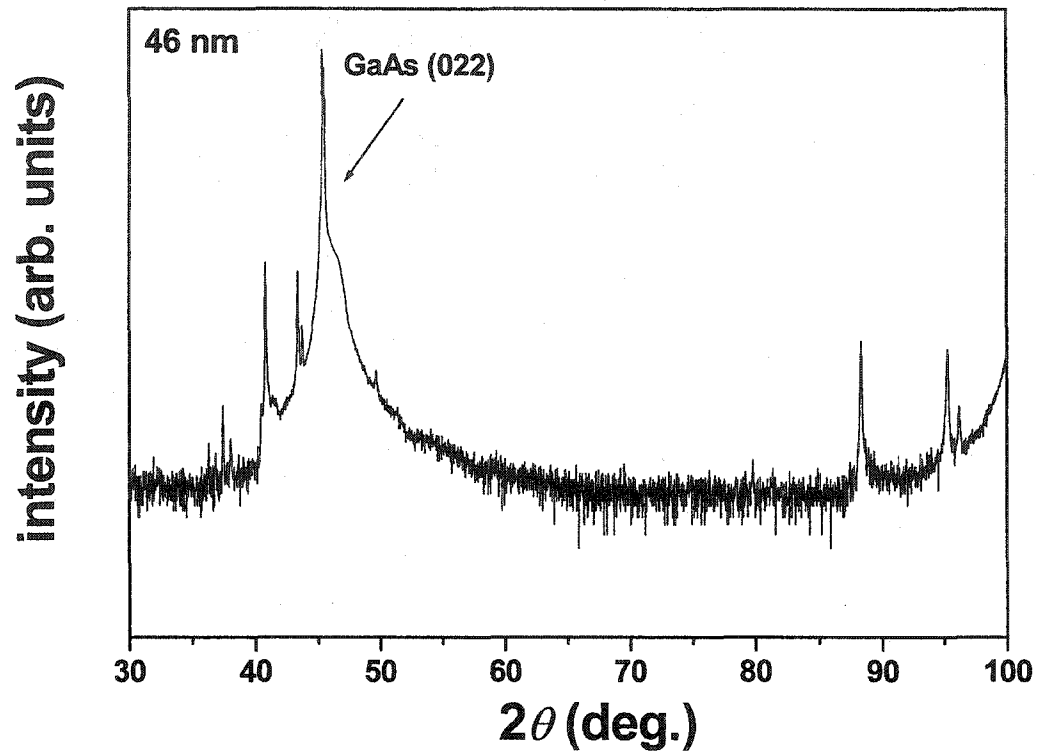


FIG. 50. High angle ω - 2θ x-ray measurement of a 46 nm thick FeNi layer on GaAs(011). The measurements were made without any ω -offset.

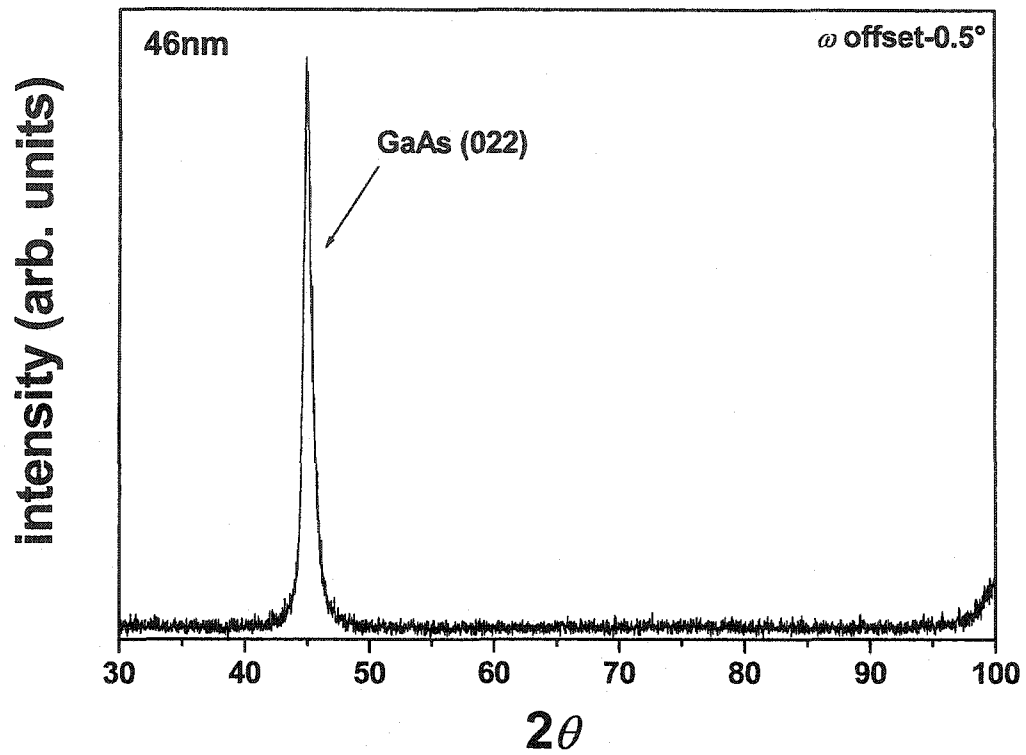


FIG. 51. Zoom in of a high angle ω - 2θ x-ray measurement of a 46 nm thick FeNi layer on GaAs(011). The measurements were made with an ω -offset of 0.5° .

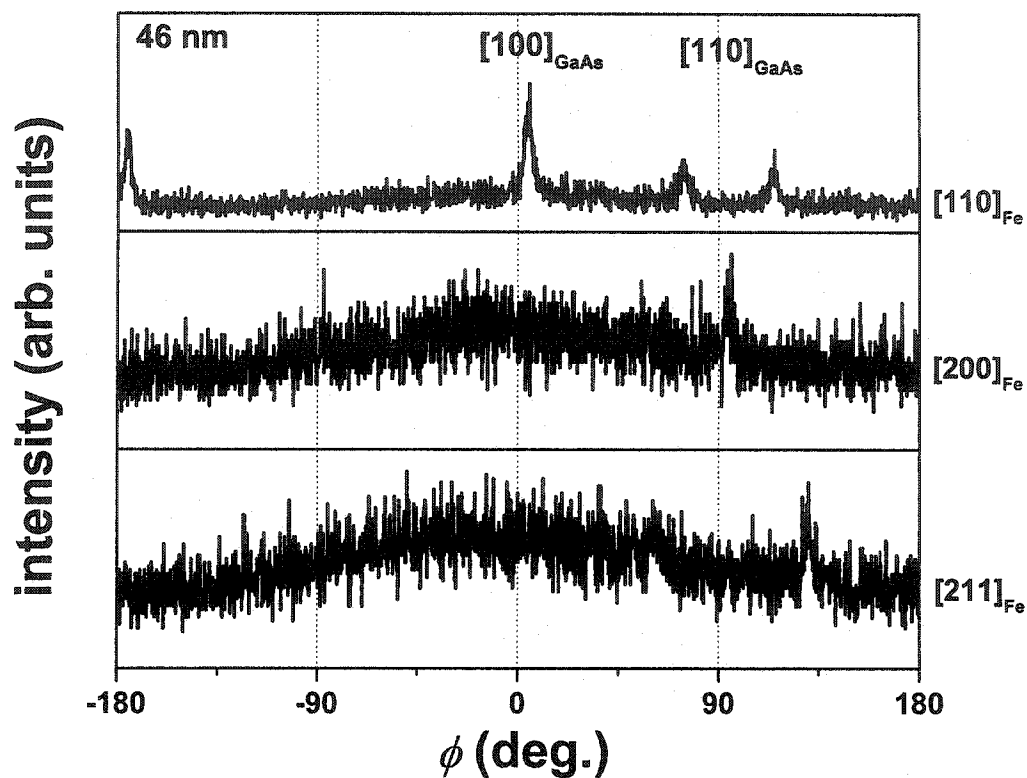


FIG. 52. Grazing incidence x-ray diffraction measurements of a 46 nm thick FeNi layer on GaAs(011) with the scattering vector oriented at $\psi = 88^\circ$ from the sample normal. The detector angle was set to the position of respectively the Fe(211), Fe(220) and Fe(110) peaks for the three scans shown. The sample was rotated around the sample normal (ϕ rotation). $\phi = 0^\circ$ corresponds to the GaAs[100] in-plane direction.

upon the possible epitaxial structure of $\text{Fe}_x\text{Ni}_{1-x}$ onto GaAs(001) though Fe(110) peaks could be observed. Some diffraction peaks of bcc Fe, however, match with the substrate peaks and can be difficult to detect. Indeed, Fe(110) peaks would be expected every 90° as if Fe would follow the epitaxial relationship $\text{Fe}(001)[100]//\text{GaAs}(001)[100]$, but Fig. 52 exhibits unreasonable positions for such peaks.

2. Magnetic properties

a. GaAs(001). (1) Figure 53 shows the angular remanence curves for respectively a 7, 19, 48 and 140 nm thick Ni film. A dominant uniaxial anisotropy with the easy axis aligned parallel to the $[110]$ direction of the GaAs(001) surface can be seen. Superimposed on this is a four-fold anisotropy with the easy axis oriented about 65° to 70° away from the GaAs $[110]$ direction.

It is interesting to note the difference between the $[110]$ and $[\bar{1}\bar{1}0]$ directions since these should be equivalent for a fcc Ni film with mixed (001) and twinned (011) orientation. Such differences were observed previously for MBE grown Fe films on GaAs(001)¹² and were ascribed to the inequivalency of the bond directions along GaAs $[110]$ and GaAs $[\bar{1}\bar{1}0]$. In addition, the superposition of the uniaxial anisotropy induced by GaAs substrate on a four-fold crystalline anisotropy have also been reported in previous work on $\text{Fe}_{1-x}\text{Co}_x$ films grown by MBE.^{78,79} The precise orientation of the easy axis direction varies slightly with thickness. With increasing Ni film thickness the dip in the remanence along GaAs $[\bar{1}\bar{1}0]$ does disappear and the easy axis direction moves from the GaAs $[100]$ direction towards the $[\bar{1}\bar{1}0]$ direction. Additionally, the remanence curve loses structure, i.e. also the uniaxial anisotropy is reduced with increasing film

thickness. The sharp peak in the remanence curve at the hard axis direction (along GaAs[110]) is reproducibly seen for all samples, a feature for which any explanation can currently be offered. As shown in the next paragraph, the simulation of the angular remanence does not exhibit any discontinuity around the minima (hard axis).

In order for the angular remanence values to be analyzed, the expected remanence values for (001), (011), and uniaxial anisotropy must be determined, so as to serve as a basis of comparison. The assumption for this analysis is that the remanence, after a saturation at some arbitrary angle will relax to the nearest easy axis and the remanent magnetization will be equivalent to the cosine of the angular separation from the applied field and the nearest easy axis. The respective free energy $E_{(001)}$, $E_{(011)}$, and $E_{(uni)}$ can be expressed as⁸⁰

$$E_{(001)} = \frac{K_1}{4} \sin^2 2\theta, \quad (10)$$

$$E_{(011)} = \frac{K_1}{4} (\sin^4 \theta + \sin^2 2\theta) + \frac{K_2}{4} (\sin^4 \theta + \cos 2\theta), \quad (11)$$

$$E_{(uni)} = K_1 \sin^2 \theta, \quad (12)$$

where K_1 and K_2 are crystalline anisotropic constants for a particular material.

Equations (10)–(12) were used to determine the easy directions and the critical points between the nearest easy directions and these were used to determine the cosines of the angular separations between the applied field and the nearest easy axis. Figure 54 shows both the expected free energy plots based on Eqs. (10)–(12) assuming bulk crystalline constants $K_1 = -0.5 \times 10^5$ erg/cm³ and $K_2 = -0.2 \times 10^5$ erg/cm³ for Ni⁸¹ and its projected remanence.

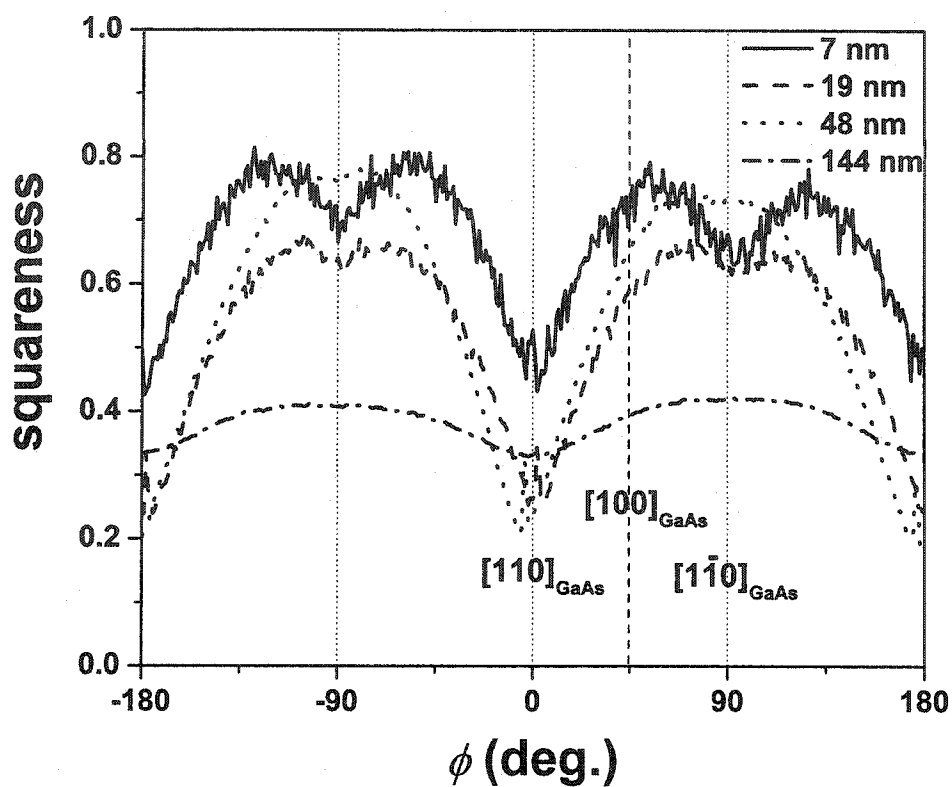


FIG. 53. Angular dependence of the remanence for Ni films grown on GaAs(001) with thicknesses indicated in the graph. A value of the sample rotation angle ϕ equal to zero corresponds to a magnetic field direction parallel to GaAs[110].

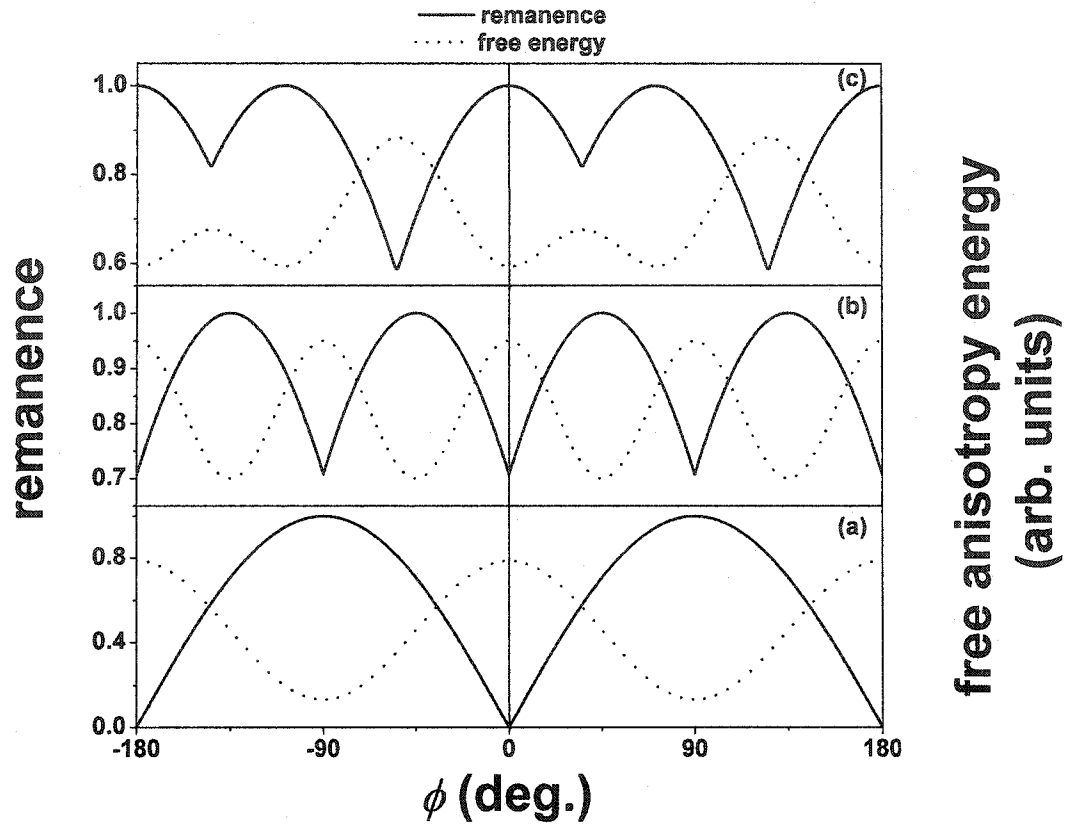


FIG. 54. Free anisotropy energy and expected remanence for: (a) uniaxial, (b) (001), and (c) (011) anisotropy as a function of in-plane angle using Eqs. (10)–(12) assuming $K_1 = -0.5 \times 10^5 \text{ erg/cm}^3$ and $K_2 = -0.2 \times 10^5 \text{ erg/cm}^3$. The (001) and (011) anisotropy are plotted following the epitaxial relationship $\text{Ni}[100](001)//\text{GaAs}[110](011)$ and $\text{Ni}[111](011)//\text{GaAs}[110](001)$ respectively. The zero degree angle corresponds to the hard axis of the system which is along the $\text{GaAs}[110]$ direction.

The easy axis is along the Ni[111] direction followed by the less easy axis along the [110] direction and the hard axis along the [100] direction. The maximum remanence predicted is 1 [$\cos(0^\circ)$] for the three anisotropy whereas the minimum is 0.71 [$\cos(45^\circ)$] and 0 for respectively the (001) and the uniaxial anisotropy. In the case of (011), the minimum remanence predicted is 0.57 [$\cos(54.7^\circ)$] with a local minimum remanence predicted 0.81 [$\cos(35.3^\circ)$]. Figure 55 shows the plot of the three remanence as present in the Ni films grown on GaAs(001) following the XRD epitaxial relationship Ni(001)[100]//GaAs(001)[110] and Ni(011)[111]//GaAs(001)[110]. The sum of the three anisotropies affected to a same weight of 0.33 is shown in Fig. 55. For such a uniform distribution of anisotropy, the maximum and minimum resulting angular remanence predicted is respectively 0.95 and 0.57. Furthermore, three local minima are present at 54.7° , 90° , and 144° which does not match with the experimental data. From Fig. 55, it is clear that the three anisotropies are present in the film with different amount in order to fit the experimental curve. Figure 56 shows the experimental angular remanence curves and its best fits for respectively a 19 nm and 48 nm thick Ni film.

The simulated curves to best fit the experimental data (Fig. 56) are dominated by the uniaxial and (001) configuration while the (011) component is barely present. Indeed, an increase of (011) amount in the simulation of the angular remanence leads to a distortion of the remanence peaks and an increase of the hard axis remanence, as Fig. 55 would suggest. It is noticed that the intensity of the simulated curves in Fig. 56 do not match the experimental, data however the shape can be reproduce as for the dip in the remanence curve along GaAs[1 $\bar{1}$ 0] characteristic of the four-fold anisotropy induced by the (001) epitaxy.

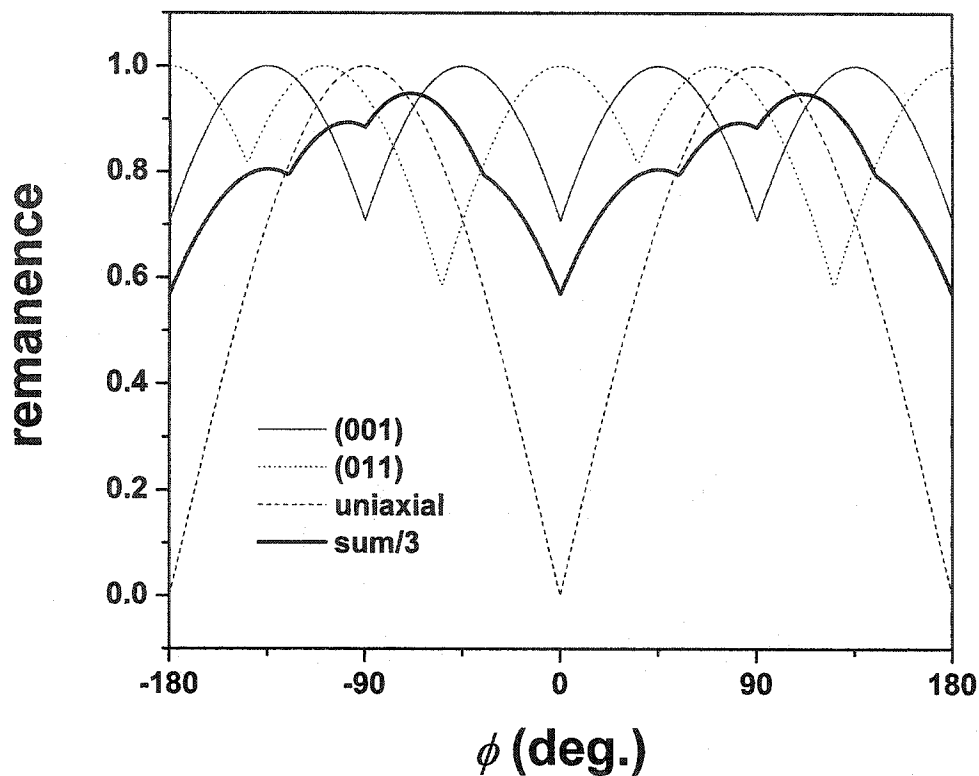


FIG. 55. Remanence simulation of respectively (001), (011), and uniaxial anisotropy expected from its respective free energy using Eqs. (10)–(12). The bold curve represents the sum of the three anisotropy affected with the same weight of 0.33. The (001) and (011) anisotropy are plotted following the epitaxial relationship Ni[100](001)//GaAs[110](011) and Ni[111](011)//GaAs[110](001) respectively. The zero degree angle corresponds to the GaAs[110] direction.

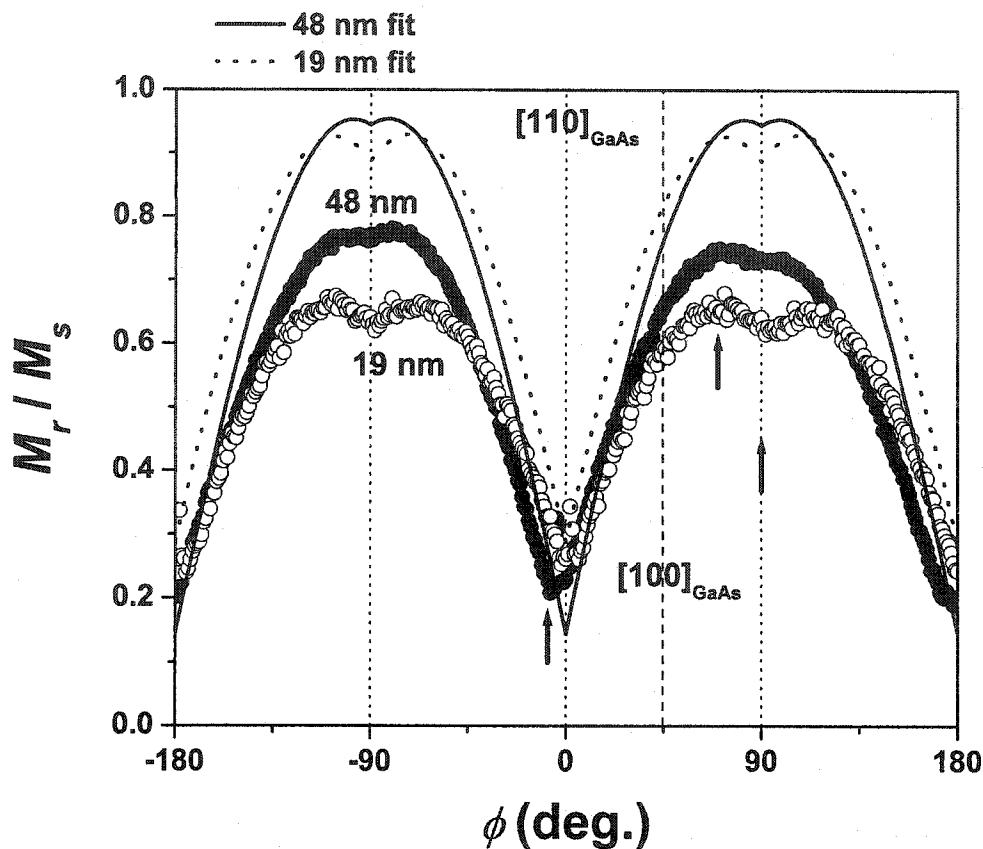


FIG. 56. Angular dependence of the remanence for a 48 nm and a 19 nm thick Ni film on GaAs(001). A value of the sample rotation angle ϕ equal to zero corresponds to a magnetic field direction parallel to GaAs[110]. The three arrows point to the characteristic positions of the remanence loops (hard axis, easy axis and 'almost-easy axis) for which individual hysteresis loops are shown in Fig. 58. The lines correspond to a fit by simulation of a mixture of a four-fold and a uniaxial anisotropy components. The amount of (011), (001) and uniaxial component in 19 nm and 48 nm thick Ni film is respectively 1.6%, 38.4%, 60% and 1%, 19%, 80%.

The amount of (011), (001) and uniaxial components in 19 nm and 48 nm thick Ni film is 1.6%, 38.4%, 60% and 1%, 19%, 80%, respectively. As shown in Fig. 57, by taking into account the in-plane azimuthal mosaic spread (3°) observed by XRD in the remanence simulation, the fits still barely match the corresponding experimental data. A very large, unreasonable ($> 60^\circ$) angular dispersion of the uniaxial anisotropy induced by the substrate would be necessary in order for the remanence intensity of the simulated curve to be reduced and match the actual data.

Figure 58 shows typical hysteresis loops for four different Ni film thicknesses. The loops were taken with the magnetic field oriented along the most prominent directions as found in the remanence curves for those films (indicated by arrows in Fig. 56), which were the hard and easy axis directions and the “almost-easy” direction parallel to GaAs $[\bar{1}\bar{1}0]$. For film thicknesses up to about 60 nm the easy axis loops are characterized by a high remanence or squareness, which weakens for large values of the Ni thickness as shown in Fig. 58. The hard axis loop is most pronounced for intermediate thicknesses. For the thinnest and thickest films the hard axis loops show little difference from the easy axis loops.

Figure 59 shows the squareness as a function of the film thickness where the thinnest and thickest films confirm the small difference between its easy and hard directions. Those thinnest films are certainly influenced by oxidation which should substantially alter the film magnetic properties. The oxidation product of Ni in the present films was found²⁸ to be Ni(OH)₂⁶⁶ rather than NiO⁶³ which is antiferromagnetic and could lead to exchange biasing effects. Very thin antiferromagnetic layers are expected to only increase the coercivity rather than to cause a loop shift.⁸²

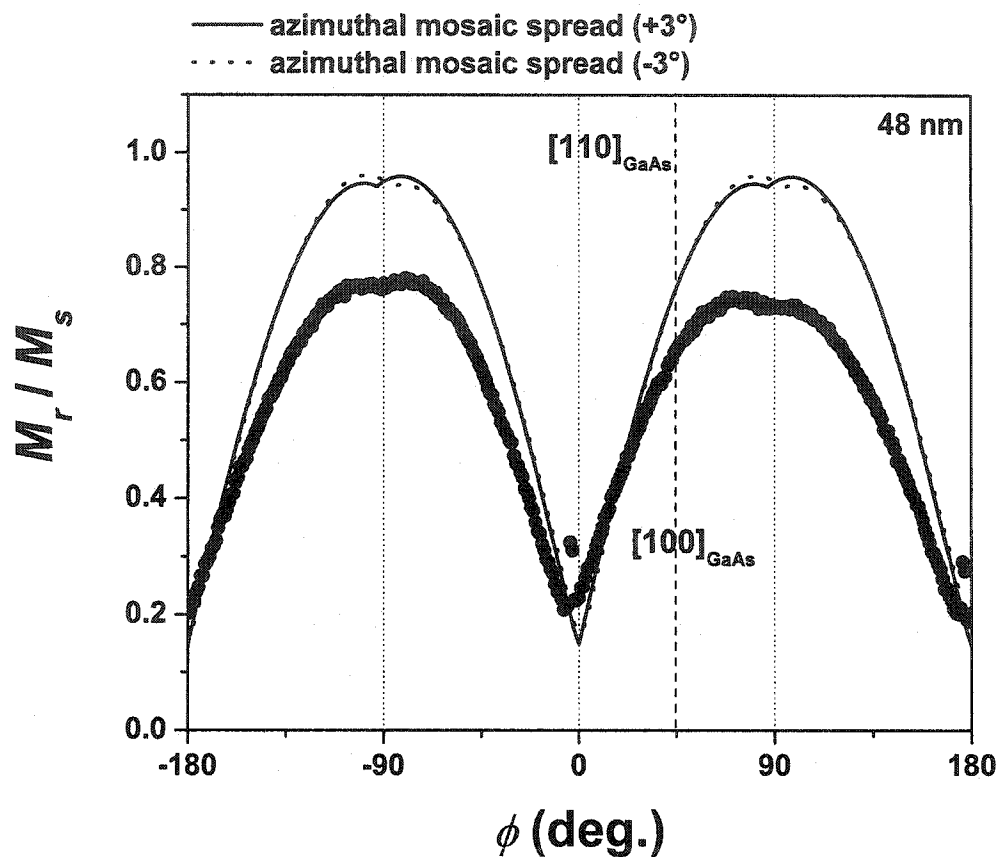


FIG. 57. Angular dependence of the remanence for a 48 nm thick Ni film on GaAs(001). A value of the sample rotation angle ϕ equal to zero corresponds to a magnetic field direction parallel to GaAs[110]. The lines correspond to a fit by simulation of a mixture of a four-fold and a uniaxial anisotropy components taking into account the azimuthal mosaic spread present in XRD data. The amount of (011), (001) and uniaxial component in the 48 nm thick Ni film is 1%, 19%, 80% respectively.

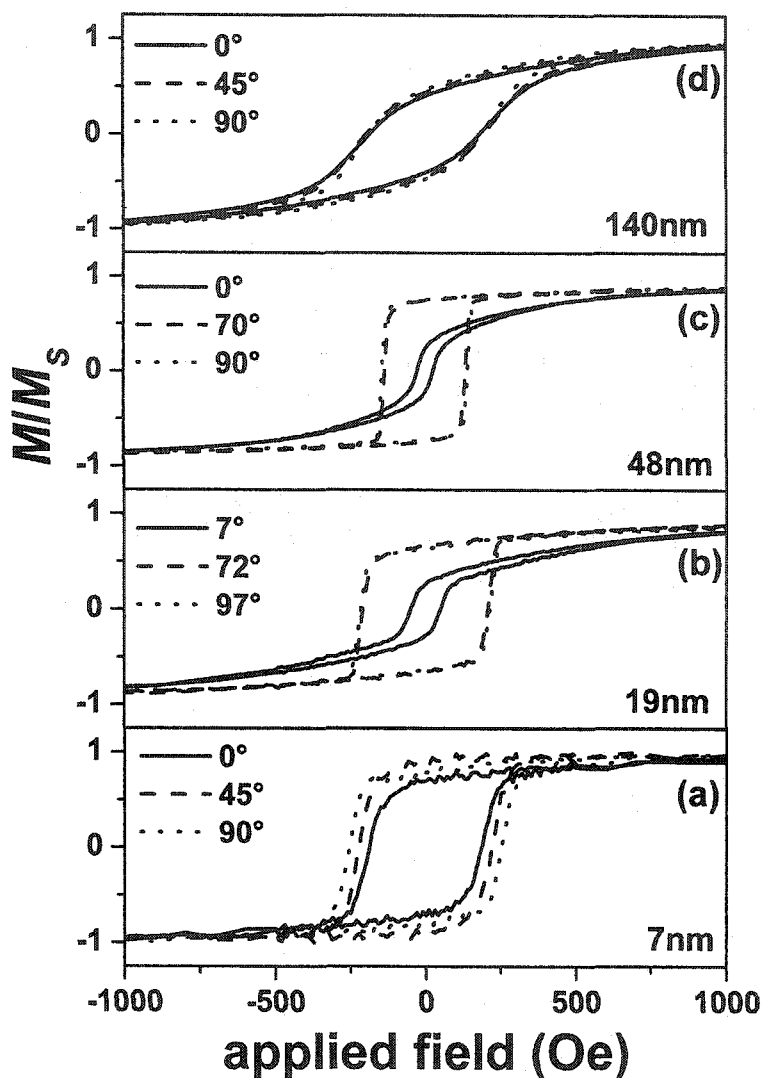


FIG. 58. Hysteresis loops of four different Ni layers grown on GaAs(001) with thicknesses indicated in the graph. The measurements actually were extended to 10 kOe to ensure saturation of the films. Shown are only parts of those loops. Each graphs does show three loops for each of which the orientation of the magnetic field with respect to the GaAs[110] direction is mentioned.

This pinning might dominate for the thinnest films allowing the clear anisotropy to develop only for thicker films. For thicker films the difference in loop shape between hard and easy axis tends to disappear [Fig. 58 (d)]. This would be in agreement with this anisotropy being caused by inequivalent GaAs[110] and $[1\bar{1}0]$ substrate directions, the influence of which should decrease with increasing film thickness. The coercivity H_c for the three dominant directions presented in Fig. 60 is shown as a function of film thickness. Easy axis coercivity values are in the range 150 Oe to 250 Oe. The initial steep increase of H_c is probably due to islanding and possible relevant oxidation of the very thinnest films. Clearly visible is the most pronounced anisotropy (largest difference in H_c between easy and hard axis directions) in the intermediate thickness range which entirely disappears for larger thickness values. Disregarding the thinnest layer, as a general trend, the coercivity for all directions decreases with increasing Ni layer thickness which is not unusual for magnetic films.⁸³⁻⁸⁵ Attenborough et al.²⁰ reported a strong uniaxial anisotropy for Ni film electrodeposited on GaAs(001) using higher current densities. The uniaxial anisotropy was associated with the film growing predominantly according to the epitaxial relationship $(011)_{\text{Ni}} // (001)_{\text{GaAs}}$ perpendicular to plane and $[111]_{\text{Ni}} // [110]_{\text{GaAs}}$ in-plane.

In Ref. 20, there is no mention of any observation of a fourfold anisotropy when both types of epitaxial growth are present although the same group did observe an anisotropy for Co on (001) GaAs³ very similar to the one observed for Ni in the present work. The data presented in Ref. 20 however do not rule out a crystalline contribution with four-fold symmetry since only two hysteresis loops are presented. However, the pH

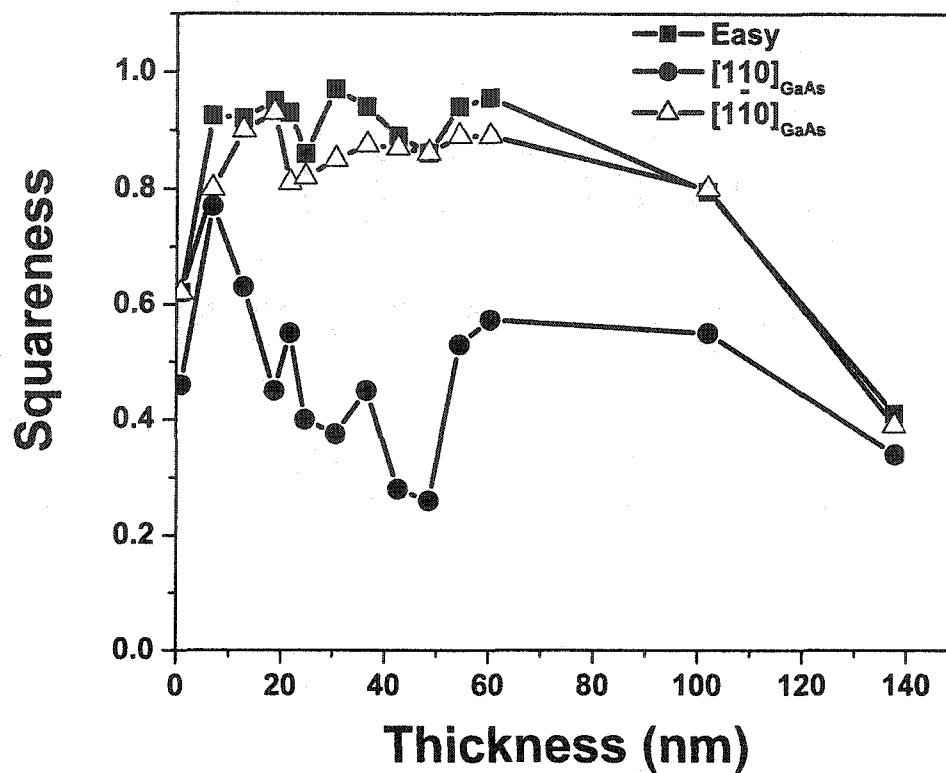


FIG. 59. The effect of film thickness on magnetic anisotropy for Ni films grown on GaAs(001) from a solution with $pH = 2.5$, squareness (M_r/M_s , normalized by M_s) as a function of film thickness.

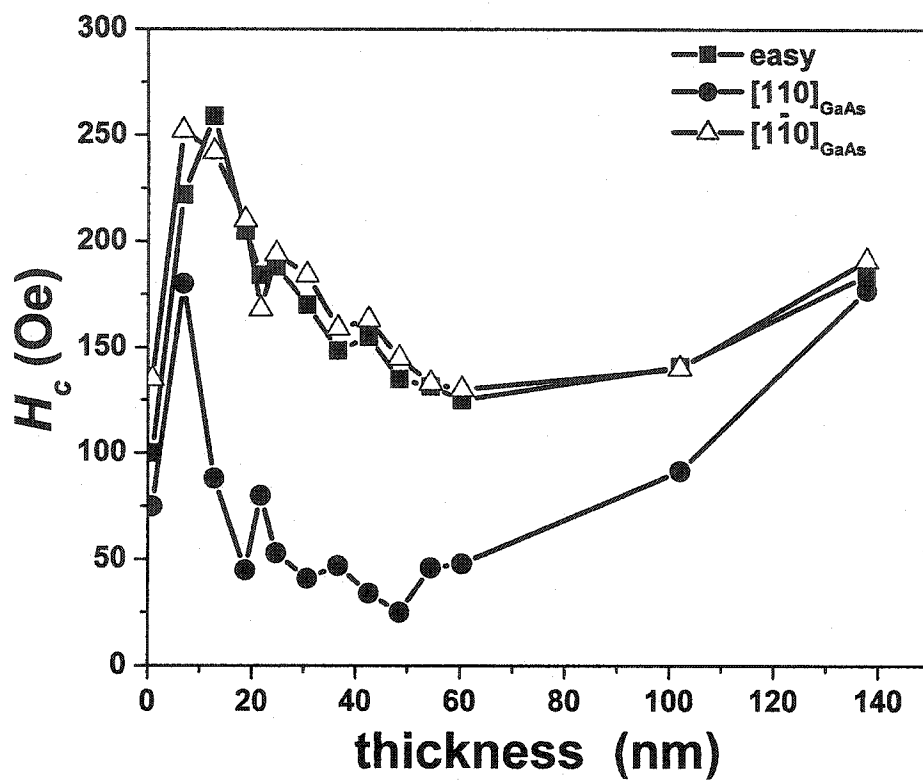


FIG. 60. Coercivity H_c as a function of Ni layer thickness for three different orientations of the magnetic field as described in the text. The lines are guides to the eye.

value of 3.9 used by Attenborough et al. could be responsible for the absence of the crystalline contribution.

In the present work, the disappearance of the crystalline anisotropy (001) accompanied by a strengthening of the uniaxial anisotropy was observed when depositing at pH 2.7 instead of pH 2.5 as shown in Fig. 61. Films grown at pH 2.7 require about 2000 Oe to saturate in the hard axis direction. Growth at pH 2.3 shows a reduced current efficiency (38%) but results in similar magnetic properties as for pH 2.5. The values of the coercivities reported in Ref. 20 are similar to those shown in the present work.

Epitaxial Ni(001) films grown on Cu(001)⁸⁶ and GaAs(001)^{87,88} had been reported to show an out-of-plane anisotropy which is ascribed to strain related effects.⁸⁹ Out-of-plane hysteresis loops measured on our samples confirm a clear in-plane anisotropy. However, the strength of the magnetic field necessary to saturate the samples in the out-of-plane direction is slightly (about 10%) below $4\pi M_s$ (as estimated from in-plane hysteresis loops) indicating the presence of anisotropy components favoring out-of-plane magnetization.

In order to investigate the ambiguity in the film anisotropy and extract anisotropy constant out of it, torque measurement have been performed. The expression of the torque exerted on a crystal per unit volume by M_s is given by⁸⁰

$$L = -\frac{dE}{d\theta}, \quad (13)$$

where E is the anisotropy energy. Applying Eq. (13) to the free energies given in Eqs. (10)–(12), the respective torques are given by

$$L_{(001)} = -\frac{K_1}{2} \sin 4\theta, \quad (14)$$

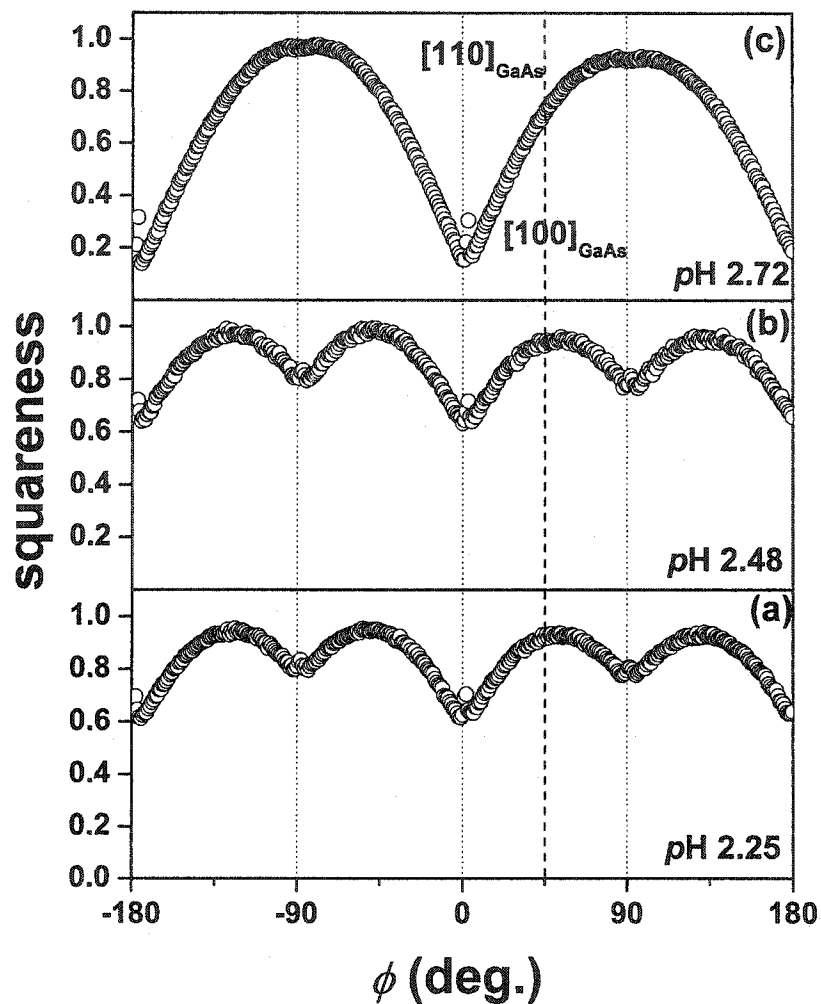


FIG. 61. Angular dependence of the remanence for 36 nm thick Ni films grown on GaAs(001) at different pH with their values indicated in the graph. A value of the sample rotation angle ϕ equal to zero corresponds to a magnetic field direction parallel to GaAs[110].

$$L_{(011)} = -\left(\frac{K_1}{4} + \frac{K_2}{64}\right)\sin 2\theta - \left(\frac{3K_1}{8} + \frac{K_2}{16}\right)\sin 4\theta + \left(\frac{3K_2}{64}\right)\sin 6\theta, \quad (15)$$

$$L_{(umi)} = -K_1 \sin 2\theta. \quad (16)$$

In each equation, the term in $\sin(2\theta)$ is the uniaxial component, the term in $\sin(4\theta)$ is the biaxial component, etc. One can then extract the experimental values K_1 and K_2 from the fitted experimental curves using Eqs. (14)–(16).

Figure 62 shows the plots of the three respective theoretical torques for bulk crystalline Ni anisotropy constants $K_1 = -0.5 \times 10^5$ erg/cm³ and $K_2 = -0.2 \times 10^5$ erg/cm³ along with their corresponding free anisotropy energy as present in the Ni films grown on GaAs(001) following the XRD epitaxial relationship Ni(001)[100]//GaAs(001)[110] and Ni(011)[111]//GaAs(001)[110]. $L_{(001)}$ presents a four-fold symmetry with a constant amplitude within a 180° rotation whereas a variation of the amplitude is present in the (011) anisotropy torque $L_{(011)}$.

Figure 63 shows the sum of the three contributing torques affected with the same weight and assuming bulk crystalline constants $K_1 = -0.5 \times 10^5$ erg/cm³ and $K_2 = -0.2 \times 10^5$ erg/cm³ as if they were present in the film in equal amount. Figure 64 shows the experimental torque curves for a 36 nm thick Ni film. The torque exhibits a four-fold symmetry within a 180° rotation with a variation in the amplitude as the theoretical would suggest. Regardless the amplitude ratio, the resulting theoretical curve has a similar trend as the experimental data. However no extraction of K_1 or K_2 is achievable using the theoretical model due to the complexity of the coexistence of the three anisotropies, the asymmetry and noise in the experimental curves. Furthermore, due to

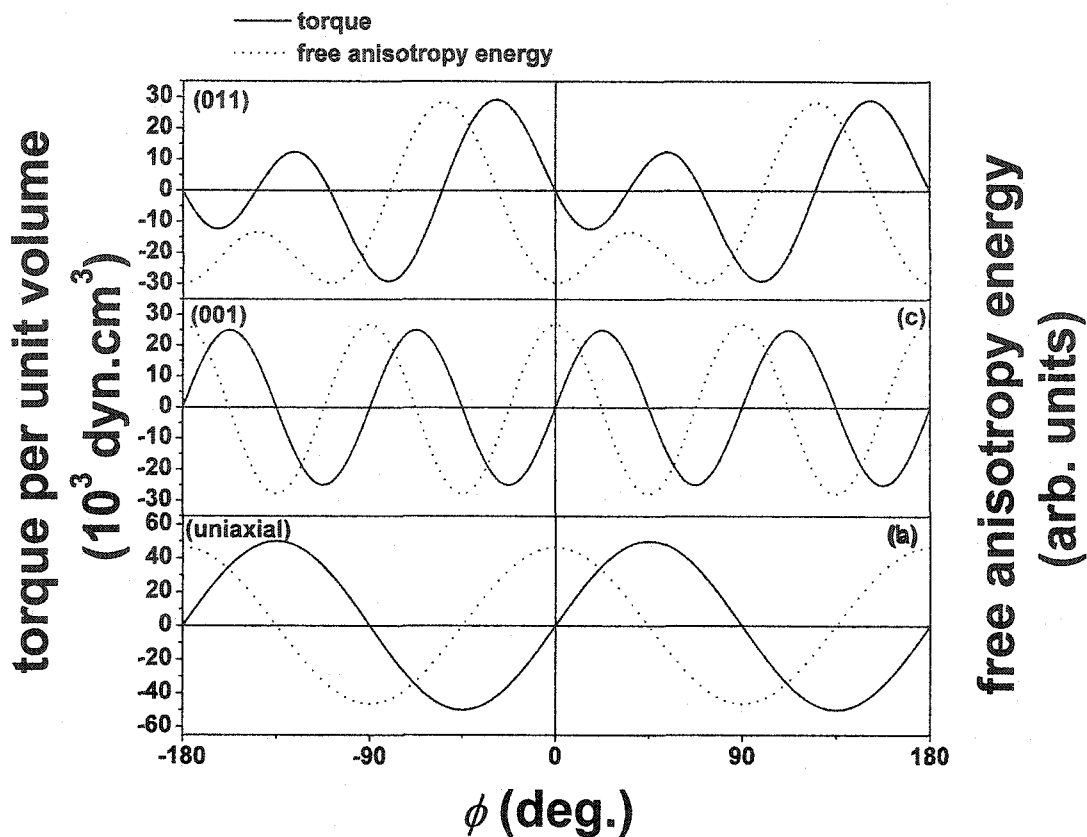


FIG. 62. Free anisotropy energy and expected torque for: (a) uniaxial, (b) (001), and (c) (011) anisotropy as a function of in-plane angle using Eqs. (10)–(12) and (14)–(16) assuming $K_1 = -0.5 \times 10^5 \text{ erg/cm}^3$ and $K_2 = -0.2 \times 10^5 \text{ erg/cm}^3$. The (001) and (011) anisotropy are plotted following the epitaxial relationship Ni[100](001)//GaAs[110](011) and Ni[111](011)//GaAs[110](001) respectively. The zero degree angle corresponds to the hard axis of the system which is along the GaAs[110] direction.

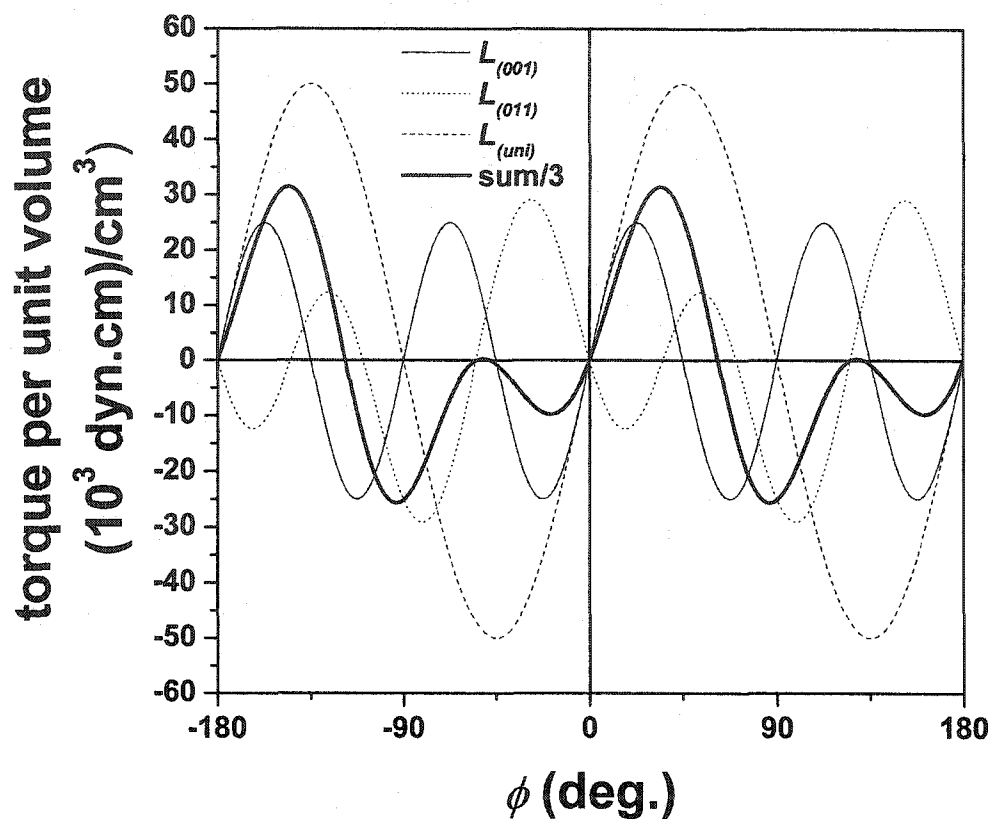


FIG. 63. Torque simulation of respectively (001), (011), and uniaxial anisotropy expected from its respective free energy using Eqs. (14)–(16) assuming $K_1 = -0.5 \times 10^5 \text{ erg/cm}^3$ and $K_2 = -0.2 \times 10^5 \text{ erg/cm}^3$. The bold curve represents the sum of the three torques $L_{(001)}$, $L_{(011)}$, and $L_{(uni)}$ affected with the same weight of 0.33. The (001) and (011) anisotropy are plotted following the epitaxial relationship Ni[100](001)//GaAs[110](011) and Ni[111](011)//GaAs[110](001) respectively. The zero degree angle corresponds to the GaAs[110] direction.

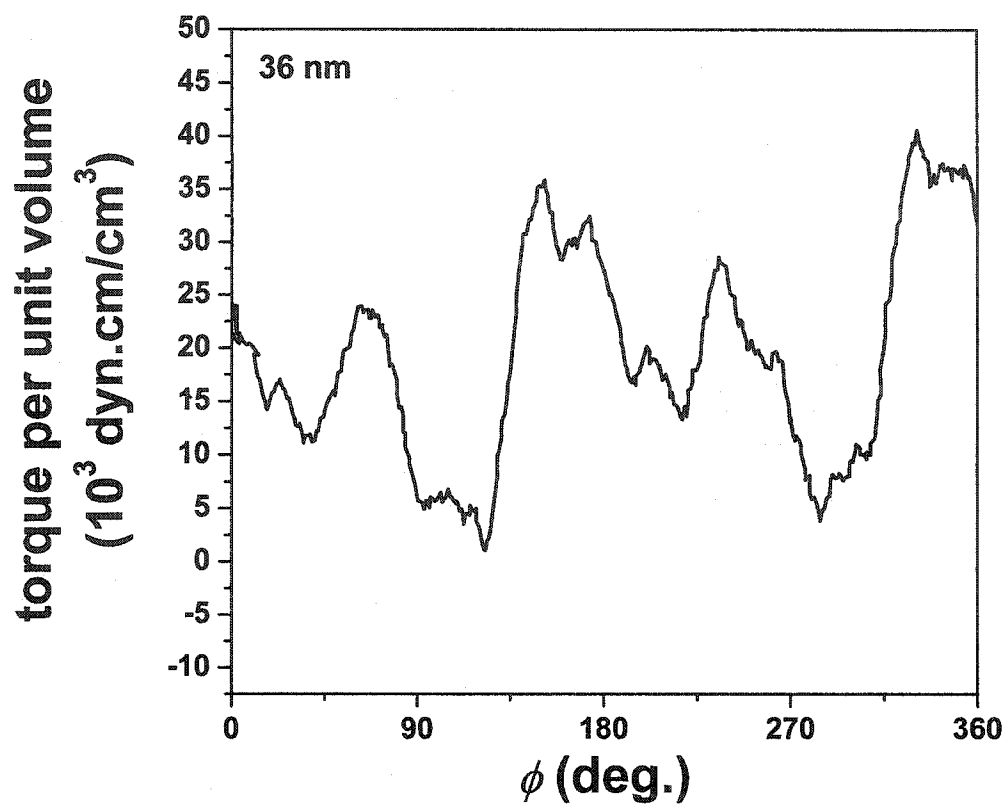


FIG. 64. Torque curves for a 36 nm thick Ni film on GaAs(001). A value of the sample rotation angle ϕ equal to zero corresponds to a random position for the magnetic field with respect to GaAs[110]. The external applied field had a value of 2000 Oe.

the dominance of the uniaxial anisotropy induced by the substrate, extraction of the crystalline constants using torque measurement remains difficult.

As a complementary characterization technique, a detailed Brillouin light scattering (BLS) investigation of the thickness dependence of magnetic anisotropy of thin Ni films grown on GaAs (001) is reported. In Figs. 65 and 66, the in-plane dispersion of the Damon-Eshbach spin wave mode on the in-plane direction of the applied magnetic field is shown for four Ni films from 7 to 35 nm. The magnetic anisotropy presents the coexistence of a four-fold (biaxial) and two-fold (uniaxial) in-plane anisotropy. This could be ascribed, as seen earlier, to the two different epitaxial relationships with the in-plane Ni directions [100] and [111] parallel to the [110] direction of the GaAs substrate or a combination of crystalline and substrate-induced uniaxial anisotropy. Fig. 65 shows the behavior of the in plane uniaxial constant K_u versus inverse thickness where a non linear dependence is observed (i.e. oscillating behavior). This could be caused by a possible lattice distortion of Ni as suspected previously.

(2) Figure 67 shows the angular remanence curves for respectively a 18, 36, 71 and 106 nm thick Co film. A dominant uniaxial anisotropy with the easy axis aligned parallel to the [110] direction of the GaAs(001) surface can be seen for the two thin films. It is interesting to note the difference between the [110] and $[1\bar{1}0]$ directions as seen for Ni on GaAs(001) since these should also be equivalent for a fcc Co film, however XRD confirmed the coexistence of a hcp phase and could also affect the magnetic anisotropy. An almost easy axis characterized by a sharper peak can be seen along the $[1\bar{1}0]$ direction separating two hard axis minima located 12° apart from the $[1\bar{1}0]$ direction.

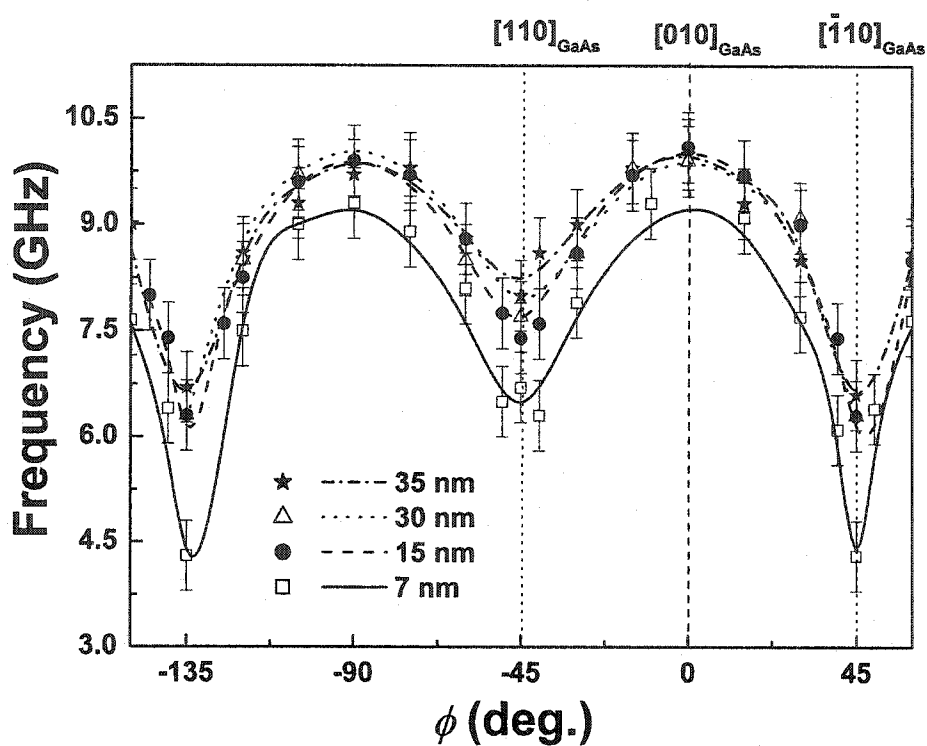


FIG. 65. In-plane dispersion of the Damon-Eshbach spin wave mode from Brillouin light scattering (BLS) on the in-plane direction of the applied magnetic field for 7, 15, 30 and 35 nm thick Ni films grown on GaAs(001) surfaces.

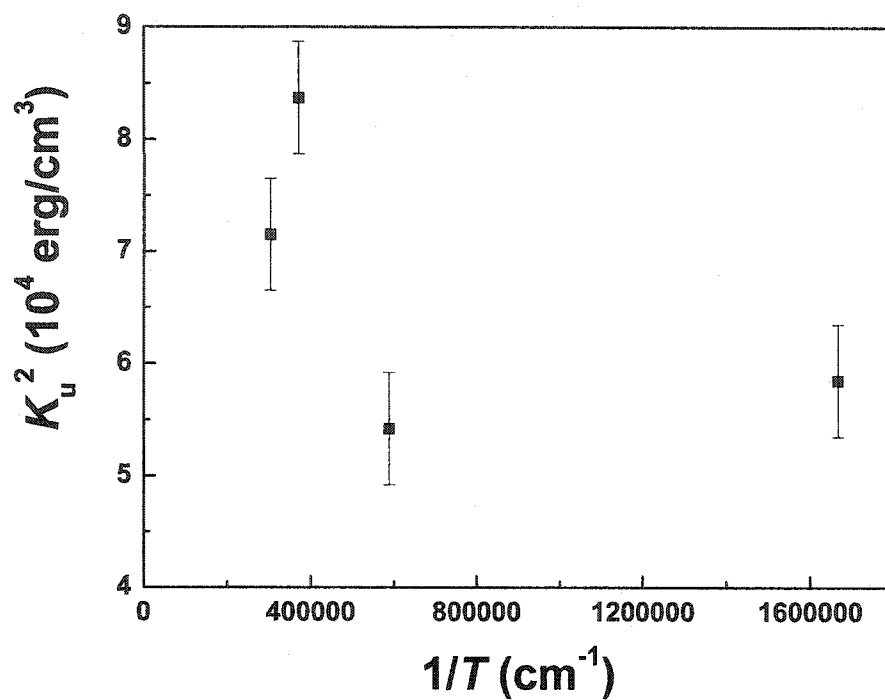


FIG. 66. Dependence of the in-plane uniaxial anisotropy constant K_u^2 from Brillouin light scattering (BLS) on the inverse Ni film thickness grown on GaAs(001) surfaces.

With increasing Co film thickness, the major uniaxial anisotropy evolves into a four-fold symmetry with the easy axis moving from the GaAs $[\bar{1}\bar{1}0]$ towards the $[100]$ direction of the GaAs(001) as previously seen.⁷³

The sharp peak along the GaAs $[\bar{1}\bar{1}0]$ is still present. The observed four-fold magnetic anisotropy is therefore consistent with the even distribution between orthogonal in-plane hcp α -Co $(1\bar{1}20)[0001]$ variants suggested earlier in XRD analysis. Deviation of the equal ratio between the two orthogonal distribution results in the development of a strong uniaxial anisotropy⁷³ which could explain the present results for thinner films without ruling out the possibility of a strain induced uniaxial anisotropy from the substrate as seen for Ni films.²³

Additionally, the remanence curve loses structure, i.e. the uniaxial anisotropy is also reduced with increasing film thickness. The sharp peak in the remanence curve at the almost easy axis direction (along GaAs $[\bar{1}\bar{1}0]$) is reproducibly seen for all samples, a feature for which any explanation can currently be offered.

Figure 68 shows typical hysteresis loops for three different Co film thicknesses. The loops were taken with the magnetic field oriented along the most prominent directions as found in the remanence curves for those films (indicated by arrows in Fig. 67) which were the hard and easy axis directions and the almost easy direction parallel to GaAs $[\bar{1}\bar{1}0]$. For all film thicknesses, the easy axis loops are characterized by a high remanence or squareness. As confirmed in the remanence curve, the easy axis moves from GaAs $[110]$ towards the $[100]$ direction as the Co film thickness increases. The hard axis loop is most pronounced for intermediate thicknesses up to 70 nm. For the thickest films, the hard axis loops show little difference from the easy axis loops in agreement

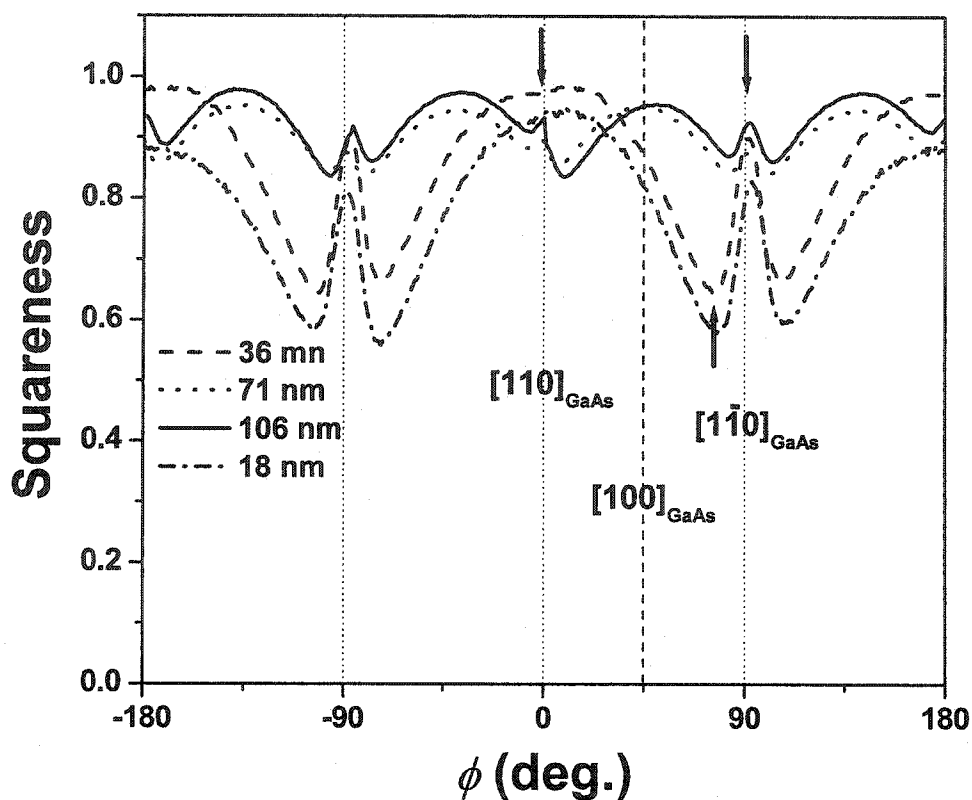


FIG. 67. Angular dependence of the remanence for Co films grown on GaAs(001) with thicknesses indicated in the graph. A value of the sample rotation angle ϕ equal to zero corresponds to a magnetic field direction parallel to GaAs[110]. The three arrows point to the characteristic positions of the remanence loops (easy axis and hard axis) of a 36 nm thick Co film for which individual hysteresis loops are shown in Fig 68.

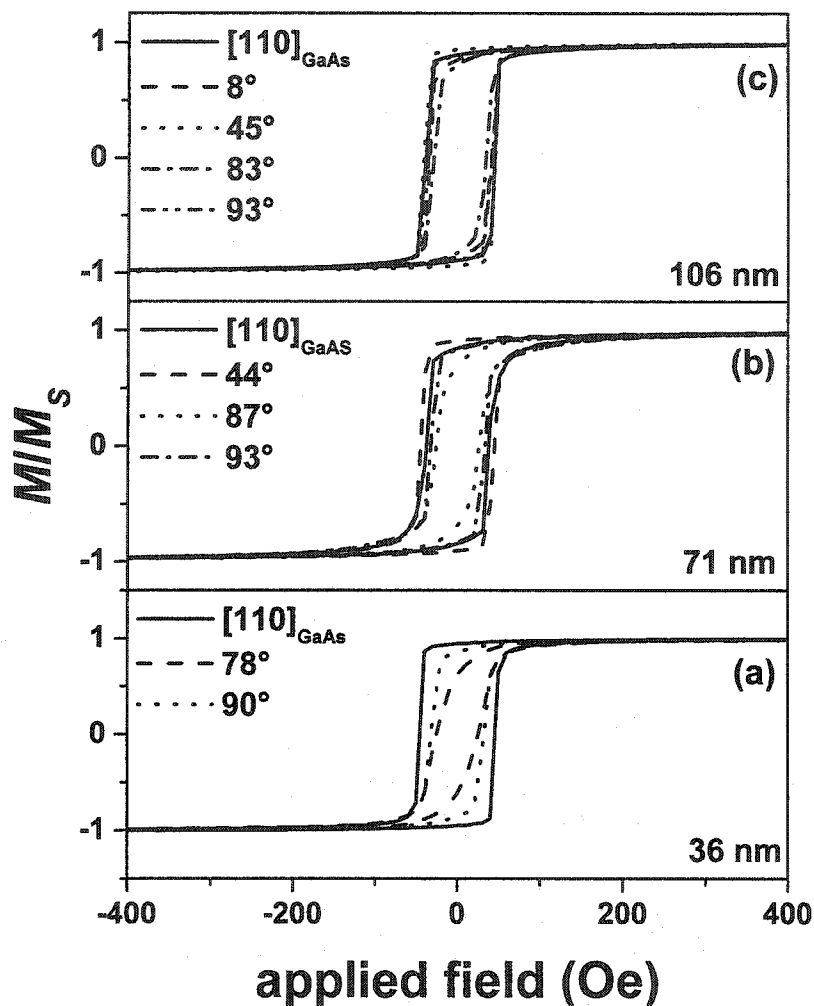


FIG. 68. Hysteresis loops of three different Co layers grown on GaAs(001) with thicknesses indicated in the graph. The measurements actually were extended to 2 kOe to ensure saturation of the films. Shown are only parts of those loops. Each graphs does show loops for each of which the orientation of the magnetic field with respect to the GaAs[110] direction is mentioned.

with Ref. 73 and the difference in loop shape between hard and easy axis tends to disappear [Fig. 68 (c)].

This would be in agreement with this anisotropy being caused by inequivalent GaAs[110] and $[\bar{1}\bar{1}0]$ substrate directions, the influence of which should decrease with increasing film thickness as for Ni film on GaAs(001).

Figure 69 shows the remanence curves for Co films grown on GaAs(001) using different pH from 2.23 to 2.9. At pH = 2.23. The uniaxial anisotropy reveals its characteristic shape with the easy axis aligned parallel to the [110] direction of the GaAs(001) surface. Superimposed is a four-fold symmetry with the easy axis oriented about -37 to $+37^\circ$ away from the GaAs[110] direction. The sharp peak along the $[\bar{1}\bar{1}0]$ direction is already present.

As the pH increases from 2.23 to 2.5, the major uniaxial anisotropy becomes more pronounced with an increase in the pseudo axis component (i.e. sharp peak along GaAs $[\bar{1}\bar{1}0]$ increases). Increasing the pH to 2.9 leads to an evolution of the major uniaxial anisotropy to a four-fold anisotropy with the easy axis along the [110] direction and a broadening of the sharp peak along the $[\bar{1}\bar{1}0]$ direction, which evolves from an almost easy to an easy axis.

(3) Due to the difficulty of obtaining homogenous Fe films below 300 nm and hence determining its thicknesses (Sec. II B 1), the magnetic properties presented in the following section were extracted from thick Fe films. The angular dependence of the remanence (M_r/M_s) and ferromagnetic resonance (FMR) field (H_r) of 400 nm thick epitaxial Fe films grown from FeSO_4 and FeCl_2 electrolyte are shown respectively in Figs. 70 and 71.

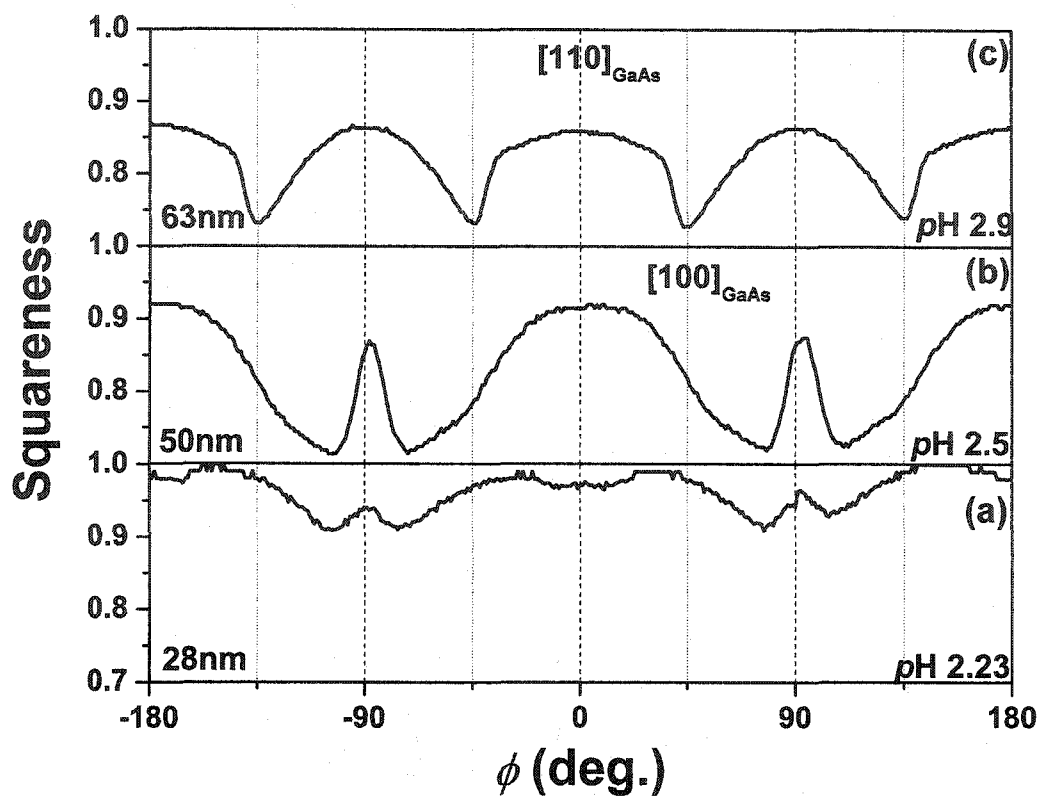


FIG. 69. Angular dependence of the remanence for Co films grown on GaAs(001) with pH and thicknesses indicated in the graph. A value of the sample rotation angle ϕ equal to zero corresponds to a magnetic field direction parallel to GaAs[110].

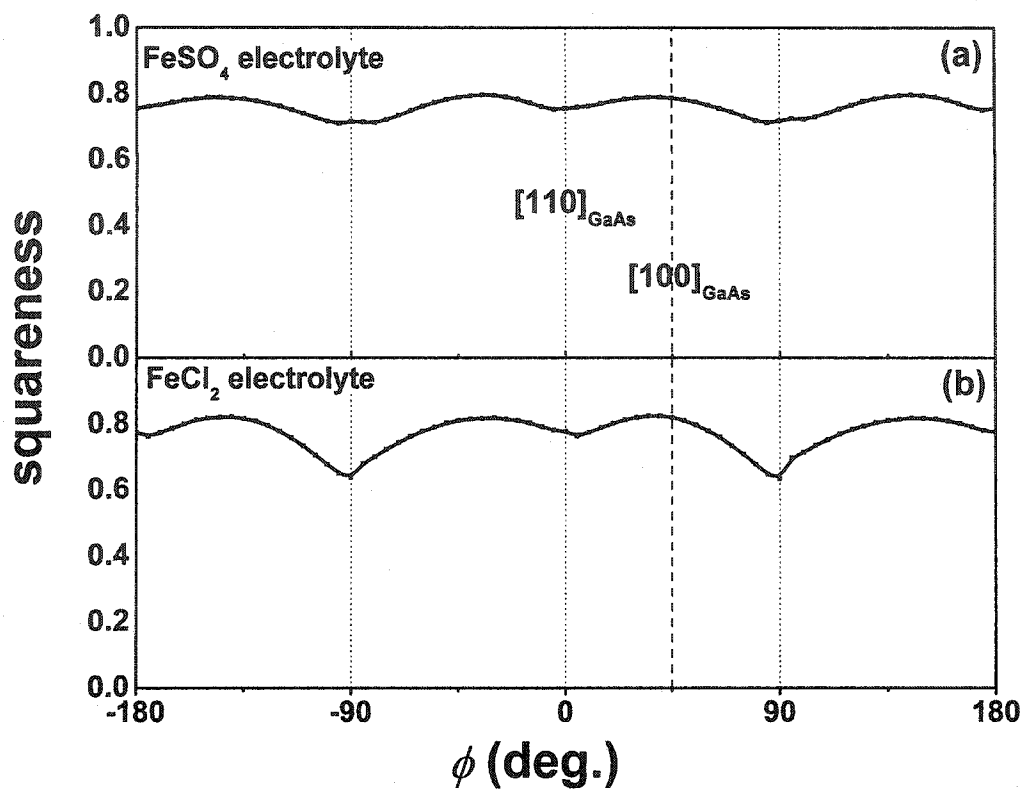


FIG. 70. Angular dependence of the remanence showing the in-plane magnetic anisotropy symmetry for 400 nm Fe films grown on GaAs(001) from: (a) a FeSO_4 solution and (b) a FeCl_2 solution. Dominant is a four-fold anisotropy.

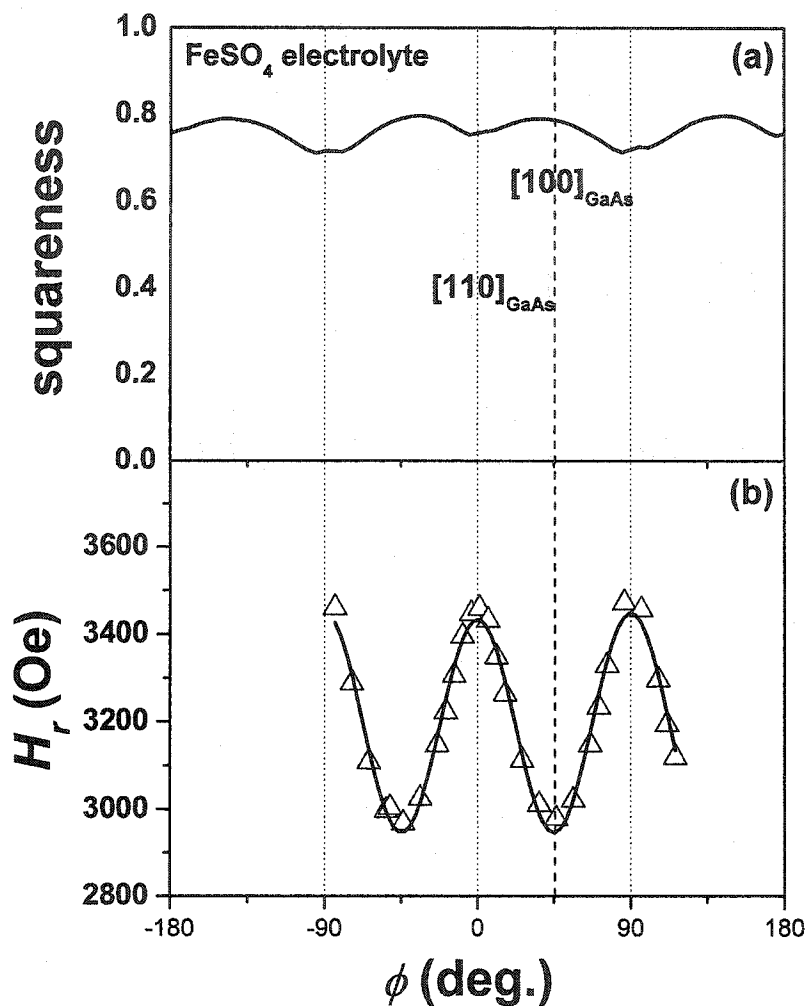


FIG. 71. (a) Angular dependence of the remanence (M_r/M_s , normalized by M_s). (b) FMR resonance field (H_r), showing the in-plane magnetic anisotropy symmetry for 400 nm Fe films deposited using FeSO₄ solutions on GaAs(001). Similar results were also observed for Fe films deposited using FeCl₂ solution. The line in (b) is a fit to the data to extract the anisotropy values. A value of the sample rotation angle ϕ equal to zero corresponds to a magnetic field direction parallel to GaAs[110].

Both indicate the symmetry of the magnetic anisotropy in the plane of the films. The plots for Fe(100) clearly show the expected four-fold symmetry, in agreement with the crystalline anisotropy of Fe with $\langle 100 \rangle$ easy axis directions. Superimposed is a weak uniaxial anisotropy which has been observed previously in ferromagnetic layers grown on GaAs(001) and is attributed to the chemical anisotropy of the substrate surface.¹² Table VII shows the magnetic properties extracted from FMR spectra for two 400 nm thick Fe films grown from FeSO₄ and FeCl₂ solutions. From these data, a relatively insignificant uniaxial component (K_u/M_s) is observed compared with the magnetocrystalline anisotropy (K_1/M_s). Remanence curves in Fig. 70 show that this uniaxial component is more pronounced in the case of FeCl₂ electrolyte but remains negligible.

TABLE VII. Magnetic properties obtained from FMR spectra for two 400 nm Fe films electrodeposited on *n*-GaAs(001) from FeSO₄ and FeCl₂ solutions. K_p is the perpendicular anisotropy.

<i>n</i> -GaAs orientation	Electrolyte (0.1 M)	K_1/M_s (Oe)	K_u/M_s (Oe)	$4\pi M_s + 2K_p/M_s$ (Oe)
(001)	FeSO ₄	136±4	4±3	20740±40
(001)	FeCl ₂	46±5	7±5	19830±60

In addition, it is to notice that the linewidths for the FMR measurements are quite large around 1000-1500 Oe, indicating the epitaxial quality is not perfect. The $4\pi M_s + 2K_p/M_s$ values, where K_p is the perpendicular anisotropy, are close to the $4\pi M_s$ value of bulk Fe,^{12,90} therefore the perpendicular anisotropy is not significant compared with M_s .⁹⁰ VSM measurements performed on those films also confirm that the M_s of these films are

close to the bulk value. The corresponding hysteresis loops for both FeSO_4 and FeCl_2 electrolyte are shown in Fig. 72. The hard axis loops do not differ much from the easy axis loops. The saturation magnetization values for both films are around 2.0 ± 0.2 T, and are thus within the error margins comparable to the value for bulk Fe. This is an indication that the electrodeposited Fe films exhibit a small percentage of voids and a small fraction of non-magnetic inclusions, such as Fe-hydroxides. It is for thinner films that one might expect a reduction of M_s .¹² The coercivity values are respectively 67 and 43 Oe for Fe films grown from FeSO_4 and FeCl_2 solution (Table VIII).

TABLE VIII. Coercivity H_c of 400 nm Fe films grown on GaAs(001) from FeSO_4 and FeCl_2 electrolyte solutions.

	Fe on GaAs(001) FeSO_4 electrolyte	Fe on GaAs(001) FeCl_2 electrolyte
[110]	67 Oe	43 Oe
90° from [110]	67 Oe	43 Oe

(4) In the case of iron rich $\text{Fe}_x\text{Ni}_{1-x}$ films ($x \geq 0.9$), no further magnetic characterization was performed since no convincing XRD data upon epitaxial growth on GaAs(001) substrate was found (Sec. II C 1 a).

b. GaAs(011). (1) Ni films show a well defined uniaxial anisotropy with the easy axis along the GaAs[100] direction as the in-plane angular remanence curves in Fig. 73 show. The hard axis is approximately at 90°, along the GaAs[110] with a single minimum present in the remanence. Simulation of the remanence assuming only uniaxial anisotropy induced by the substrate is shown in Fig. 73 (a). The fit is close but does not agree exactly with the experimental data likewise Ni on GaAs(001). Addition of a

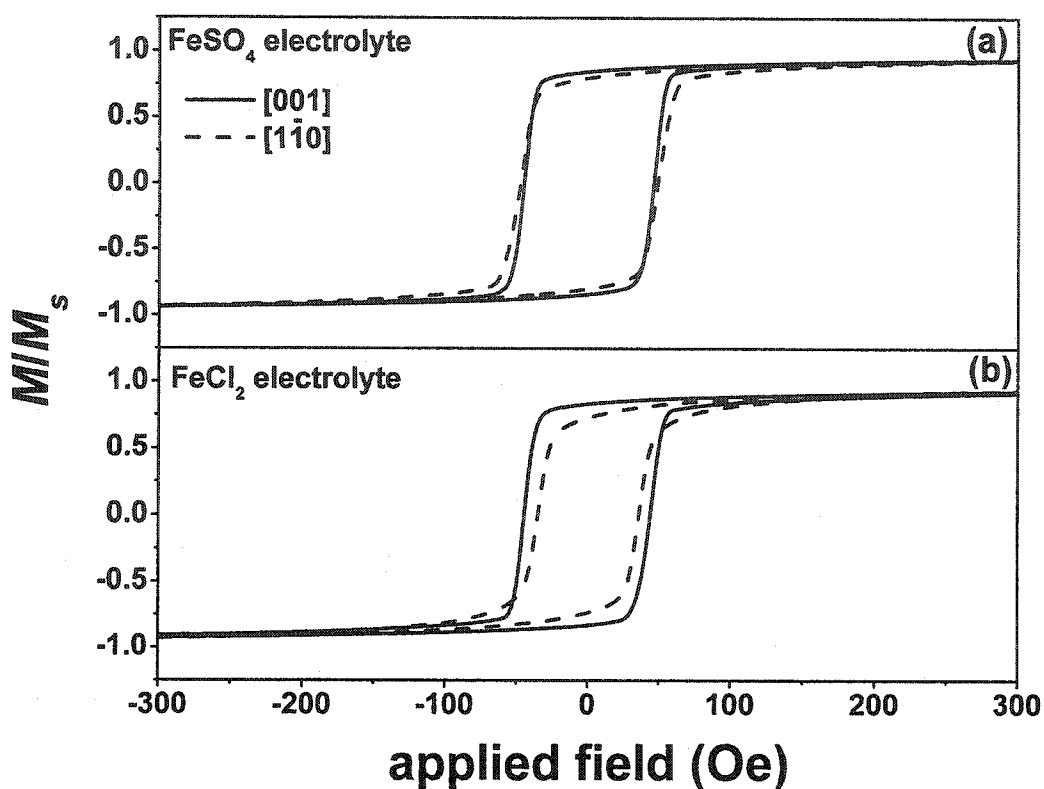


FIG. 72. Hysteresis loops showing the in-plane hysteresis behavior for 400 nm Fe films grown on GaAs (001) from: (a) a FeSO_4 solution and (b) a FeCl_2 solution. The field is applied along the [001] (solid line) and the $[\bar{1}\bar{1}0]$ (dashed line) directions for (a) and (b). Shown are only the low field parts of the hysteresis loops which were measured between ± 10 kOe.

superposition of a (111) six-fold crystalline anisotropy (expected from XRD epitaxy) does not allow a better fit of the experimental data.

Above a certain thickness (~ 80 nm), the Ni films exhibit two minima in the remanence [Fig. 73 (b)] around GaAs[110] corresponding to the two Ni[110] variants observed in the in-plane XRD ϕ scans described in Sec. II C 1 b (Fig. 40). In addition the presence of a local maximum in the remanence exactly along the GaAs [110] [Fig. 73 (a)] becomes more pronounced with increasing thickness [Fig. 73 (b)]. Nevertheless, as shown in Fig. 74, the squareness values measured along the easy and hard axis is not affected significantly by the thickness. With the exception of the thinnest films, the easy axis squareness remains constant ~ 0.95 . The magnetic properties of the thinnest films will be most susceptible to the influence of the surface oxide layer.²⁸

A small increase in the squareness of the hard axis is observed, but the films maintain a good anisotropy for thickness up to 75 nm. A modification of the pH (2.2–2.8), as shown in Fig. 75, does not influence the squareness and hence the good magnetic anisotropy properties of the Ni films on GaAs(011) in this thickness range.

Figure 76 shows the hysteresis loops of a 14, 30, and 85 nm thick Ni film with the easy axis found along the GaAs[100] direction. The two Ni[110] variants observed in the XRD ϕ scans (Fig. 40) in general prevent the observation of a hard axis with zero coercivity along GaAs[110]. For thin films (< 20 nm) a hard loop with essentially zero coercivity can be observed corresponding to the single remanent minima [Fig. 76 (a)]. Along these directions, magnetization would switch by purely rotational processes, avoiding slow and noisy domain wall motion phenomena.

For thicker films [Figs. 76 (b) and 76 (c)], the hard loop is more open giving rise

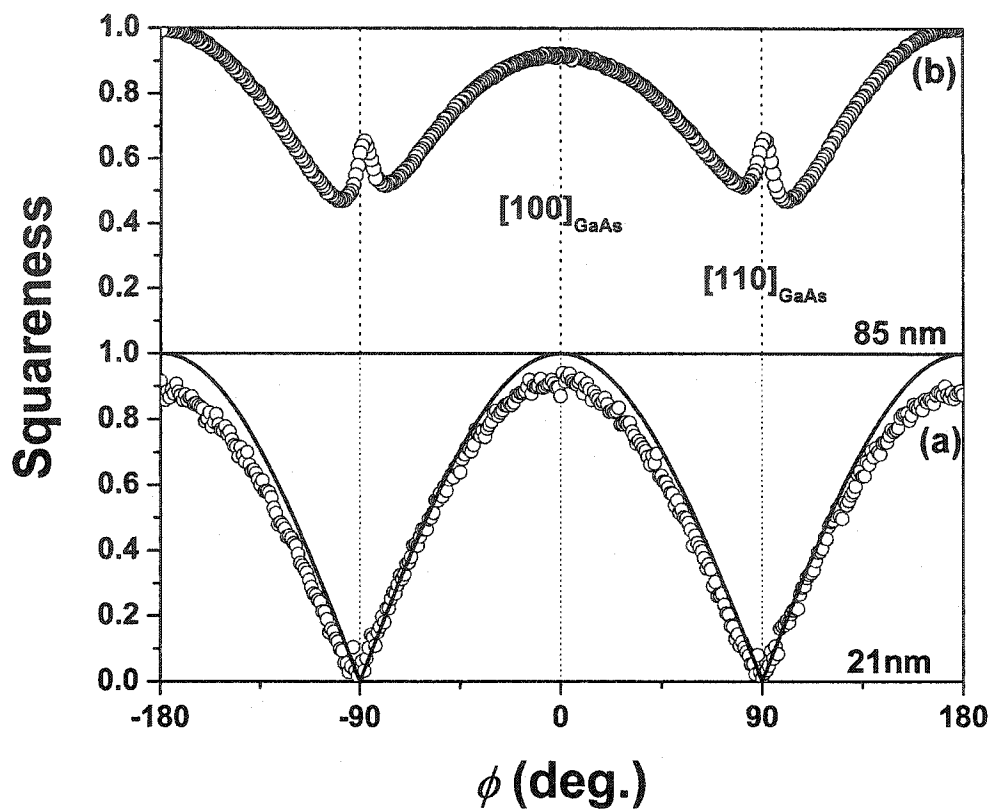


FIG. 73. Angular dependence of the remanence for a 21 nm and 85 nm thick Ni films grown on GaAs(011). A value of the sample rotation angle ϕ equal to zero corresponds to a magnetic field direction parallel to GaAs[100].

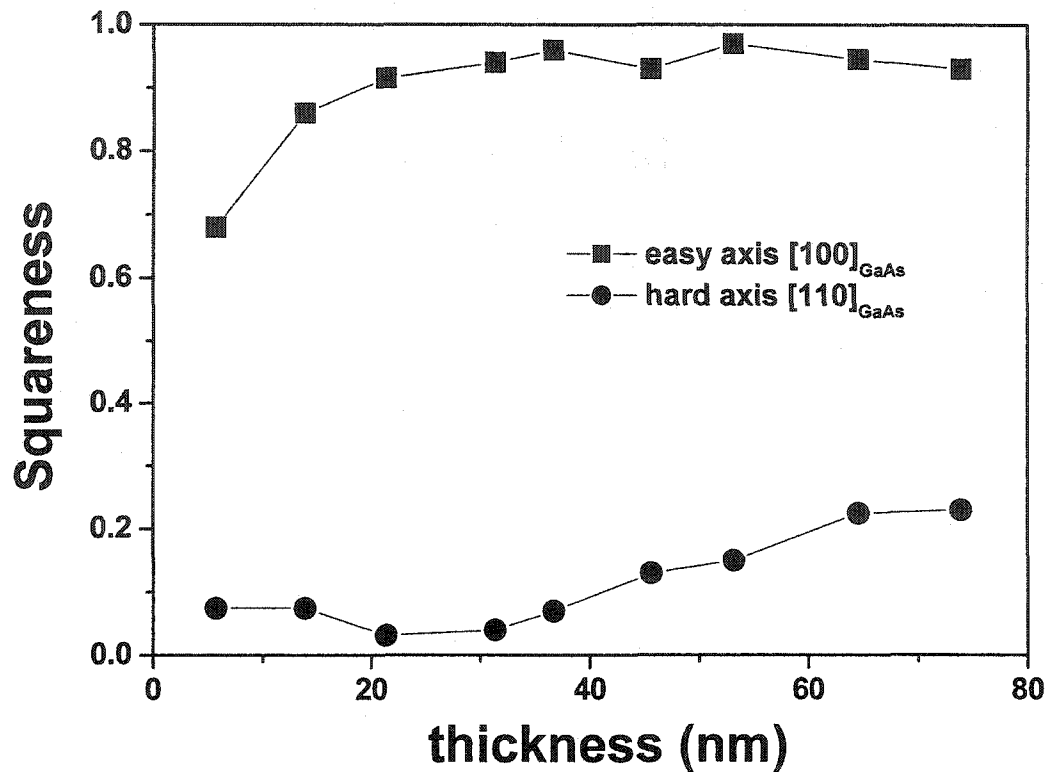


FIG. 74. Squareness (M_r/M_s , normalized by M_s) of Ni films grown on GaAs(011) as a function of the film thickness for orientation of the magnetic field along easy and hard axis of the films.

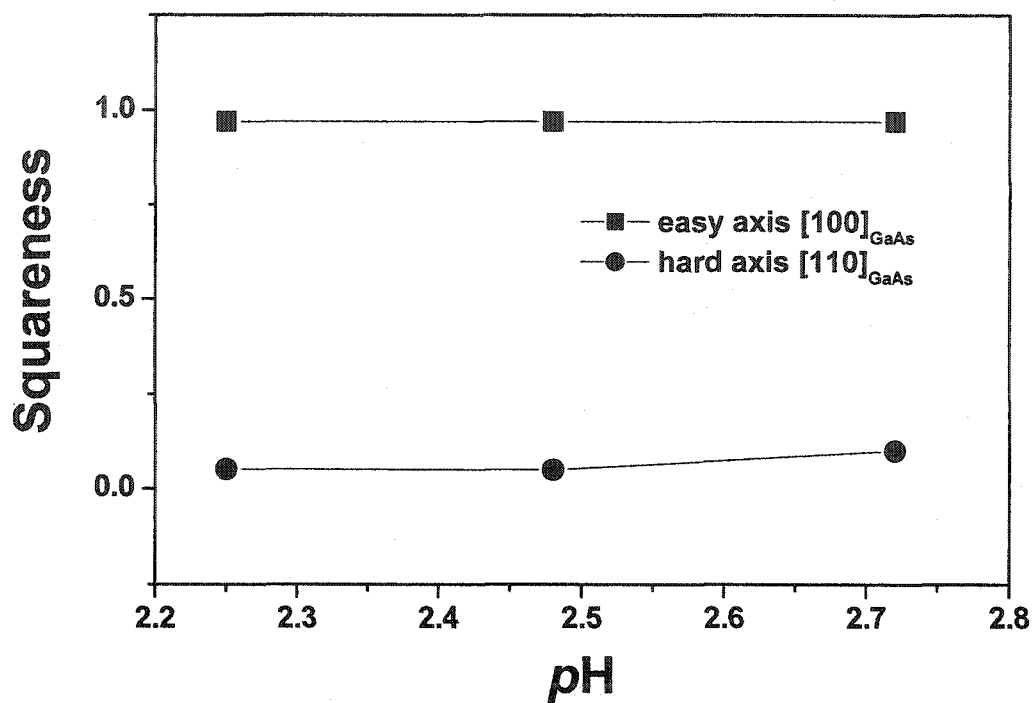


FIG. 75. Squareness (M_r/M_s , normalized by M_s) of Ni films grown on GaAs(011) as a function of the pH of the electrolyte solution for orientation of the magnetic field along easy and hard axis of the films.

to higher coercivity values. Indeed, for the 30 nm thick Ni film, the two minima next to the hard axis (GaAs[110]) at $\pm 7^\circ$ present in the remanence (not shown) leads to a closed hard hysteresis loop as shown in Fig. 76 (b), whereas the hysteresis loop along the hard axis exhibits a more open shape.

A value for the anisotropy field H_k of 500 Oe can be extracted from the saturation field of the hysteresis loop with the field applied along the hard axis for a 30 nm thick Ni film [Fig. 76 (b)]. This is approximately twice the maximum crystal anisotropy for bulk Ni (235 Oe).⁹¹ Hence there must be a magnetostrictive contribution due to film stress originated by the lattice mismatch between Ni and GaAs.

Figure 77 shows the in-plane anisotropy field values extracted from hysteresis loop as a function of thickness. H_k decreases with increasing thickness which is an indication that the structurally anisotropic GaAs(011) substrate is the cause of the magnetic anisotropy of the films with the influence of the substrate diminishing as the film thickness increases. Values of H_k of up to 1000 Oe are seen for thinnest (6 nm) Ni films which will be most susceptible to the influence of a surface oxide layer, whereas lower values around 200 Oe are observed for 70 nm Ni thick films. Figure 78 shows the easy and hard coercivity values (H_c) as a function of Ni film thickness. With increasing thickness (10–80 nm), sample coercivity does not follow a definite trend however easy (hard) H_c decreases from around 250 Oe (80 Oe) for the thinnest films, to a constant value of 100 Oe (30 Oe) for thicknesses larger than 30–40 nm.

As for the (001) orientation, BLS measurements have been performed on Ni thin films for a thickness range of 8 to 35 nm. Figure 79 shows the in-plane dispersion of the Damon-Eshbach spin wave mode on the in-plane direction of the applied magnetic field.

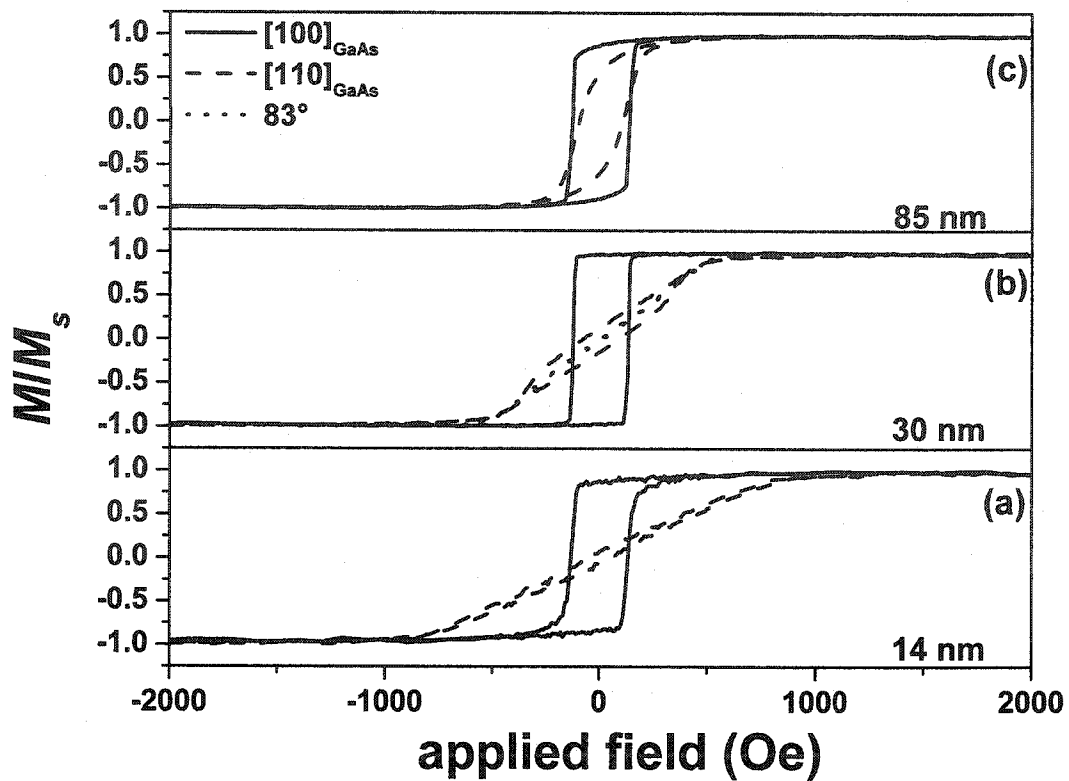


FIG. 76. Hysteresis loops of Ni films grown on GaAs(011) with thicknesses indicated in the graph. The graph does show two loops for each of which the orientation of the magnetic field with respect to the GaAs directions is mentioned. The dotted line in (b) shows the hard axis loop located at 83° away from GaAs[110].

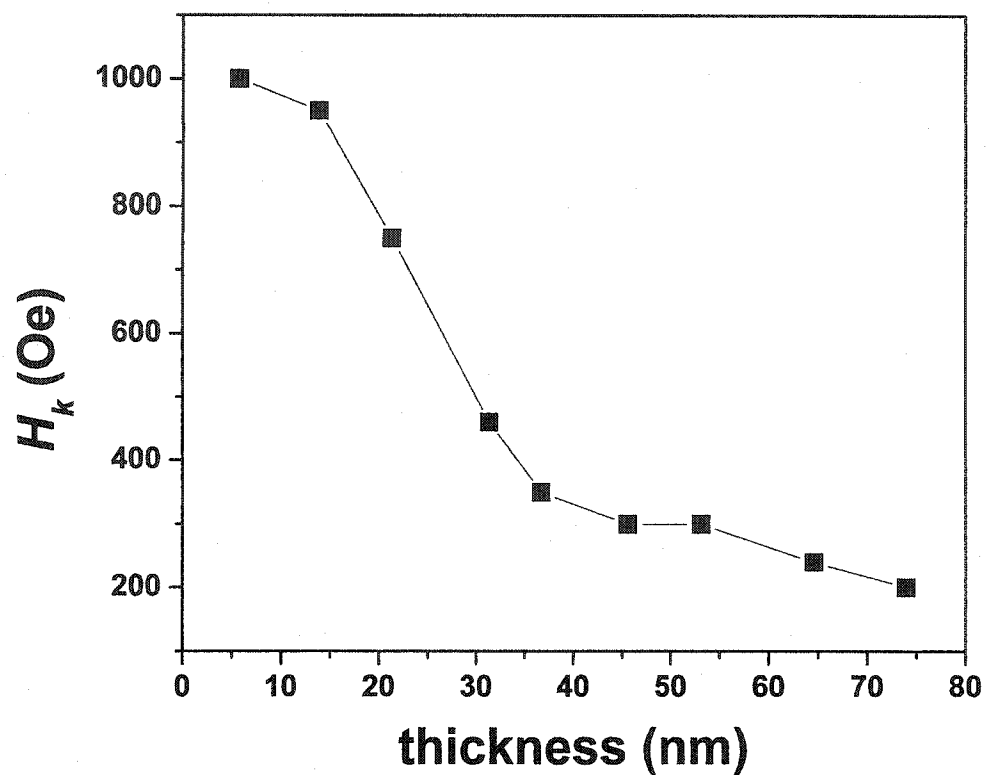


FIG. 77. Anisotropy field (H_k) versus thickness for Ni films grown on GaAs (011). The line is a guide to the eye.

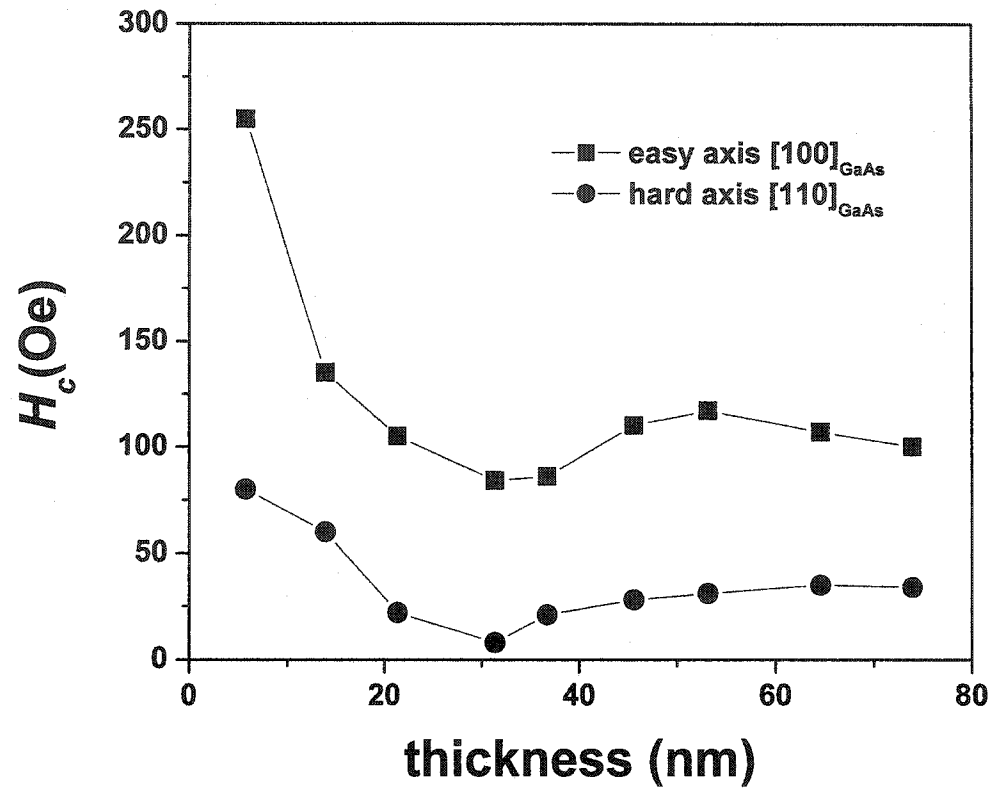


FIG. 78. Coercivity H_c as a function of Ni layer thickness for two different orientations of the magnetic field as described in the text. The lines are guides to the eye.

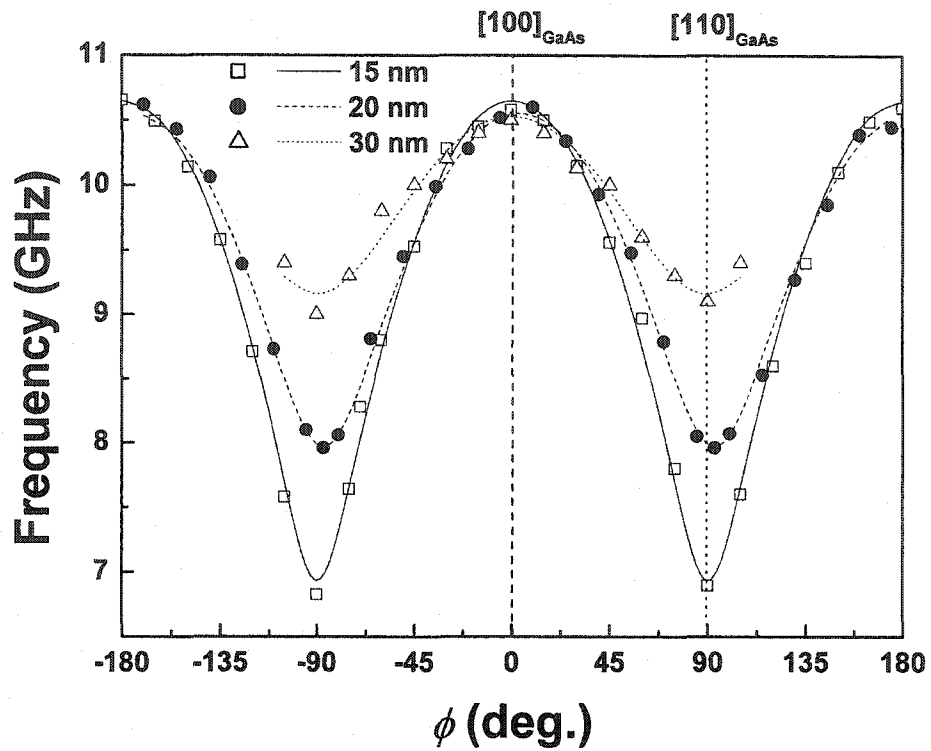


FIG. 79. In-plane dispersion of the Damon-Eshbach spin wave mode from Brillouin light scattering (BLS) on the in-plane direction of the applied magnetic field for 15 , 20 and 30 nm thick Ni films grown on GaAs(011) surfaces.

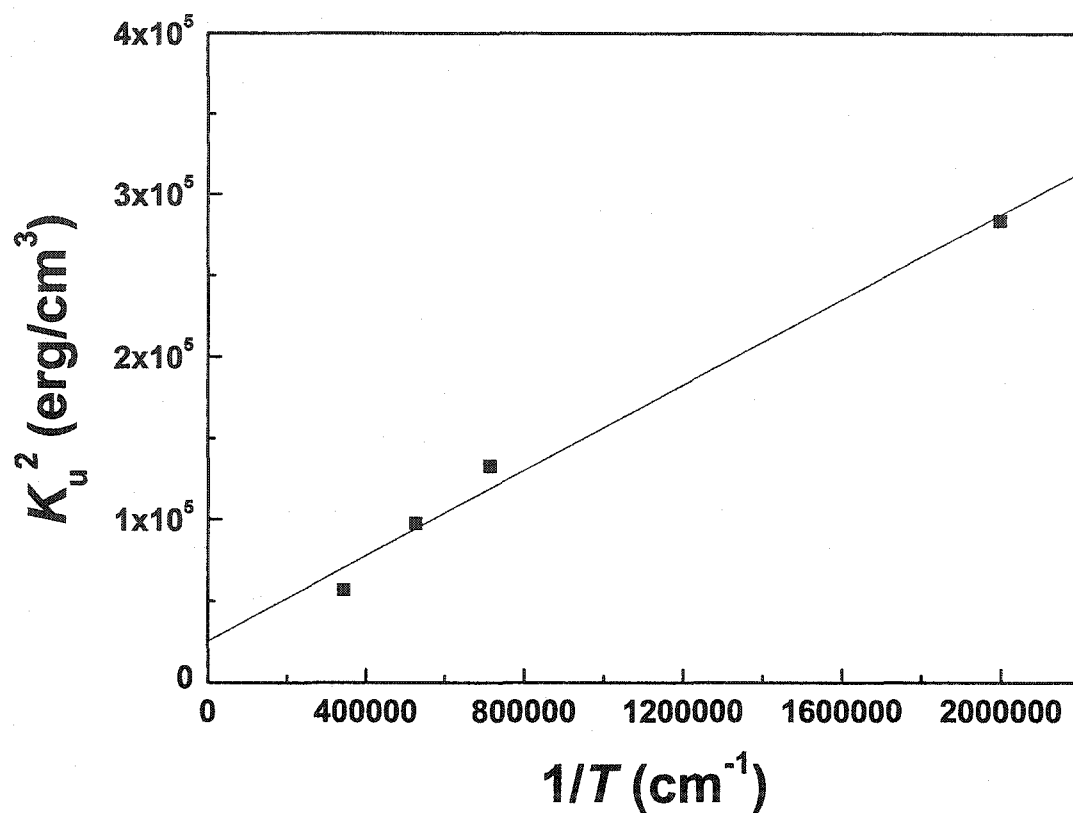


FIG. 80. Dependence of the in-plane uniaxial anisotropy constant K_u^2 from Brillouin light scattering (BLS) on the inverse Ni film thickness grown on GaAs(011) surfaces.

A clear in plane uniaxial anisotropy is found which depends linearly on the inverse Ni thickness as shown in Fig. 80. The possible lattice distortion responsible of such behavior could not be confirmed by XRD due to poor resolution/noise ratio.

Figure 81 show torque data for a 36 nm thick Ni film grown on GaAs(011). According to the XRD measurements, Ni grows with the epitaxial relationship Ni(111)[110]//GaAs(011)[110]. The free anisotropy energy $E_{(111)}$, plotted in Fig. 82, can be expressed as⁸⁰

$$E_{(111)} = \frac{K_2}{4} + \left(\frac{K_2}{108}\right)(1 - \cos 6\theta), \quad (17)$$

and applying Eq. (13) to Eq (17), the corresponding torque can be written as

$$L_{(111)} = -\frac{K_2}{18} \sin 6\theta. \quad (18)$$

The torque curve is a simple sine curve, repeating itself every 60°, with amplitude of $K_2/18$ as shown in Fig. 82. Therefore, torque measurement on a (111) surface should lead to a straightforward determination of K_2 and thus H_k . In practice, however, (111) surface often yield distorted curves, presumably because slight misorientation of the specimen gives a relatively large contribution of K_1 . Experimental data (Fig. 81) exhibit a uniaxial behavior (i.e. two-fold symmetry) with distorted major peaks instead of an expected six-fold symmetry for (111) orientation. The distortion is ascribed to the external field strength (2000 Oe) used to perform the torque, this one being close to the anisotropy field strength H_k (350 Oe). Since the uniaxial substrate anisotropy is predominant upon the crystalline anisotropy, no extraction of K_2 could be possible.

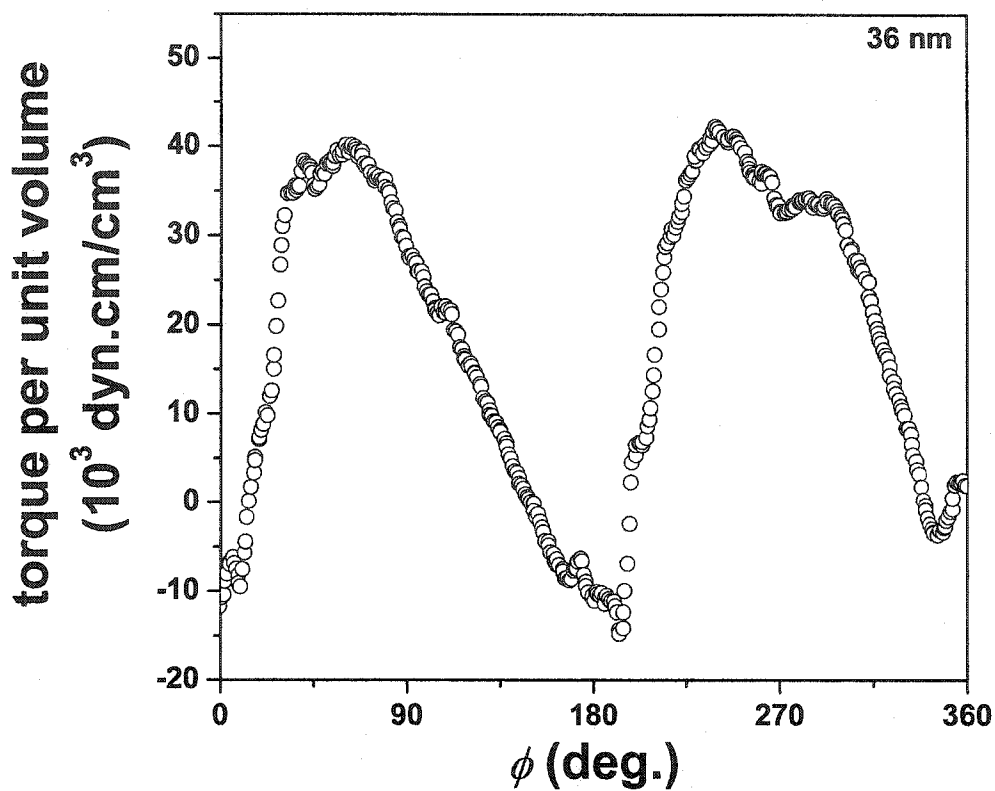


FIG. 81. Torque data of a 36 nm thick Ni layer grown on GaAs(011) with thicknesses indicated in the graph. The measurements were performed under an external magnetic field of 2000 Oe. The orientation of the magnetic field with respect to the GaAs[100] direction is random.

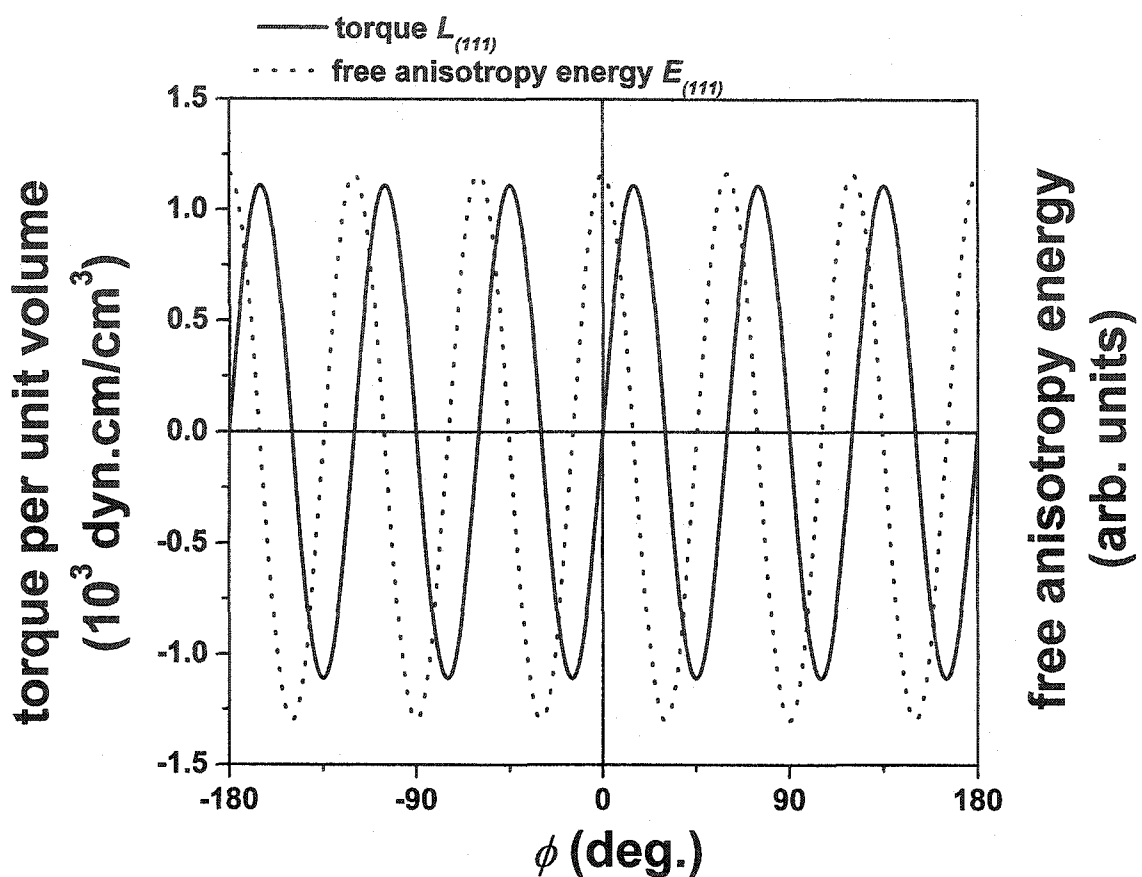


FIG. 82. Free anisotropy energy and expected torque for (111) surface as a function of in-plane angle using Eqs. (17)–(18) assuming $K_1 = -0.5 \times 10^5$ erg/cm³ and $K_2 = -0.2 \times 10^5$ erg/cm³ and the epitaxial relationship Ni(111)[110]//GaAs(011)[110]. The zero degree angle corresponds to the hard axis of the system which is along the GaAs[110] direction.

(2) Figure 83 shows the in-plane angular remanence curves for respectively a 18 nm, 71 nm and 106 nm thick Co films grown on GaAs(011). A dominant uniaxial anisotropy with the easy axis aligned parallel to the [110] direction of the GaAs(011) surface can be seen for all films. Like for Ni films, a sharp peak can be seen along the [100] hard direction, however it does not evolve with increasing thickness. Unlike for GaAs(001) orientation, the dominant uniaxial anisotropy remains with increasing Co film thickness, with the easy axis along the GaAs[110] and no loss of structure (i.e. also the uniaxial anisotropy is not reduced with increasing film thickness). The sharp peak in the remanence curve at the hard axis direction (along GaAs[100]) is reproducibly seen for all samples, a feature for which any explanation can currently be offered.

Figure 84 shows the typical hysteresis loops of a 6, 12, 18 and 24 nm thick Co film. The loops were taken with the magnetic field (2000 Oe) oriented along the most prominent directions as found in the remanence curves for those films (indicated by arrows in Fig. 83). As remanence data predicted, the easy and hard axis are found respectively along the GaAs[110] and GaAs[100] direction. The easy axis loops are characterized by a high remanence or squareness which is independent of the Co thickness.

Figure 85 shows the squareness as a function of the film thickness where the easy and hard axis values remain constant respectively around 0.95 and 0.1 even for large thicknesses up to 300 nm. The thinnest film exhibit lower (higher) easy (hard) axis squareness values due to most likely the influence of a surface oxide layer as for Ni films. Anisotropy field value H_k extracted from the hysteresis loop for various thicknesses are presented in Fig. 86. As a general trend, as was found for Ni films on GaAs(011), H_k

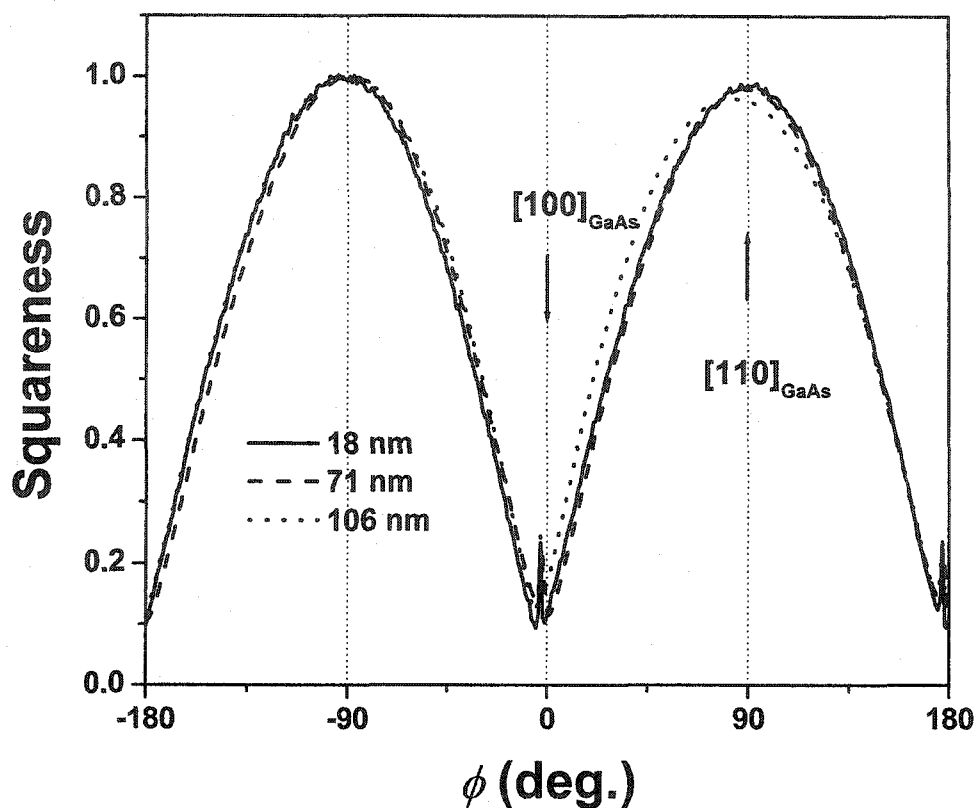


FIG. 83. Angular dependence of the remanence for Co films grown on GaAs(011) with thicknesses indicated in the graph. A value of the sample rotation angle ϕ equal to zero corresponds to a magnetic field direction parallel to GaAs[100]. The two arrows point to the characteristic positions of the remanence loop (easy axis and hard axis) of a 18 nm thick Co film for which individual hysteresis loops are shown in Fig. 84.

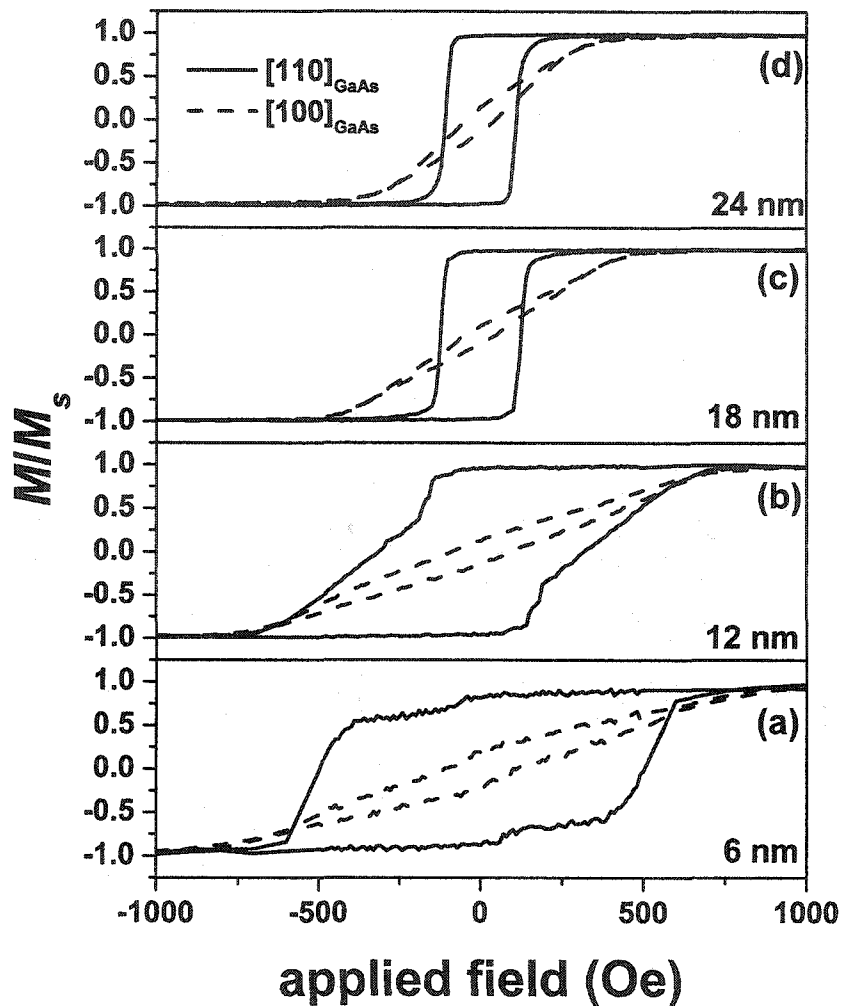


FIG. 84. Hysteresis loops of four different Co layers grown on GaAs(011) with thicknesses indicated in the graph. The measurements actually were extended to 2 kOe to ensure saturation of the films. Shown are only parts of those loops. Each graph does show two loops for each of which the orientation of the magnetic field with respect to the GaAs direction is mentioned.

decreases with increasing Co film thickness from ~ 800 Oe for thinnest films to 350 Oe for films above 60 nm. This indicates that the GaAs(011) is the cause of the magnetic anisotropy of the films, with the influence of the substrate diminishing as the film thickness increases.

Figure 87 shows the easy and hard coercivity values H_c as a function of Co film thickness. With increasing thickness (6–300 nm), sample coercivity does not follow a definite trend however easy (hard) H_c decreases from around 500 Oe (120 Oe) for the thinnest films, to a constant value of 90 Oe (40 Oe) for thicknesses larger than 25 nm.

A pH investigation of Co films on GaAs(011) substrate indicates a loss of anisotropy with increasing pH . Figure 88 shows the in-plane angular remanence of a 36 nm thick Co film grown at $pH = 3.35$ and current density $J = 11$ mA/cm². The three arrows point to the characteristic positions of the remanence curve for which hysteresis loops are taken. The dominant uniaxial anisotropy with the easy axis aligned parallel to the [110] direction of the GaAs(011) surface seen in previous films is strongly reduced. Superimposed is a four-fold symmetry with its easy axis along the GaAs[100]. It is noticed that the sharp peak along the “ex-hard” axis (GaAs[100]) has disappeared and the new hard direction is located 45° away from the easy axis.

Figure 89 shows the corresponding hysteresis loops measured along the three major directions for the 36 nm thick Co film. No anisotropy is seen, the three directions loops presenting very little difference. Therefore, an increase of the pH value leads to a loss of magnetic anisotropy. Table IX shows a description of Co films grown on GaAs(011) substrate under different growth conditions (pH , J). The pH values are varied

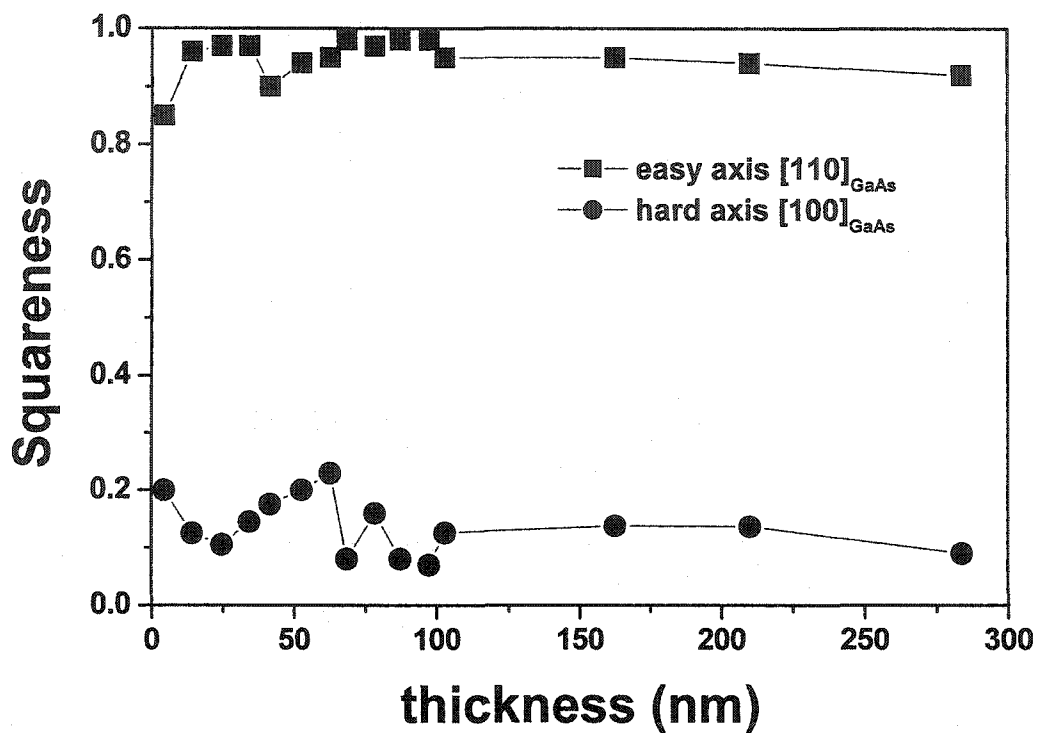


FIG. 85. Squareness (M_r/M_s , normalized by M_s) of Co films grown on GaAs(011) as a function of the film thickness for orientation of the magnetic field along easy and hard axis of the films.

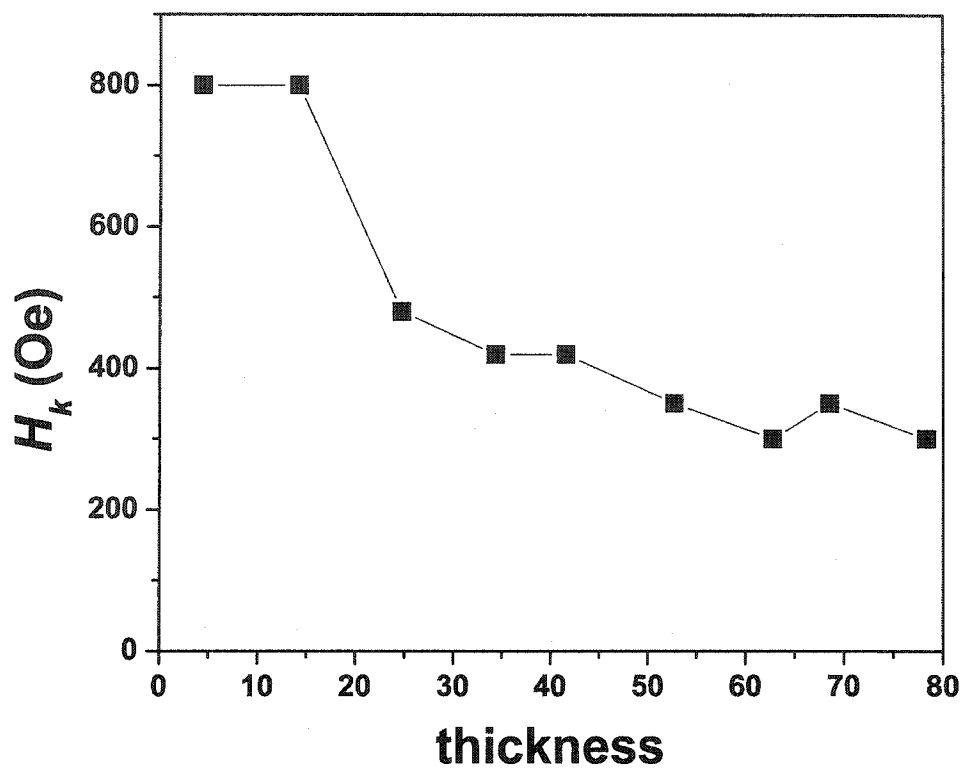


FIG. 86. Anisotropy field (H_k) versus thickness for Co films on GaAs(011). The line is a guide to the eye.

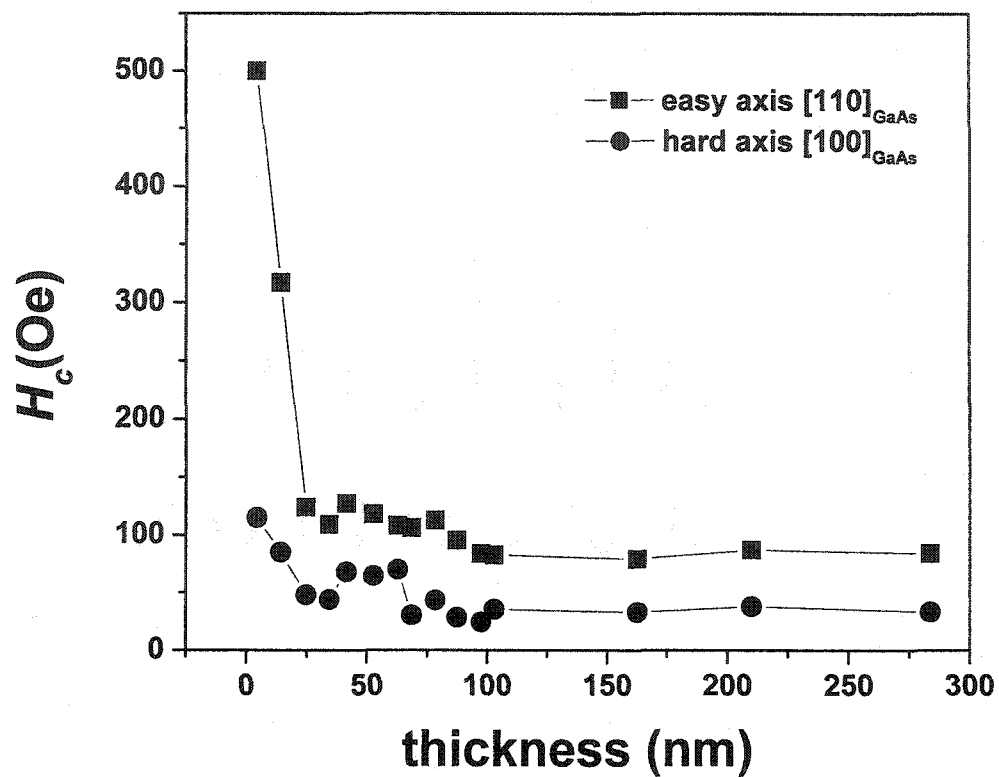


FIG. 87. Coercivity H_c as a function of Co layer thickness for two different orientations of the magnetic field as described in the text. The lines are guides to the eye.

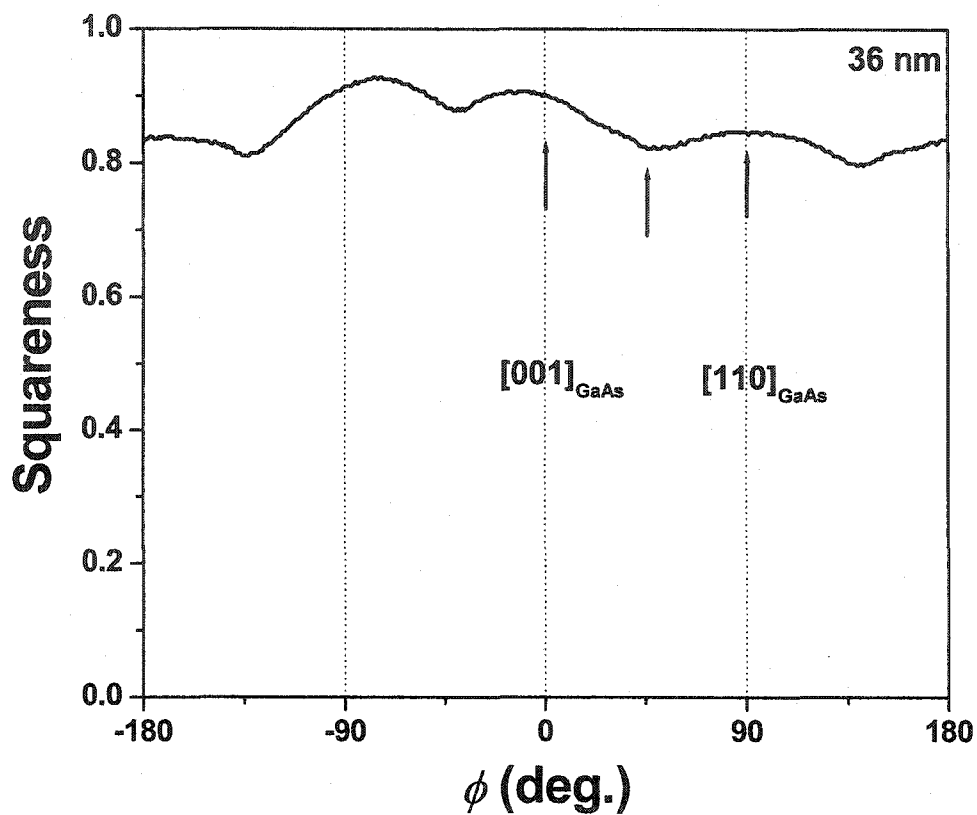


FIG. 88. Remanence curve of a 36 nm thick Co layer grown on GaAs(011) with a current density of 11 mA/cm^2 and a $p\text{H}$ of 3.35. A value of the sample rotation angle ϕ equal to zero corresponds to a magnetic field direction parallel to GaAs[001]. The three arrows point to the characteristic positions of the remanence loop (easy axis and hard axis) for which individual hysteresis loops are shown in Fig. 89.

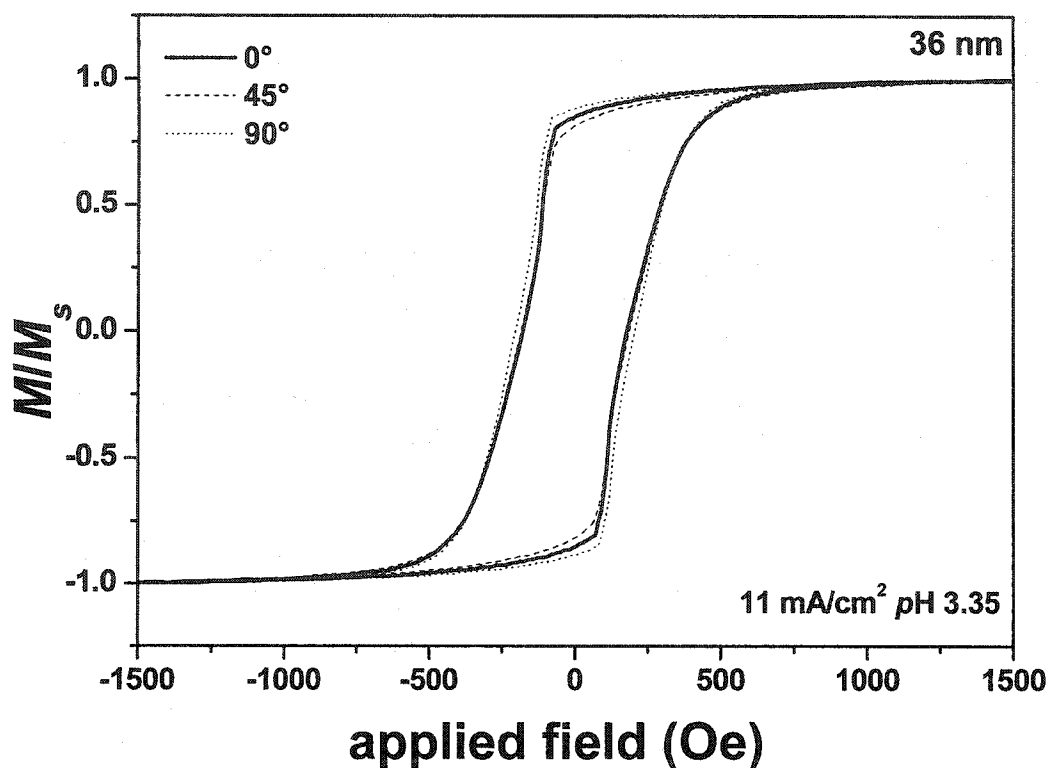


FIG. 89. Hysteresis loop of a 36 nm thick Co layer grown on GaAs(011) at a current density of 11 mA/cm² and a pH of 3.35. The measurements actually were extended to 2 kOe to ensure saturation of the films. Shown are only parts of those loops. The graph does show three loops for each of which the orientation of the magnetic field with respect to the GaAs[001] direction is mentioned.

TABLE IX. Description of Co layers grown on GaAs (011) under different growth conditions as indicated in the table.

<i>pH</i>	current density (mA/cm ²)	deposition time(sec)	film description
3.68	4	60	poor film/ no deposit
3.68	12	20	Shiny film
3.35	4	60	poor film/ no deposit
3.35	12	20	Shiny film
3.03	4	60	Shiny film
3.03	12	20	Shiny film
3.03	20	12	Shiny film

from 3 to 3.7 in which range the films lose their magnetic anisotropy. Furthermore, high current densities ($> 10 \text{ mA/cm}^2$) are required to obtain good surface quality films.

It appears that the best growth conditions for Co films on GaAs(011), in terms of magnetic anisotropy and epitaxial quality, are the use of a low *pH* (between 2.3 to 2.7) and current density around 3.5 mA/cm^2 .

(3) As mentioned earlier for Fe on GaAs(001), due to the difficulty of obtaining homogenous Fe films below 300 nm and hence determining its thicknesses, the magnetic properties presented in the following section were extracted from thick Fe films. The angular dependence of the remanence (M_r/M_s) and FMR field (H_r) of 400 nm thick epitaxial Fe films grown from FeSO_4 and FeCl_2 electrolyte are shown respectively in Figs. 90 and 91. Both indicate the symmetry of the magnetic anisotropy in the plane of the films. The remanence curves of the Fe(011) layers are dominated by an uniaxial anisotropy. This uniaxial anisotropy is opposite to the magnetocrystalline anisotropy.

Table X shows the magnetic properties obtained from FMR spectra for two 400 nm thick Fe films grown from FeSO_4 and FeCl_2 solutions. In the FMR result, this uniaxial component (K_u/M_s) is not dominating compared with the magnetocrystalline anisotropy (K_1/M_s) as shown in Fig. 91 (a) and Table X, with a clear indication of the crystalline anisotropy.

TABLE X. Magnetic properties obtained from FMR spectra for two 400 nm Fe films electrodeposited on $n\text{-GaAs}(011)$ from FeSO_4 and FeCl_2 solutions. K_p is the perpendicular anisotropy.

$n\text{-GaAs}$ orientation	Electrolyte (0.1 M)	K_1/M_s (Oe)	K_u/M_s (Oe)	$4\pi M_s + 2K_p/M_s$ (Oe)
(011)	FeSO_4	151 ± 4	29 ± 3	20500 ± 30
(011)	FeCl_2	100 ± 5	33 ± 4	20110 ± 30

The discrepancy between remanence and FMR data might be due to the different sample thicknesses used for the measurements leading to different degrees of strain. Remanence measurements are also not a true indicator of anisotropy as the type of remagnetization process does play a role. A possible explanation for the uniaxial anisotropy might be stress caused by the uniaxial substrate surface similarly to the uniaxial behavior of (non-epitaxial) FeNi and Co layers grown by electrodeposition on $\text{GaAs}(011)$.²⁹ The secondary maxima at $\pm 90^\circ$ [corresponding to the in-plane $\langle 100 \rangle$ directions; Fig. 91 (a)] could be reminiscent of the magnetocrystalline-induced anisotropy of bcc Fe with easy axes along $\langle 100 \rangle$. It was reported by B. Heinrich et al.⁹² that the anisotropy did vary with thickness for ultra-thin Fe films of a few monolayers. Nevertheless, the observation clearly indicates the existence of the uniaxial component and its orientation in the $\text{Fe}(011)$ case.

In addition, as for the GaAs(001) orientation, it is noticed that the line widths for the FMR measurements are quite large around 1000–1500 Oe, indicating the epitaxial quality is not perfect. From Table X, the $4\pi M_s + 2K_p/M_s$ values are close to the $4\pi M_s$ value of bulk Fe,^{12,90} therefore the perpendicular anisotropy is not significant compared with M_s .⁹⁰ VSM measurements performed on those films also confirm that the M_s of these films are close to the bulk value. The corresponding hysteresis loops for both FeSO₄ and FeCl₂ electrolyte are shown in Fig. 92. The hard axis loops show a more pronounced hard axis behavior for the Fe films on GaAs(011) compared to Fe films on GaAs(001), in particular for the one grown from the FeSO₄ solution. The saturation magnetization values for both films are around 2.0 ± 0.2 T, and are thus within the error margins comparable to the value for bulk Fe. This is an indication that the electrodeposited Fe films exhibit a small percentage of voids and a small fraction of non-magnetic inclusions, such as Fe-hydroxides. It is for thinner films that one might expect a reduction of M_s .¹² From Table XI, the coercivity values are respectively 51 and 66 Oe for Fe films grown from FeSO₄ and FeCl₂ solution.

TABLE XI. Coercivity H_c of 400 nm Fe films grown on GaAs(011) from FeSO₄ and FeCl₂ electrolyte solutions.

	Fe on GaAs(011) FeSO ₄ electrolyte	Fe on GaAs(011) FeCl ₂ electrolyte
[110]	51 Oe	66 Oe
90° from [110]	47 Oe	66 Oe

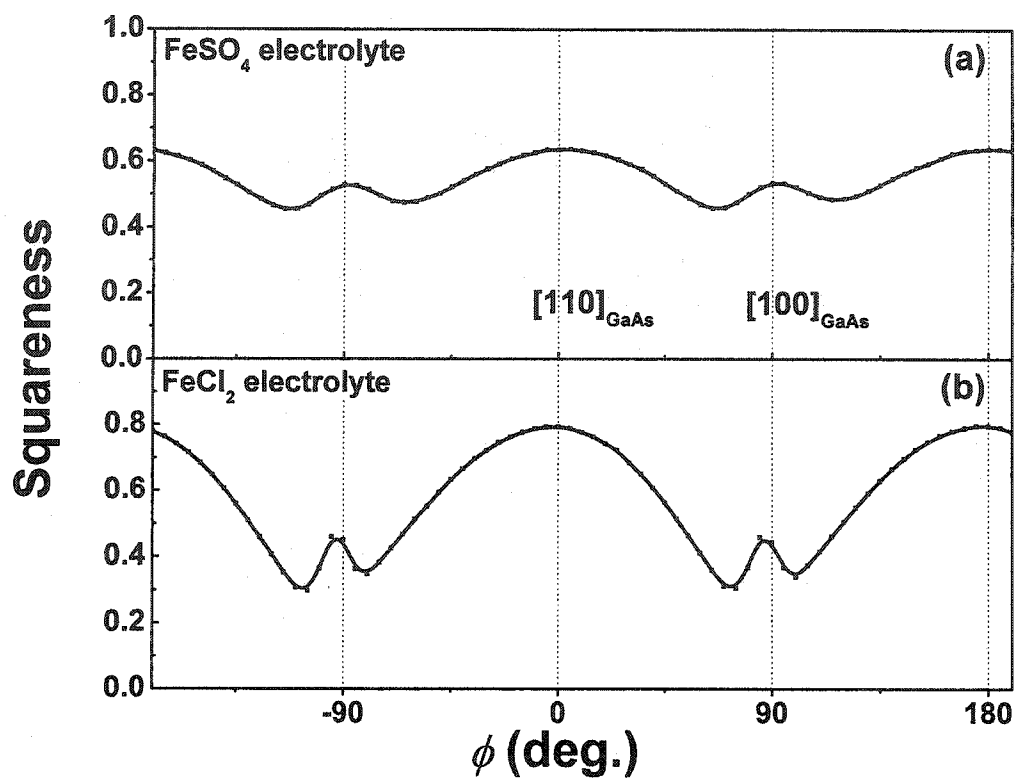


FIG. 90. Angular dependence of the remanence showing the in-plane magnetic anisotropy symmetry for 400 nm Fe films grown on GaAs(011) from: (a) a FeSO_4 solution and (b) a FeCl_2 solution. Dominant is an uniaxial anisotropy.

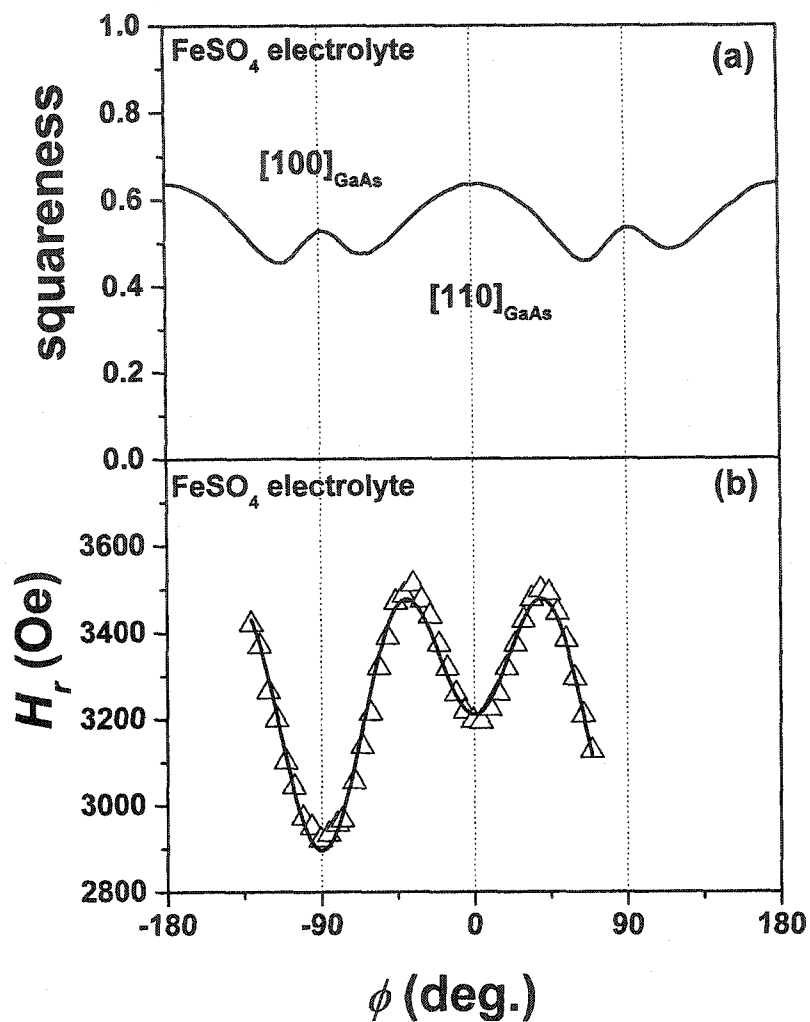


FIG. 91. (a) Angular dependence of the remanence (M_r/M_s , normalized by M_s) and (b) FMR resonance field (H_r), showing the in-plane magnetic anisotropy symmetry for 400 nm Fe films deposited using FeSO₄ solutions on GaAs(011). Similar results were also observed for Fe films deposited using FeCl₂ solution. The line in (b) is a fit to the data to extract the anisotropy values.

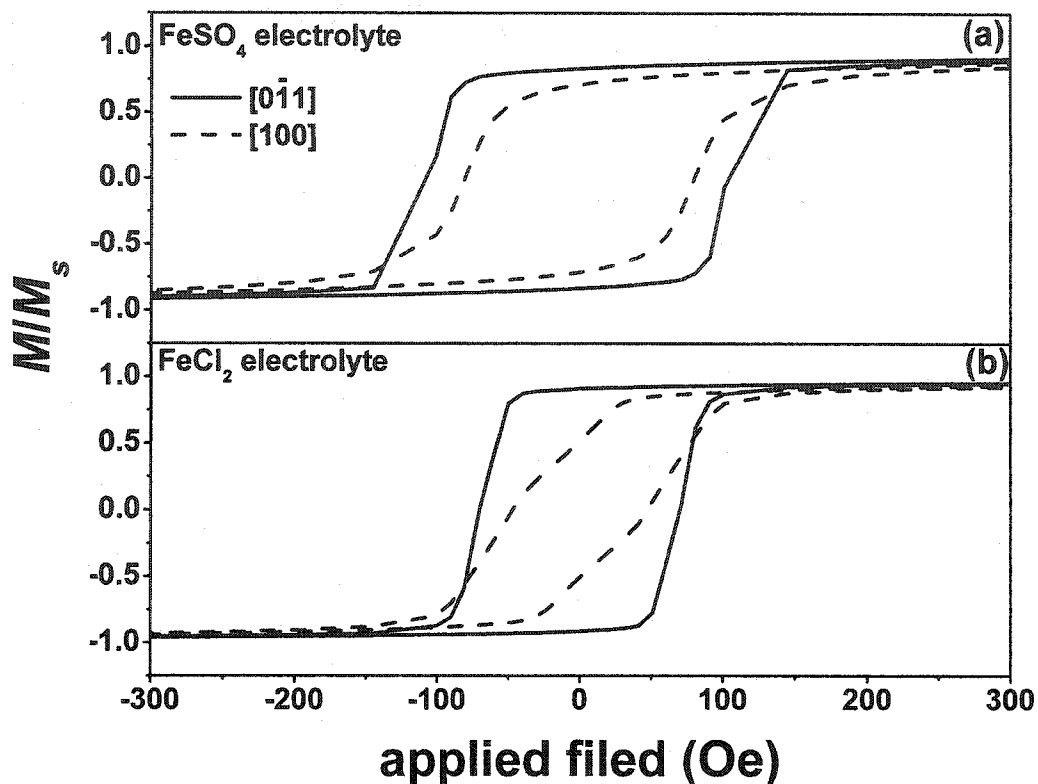


FIG. 92. Hysteresis loops showing the in-plane hysteresis behavior for 400 nm Fe films grown on GaAs(011) from: (a) a FeSO_4 solution and (b) a FeCl_2 solution. The field is applied along the $[0\bar{1}1]$ (solid line) and the $[100]$ (dashed line) directions for (a) and (b). Shown are only the low field parts of the hysteresis loops which were measured between ± 10 kOe.

(4) Figure 93 shows the in-plane angular remanence curves for 5, 18 and 46 nm thick $\text{Fe}_x\text{Ni}_{1-x}$ films, respectively, grown on GaAs(011). A dominant uniaxial anisotropy with the easy axis aligned parallel to the [110] direction of the GaAs(011) surface can be seen for all films. Like for Ni and Co films, a sharp peak, which increases slightly with increasing thickness, can be seen along the [100] hard direction. A possible explanation for the uniaxial anisotropy might be stress caused by the uniaxial substrate surface similarly to the uniaxial behavior of Fe and Co layers grown by electrodeposition on GaAs(011). The remanence uniaxial property seems independent of film thickness range (0–50 nm).

Figure 94 shows the typical hysteresis loops of a 5, 18, and 46 nm thick Co film. The loops were taken with the magnetic field (2000 Oe) oriented along the most prominent directions as found in the remanence curves for those films (indicated by arrows in Fig. 93). As remanence data predicted, the easy and hard axis are found respectively along the GaAs[110] and GaAs[100] direction. The easy axis loops are characterized by a high remanence or squareness which is independent of the film thickness (0–50 nm). Figure 95 shows the squareness as a function of the film thickness where the easy and hard axis values remain constant respectively around 0.95 and 0.2. The thinnest films exhibit lower (higher) easy (hard) axis squareness values due most likely to the influence of a surface oxide layer as for Ni and Co films. Anisotropy field values H_k extracted from the hysteresis loop for various thicknesses are presented in Fig. 96. As a general trend, as was found for Ni and Co films on GaAs(011), H_k decreases with increasing $\text{Fe}_x\text{Ni}_{1-x}$ film thickness from ~ 650 Oe for thinnest films to 350 Oe for films around 50 nm. This indicates that the GaAs(011) is the cause of the magnetic

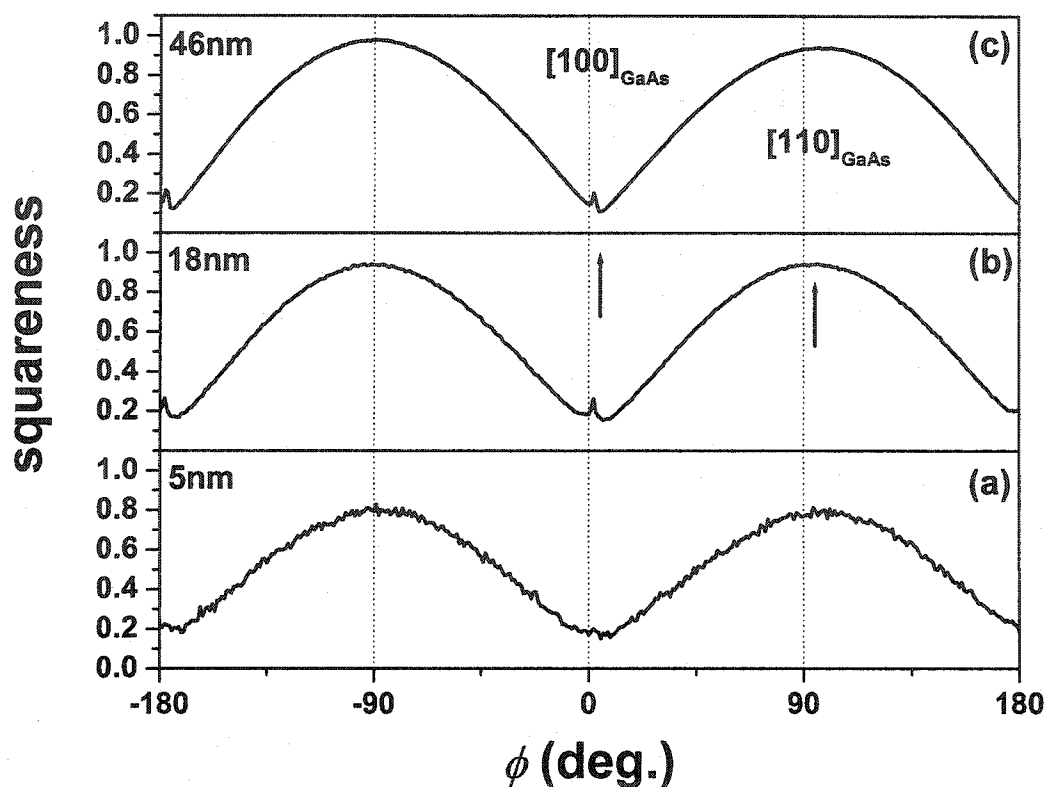


FIG. 93. Angular dependence of the remanence for FeNi films grown on GaAs(011) with thicknesses indicated in the graph. A value of the sample rotation angle ϕ equal to zero corresponds to a magnetic field direction parallel to GaAs[100]. The two arrows point to the characteristic positions of the remanence loops (easy axis and hard axis) for which individual hysteresis loops are shown in Fig. 94.

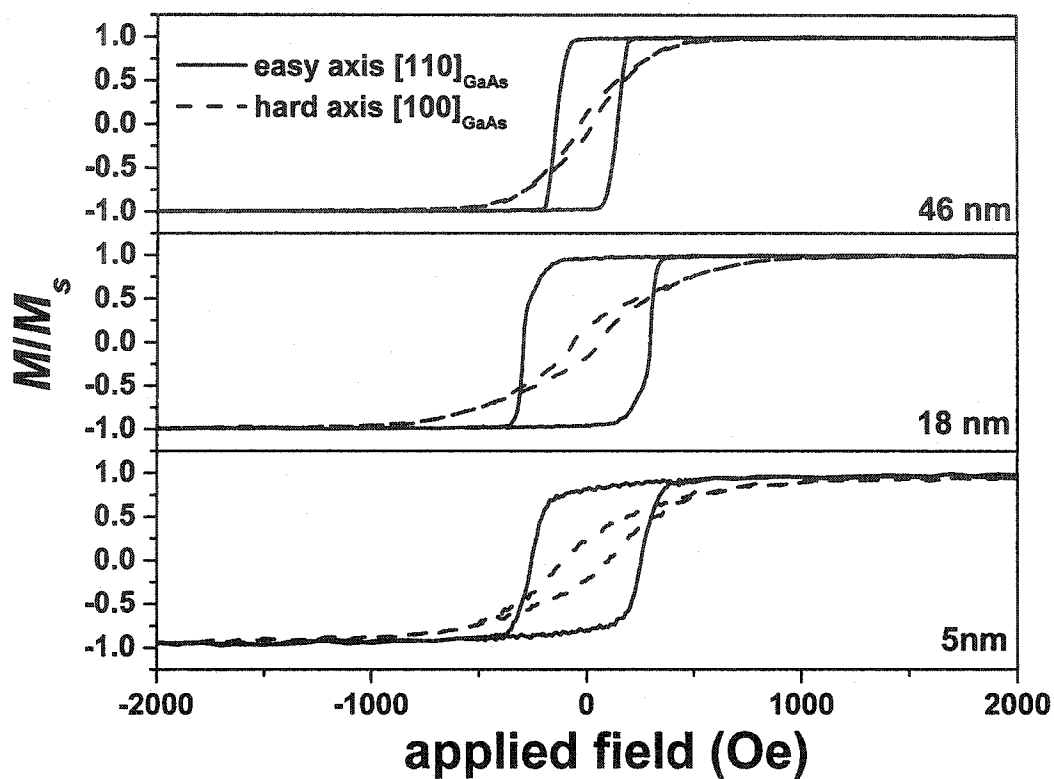


FIG. 94. Hysteresis loops of FeNi films grown on GaAs(011) with thicknesses indicated in the graph. The measurements actually were extended up to 5 kOe to ensure saturation of the films. Shown are only parts of those loops. The graph does show two loops for each of which the orientation of the magnetic field with respect to the GaAs directions is mentioned.

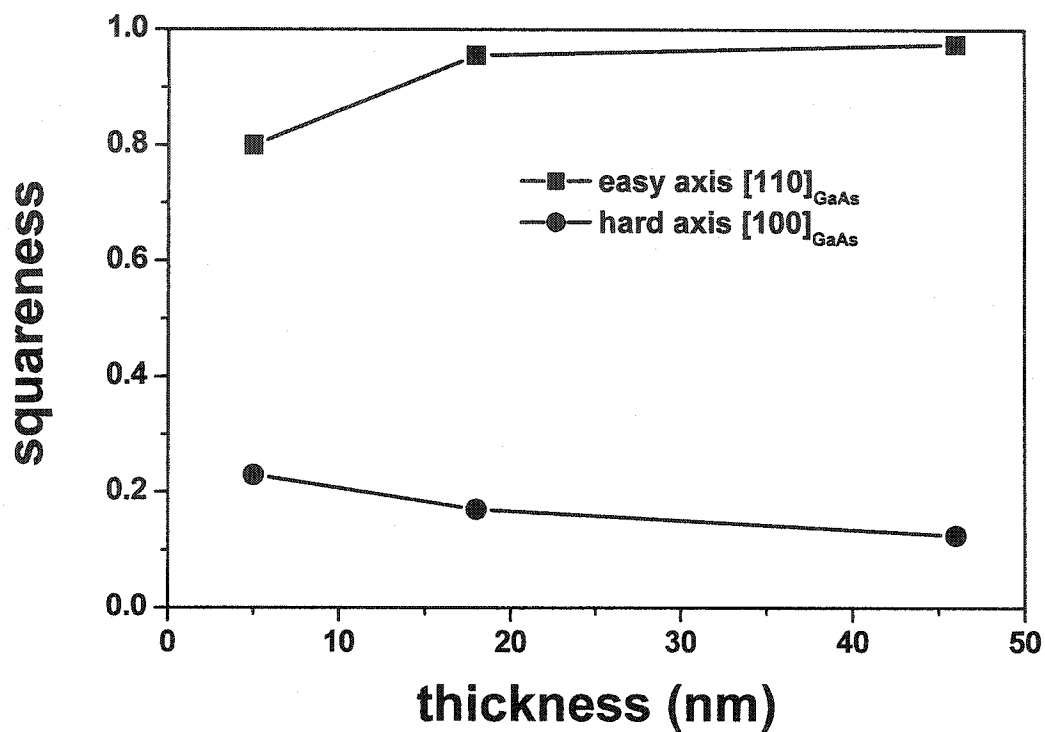


FIG. 95. Squareness (M_r/M_s , normalized by M_s) of FeNi films grown on GaAs(011) as a function of the film thickness for orientation of the magnetic field along easy and hard axis of the films.

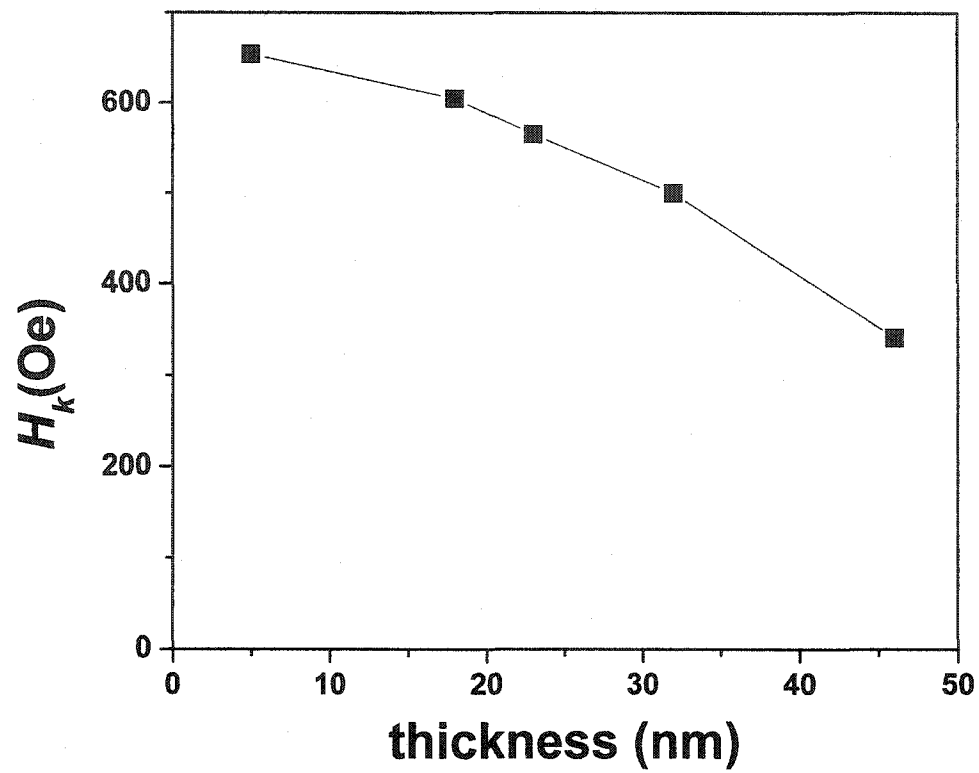


FIG. 96. Anisotropy field (H_k) versus thickness for FeNi films on GaAs(011). The line is a guide to the eye.

anisotropy of the films, with the influence of the substrate diminishing as the film thickness increases.

Figure 97 shows the easy and hard coercivity values H_c as a function of film thickness. With increasing thickness (10–50 nm), the sample coercivity H_c along the easy axis decreases from around 350 Oe for the 10 nm thick film to 150 Oe for the thickest film (46 nm). For the hard axis, H_c does not follow a definite trend, however H_c decreases from around 100 Oe for the thinnest films to a constant value of 30 Oe for thicknesses larger than 20 nm.

3. Intermixing/Interface properties of Ni on GaAs(001)

Ferromagnetic (FM) materials epitaxially grown on GaAs by evaporation or sputtering often show outdiffusion of As and Ga into the FM layer, which results in reduced magnetization and increased resistivities.¹² More recent work showed that Fe intermixing with GaAs(001) substrates can be avoided by room temperature (RT) deposition on specially prepared surfaces while good epitaxial growth can still be obtained.^{15,93} One promising deposition technique to overcome the problem of interface intermixing might be electrodeposition (ECD), as it is a RT equilibrium process, which can yield high quality epitaxial layers.²¹⁻²⁷

a. XPS analysis. The degree of possible diffusion of Ga or As into the Ni layer was analyzed²⁸ using XPS. The XPS spectrum of a 6 nm thick Ni film taken at the position of the Ga-2p peak [Fig. 98 (a)] shows no trace of Ga. The Ga 2p photoelectrons have a rather short mean free path (mfp) of 0.75 nm⁹⁴ resulting in an effective attenuation of the Ga 2p photoelectrons originating from the substrate ($T_{Ni} = 8 \times \text{mfp}$). The absence

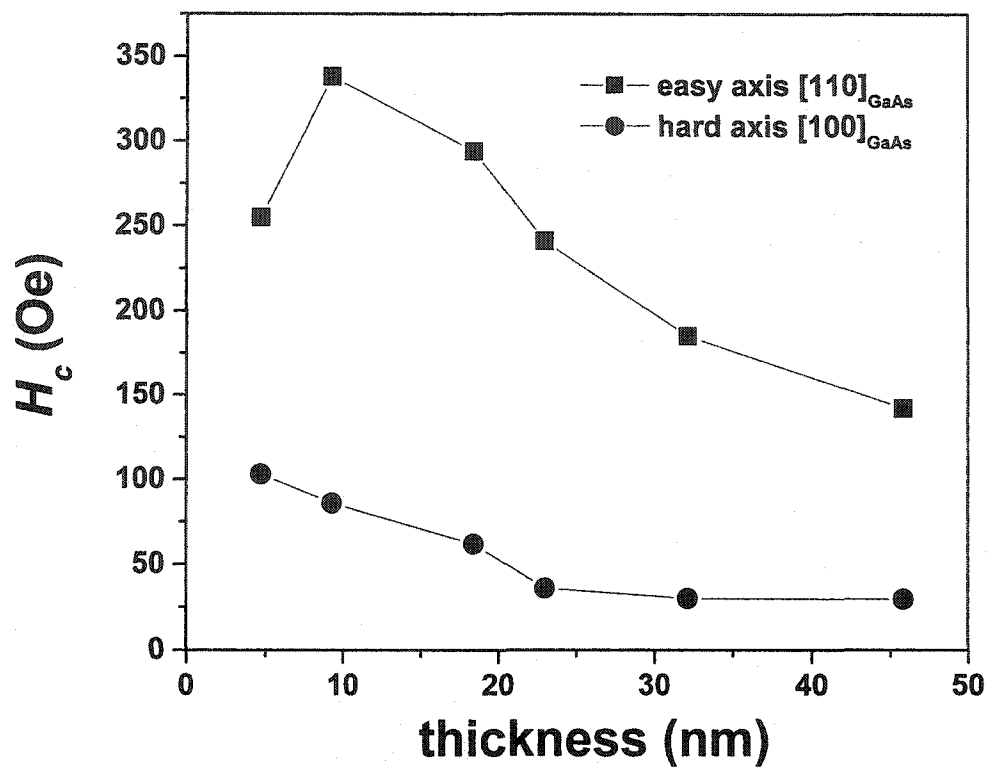


FIG. 97. Coercivity H_c as a function of FeNi layer thickness for two different orientations of the magnetic field as described in the text. The lines are guides to the eye.

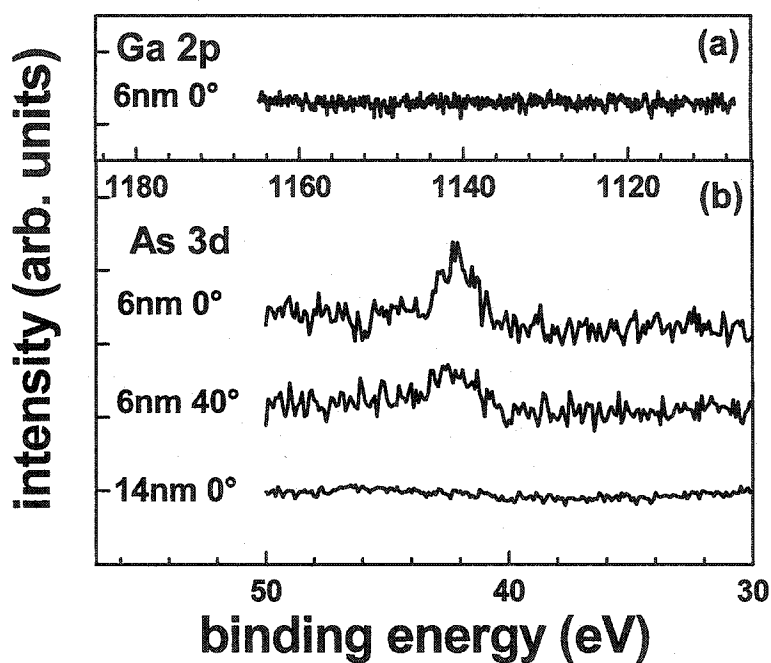


FIG. 98. (a) XPS spectra in the energy range of the Ga $2p$ peak measured on a 6 nm thick Ni layer. No Ga peak is observed. (b) XPS spectra in the energy range of the As $3d$ peak. The three spectra shown were measured on a 6 nm thick Ni layer and a 14 nm thick Ni layer, respectively. The two spectra of the 6 nm thick layer were measured at different detector angles as indicated.

of a Ga 2p peak rules out the possibility of Ga segregation on the Ni surface or of considerable diffusion of Ga into the Ni layer. Hence, Ga diffusion into the Ni layer is very small or altogether absent.

Figure 98 (b) shows the As 3d spectra collected respectively on a 6 nm and a 14 nm thick Ni film for two different electron detector angles ($\theta = 0^\circ$ and $\theta = 40^\circ$). The As 3d photoelectrons have a mfp of 2.22 nm.⁹⁴ The absence of an As peak for the 14 nm thick film rules out both As segregation to the Ni layer surface and major As diffusion into the bulk of the Ni layer. For the 6 nm thick Ni film ($T_{\text{Ni}} = 3 \times \text{mfp}$), however the As 3d peak is visible, the intensity of which decreases as the detector angle is increased to $\theta = 40^\circ$ from the surface normal. This allows for a longer escape distance for the photoelectrons and higher surface sensitivity. This shows that As diffusion into the Ni layer is, if present at all, limited to a very narrow region at the Ni/GaAs interface. The XPS data are essentially consistent with a complete absence of Ga or As diffusion into the Ni layers, with the small As signal in Fig. 98 (b) being due to As in the substrate.

b. Resistivity and magnetic analysis. Figure 99 shows a sketch of the Van Der Pauw resistivity four-probe configuration. As defined in L. J. van der Pauw theory, the resistivity of a flat sample of arbitrary shape can be written as⁹⁵

$$\rho = \frac{\pi T}{\ln 2} \frac{R_{AB,CD} + R_{BC,DA}}{2} \cdot f, \quad (20)$$

where T is the thickness of the sample, f is a factor which is a function only of the ratio $R_{AB,CD}/R_{BC,DA}$, as plotted in Fig. 100. Between the factor f in Eq. (20) and the ratio there exists the relation⁹⁵

$$\cosh\left[\frac{(R_{AB,CD}/R_{BC,DA}) - 1 \ln 2}{(R_{AB,CD}/R_{BC,DA}) + 1 f}\right] = \frac{1}{2} \exp\left(\frac{\ln 2}{f}\right), \quad (21)$$

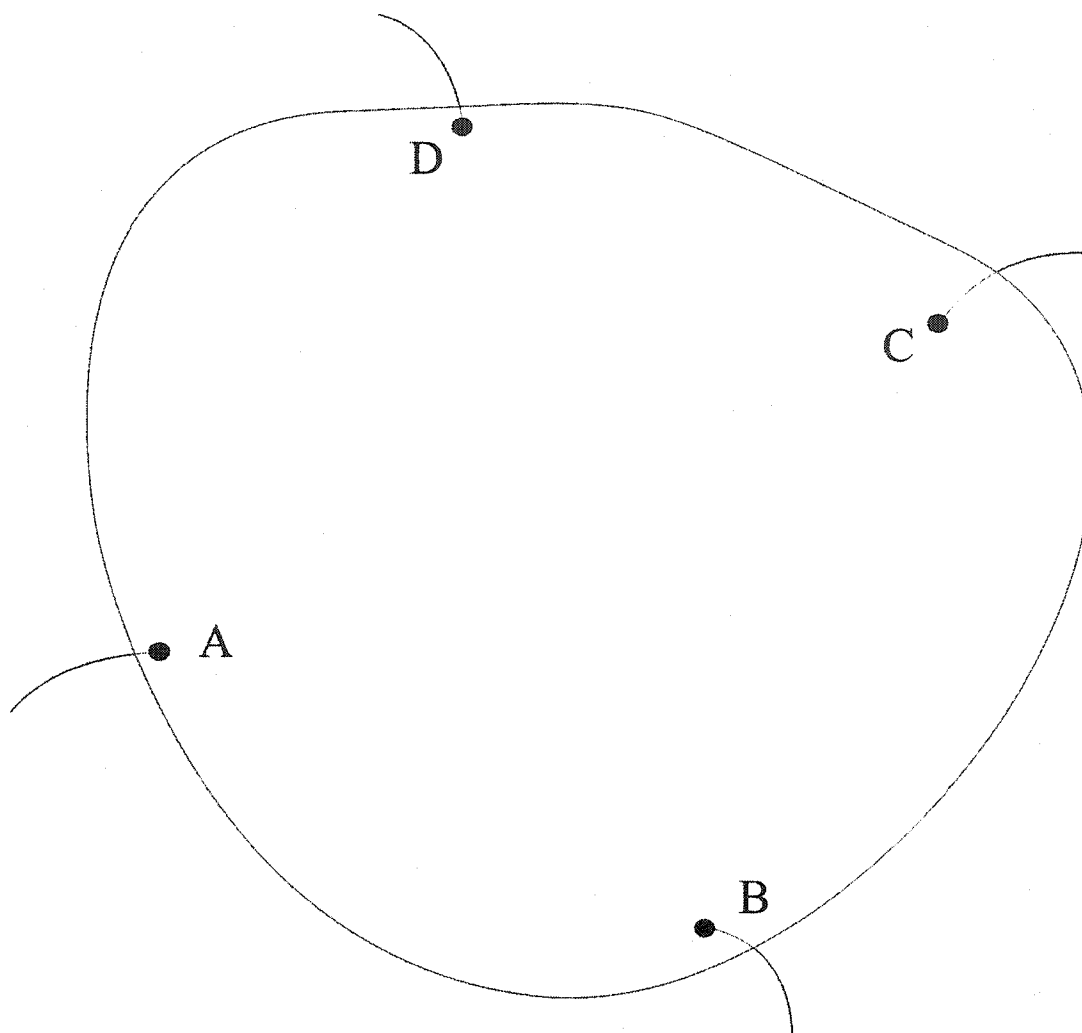


FIG. 99. Van der Pauw configuration for resistivity measurements. The first resistance is defined as $R_{AB,CD} = (V_D - V_C)/i_{AB}$, when a current i_{AB} is applied to contact A and take off at contact B while the potential difference is measured between contacts C and D.

Analogously, the second resistance is defined as $R_{BC,DA} = (V_A - V_D)/i_{BC}$. The resistivity is

then calculated from Eq. (20) as $\rho = \frac{\pi l}{\ln 2} \frac{R_{AB,CD} + R_{BC,DA}}{2} \cdot f$.

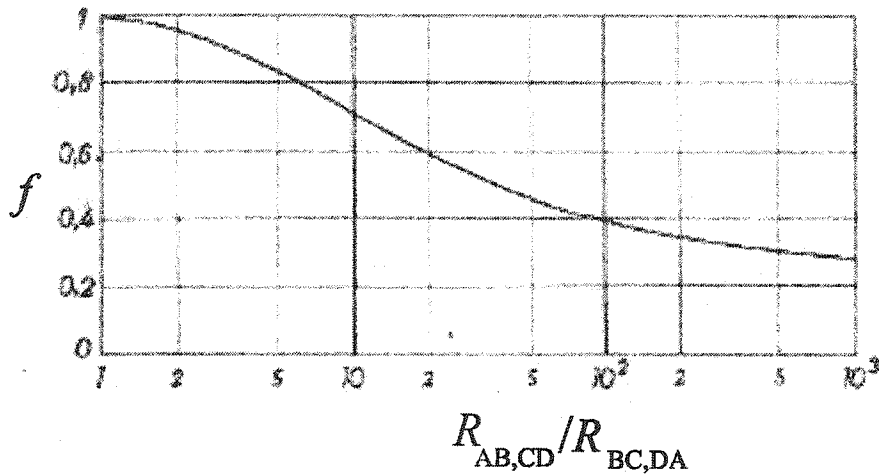


FIG. 100. Plot of the factor f from Eq. (21) which is a function only of the ratio $R_{AB,CD}/R_{BC,DA}$. The relation between f and the ratio is given by

$$\cosh\left[\frac{(R_{AB,CD}/R_{BC,DA}) - 1 \ln 2}{(R_{AB,CD}/R_{BC,DA}) + 1 f}\right] = \frac{1}{2} \exp\left(\frac{\ln 2}{f}\right).$$

thus to determine ρ , one first calculates the ratio $R_{AB,CD}/R_{BC,DA}$, then read from Fig. 100 the corresponding value of f and then evaluate ρ from Eq. (20).

Resistivity and magnetic measurements were made in order to verify the low level of intermixing. The saturation magnetization per unit area ($M_s \times T$) or per unit volume (M_s) was calculated from the sample dimensions and the saturation moment estimated from hysteresis loops.

Figure 101 (a) shows $M_s \times T$ as a function of Ni layer thickness compared against the line obtained assuming the Ni bulk value of $M_{\text{bulk}} = 484 \text{ emu/cm}^3$.⁹⁶ Although for the thinnest Ni films the poor signal to noise ratio of the corresponding hysteresis loops results in a rather large error in the estimation of M_s , the data suggest a 20% reduction in M_s (compared to bulk Ni) at around 5 nm Ni layer thickness [see inset of Fig. 101 (a)]. For thicknesses ≥ 10 nm, all films show bulk magnetic properties. The reduction in M_s at small thickness can be ascribed to experimental error or to reduced Ni moments at the Ni/GaAs or the Ni/Ni(OH)₂ interfaces.

The product of resistivity times thickness as a function of Ni layer thickness is shown in Fig. 101 (b). This plot follows approximately a straight line, in agreement with the prediction of Fuchs' theory⁹⁷ which gives the resistivity as

$$\rho(T) = \rho_{\infty} + \frac{3(1-p)(\rho_{\infty} \cdot l_{\infty})}{8T} \quad (22)$$

with bulk resistivity ρ_{∞} , bulk mfp l_{∞} , and reflectivity coefficient p . The slope of this straight line yields $\rho_{\infty} = 12.8 \mu\Omega\text{cm}$, which is higher than the bulk value for Ni ($6.8 \mu\Omega\text{cm}$) possibly due to impurities. A small deviation however is visible around $T = 5$ nm [see inset of Fig. 101 (b)]. Fuchs' theory, although quite successful in describing

experimental data of the thickness dependence of the resistivity,⁹⁸ is based on rather simple assumptions and deviations from it should not be too surprising. Simple film thickness fluctuations for example are known to lead to an increased resistivity at low thicknesses.⁹⁹

In comparison, Fe layers grown on GaAs by molecular beam epitaxy (MBE) typically show strong diffusion of As and, to a lesser extent, Ga.^{13,76,100,101} Only Fe deposition at room temperature on specially prepared, As depleted $p(4 \times 6)$ reconstructed, surfaces ensured good magnetic properties,^{14,15} although surface segregation of As was still observed.¹⁴ For Ni grown on semiconductor surfaces, a strong interfacial reaction was observed with GaAs(001) substrates,¹⁰² while Se interdiffusion accompanied by a strong reduction of the magnetization was reported for Ni on ZnSe.¹¹

In the present electrodeposited Ni films, the slight increase of resistivity in combination with the reduction in M_s for the thinnest films might hint at a limited intermixing at the Ni/GaAs(001) interface. In combination with the XPS data, which do not show diffusion of As or Ga into the Ni layer, this rather suggests that electrodeposition is capable of producing chemically sharp FM/semiconductor interfaces without requiring special surface preparation. In addition, electrodeposition of Ni on GaAs(001) yields epitaxial growth of fcc Ni,²¹⁻²⁴ which is hard to achieve using MBE.^{87,102}

In order to investigate qualitatively the Ni/GaAs interface, transmission electron microscope (TEM) cross-section analysis was performed on a 9.5 nm thick Ni film on GaAs(001).

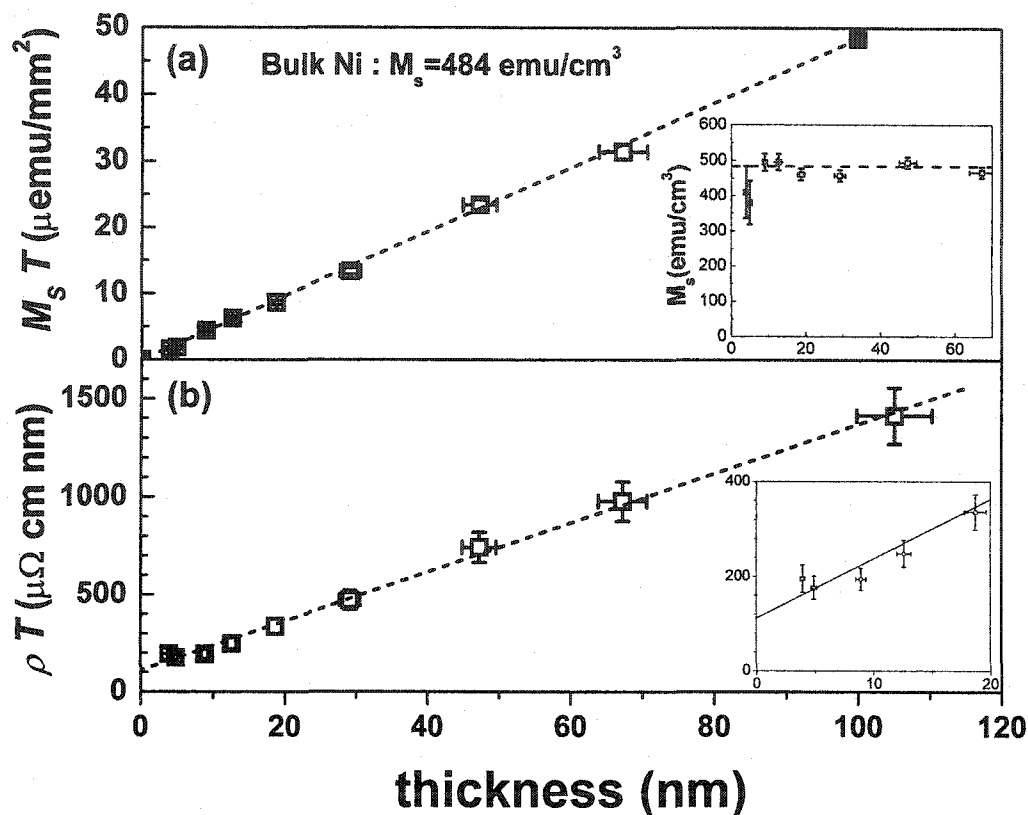


FIG. 101. (a) Saturation magnetization per unit area $M_s \times T$ of Ni films as a function of layer thickness (data points). The dashed line corresponds to the values expected for bulk Ni. The insert shows the saturation magnetization M_s , which reveals a small deviation from the bulk properties (dashed line) for the thinnest films. (b) Room-temperature resistivity times layer thickness as a function of Ni layer thickness (data points). The straight line is a linear fit to the experimental data according to Fuchs' model. The insert shows a magnification of (b) in the thickness range 0–20 nm.

The TEM cross section image shown in Fig. 102 reveals three defined regions delimited by white lines, which were drawn as a guide to the eye. These regions can be attributed respectively, from bottom to top, to the GaAs(001) substrate, an amorphous Ni layer (Ni_{amor}), and the crystalline Ni film (Ni_{crys}). The interface $\text{Ni}_{\text{amor}}/\text{GaAs}$ is sharp and well defined whereas $\text{Ni}_{\text{amor}}/\text{Ni}_{\text{crys}}$ is unclear. It is unrealistic for an amorphous layer to evolve into a crystalline layer such as here since epitaxial Ni film is expected to grow on GaAs(001). Therefore, the presence of Ni_{amor} layer has been most likely influenced by the critical sample preparation for TEM analysis. Indeed, the delicate thinning process in TEM sample preparation for cross-section analysis requires ion-milling step to create a transparent area with a centered hole in the specimen. This process among other initial polishing manipulation can alter the sample structure.

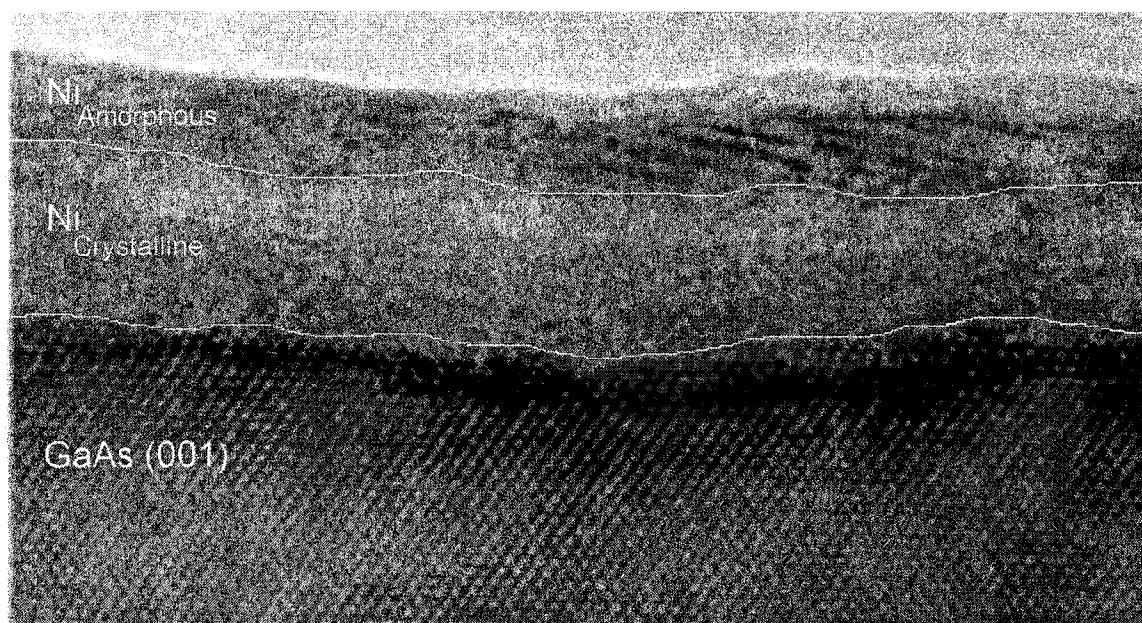


FIG. 102. Transmission electron microscope (TEM) cross section picture of a Ni film grown on GaAs(001).

c. I-V Schottky characterization. In order to understand the relationship between the Ni/GaAs interface property and the Schottky electrical properties, $I-V$ Schottky measurements along with XPS analysis after different annealing temperatures have been applied. The substrates were single crystalline, epi-ready, n -doped (carrier concentration $2 \times 10^{17} \text{ cm}^{-3}$, resistivity $0.005 \text{ } \Omega\text{-cm}$) GaAs(001). Prior to deposition, for later $I-V$ measurements, two ohmic back contacts were prepared by sputtering a Ni (25 nm)/Ti (75 nm) double layer followed by a 20 min annealing process at $450 \text{ }^\circ\text{C}$.¹⁰³ The electrodeposition ($J = 3.5 \text{ mA/cm}^2$) was carried out at RT. The area of deposition on the substrate for $I-V$ Schottky measurements was approximately 0.3 cm^2 . The thicknesses of the deposited films were 9.5 nm and 200 nm for the XPS analysis and $I-V$ electrical measurements, respectively. $I-V$ Schottky diode characterization was performed first at RT using a 3-point probe technique (separate current and voltage contacts on the semiconductor side and one common current/voltage contact on the metal side). $I-V$ measurements were made on successively vacuum-annealed ($< 10^{-6} \text{ Torr}$) samples while chemical analysis on in-situ annealed samples was done using XPS.

Schottky diode barrier heights were estimated from $I-V$ curves ($V = -0.4$ to 0.3 V) assuming thermionic-emission model for the rectifying current density, which reads¹⁰⁴

$$J(V, T) = J_0 e^{(qV/nk_B T)} [1 - e^{(-qV/k_B T)}], \text{ where}$$

$$J_0(T) = J(0, T) = A^{**} T^2 e^{(-q\Phi_{e0}/k_B T)} \quad (23)$$

with the electron charge q (eV), the ideality factor n , the Boltzmann's constant k_B , the sample temperature T (K), the bias potential across the diode V (V), the effective Richardson constant A^{**} ($4.4 \times 10^4 \text{ A/m}^2\text{k}^2$ for GaAs¹⁰⁵) and the zero bias diode barrier

height Φ_{e0} (eV). I - V characteristics for different annealing temperatures are shown in the inset of Fig. 103. However, in order to determine Φ_{e0} and n , Eq. (23) can be rewritten as

$$\ln\left[\frac{J}{1 - e^{(-qV/k_B T)}}\right] = C_1(\Phi_{e0}) + C_2(n) \cdot V \quad (24)$$

with C_1 and C_2 two constants respectively function of the barrier height and the ideality factor. As shown in Fig. 103, Φ_{e0} and n can easily be determined for different annealing temperatures by respectively taking the intercept and the slope of the corresponding straight lines described by Eq. (22).

Figure 104 shows the barrier height determined from Schottky barrier I - V measurements of a 200 nm thick Ni film on GaAs(001) and corresponding XPS As 3*d* peak intensity (for a 9.5 nm thick Ni film) for different annealing temperature. An increase in the Ni/GaAs barrier height is observed starting at around 200 °C to drastically intensify at and above 250 °C. The barrier height is found to be 0.765 eV up to an annealing temperature of 200 °C (as compared to 0.77 eV in previous work^{106,107}) and increases to 0.805 eV at 250 °C. Likewise, the As 3*d* (as well as Ga 2*p*) XPS peak height signal intensity, which reflects an increased degree of intermixing (not present at RT), shows a similar trend as shown in Fig. 98. Data from AFM analysis exhibited no exposure of the GaAs surface. In addition, as shown in Fig. 105, RMS roughness decreases from 2.5 nm (RT) to 1 nm (300 °C) with increasing annealing temperature. Therefore, the increase of As 3*d* XPS signal does not come from the exposed GaAs surface. Therefore, the increase of barrier height can be correlated to the level of

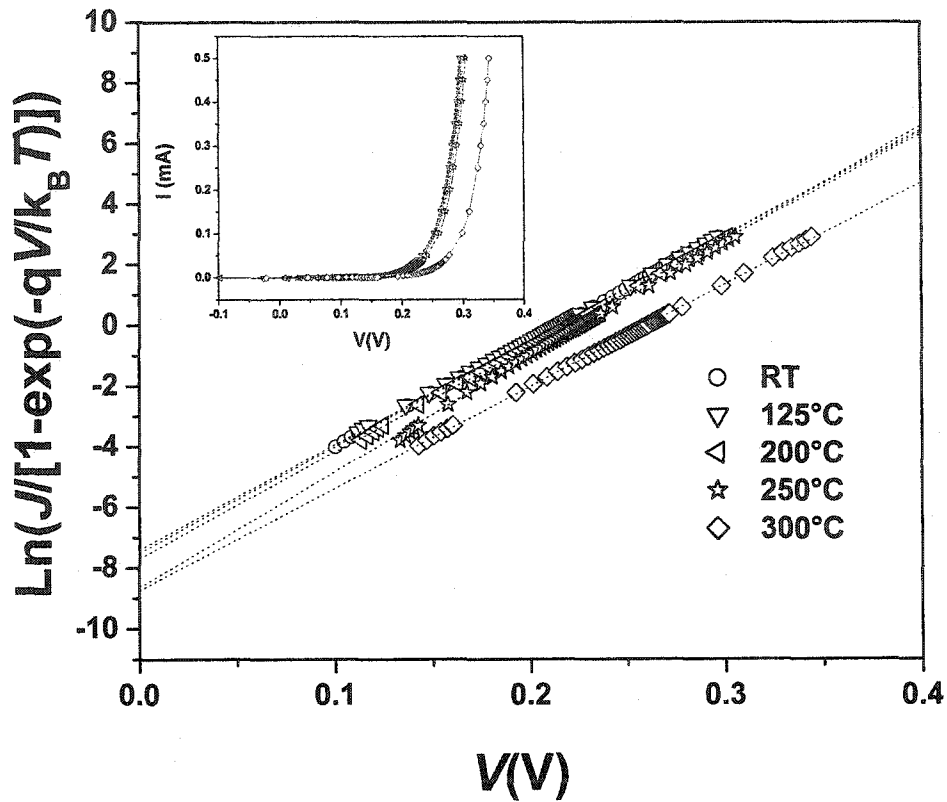


FIG. 103. Graph allowing the extraction of both ideality factor and barrier height according to Eq. (24). The insert shows the current versus bias voltage characteristics for different annealing temperatures as indicated in the graph

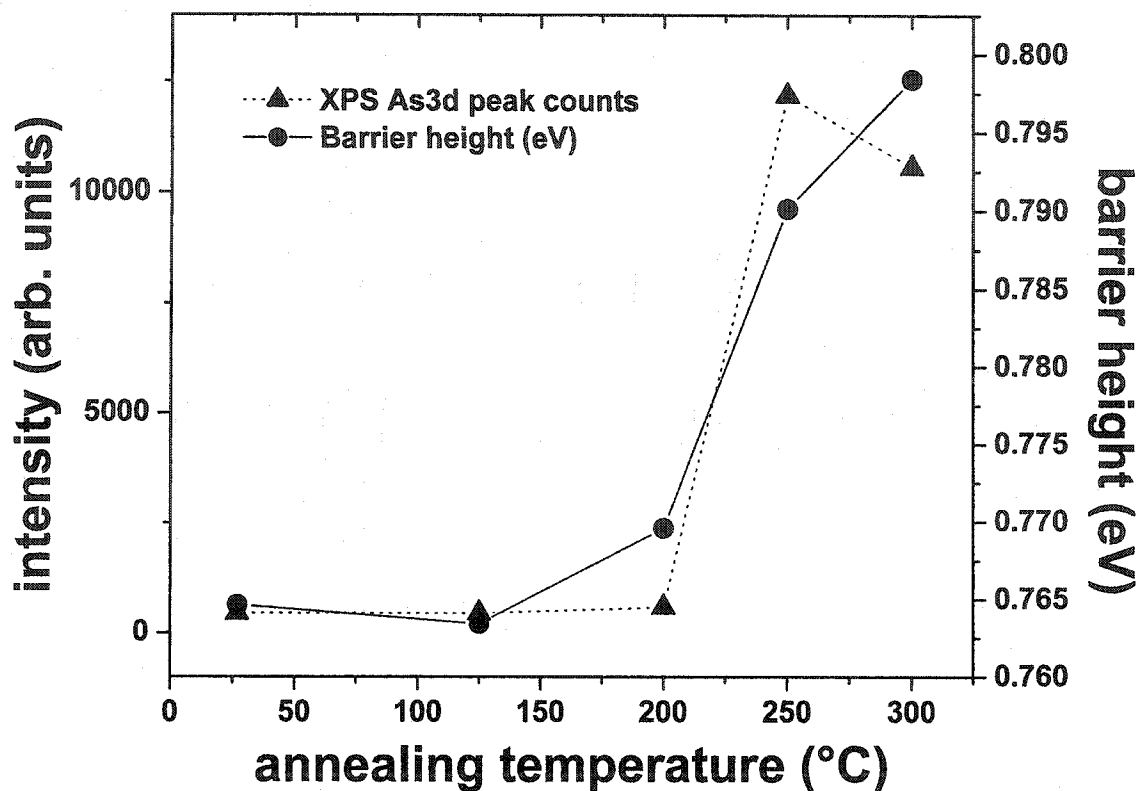


FIG. 104. Barrier height (determined from Schottky barrier I - V measurements) of a 200 nm Ni film on GaAs(001) and corresponding XPS As 3d peak intensity (for a 9.5 nm thick Ni film) for different annealing temperatures.

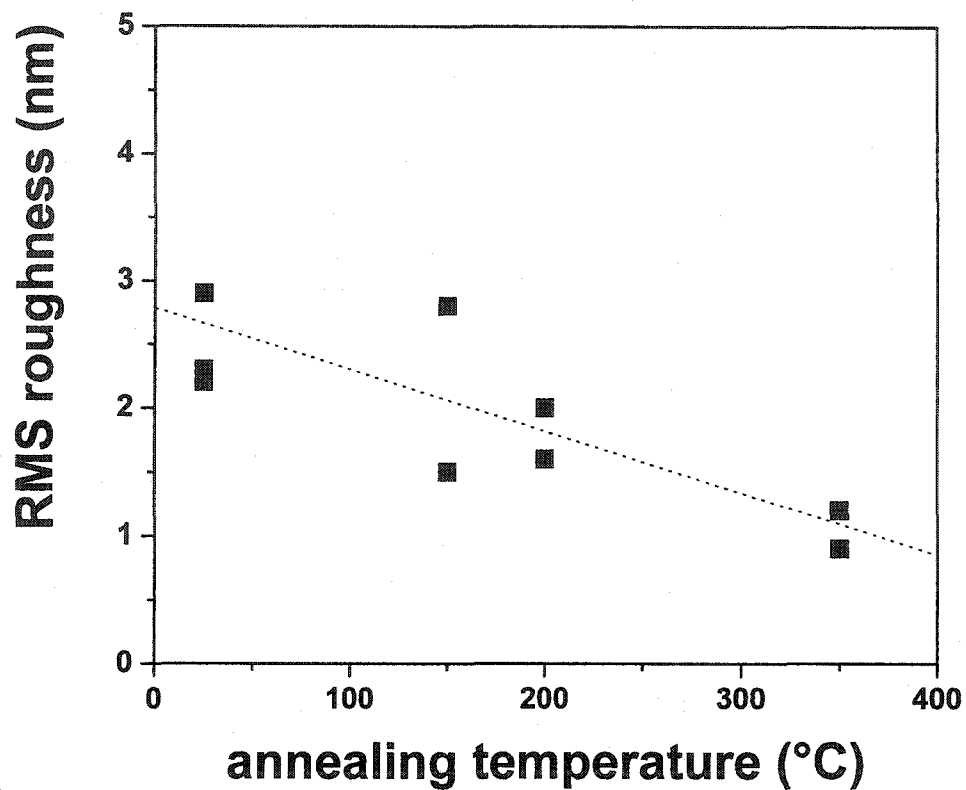


FIG. 105. Temperature dependence of the RMS roughness of a 200 nm Ni film grown on GaAs(001). For each temperature, roughness analysis was made at different area of the surface of the film using a AFM scanning probe. The dashed line is a guide to the eye.

intermixing at the interface. The ideality factor of the formed diode Ni/GaAs used in these barrier height measurements is estimated to be between 1.03 and 1.14. Interfacial diffusion between Ni and GaAs can lead to atomic mixtures and/or formation of Ni–Ga–As phases of a few monolayers at the interface.¹⁰² Modifications of the band structures and/or the Ni–Ga–As phase at the interface are the possible reasons for the increase of the barrier height related.

Further future work related to temperature dependence (<300 K) I - V Schottky diode characterization though needs to be considered on these films in order to investigate the electrical transport mechanism and examine the validity of thermionic-emission model assumption in the evaluation of the barrier height.

Nevertheless, these results are promising for future spintronic experiments such as spin-injection from a metal into a semiconductor. More recent work showed that spin-injection using MBE grown Fe layers on AlGaAs lead to encouraging results.¹⁶

D. Conclusion

High quality epitaxial Ni from NiSO₄ electrolyte, mixed hcp/fcc phases of Co with in-plane registry with the substrate from CoSO₄ electrolyte and high quality epitaxial Fe films from FeSO₄ and FeCl₂ electrolytes growth on GaAs(001) and GaAs(011) substrates using RT electrodeposition have been demonstrated in the present work.

The crystalline structure of partially epitaxial Ni films on GaAs(001) using electrodeposition is characterized by a mixture of two phases (Ni(001)[100]//GaAs(001)[110] and Ni(011)[111]//GaAs(001)[110]), dominantly (001),

and rather wide rocking curves. It is interesting to notice that electrodeposition of Ni on GaAs(001) yields epitaxial growth of fcc Ni, which is hard to achieve using MBE. The quality of the epitaxy of these films is not comparable to the structural quality of MBE grown Fe layers on GaAs. To some extent, this might be caused by the rather large lattice misfit between Ni and GaAs (12%) giving no orientation a clear preference above others. The magnetic properties show a clear anisotropy for the intermediate thickness range with contributions from crystalline components and uniaxial anisotropy leading to a mixed two- and four-fold symmetry, with the easy axis in-plane for all thicknesses. The saturation magnetic moment increases linearly with thickness indicating limited interface intermixing between substrate and film due to the low-energy electrodeposition process. The exact value of the pH of the electrolytic Ni solution is very important in determining the film magnetic properties. Films grown at lower pH (2.25) have similar magnetic properties whereas for higher pH (2.7) the four-fold in-plane anisotropy disappears and only a more pronounced uniaxial anisotropy remains.

Electrodeposited Ni films do not show outdiffusion of As or Ga at RT. This suggests that electrodeposition is capable of producing excellent epitaxial sharp FM/semiconductor interfaces without requiring special surface preparation for further spin-electronics applications. The sharpness of Ni/GaAs(001) interface (i.e. no intermixing) up to 200 °C along with a clear deterioration at higher annealing temperatures have been demonstrated. The increasing degree of intermixing causes the diode barrier height to increase above 250 °C. Co films grow on GaAs(001) with a mixture of fcc and hcp phases, which are difficult to discriminate with XRD. The films show a weak four-fold magnetic anisotropy which disappears with increasing thickness.

Fe films grow on GaAs(001) following the epitaxial relationship Fe(001)[100]//GaAs(001)[100], which is in agreement with the structure of epitaxial Fe layers grown by MBE. Fe films of better crystalline quality electrolytes were produced using FeSO₄, and films show weak but discernable crystalline anisotropy. No further characterization could be done since the growth of thin homogenous Fe films is difficult to achieve at the moment, preventing thickness calibration, resistivity measurement, XPS analysis, etc.

Unlike GaAs(001) substrate, metallic films (Ni, Fe, Co, Fe_xNi_{1-x}) grown on GaAs(011) showed a well defined uniaxial anisotropy with square hysteresis loops for a wide range especially for Co. Ni films were found to grow following the epitaxial relationship Ni(111)[110]//GaAs(011)[110] and exhibited a clear uniaxial magnetic anisotropy with easy axis along GaAs[100]. Ni films less than 20 nm show an anisotropy field H_k larger than would be expected for pure crystalline anisotropy. Co films grow with a mixture of fcc and hcp phases, which is difficult to discriminate with XRD; however, in-plane registry could be identified, whereas Fe_xNi_{1-x} epitaxial growth could not be confirmed with XRD. The uniaxial magnetic anisotropy for Co, Fe and Fe_xNi_{1-x} films was found with the easy axis along GaAs[110], which is opposite to Ni (i.e. easy axis along GaAs[100]). Fe films grow with the epitaxial relationship Fe(011)[100]//GaAs(011)[100], which is in agreement with the structure of epitaxial Fe layers grown by MBE. Unlike on GaAs(001), those Fe films have a significant substrate induced uniaxial anisotropy.

It has been demonstrated that electrodeposition technique can produce very high quality epitaxial metallic films onto GaAs(001)/(011) substrates with desirable

magnetic/electrical properties (uniaxial anisotropy, etc). Furthermore, Ni films grown on GaAs(001) show sharp metal/semiconductor interface with no intermixing. Thus, it is suggested that electrodeposition might be conceived as a practical, inexpensive, and alternative technique in the production of prospective spin-electronic devices.

III. SELECTIVE DEPOSITION OF METALLIC FILMS ONTO SEMICONDUCTOR SUBSTRATES

A. Photoinduced electrochemical deposition of Cu on *p*-type Si substrates

Spontaneous Cu reduction on Si is possible because E_{redox} of Cu^{2+}/Cu is close to the top of the valence band of *p*-Si, as schematically shown in the band diagram in Fig. 106 (a), which facilitates spontaneous deposition. The possibility of *selectively* depositing Cu on Si by laser illumination is thus related to the capability to avoid spontaneous Cu reduction, for example, by a suitable choice of the Cu solution. As shown in Fig. 106, laser illumination generates a large increase of the electron density from the valence band (VB) to the conduction band (CB) which, facilitated by the band bending, diffuses towards the surface and locally enable deposition.

In this work, experimental results to elucidate the electroless growth of Cu structures from CuSO_4 based solutions on *p*-Si upon laser illumination are presented. The dependence of the structure dimensions on duration, intensity, and wavelength of the illumination and on the carrier lifetime in the *p*-Si semiconductor substrate is demonstrated. The effect of spontaneous background plating is studied as a function of the composition of the plating solution.

1. Experiment

Copper deposition was carried out on *B*-doped *p*-type Si with a resistivity of 5–25 Ω cm. The variation of open circuit potential (OCP) with time upon surface illumination

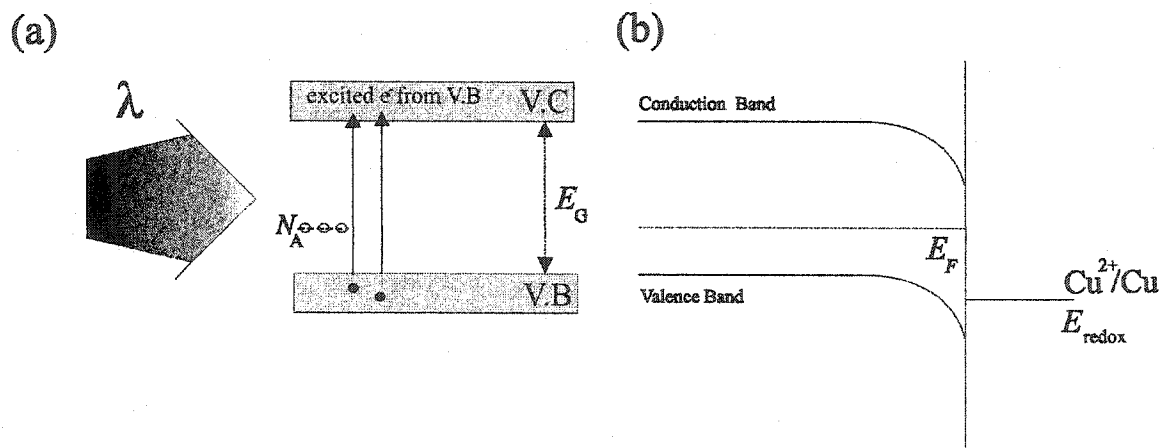


FIG. 106. Sketch of (a) the principle of photoinduced deposition on a *p*-type semiconductor and (b) schematic band diagram of *p*-Si in aqueous solution before contact.

was measured on the above-mentioned *p*-type as well as on *n*-type Si with a resistivity of 0.01–0.025 Ω cm. In order to vary the carrier recombination rates, defects were introduced in the near-surface region of some Si substrates by ion irradiation, using 180-keV P ions with a dose 2×10^{13} cm⁻². This process generates an implantation region in the interior of the Si substrates (average implantation depth is about 250 nm) and leaves behind implantation damage near the surface. No subsequent annealing was applied in order to avoid activation of the implanted P and to maintain the irradiation damage.

Before deposition, the native oxide on the Si substrates was removed by immersion in a 10% HF solution for 1 min; the substrates were subsequently rinsed in deionized water (DW) for 30 sec. All the solutions described here and in the following were prepared using DW with resistivity 18 M Ω cm. The above surface preparation steps proved to be photosensitive and to have an influence on the subsequent photoinduced plating; consequently, they were always performed in a dark environment. The substrate was immersed into the plating solution in less than 1 min after having been removed from the DW.

The standard electrolyte for copper deposition contained 0.1 mol/L CuSO₄, 0.02 mol/L NH₄F, 0.01 mol/L ascorbic acid, and 0.005 mol/L sodium potassium tartrate (SPT).⁴² The pH value of the solution was around 2.7. Other electrolyte formulations were also used, as specified in the text.

The deposition was carried out in a thin layer cell, maintaining a distance between the substrate and the surface of the solution of about 2 mm. The solution was at room temperature; it was estimated that laser illumination caused a negligible increase in the solution temperature. An optical microscope was used to focus a laser beam onto the

surface of the Si wafer, which was submerged in the electrolytic solution. Deposition took place spontaneously on the illuminated region, thus no electrodes or external voltages were used. Two diode lasers were used as sources of the focused light beams. One laser generates red laser light at the wavelength λ of 660–680 nm with an intensity of about 1 mW and the other produces green laser light at the wavelength of 532 nm with an intensity of about 5 mW. A 150-mW argon ion laser was used to illuminate *n*-Si and *p*-Si surfaces to compare their OCP's. An Olympus BH-2 optical microscope was used to focus the laser beam, entering through one of the eye pieces, to 1–2 μm spot size on the SC surface as shown in Fig. 107. The sample was observed and the focal spot was adjusted by looking through the other eye piece. After illumination, the substrate was removed from the solution, rinsed with DW within 1 min, and successively dried. The Olympus microscope was equipped with a polaroid DMC-1 digital microscope camera, which was used to take digital images of the sample thus obtained. The structure sizes were determined by these high-resolution digital photos, with an error of less than 1 μm .

A polarizing filter allowed to vary the laser beam intensity. It is noted here that high or low intensities in the following are only relative to a given wavelength, and should not be used for cross-wavelength comparison. The green laser beam does have a higher intensity than the red laser beam. Thickness and surface morphology of the deposited Cu features were measured using the tapping mode AFM. Some AFM tips were etched with H_2O_2 followed by DW rinsing to reduce the sensitivity to the surface roughness for thickness measurements. In roughness measurements, tips were used as received. The profilometer was used to make scratches/indentations on the Cu surface, which were used for thickness measurements.

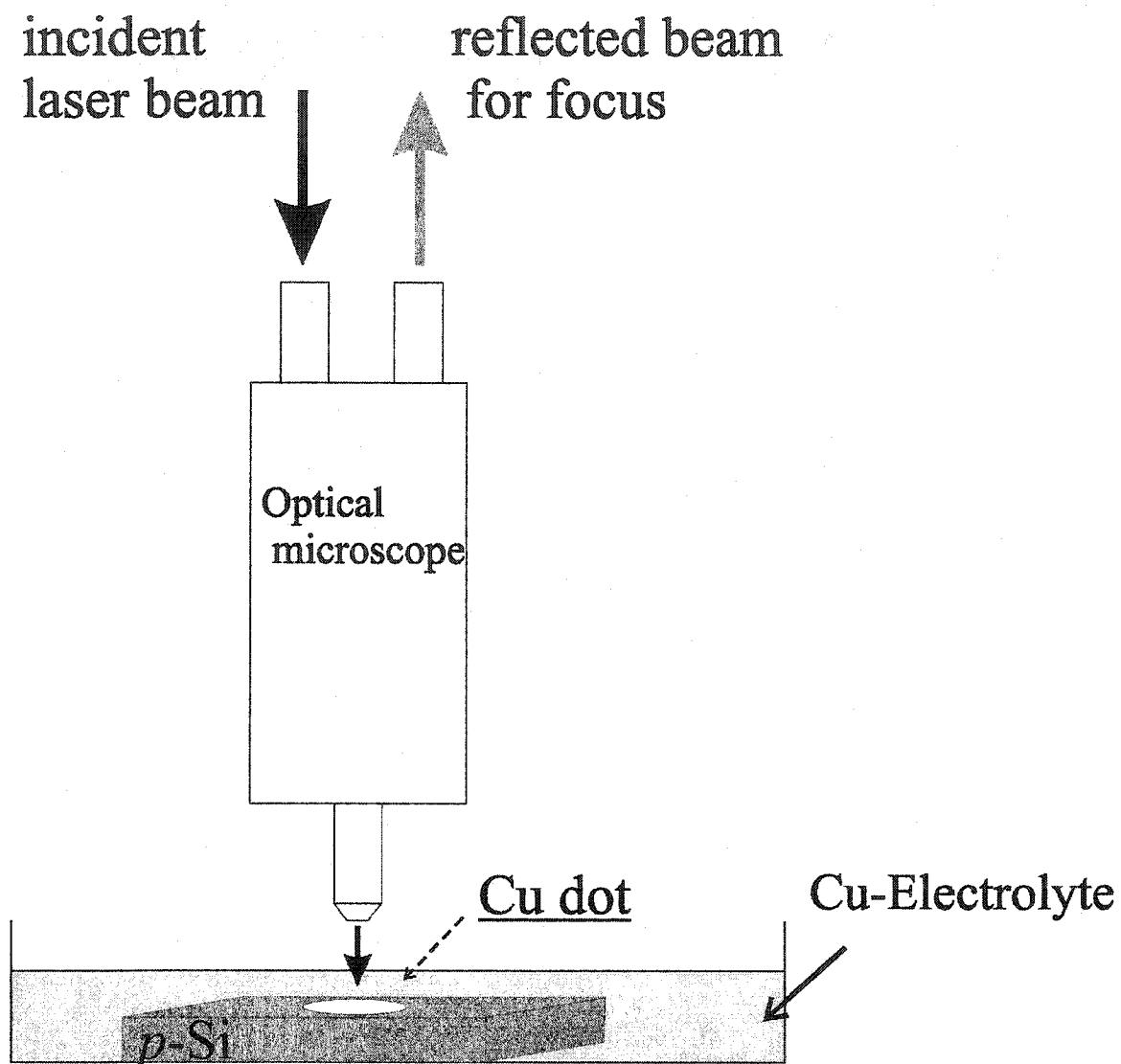


FIG. 107. Experimental set up for photoinduced electrodeposition of Cu on *p*-Si substrate.

2. Results and discussion

a. Open circuit potential of Si in the electrolyte. The effect of laser illumination on the OCP for *n*- and *p*-Si in the standard copper solution, measured against a saturated calomel electrode (SCE), is shown in Fig. 108. In the dark, both types of substrates are cathodic with respect to SCE, with the *p*-Si being nobler than *n*-Si. Upon illumination of the substrate with a 2-mm laser spot, the OCP of the *p*-Si increases significantly, while only a small change is noted in the OCP of *n*-Si, which becomes slightly more negative. These trends are the result of the trapping of minority carriers in the surface states. The extent of the effect depends on the resistivity of Si and the minority carrier lifetime.⁴⁵ However, the comparison between *n*- and *p*-type Si is only qualitative in their opposite signs of OCP upon illumination since specific doping concentration affects the quantitative values. Upon removal of the substrate from the solution, Cu deposition in the region illuminated by the laser spot is observed on the *p*-Si, while no Cu is visible by the naked eye on the *n*-Si. Deposition on *p*-Si is inhibited without illumination because of its small electron density. Illumination by the laser generates a large relative increase of the minority carrier (electron) density, which will diffuse towards the surface and locally enable deposition.

b. Morphological features of the dots. Optical images (top view) of two typical deposited features using red laser light are shown in Fig. 109 (a) (60 s of illumination) and Fig. 109 (b) (5 s of illumination). The Cu dots which appear shiny to the naked eye have an inner bright circular area with a diameter D_i and a dark ring that contributes to the outer (or total) diameter D_o as shown in Fig. 109 (a).

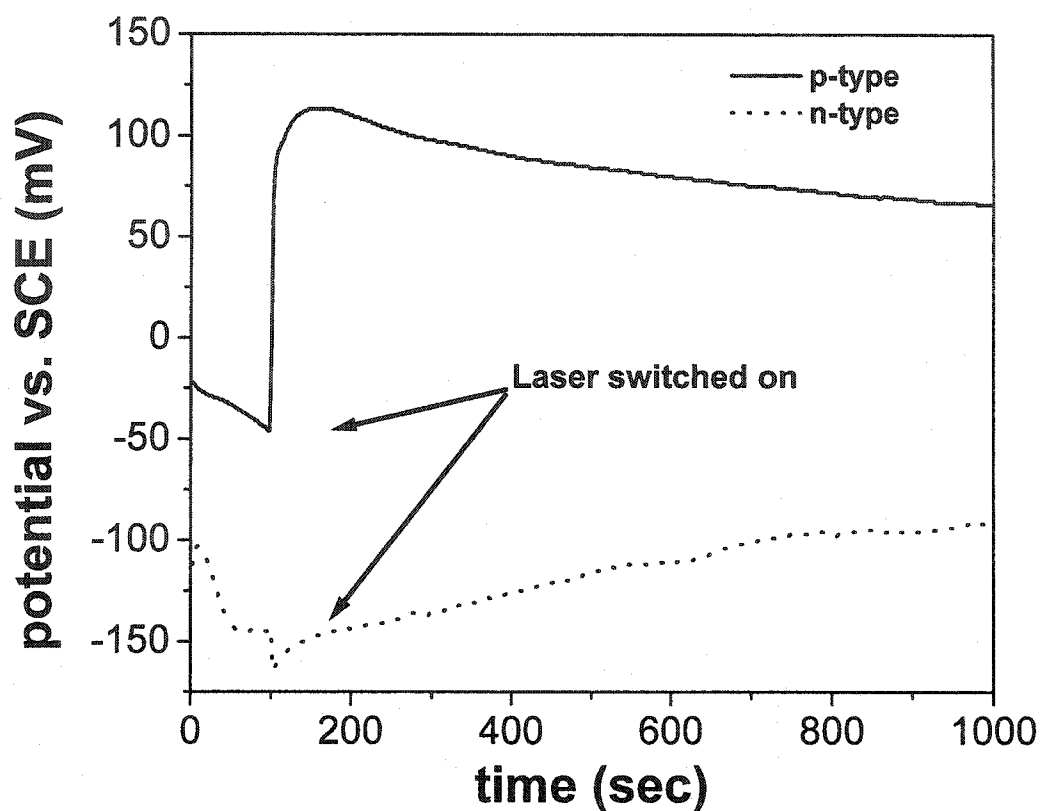


FIG. 108. The open cell potential, measured against a SCE of *n*-Si and *p*-Si in the CuSO_4 solution used for deposition. Electrical contact is made to the back of the Si substrate using Ga-In eutectic. The laser is switched on after 100 s and it illuminates an area $\sim 4 \text{ mm}^2$. These are the original data without any shifting of the curves and show the qualitative trend of the opposite OCP signs of *n*- and *p*-type Si upon illumination.

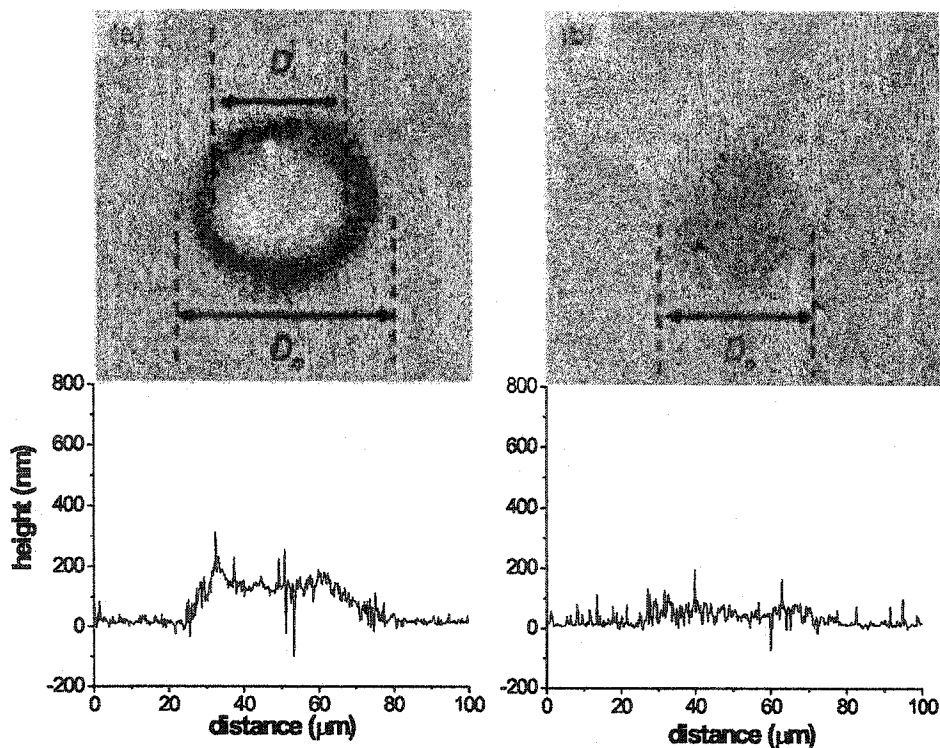


FIG. 109. Optical images ($100 \times 100 \mu\text{m}^2$ area) and AFM cross-section profiles of two typical Cu dots formed by illuminating *p*-Si with a $\sim 1\text{--}2 \mu\text{m}$ diameter laser spot. (a) An optical image for the dot formed after 60 s of red laser illumination. (b) An optical image for the dot formed after 5 s of red laser illumination. (c) AFM cross-section profile for the dot in (a). (d) AFM cross-section profile for the dot in (b). There is a dark ring surrounding the inner shiny area as shown (c). Inside the dark ring, islands of Cu clusters with Cu metallic color are identified using both a high magnification lens and an AFM. For the dark Cu spot, no distinct inner area can be differentiated and the diameter is represented by D_o only, as shown in (d).

The bright area appears continuous under the optical microscope. The dark ring on the other hand consists of separated islands, as revealed by AFM images. When plating for short times the dots appear entirely dark [Fig. 109 (b)], without any shiny area visible. The isolated submicrometer sized Cu islands in the dark ring of shiny dots or in the entire area of dark dots are indeed grown by the laser-induced electrodeposition. However, their individual positions and sizes cannot be controlled selectively, thus these deposition conditions cannot be used as a reliable method to grow nanometer scale islands. The relation between optical appearance and surface morphology is discussed further in Sec. III D.

AFM cross-sectional profiles of the islands imaged in Figs. 109 (a) and 109 (b) are shown in Figs. 109 (c) and 109 (d), respectively. It is noticed that the dark ring coincides with the sloped area at the edge of the Cu dot as shown in Fig. 109 (c).

The dot diameters typically exceed the diameter of the original laser spot size by about one order of magnitude. The origin of this phenomenon is addressed in the following section.

c. Structure dimensions. The size of the copper features will generally depend on the diffusion length of the photoexcited minority electrons, i.e., the mean distance they can diffuse away from the location of their generation before being annihilated, either through Cu ion reduction or carrier recombination. In this section we discuss the observed structure sizes as a function of illumination time, beam intensity, and wavelength, and Si substrate preparation. The thicknesses of the dots estimated from the AFM profiles shown in Figs. 109 (c) and 109 (d) are about 100 nm and 50 nm, respectively. Using this technique, it is observed that the thickness of the deposited

features reaches 100 ± 20 nm after 10 sec of laser illumination and does not further increase thereafter. The growth in the vertical direction is, obviously, limited by the transmission of light through the growing Cu film.

The average D_o (deposition time up to 60 s), as a function of the laser wavelength/intensity and substrate preparation, is shown in Fig. 109. It is not surprising that the dot diameter depends only slightly on illumination duration (an increase is observed up to 15–20 s) since the diameter of the dots is determined mostly by the electron diffusion in the sub-surface region of the substrate. The average D_i (not shown here) follows the same trend.

First, it is important to notice that the size of the copper features typically exceeds the diameter of the original laser spot size ($1\text{--}2 \mu\text{m}$) by about one order of magnitude. Second, this size appears to be much smaller than the diffusion length, i.e., the mean distance photoexcited minority electrons can diffuse from where they are generated before being annihilated, either through carrier recombination or reduction of Cu ions.

The charge carrier diffusion length l in bulk Si is given by $l \equiv (D\tau)^{1/2}$, where D and τ are the diffusion coefficient and the minority carrier lifetime in the SC.⁴⁵ D is defined as $\mu k_B T / e$, where μ is the charge-carrier mobility, k_B is the Boltzmann's constant, T is the temperature, and e is the electron charge.⁴⁵ Since μ for p -Si with the resistivity range used in this work is around $450 \text{ cm}^2 \text{ V}^{-1} \text{ s}^{-1}$,¹⁰⁸ $T \approx 300 \text{ }^\circ\text{K}$ and τ is in the millisecond range, say 0.4 ms .⁴⁵ D and l are thus estimated to be $11.6 \text{ cm}^2 \text{ s}^{-1}$ and $680 \mu\text{m}$, respectively. The observed dot diameters are much smaller than the diffusion length thus determined; consequently, other contributions tend to limit electron diffusion. First, the electron consumption due to the plating process must be taken into account. Eriksson *et*

al. have shown that this effect can significantly decrease the deposited spot diameter. Second, band bending effects (schematically shown in Fig. 106) will accelerate electrons towards the surface and thus “collimate” the electron flux rather than allowing a free diffusive spreading of the electrons. Once at the surface, the electrons typically experience a higher recombination rate due to the larger defect density there. Additionally, electron diffusion along the surface will be slow due to trapping centers reducing the mobility. This all will contribute to the observed reduction in dot diameter. Possibilities to further reduce the structure sizes would be to reduce the penetration depth of the laser light,^{37,109} and to reduce the carrier life time τ .

A reduction of the light penetration depth would generate the carriers, on the average, closer to the surface. Following the field generated in the band bending region, they would reach the surface faster, thus reducing the lateral spread through diffusion. The photon flux at a depth d beneath the illuminated SC surface is $\Phi(d) = \Phi_0 e^{-\alpha d}$, where α is the (wavelength dependent) absorption coefficient and Φ_0 is the incident photon flux at the SC surface.¹⁰⁸ Therefore, the penetration depth can be characterized by $1/\alpha$.⁴⁵ For the red (green) laser light used here, the photon energy E_p is 1.88 eV (2.33 eV) yielding an absorption coefficient of 3000 cm^{-1} ($11\,000 \text{ cm}^{-1}$).^{108,110} The resulting penetration depth is then estimated to be $3.3 \mu\text{m}$ for the red laser beam and $0.9 \mu\text{m}$ for the green laser beam. The effect of the reduced penetration depth on dot size is demonstrated in Figs. 110 (a) and 110 (b) by comparison of dot diameters produced using red laser light with those produced by excitation with green laser light. The dot diameters obtained by illumination with red laser light are typically about 50% larger than those produced using green laser light.

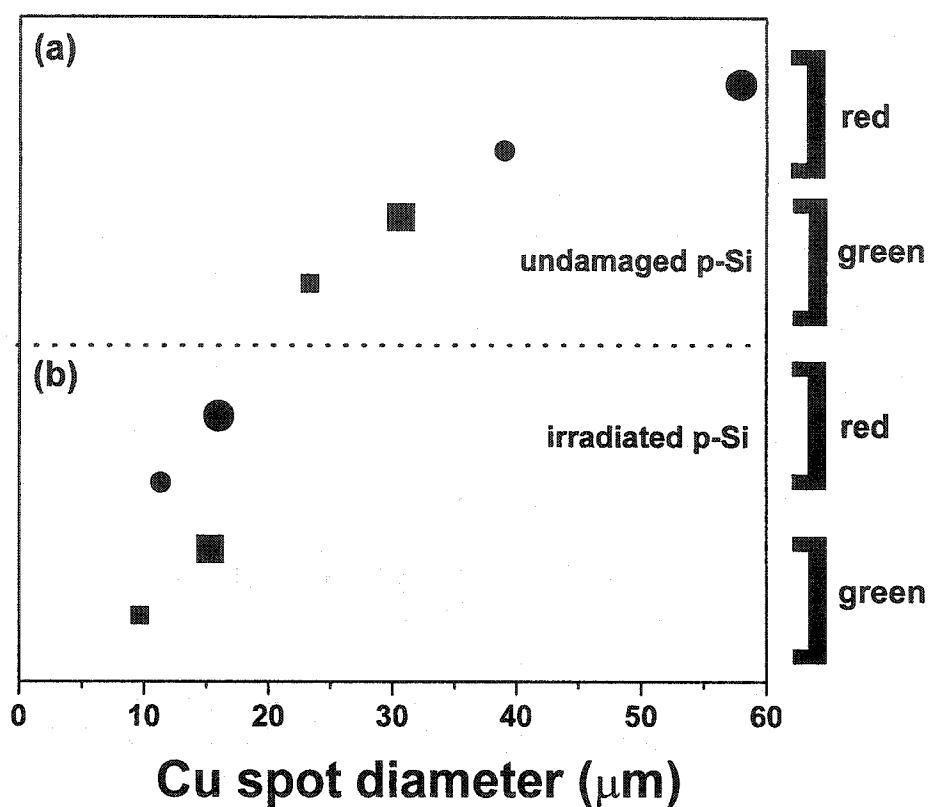


FIG. 110. Average outer diameter D_o of a time dependence series (0–60 s) of Cu dots formed by laser illuminating of p -Si substrates, indicating the effects of wavelength, beam intensity and substrate surface defect density [(a) undamaged Si; (b) ion irradiated Si]. Small and large circles (squares) indicate illumination with low and high intensity red (green) laser light, respectively.

An increased defect density in the Si material would reduce the mobility and thus the diffusion constant, and also shorten the carrier lifetime τ . This would reduce the distance the electrons can diffuse before being consumed by recombination and should reduce the resulting dot diameter. The effect of a reduced mobility and minority carrier lifetime in the Si wafer was demonstrated by increasing the defect density through ion implantation. Cu dots obtained by laser illumination on irradiation damaged *p*-Si are shown in Figs. 110 (c) and 110 (d), showing that D_i and D_o are roughly (40–50)% smaller than the corresponding values for dots deposited on undamaged *p*-Si under identical conditions. Obviously, the reduced minority carrier lifetime due to the increased defect density reduces diffusion and restricts the surface area receiving a sufficient carrier concentration to enable the Cu deposition. Experiments we have performed on amorphous *p*-doped Si layers show however that too high a surface defect density is not practical as it enables spontaneous Cu deposition also without illumination, probably due to a relevant density of surface states in these samples. The influence of the laser beam intensity on the dot diameter is obvious from Fig. 110 for both red and green laser light and also for irradiation damaged wafers. The observed reduction in dot size for lower light intensity might be related to the observation that a minimum light intensity is required to enable Cu deposition. This is likely due to the minimum number of adsorbed Cu atoms required to allow the formation of a stable nucleus. Thus for the higher light intensities, the reduction rate of Cu at the surface will be higher and the population of adsorbed Cu atoms will be sufficient to enable nucleation even at larger distances away from the illuminated area compared to lower light intensity.

d. Surface roughness. The morphological features of a surface can be quantitatively described through a function $g(L)$, called the surface width and defined as

$$g(L) \equiv \langle [z(r) - z(r')]^2 \rangle, \quad (25)$$

where $z(r)$ and $z(r')$ are the surface heights at r and r' , and the average is taken over a surface with linear dimensions L . $g(L)$ is given by the scaling formula:

$$g(L) \equiv \langle [z(r) - z(r')]^2 \rangle = 2\sigma_\infty^2 \{1 - \exp[-(L/\xi)^{2H}]\}, \quad (26)$$

with σ_∞ the surface rms roughness averaged over an infinite large image and ξ the lateral correlation length. The surface width g increases as L^H for small L and is independent of L for large L , H being the Hurst exponent. The crossover between the two behaviors takes place at $L = \xi$, which gives the maximum extent of the lateral correlations.

Figure 111 shows $\log[g(L)]$ for four representative samples, as detailed in the figure caption. It was noted that $\log[g(L)]$ of all samples saturates within the AFM measurement range and therefore this analysis should provide correct roughness information. It is noted that both the vertical and horizontal axes in Fig. 111 are in logarithmic bases. Analysis of the AFM images of Cu dots generated by red and green laser illumination on p -Si for durations varying from 5 to 60 s yield the values of σ_∞ and ξ shown in Fig. 112. The thicknesses of the dots are $\approx 60 \pm 5$ nm at 5 s of illumination and $\approx 100 \pm 20$ nm for ≥ 10 of illumination. The rms roughness is fairly independent of illumination time, wavelength, and intensity and is in the range 12–24 nm. The lateral correlation length is about 400 nm except for dots generated through illumination with low intensity red laser light, for which $\xi = 200$ –300 nm.

In an attempt to reduce the surface roughness, intermittent illumination was compared to continuous illumination (Fig. 111). The dot corresponding to curve A (C) in

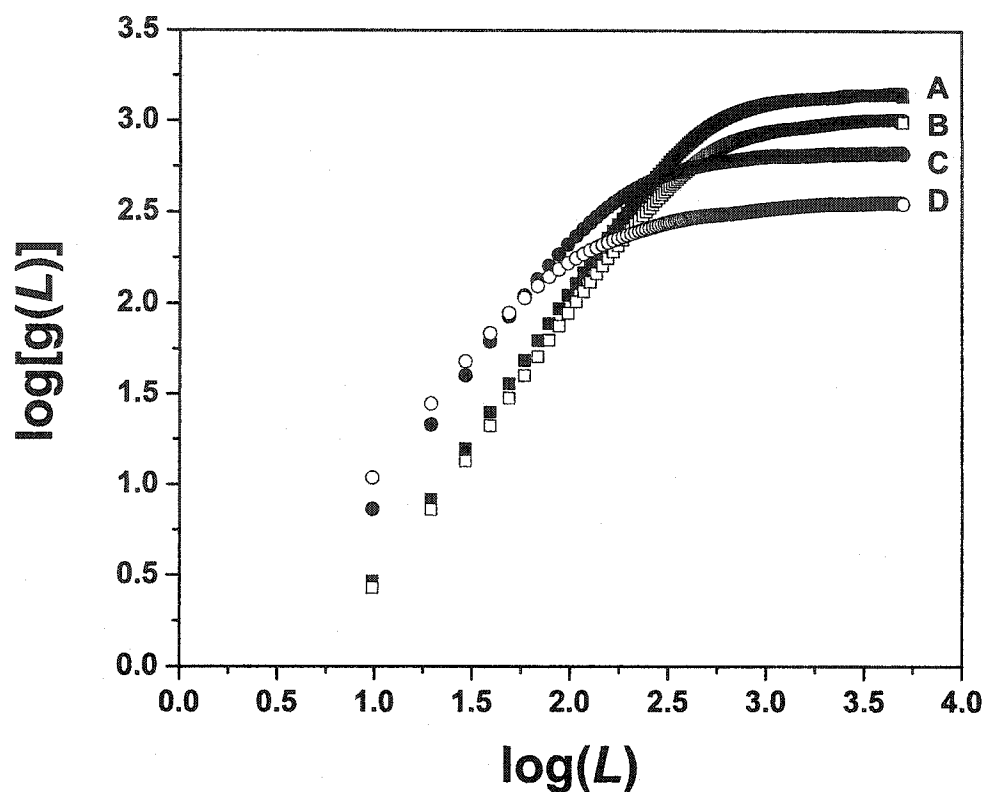


FIG. 111. Surface roughness σ_r and correlation length ξ for four Cu dots inside D_i using surface fractal analysis, showing the effect of intermittent illumination and the method used in the surface analysis. Both the vertical and horizontal axes are in logarithmic bases. All have total 10 s of illumination. Curve *A* is made by green laser beam with no interruption, curve *B* is made by green beam also with a 1 s of no illumination between ten 1 s of illumination. Curves *C* and *D* are the counterparts of curves *A* and *B* by red laser beam, respectively. Cross-wavelength comparison is not intended due to the complication of the wavelength effect on the growth of Cu features.

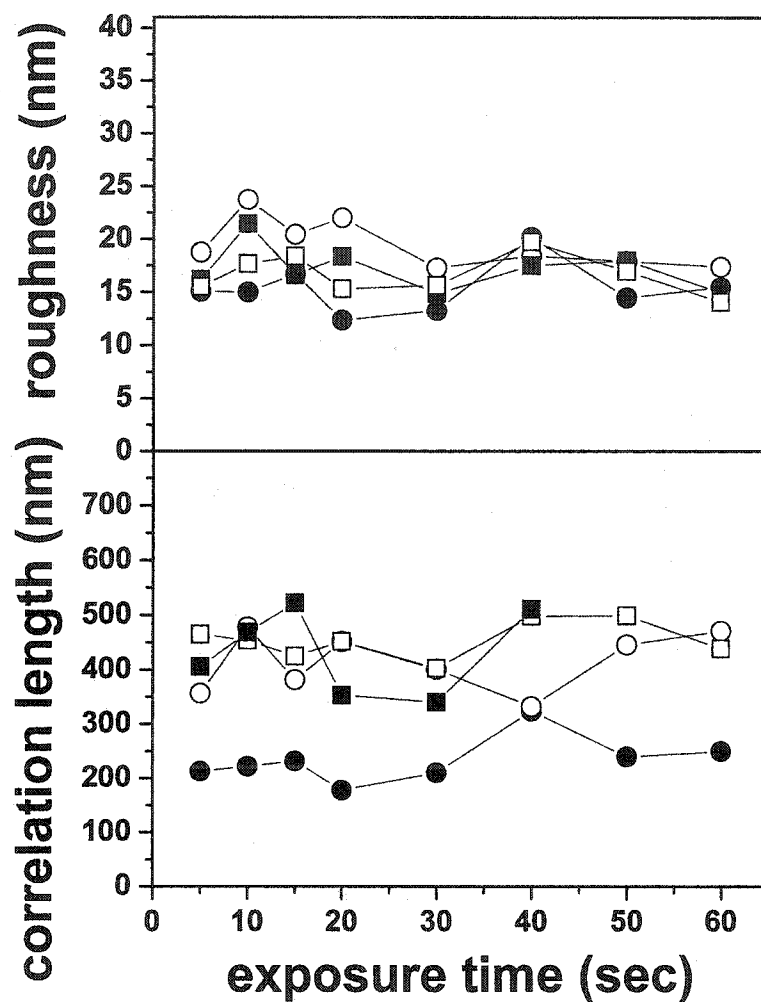


FIG. 112. Roughness σ_r and correlation length ξ inside D_i of Cu dots formed by illuminating the p -Si substrate using a red laser beam for 5–60 s. The open and closed circles indicate data points for the Cu dots generated by the red laser illumination at high and low intensities, respectively. The open and closed squares are for the counterparts in the case of green laser illumination.

Fig. 111 is obtained by continuous illumination for 10 s using the green (red) laser while dot B (D) is grown by intermittent illumination (1 s on, 1 s interruption repeated 10 times). It is observed that features grown with the intermittent laser light have smaller roughness values than those grown continuously. This effect could be a consequence of the disruption of continuous columnar growth during the “dark” period and of the formation of new nuclei with corresponding enhancement of the nucleation density at the beginning of the second illumination period. Another possibility is that copper grows under diffusion limited conditions when illumination is continuous, with depletion of copper ions in the vicinity of the growth sites. Under these conditions, growth would take place preferentially at protruding features, thus enhancing existing roughness. An interruption of the growth process, hence, would allow homogenization of Cu ions concentration in the solution and reestablishment of kinetically controlled growth, leading to a reduction of the surface roughness.

Results of the surface roughness analysis on different regions of some typical structures are listed in Table XII.¹¹¹ It is found that σ_o is two to four times larger in areas where the deposited Cu layer appears dark [ring area between D_i and D_o , Fig. 109 (a) and entirely dark dots, Fig. 109 (b) than in shiny areas [region inside D_i , Fig. 109 (a) and background plating, see the following section]. The lateral correlation length ξ does not appear on the other hand to be correlated with the optical reflectance of the dots.

Rougher surfaces scatter light more uniformly into different directions and therefore appear less shiny. The reflectivity of a rough surface depends on σ_o/λ and ξ/λ .¹¹² However, in the limit of normal incidence and small angle scattering,

TABLE XII. Surface roughness analysis in the apparent shiny and dark areas.

Time(s)	Location	Appearance ^a	σ_{∞} (nm)	ξ (nm)
60	$r^b < D_i$	shiny	23	393
50	$r < D_i$	shiny	26	436
60	$D_i < r < D_o$	dark	52	522
50	$D_i < r < D_o$	dark	65	426
5	$r < D_o$	dark	39	593
5	$r < D_o$	dark	40	434
Background	$r \gg D_o$	shiny ^c	15	315
Background	$r \gg D_o$	shiny	6	437

^a 5 \times objective lens, illumination from top. All are bright with Cu metallic color if >50 \times objective lens is used.

^b Here r means the distance from the measurement area to the center of the deposited Cu dot.

^c The background shininess is suggested to be the flat Si surface and/or the thin Cu precipitation

which is the case here, specular reflection from a material with a rough surface is described by¹¹³⁻¹¹⁵

$$R = R_0 \exp[-(4\pi\sigma_{rms}/\lambda)^2], \quad (27)$$

where R_0 is the Fresnel reflection coefficient, σ_{rms} is the root-mean-square roughness and λ is the wavelength of light. Therefore, larger σ_{rms} (or σ_{∞}) leads to smaller reflection. This is in agreement with our observations. It is further noted, as mentioned above, that a thin Cu deposit is present also in the nonilluminated area and causes the roughness there to be higher than the bare Si surface. The presence of Cu in the background is discussed in the following section.

e. Significance of the electrolyte chemical composition. Spontaneous Cu background deposition was frequently observed in the nonilluminated areas, albeit at a slower rate. Background plating on the entire Si area is possible due to the availability of electrons generated by the anodic half reaction between Si and F^- .^{40,41,43} Since anodic electrochemical processes are essential for the occurrence of background plating, and

these are partly dependent on the solution composition, we studied in more detail the dependence of both the dot morphology and the extent of background plating on the chemical composition of the plating solution.

The solutions investigated were obtained by adding various chemical reagents, as detailed in Table XIII, to a basic 0.1 mol/L CuSO_4 solution.

TABLE XIII. Effect of solution on Cu background plating.

	Solution				XPS Cu2p peak/ Background
	$\text{CuSO}_4(\text{M})$	$\text{NH}_4\text{F}(\text{M})$	Ascorbic Acid(M)	SPT(M)	
a	0.1	0	0	0	No
b	0.1	0	0.01	0.005	Yes
c	0.1	0.0025	0.01	0.005	Yes
d	0.1	0.01	0.01	0.005	Yes
e	0.1	0.02	0.01	0.005	Yes (weak)

The effect of the various reagents on the morphology of the deposited Cu dots is shown in Fig. 113. A discontinuous distribution of Cu nucleation sites is observed even after 60 s of illumination with the red laser beam if no NH_4F or other additives [solution (a)] are present in the solution [Fig. 113 (a)]. Presence of ascorbic acid and SPT without NH_4F in solution (b) increases D_o as shown in Fig. 113 (b). Presence of ascorbic acid, SPT, and 0.0025 mol/L NH_4F [solution (c)] generates an inner shiny circle with slight contrast from the darker ring area as shown in Fig. 113 (c). A much larger contrast between the inner circle and the ring appears [Fig. 113 (d)] when the Cu dot is deposited

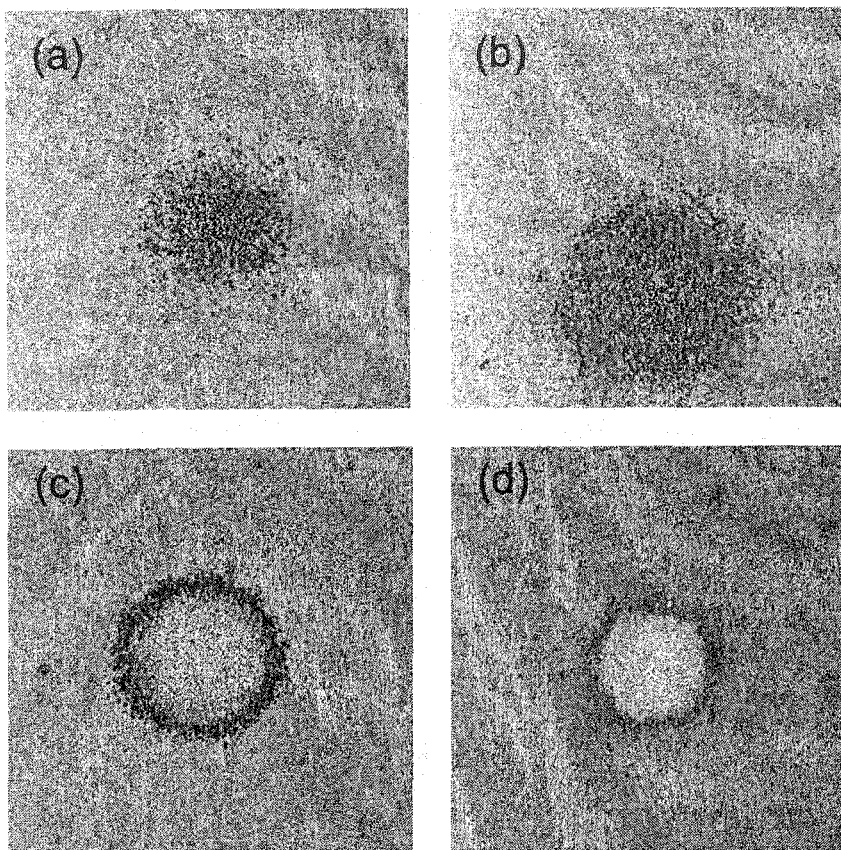


FIG. 113. Optical images ($150 \times 150 \mu\text{m}^2$) of Cu dots formed by illuminating *p*-Si using a red laser beam of $\sim 1\text{--}2 \mu\text{m}$ focused spot size for 60 s with (a) no additives, (b) 0.01 mol/L ascorbic acid and 0.005 mol/L SPT but no NH_4F , (c) 0.01 mol/L ascorbic acid, 0.005 mol/L SPT, and 0.0025 mol/L NH_4F , (d) 0.01 mol/L ascorbic acid, 0.005 mol/L SPT, and 0.02 mol/L NH_4F , in the $\text{CuSO}_4 + \text{DW}$ solution.

in the solution with the same amount of ascorbic acid and SPT, but with 0.02 mol/L NH_4F [solution (e)], the typical concentration of NH_4F used in this work.

XPS spectra were measured on the surface area away from the Cu dots in order to study the effect of the various reagents on Cu background precipitation. The XPS spectra for the background of deposits from the solutions listed in Table XIII are shown in Fig. 114. Only the solution containing solely 0.1 mol/L CuSO_4 and DW prevents Cu background plating [Fig. 114 (a)]. This is consistent with previous report³⁸ that dilute HF or NH_4F in the CuSO_4 renders possible Cu deposition even in the absence of light. In the presence of additives (ascorbic acid and SPT) and absence of NH_4F or only small concentrations of it, Cu background plating is observed; in addition, the shift in the Cu XPS peaks [Figs. 114 (b) and 114 (c)] indicates growth of a Cu oxide rather than its metallic form. With higher concentrations of NH_4F added to the solution, the background plated Cu is in the metallic state, as indicated by the Cu peaks shown in Figs. 114 (d) and 114 (e).

Optical and AFM images (partial top view) of a deposited dot formed by red laser illumination using solution (e) are shown in Figs. 115 (a) and 115 (b). The scratch was made using a profilometer. The presence of a Cu background layer on the substrate is indeed revealed from AFM scans across this scratch and in the area away from the dot. Even though solution (a) successfully prevents Cu background from forming, the presence of NH_4F [solution (c)–(e)] is crucial for generating a continuous contrasted (bright inner circle and its surrounding ring) in the Cu dot otherwise a discontinuous distribution of Cu nucleation sites is observed even after 60 s of illumination.

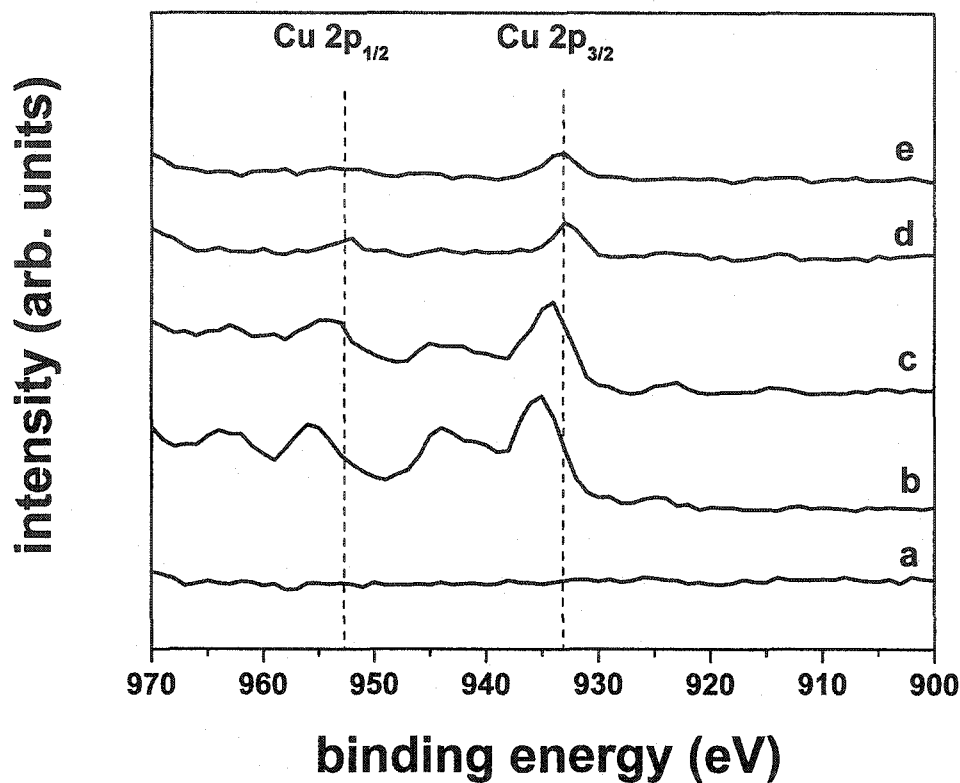


FIG. 114. XPS spectra measured in the background region away from any visible Cu dots for solutions containing (a) no additives, (b) all additives but no NH₄F, (c) all additives, 0.0025 mol/L NH₄F, (d) all additives, 0.01 mol/L NH₄F, and (e) all additives, 0.02 mol/L NH₄F. Only (a) has no XPS signal for Cu. Table XIII lists the additives and their concentrations in these solutions.

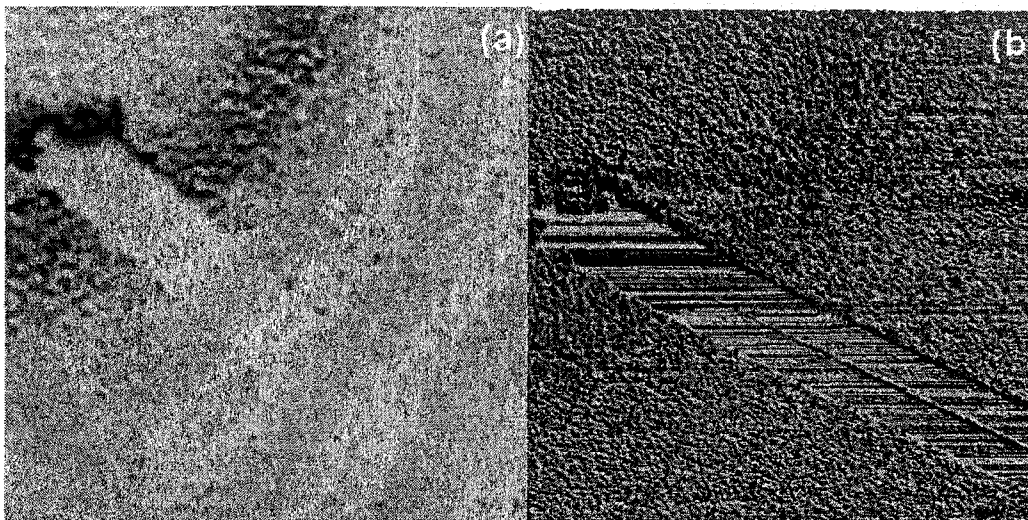


FIG. 115. (a) Optical and (b) AFM images ($10\ \mu\text{m} \times 10\ \mu\text{m}$ area) of part of a Cu dot formed by illuminating undamaged *p*-Si with a 1–2 μm diameter red laser spot using solution (e). The scratches result from profilometry

f. Selective plating through an optical mask. A preliminary work has been initiated on photoinduced deposition of patterned Cu on *p*-Si substrate through an optical mask. The advantage of this electroless technique is the absence of lithography step on the substrate surface to fabricate a mask. The experimental set up is illustrated in Fig. 116. An iris is first positioned after a 150-mW green laser in order to clean the beam from scattered light. The beam is then expanded by means of a divergent lens to provide a fully coverage of the cm-sized optical mask ("MINT") placed further away. The patterned light is hence directed to the substrate and focused to the desired size through a convergent lens. The standard electrolyte solution for copper deposition contained 0.1 mol/L CuSO₄, 0.01 NH₄F, 0.01 mol/L ascorbic acid, and 0.005 mol/L SPT. The *pH* value of the as prepared solution (*pH* ~ 3) was increased to ~ 4.8 by addition of NaOH. Subsequently, the solution was left at rest and filtered through paper filter. Alternative solution with *pH* value ~ 2.5 obtained by addition of sulfuric acid from the as prepared electrolyte was used.

Figure 117 shows a sharp "MINT" Cu feature photoinduced on a *p*-Si substrate in the μm -size range after a 45 s duration illumination from a *pH* = 4.8 solution. Further increase in the focusing of the patterned light (i.e. reduction of the feature size) leads to a degradation of the feature resolution. Indeed, the letters from the resulting Cu pattern are unidentifiable and the feature reduces into a dot. In the present experiment, focusing of the beam and *pH* of the solution are critical factors in obtaining electroless growth of Cu on *p*-Si. A modification of the *pH* value from 4.8 to 2.5 implies the use of electrode in the solution (a bias voltage of -0.1 V for 10 s is sufficient though) to allow selective Cu deposition through the optical mask. However, electroless deposition of Cu is still

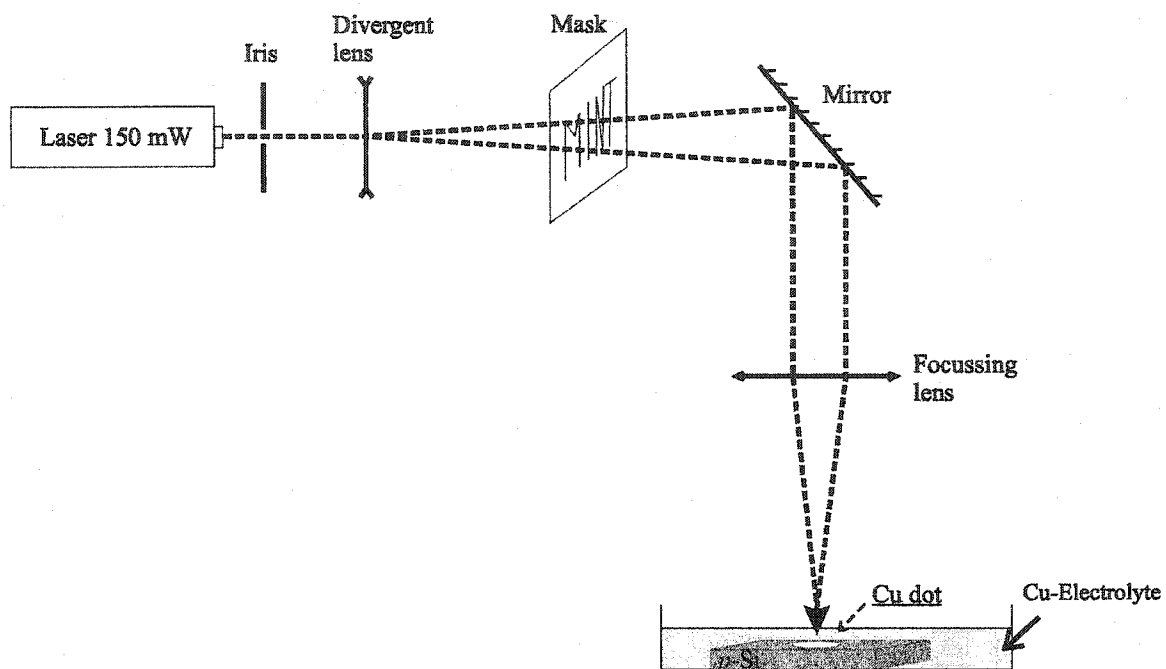


FIG. 116. Experimental set up for photoinduced deposition of Cu features onto *p*-Si substrate through an optical mask.

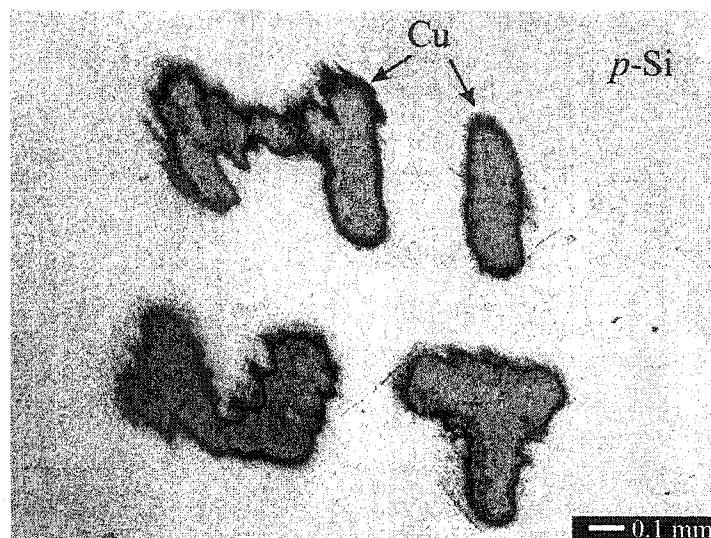


FIG. 117. Optical picture of photoinduced electrodeposition of Cu on *p*-Si substrate through a mask using 150 mW green laser beam.

possible at such pH in the absence of optical mask if the beam is sufficiently focused. Several attempts have been made to improve the resolution of the system (down to $\sim 10 \mu m$ as seen in Sec. III A 3 c) however the configuration and geometry of the optics involved were difficult to optimize. Furthermore, optical diffraction of light still remains a limiting factor for the finale feature size ($\sim 0.5 \mu m$) unless near field optics is used.

The particularity of Cu is its potential to grow under electroless conditions, however Cu is not a ferromagnetic material. Thus, selective deposition of Ni has been explored in this work using the previous photoinduced technique with the adjunction of an applied bias voltage. Figure 118 shows an illustration of the experimental configuration in which the cell is equipped with vertical electrodes: a graphite as counter electrode and the p -substrate (Si, GaAs) as the working electrode. The electrolyte solution contains 0.2 mol/L $NiSO_4$, 0.4 mol/L boric acid (H_3BO_3), and 0.25 mol/L sodium sulfate (Na_2SO_4) and the pH value is around 2.5. The p -Si and GaAs substrate require to be biased (negative) and laser activated in order for the Ni selective plating to occur.

Selective deposition of Ni on p -Si through the optical mask takes place at around -0.5 V up to 1 V, however only part of the pattern could be clearly reproduced. For instance, at bias voltage -0.9 V, duration illumination of 15 s and maximum laser light intensity, only one sharp letter appears on the substrate. As the beam intensity is reduced, the previous feature is partially reproduced.

In the case of p -GaAs (carrier density $9 \times 10^{17} \text{ cm}^{-3}$) substrate, selective photoinduced ECD is achieved using a well focused high intensity laser beam but in the absence of optical mask. In the present experiment, the focus and diameter of the

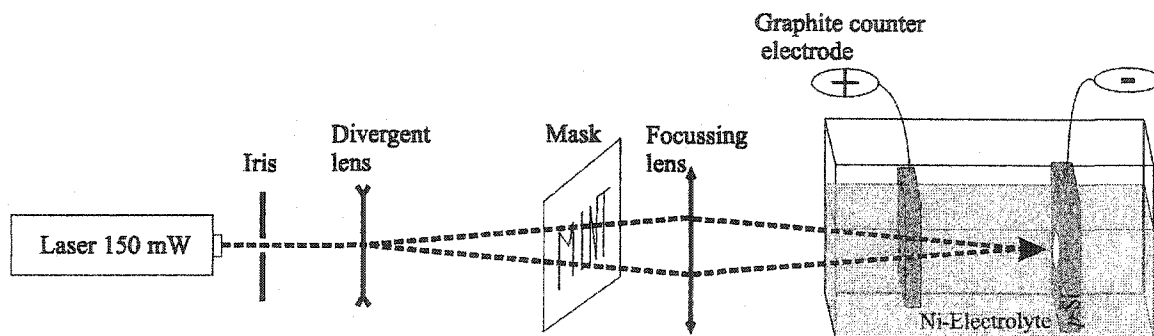


FIG. 118. Experimental set up for photoinduced electrodeposition of Ni onto *p*-Si and *p*-GaAs substrates.

laser light beam remain inaccurate since it is controlled through a movable lens and set according to the naked eye, leading to scattered results. Indeed, between a voltage range -0.7 to -0.9 V, the following scenarios occurred: (a) no deposition (-0.8 V), (b) selective deposition (-0.7 and -0.9 V), and (c) full coverage (deposition) of the substrate (-0.85 V). It should be mentioned that Co had been chosen as an alternative candidate for photoinduced ECD; unfortunately, no conclusive results could be extracted. As a matter of fact, cobalt sulfate solution appears red and tends to absorb the green laser light, making the focusing of the beam difficult onto the surface of the substrate. Furthermore, later experiments on photoinduced Co on *p*-GaAs substrate using red light laser pointer showed selective deposition in a very narrow window for the bias voltage. Therefore, a rigorous control of the optics configuration, solution and laser light is required to investigate deeper the photoinduced plating of Ni and Co onto *p*-Si and *p*-GaAs substrates.

B. Selective metal electrodeposition of FM materials through doping modulation of SC surfaces.

The work presented here was motivated by the observation of the different electrochemical response of *p*- or *n*-doped GaAs surfaces in electrolytic solutions. Figure 119 shows the variation of the plating current as the cathodic polarization of the GaAs semiconductor substrate is increased against a 0.1 mol/L CoSO₄ plating solution. The measurements were performed on standard GaAs(001) wafer material (*n*-type: 7×10^{17} cm⁻³, *p*-type: 8×10^{17} cm⁻³). The *p*-doped GaAs forms a diode in reverse bias requiring a larger threshold voltage of $V_{th} = -1.6$ V (voltage here and in the following measured against a standard calomel electrode) to initiate deposition as compared to the *n*-doped

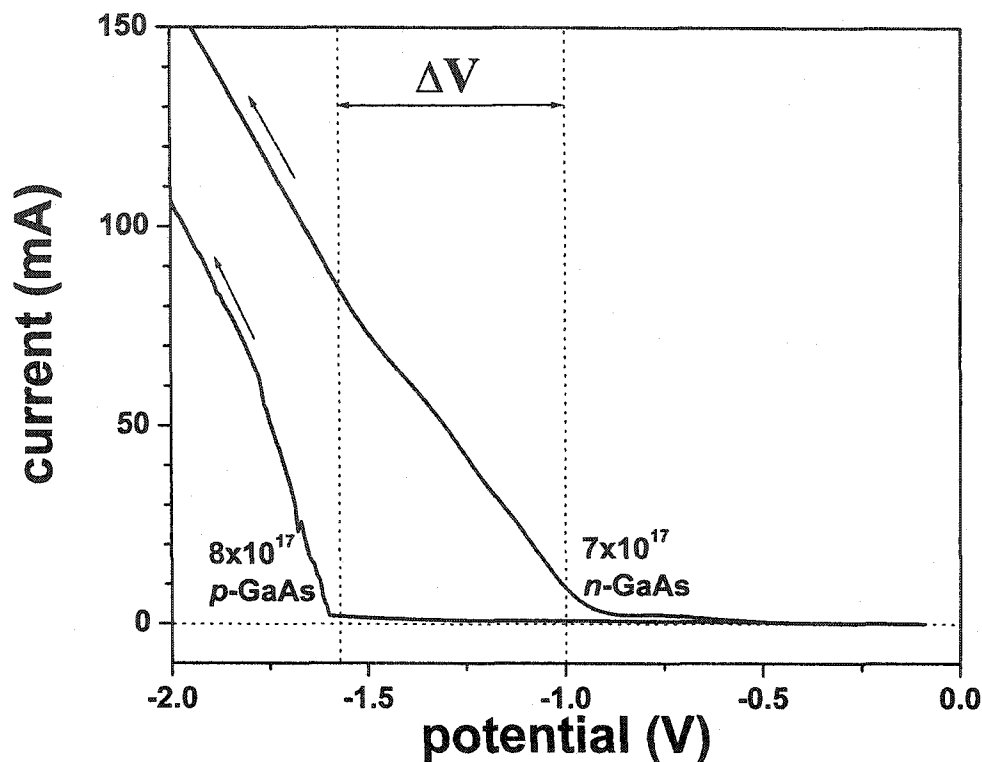


FIG. 119. Current-voltage characteristic for electrodeposition on *p*- and *n*-type GaAs. Applying an increasing cathodic potential to the *n*- or *p*-type GaAs substrate while monitoring the current flow allows to identify the onset of the electrochemical deposition of Co. Deposition starts at -0.9 V (vs. standard calomel electrode) for *n*-type GaAs ($7 \times 10^{17} \text{ cm}^{-3}$ carrier concentration) substrates and -1.6 V for *p*-type GaAs ($8 \times 10^{17} \text{ cm}^{-3}$ carrier concentration). In the corresponding intermediate potential range with width $\Delta V = 0.7$ V Co deposition would occur selectively, being enabled on *n*-doped surfaces and inhibited on *p*-type areas.

GaAs sample ($V_{th} = -0.9$ V) which forms a forward biased diode with the solution. At large applied voltages, charge transfer can also take place across the reverse biased diode through thermionic emission. At lower voltages, however, this opens a window of operation in which deposition on *n*-doped GaAs will be possible while being inhibited on *p*-doped GaAs surfaces. This should still hold when both *p*- and *n*-doped regions are combined on a single surface, thus allowing self-aligned growth of metals on semiconductors with a *p/n* surface pattern. The precise values of these threshold voltages do depend both on the electronic properties (work function, doping concentration, surface defects) of the semiconductor material and on the plating solution chemistry, and will have to be estimated individually. Too high a *p*-type doping density will yield doping bands which would facilitate plating and thus have to be avoided. In addition, surface states would enable electron transfer from the semiconductor to the ions in solution also under reverse bias conditions. For instance, a large density of surface defects would generate surface states and thus allow nucleation on GaAs surfaces of either doping polarity.³¹ Therefore clean and smooth substrate surfaces are required for successful selective electrochemical deposition. The ensuing experiments were carried out both on large structures (mm sized) for demonstration of the principle and on smaller linear doping modulations with dimensions of several μm .

1. Co on etched *n-p*-GaAs

- a. Experiment. The samples were fabricated from a layered GaAs structure which consists of a 500 nm thick *n*-doped ($1 \times 10^{18} \text{ cm}^{-3}$) GaAs layer grown by molecular beam epitaxy on a *p*-doped ($5 \times 10^{17} \text{ cm}^{-3}$) GaAs(001) substrate. In a subsequent lithographic

step, a pattern was etched into the surface in order to expose *p*- and *n*-doped surface areas. The chemical etching was performed using a two-step process as illustrated in Fig. 120: a) immersion in $\text{H}_2\text{O}_2/\text{NH}_4\text{OH}/\text{H}_2\text{O}$ 3:1:8 solution for 10 s to produce the profile geometry; b) immersion in $\text{H}_2\text{O}_2/\text{NH}_4\text{OH}/\text{H}_2\text{O}$ 3:1:10 solution for 30 s to smoothen the surface. Electrodeposition experiments were performed using a $\text{Ga}_{75}\text{In}_{25}$ eutectic electrical contact to the GaAs. Immediately prior to deposition, the substrates were etched for 30 seconds in a 10% ammonia solution in order to remove surface oxides. Electrodeposition was carried out under potentiostatic control at 25 °C using a graphite counter electrode. Co was deposited from a 0.1 mol/L CoSO_4 solution at $\text{pH} = 2.5$ without agitation of the solution at a potential of -1 V for 150 s resulting in a film thickness of about 70 nm.

b. Results and discussion. Figure 121 shows examples of the selective replication of the *p/n* surface doping relief. The selective nature of the process was verified by chemical analysis using XPS showing Co deposition on the *n*-doped regions and absence of Co on the *p*-doped areas. A VSM was used to confirm the ferromagnetic properties of the deposited Co layer, which exhibits a square hysteresis loop with a coercivity of 100 Oe.

This method of self-assembled Co deposition works consistently on structures either with wide *n*-doped areas separated by narrow *p*-doped ditches [Figs. 121 (a) and 121 (b)] or narrow *n*-doped ridges isolated through wide *p*-doped “valleys” [Fig. 121 (c)]. Thus, this selective deposition technique is applicable on complex surface topographies. It is also noted that it turned out to be irrelevant as to where the electrical contact to the semiconductor substrate was made, either to the *n*- or the *p*-doped region. Even isolated

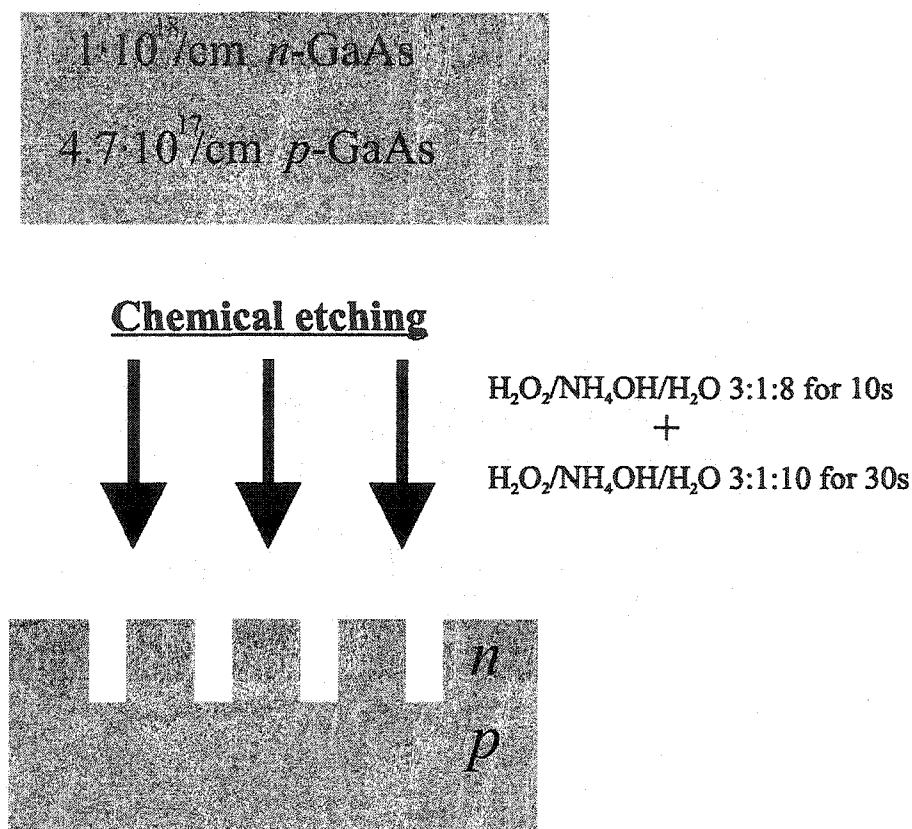


FIG. 120. Sample preparation for selective ECD of Co/Ni on patterned etched *n-p*-GaAs. A 500 nm thick *n*-doped GaAs layer is grown by Molecular Beam Epitaxy on a *p*-type GaAs substrate (a). Subsequently, through masking and a chemical etch, pits are formed with their depth extending into the *p*-doped substrate (b). This way both *n*-doped and *p*-doped regions are exposed at the sample surface. Samples were prepared with structure sizes ranging from mm to a few μm .

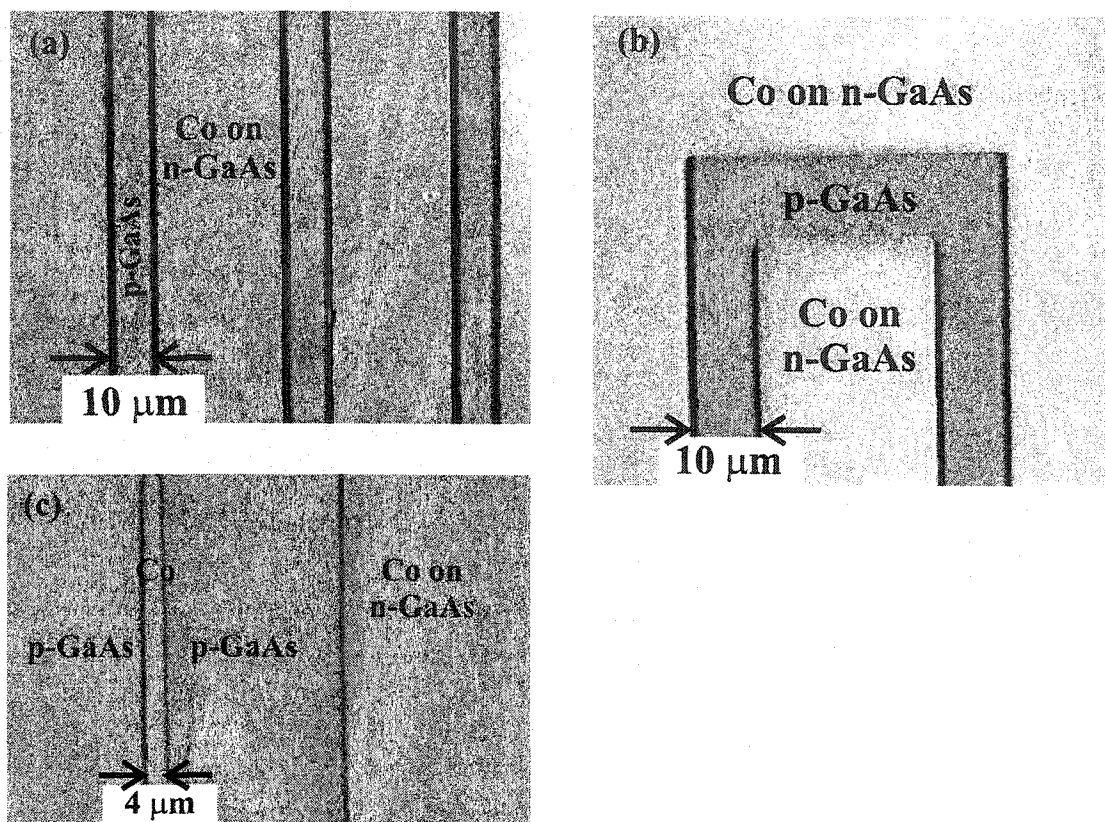


FIG. 121. Demonstration of selective Co growth on patterned n - p -GaAs. Optical micrographs showing three examples of selective electrodeposition of Co on n -doped surface areas of GaAs while leaving p -doped areas uncovered. The deposition was done at a cathodic potential corresponding to the voltage range between the onset of deposition on n -type GaAs and that of p -type GaAs (Fig. 119). The bars in the lower left corner of each panel correspond to a length of $10 \mu\text{m}$.

n-regions were successfully plated upon although the current flow had to pass through a *p/n* barrier inside the GaAs substrate.

As shown in Fig. 122, surface examination of samples with large *p*-doped areas showed few defects in the *p*-doped regions which, upon analysis using energy dispersive x-ray (EDX) spectroscopy in a scanning electron microscope, were identified to be Co. The spatial distribution of those was irregular and the area density was found to coincide with the so-called etch-pit density of the GaAs wafer material.

This etch-pit density relates to the area density of bulk screw dislocations emerging at the GaAs single crystal surface. Such local disturbances of the electronic surface structure due to a screw dislocation likely enable electrodeposition of Co on the otherwise inhibited *p*-doped GaAs surface. The peculiar, pointed shape of these Co clusters, as measured using AFM (Fig. 123), is a consequence of the small initial nucleation size in combination with the diffusion limited growth process, leading to preferential growth on protrusions. True selective deposition onto *n*-doped regions would thus require very low defect density in the starting semiconductor material.

2. (Co, Ni) on ion implanted n-p-Si

Another way of generating a *p/n* pattern SC substrate is to create *n*-regions into a *p*-doped substrate by ion implantation, with the advantage of leaving a flat pattern surface as opposed to the previous technique using chemical etching.

a. Experiment. Cobalt and Ni deposition were carried out on locally irradiated B-doped *p*-Si (resistivity: 5–25 Ω cm) using a tantalum (Ta) mask template. The substrate

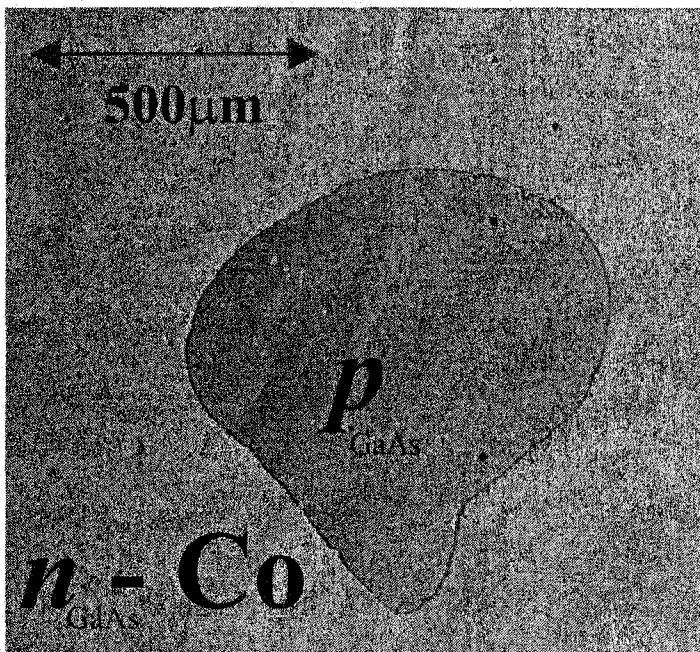


FIG. 122. Optical picture of a Co film selectively plated on (500 nm)*n*-GaAs/*p*-GaAs etched substrate. The deposition of small Co pits in the center of the picture coincides with the dislocation of the substrate (500 nm)*n*-GaAs/*p*-GaAs.

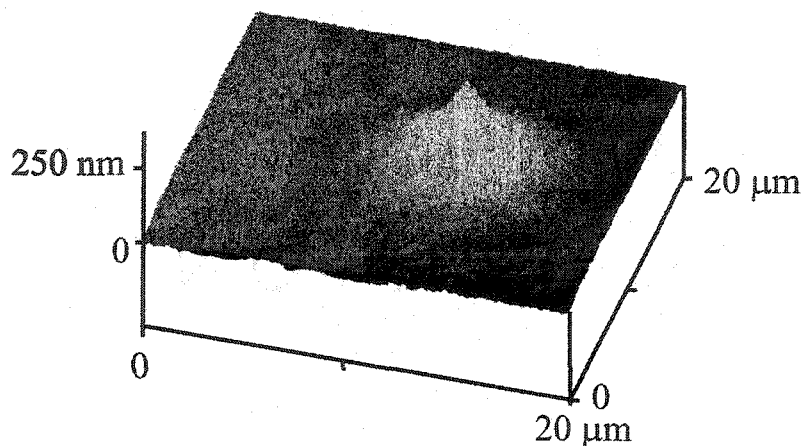


FIG. 123. AFM micrograph of defect plating. On larger areas of *p*-doped GaAs surfaces small defects in form of conical protrusions are found. The defects are small Co deposits on the surface regions which inhibit Co deposition. The dimensions in this example are about 200 nm height with a 10 μm diameter. The area density of these defects corresponds to the density of screw dislocations ending at the surface. We believe that these Co deposits are formed through nucleation enabled through electronic defect states in the vicinity of screw dislocations.

preparation steps are shown in Fig. 124. A 825 Å thick Ta layer was first deposited on *p*-Si by sputtering (model Key-system ACP 2000) in order to define the ion beam energy for irradiation and ensure the implantation depth of the ions to be near the *p*-Si surface. Subsequently, a photoresist mask was deposited on top using lithography technique. Finally, a 4600 Å thick Ta layer was sputtered under the same conditions as previously and the photoresist mask lifted off, revealing a Ta pattern with sequences of valley (825 Å) and hills (5425 Å) as shown in Figs. 125 (a) and 125 (b). In those figures, a white light is shining from the left side in order to reveal the topography of the mask before ion implantation, the bright lines indicating thicker features (hills). The thicker features of the Ta mask prevent the *p*-Si from being irradiated, leaving the underneath regions intact (*p*-type), whereas thinner regions allow ion implantation in the near-surface of *p*-Si. The substrate was irradiated by ion implantation using 200 KeV phosphorus (P) ions with a dose $2 \times 10^{13} \text{ cm}^{-2}$. Afterward, the Ta mask was etched away by immersion into a 10% HF solution for approximately 1 min and the sample annealed at 950 °C for 30 min to ensure electronic activation of implanted P ions and suppression of the irradiation damage. Immediately prior to Ni or Co deposition, the native oxide on the Si substrate was etched away by immersion in a 10% HF solution subsequently followed by a rinse in DW for 30 seconds. Graphite was used as a counter electrode and Ga₇₅In₂₅ eutectic as an electrical back and front contact to the substrate. Nickel (cobalt) was afterward selectively deposited on *n*-regions (i.e. P implanted regions) from a 0.1 mol/L NiSO₄ (CoSO₄) electrolyte at a pH value of ~ 2.5.

b. Results and discussion. Figures 125 (c) and 125 (d) show optical pictures of Ni features deposited on p/n pattern Si substrate using a bias voltage of -1.5 V for 220 s.

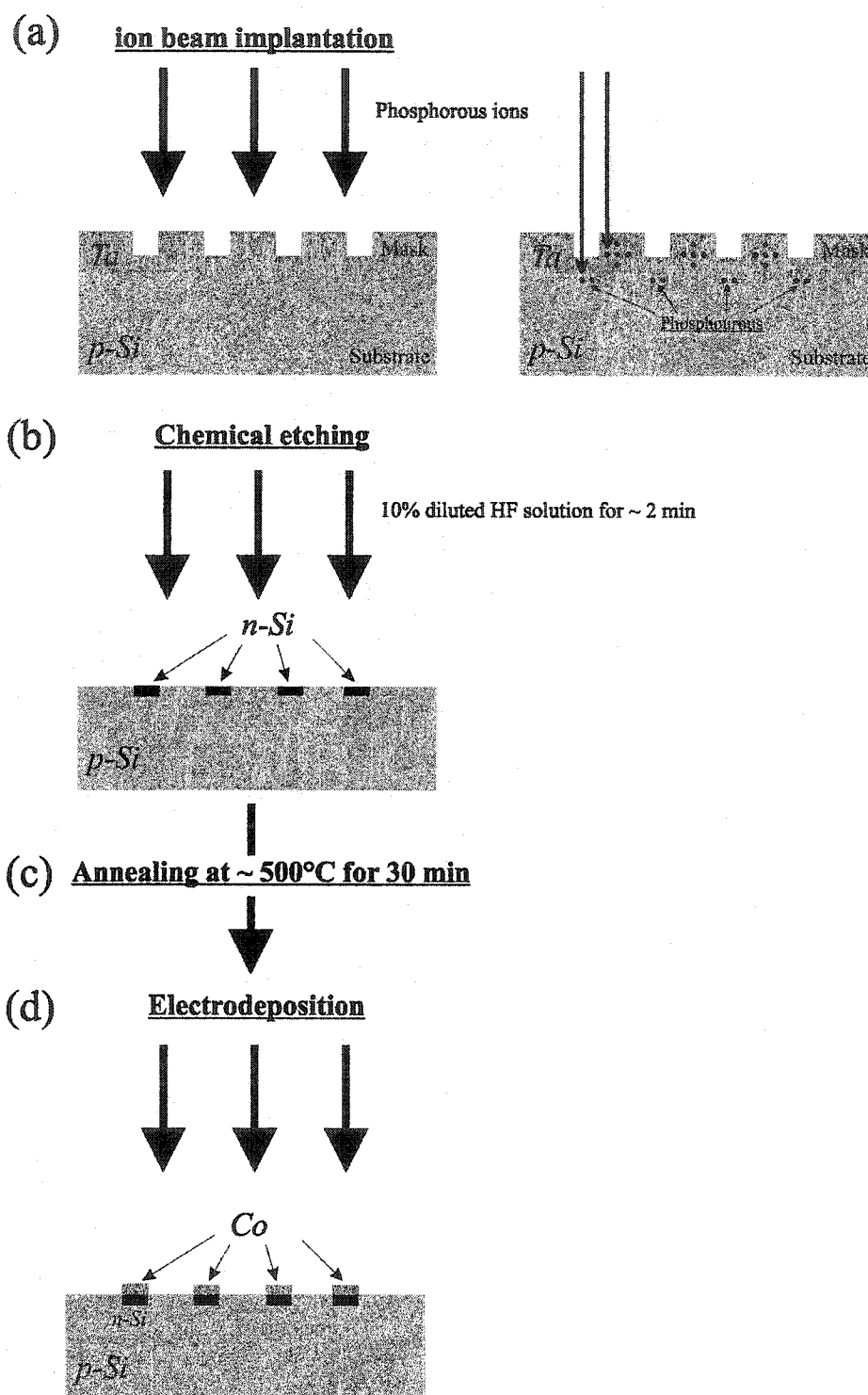
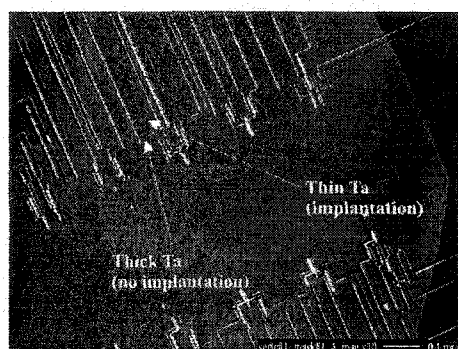
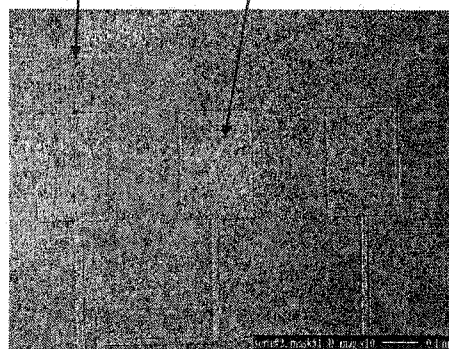


FIG. 124. Substrate preparation for selective electrodeposition of Co on ion implanted *p-Si* substrate.

(a) Ta masks/*p*-Si

Thin Ta (implantation) Thick Ta (no implantation)



(1) Ion implantation, (2) mask lift-off, (3) annealing ~ 950 °C for 30s, and (4) electrodeposition of Ni

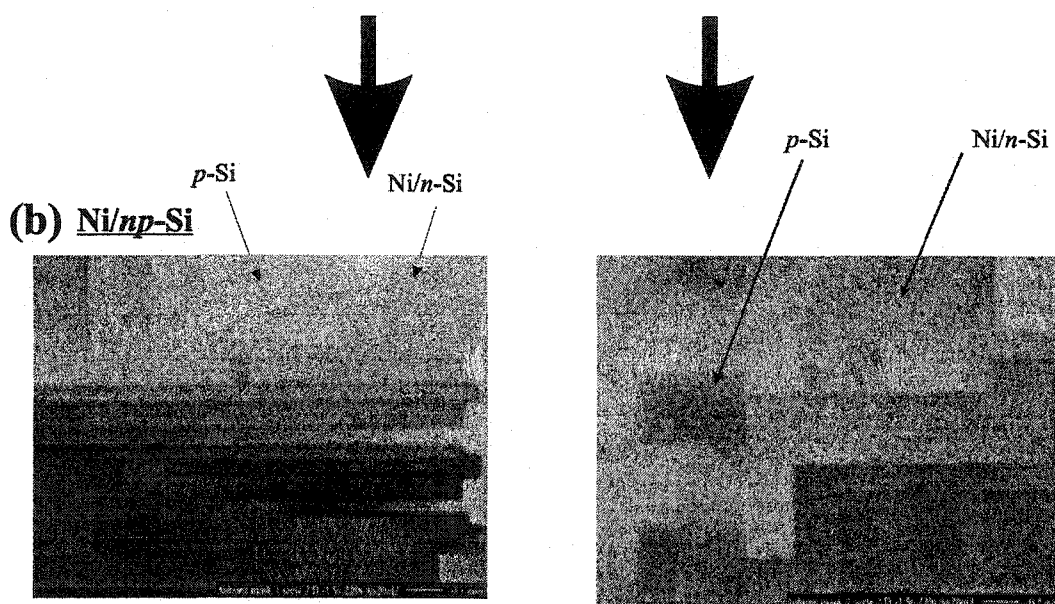


FIG. 125. (a) Optical pictures of a Ta pattern sputter deposited on *p*-Si substrate. A white light is shining from the left in order to reveal the topography of the mask features. The reflection of the lights (bright lines) indicates higher features on the Ta surface. (b) Optical pictures of Ni film selectively electroplated on the *n*-Si features on the corresponding ion implanted *p*-Si wafer under -1.5 V for 220 s. It is to notice the unusual progressive deposition of material.

Surprisingly, the deposition occurs progressively starting preferentially from the front contact electrode avoiding the p -Si regions. Figure 126 shows the P ions implantation profile (gaussian) after penetration through the thin Ta layer. The 200 KeV P ion beam projected range (penetration depth) in Ta is $\sim 828 \text{ \AA}$ with a corresponding longitudinal straggling depth of 700 \AA .

As shown in Fig. 126 (a), the expected implanted P ions forming the n -regions should be located to an approximately 35 nm thick activating n -region in the near p -Si surface since the thin Ta layer is 825 \AA thick (i.e. the projected range matches the Ta thickness layer). However, at the junction between p -Si and the new n -implanted region, a depletion region takes place clearing out most of the implanted region. As a consequence, the electrodeposition process is disfavored (i.e. lack of carrier density) until some metal has been deposited to allow deposition again leading to a progressive plating of n -regions. Hence, to overcome the effect of depleted region that occur at p/n interface, a larger implantation depth (higher beam energy) and increase of the P ion dose are desirable. As a result, a reconsideration of the irradiation conditions on Ta/ p -Si has been necessary. The dose was increased to $4 \times 10^{14} \text{ cm}^{-2}$ (i.e. the corresponding resistivity of n -implanted regions obtained is $\sim 0.01 \text{ \Omega cm}$) and the implantation depth optimized [Fig. 126 (b)] by adjusting the P ion beam energy.

Selective deposition of FM materials (Ni, Co) is achieved using the previous chemistry and the conditions above; however, no improvement is noticed and the deposition remains progressive. The drop of potential ΔV across 1 cm of pattern area can be estimated using the relation $\Delta V = \rho I/A$ where ρ is the resistivity of the n -region ($\sim 0.01 \text{ \Omega cm}$), I the total current flowing in the n -regions and A the crosssection area.

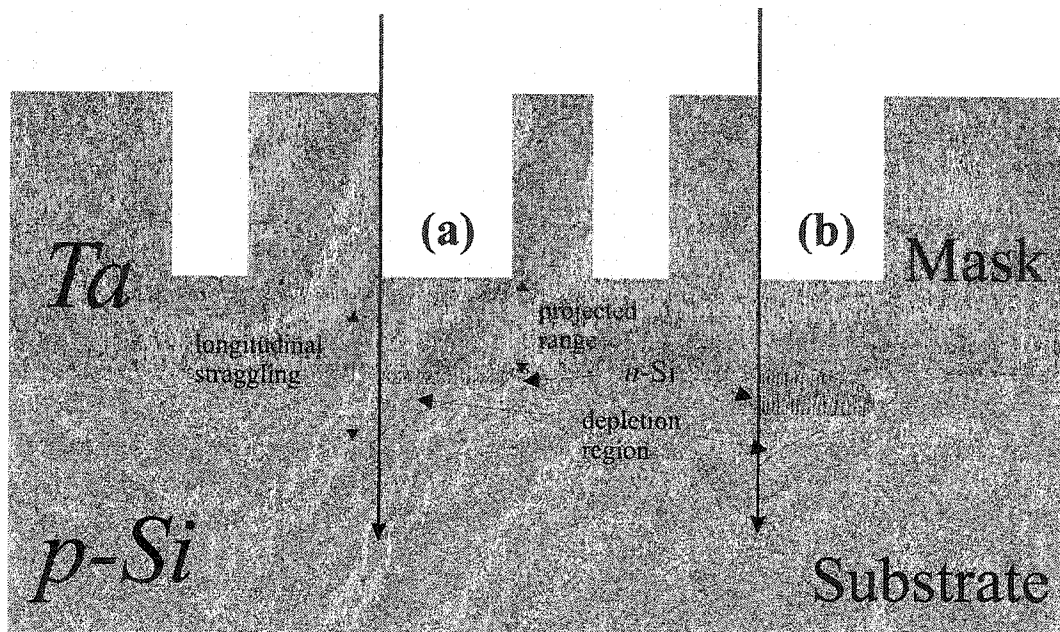


FIG. 126. Implantation profile of P ions irradiated on a pattern Ta/p-Si substrate.

An estimation of ΔV yields a value of ~ 1 V, which is not negligible compared to the applied bias voltage. Therefore, all regions away from the starting contact electrode experience a difference of potential with increasing distance.

ECD mechanism requires a threshold voltage V_{th} (~ -1 V in the present case) to operate, therefore deposition occurs in n -regions for which the potential is greater than V_{th} which corresponds to restricted regions within a define distance away from the initial potential. As the material is deposited, the allowed plating distance shifts to the next available regions leading to a progressive plating. As a consequence, attenuation of the voltage drop (i.e. current density) across the implanted sheet is necessary to avoid progressivity in the deposition process.

This is achieved by reducing the concentration of ions in the electrolyte by a factor of a hundred (0.001 mol/L). In addition, the temperature of the solution is maintained at 5 °C to slow the carrier. Although deposition under such conditions leads to much smaller growth rate and takes place selectively on n -doped regions, the characteristic progressive plating remains.

As a conclusion, selectivity on p/n pattern SC is achievable, however, implantation parameters and growth conditions are crucial to allow homogenous deposition across the patterned area.

3. “Side-plating” ECD of Co nanowires on n-p-Si

The selectivity property of ECD on p/n SC has been used to generate self-assembled long nanowires by modification of ECD configuration. As shown in Fig. 127,

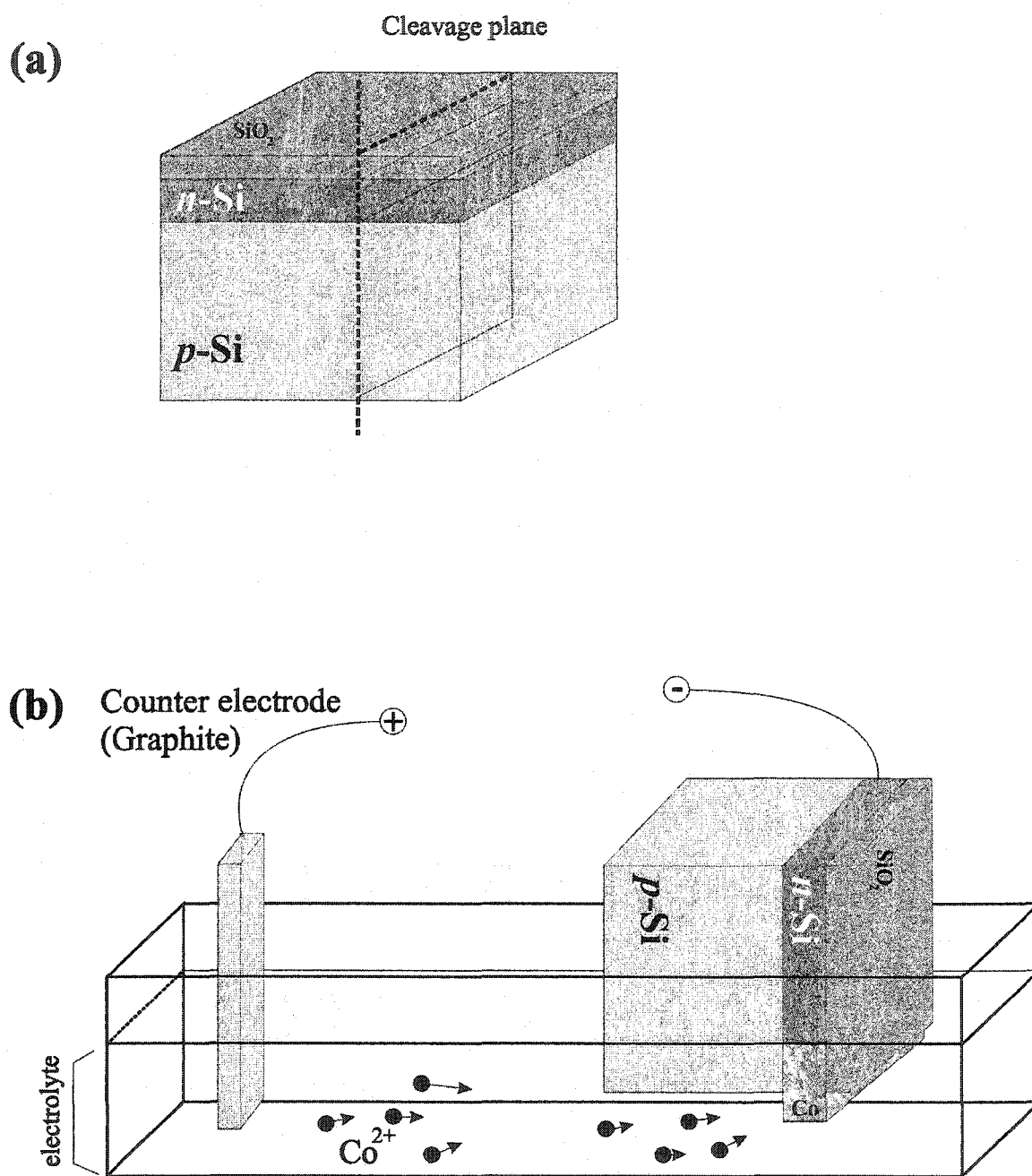


FIG. 127. Drawing of the side plating sample preparation and experimental set up.

the procedure consists of exploiting the cleaved edge of a multilayer ($\text{SiO}_2/n\text{-SC}/p\text{-SC}$) substrate and deposit FM material along its edge ($n\text{-SC}$ layer). The width of the deposited wire is thus controlled by the thickness of the $n\text{-seed}$ layer. This method could lead to self-assembled nanowires with a well-controlled lateral and longitudinal resolution.

a. Experiment. Three substrate preparations have been investigated in the present work. (1) Two 10 nm thick Cu layers separated by a 60 nm thick silicon dioxide (SiO_2) layer was sputter deposited on a glass substrate followed by a 50 nm thick SiO_2 cap layer. Subsequently, the resulting substrate was cleaved [Fig. 127 (a)] and immersed into a 0.01 mol/L NiSO_4 or CoSO_4 electrolyte at $\text{pH} \sim 2.5$ [Fig. 127 (b)]. Graphite was used as the vertical counter electrode and a bias voltage of -1.5 V was applied for 30s.

(2) The second preparation uses $p\text{-Si}$ as substrate and chromium (Cr) as an alternative metallic material for the seed layer. Cr was preferred as Cu for its structure quality (i.e. sharp cleavage at liquid nitrogen temperature).¹¹⁶ The dimension of the metallic layers is increased for better imaging of the deposited wires. Two 500 nm thick Cr layer separated by a 50 nm thick SiO_2 insulating layer were sputter deposited on B-doped $p\text{-Si}$ followed by 50 nm thick SiO_2 cap layer. Subsequently, the resulting substrate was cleaved in liquid nitrogen and immersed into the plating solution.

(3) The third substrate preparation consists of replacing the metallic seed layer by a $n\text{-Si}$ for its attractive application (FM contacts on SC). A 800 nm thick $n\text{-Si}$ layer was sputter deposited on $p\text{-Si}$ from a Te-doped $n\text{-Si}$ (resistivity: $0.02 \Omega \text{ cm}$) wafer target and the cap SiO_2 layer thickness increased from 50 to 200 nm for better imaging of the wire dimensions.

b. Results and discussion. (1) SEM pictures of plated Ni on Cu cleaved edge regions showed an irregular and undefined Ni feature due to the deformation of Cu layer during the cleavage. Indeed, as deposited substrate shows uneven cleaved Cu edge, the layer being sheared instead of sharply cut. Thus, Cr material was preferred for its crystal properties.

(2) Figure 128 (a) shows a $\sim 1.5 \mu\text{m}$ wide Co wire selectively deposited on (50 nm)SiO₂/(100 nm)Cr/(50 nm)SiO₂/(100 nm)Cr/*p*-Si substrate, avoiding mainly *p*-Si and SiO₂ layers. Attempts have been made to grow two 500 nm thick defined wires by succession of Cr seed layer and insulating SiO₂ layer, however, the selective plated wires are overlapping forming a single wire wider than expected ($1.5 \mu\text{m}$ instead of $1 \mu\text{m}$). This might be incremented to an overtime deposition. In addition, Co contamination in the *p*-regions can be seen due to high current density.

(3) Figure 128 (b) show a SEM image of a $\sim 1 \mu\text{m}$ wide Co wire deposited on a (200 nm) SiO₂/(800 nm)*n*-Si/*p*-Si substrate for 30 s at -1.5 V . Plating occurs on *n*-Si layer leaving SiO₂ and *p*-Si regions almost free of Co. Nevertheless, as seen in Fig. 128, it is important to notice that overtime deposition and higher bias voltage can lead to a partial Co coverage of *p*-Si regions. Figure 129 shows a SEM picture of a $1.2 \mu\text{m}$ wide Co wire plated on a 800 nm *n*-Si seed layer from a (200 nm)SiO₂/(800 nm)*n*-Si/*p*-Si substrate for 20 s at -1.5 V . No significant contamination of Co on *p*-Si and SiO₂ regions is observed. The sample is tilted (40°) for estimation of the wire thickness which is evaluated at $\sim 200 \text{ nm}$. It should be noticed that the final expected width of the wire is larger than the *n*-Si seed layer thickness, which is due to long deposition time.

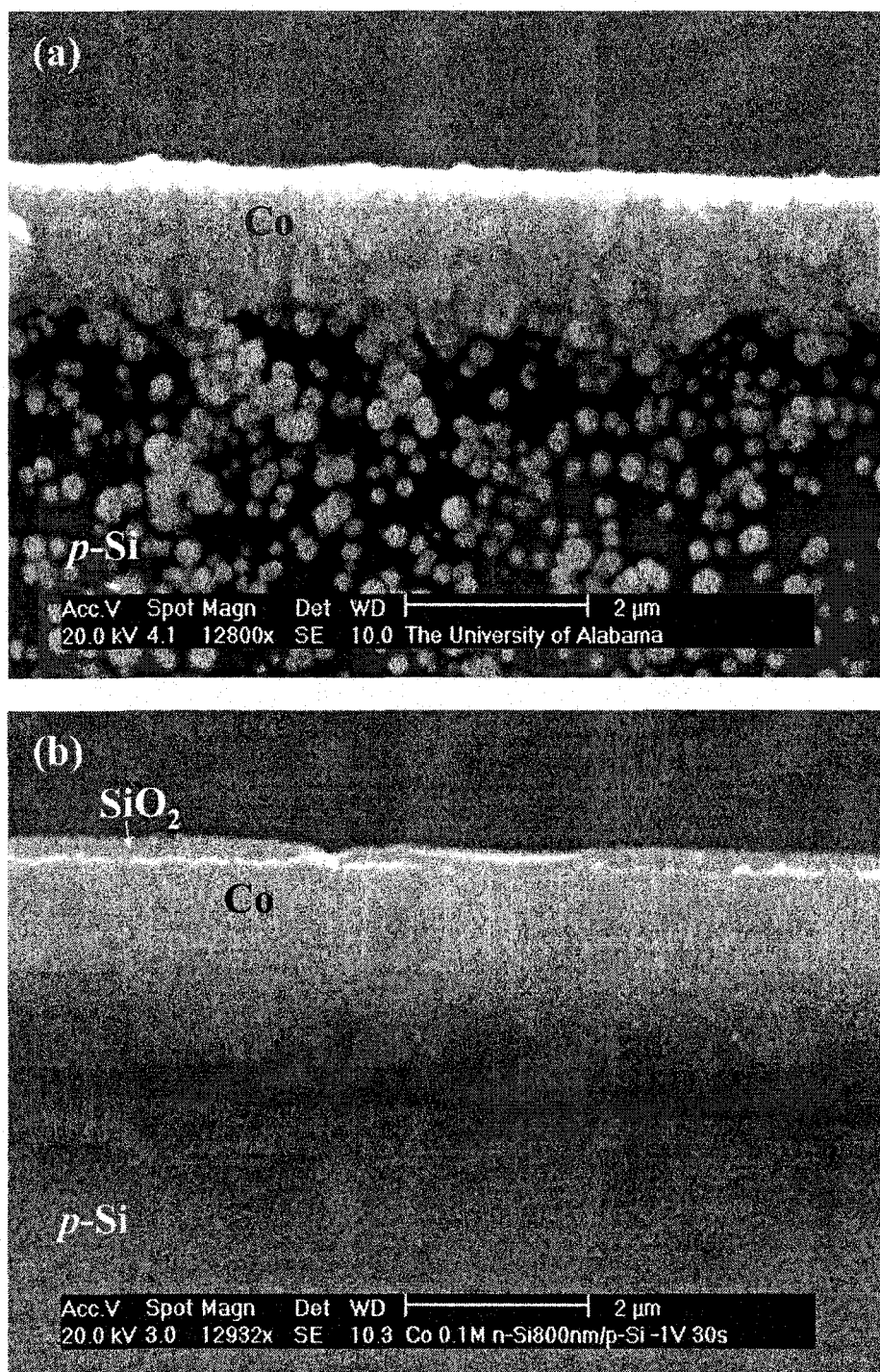


FIG. 128. SEM picture of (a) $\sim 1.3 \mu\text{m}$ and (b) $\sim 800 \text{ nm}$ wide Co wire “electro-deposited” on $(50 \text{ nm})\text{SiO}_2/(500 \text{ nm})\text{Cr}/(50 \text{ nm})\text{SiO}_2/(500 \text{ nm})\text{Cr}/p\text{-Si}$ and $(200 \text{ nm})\text{SiO}_2/(800 \text{ nm})n\text{-Si}/p\text{-Si}$ substrate respectively.

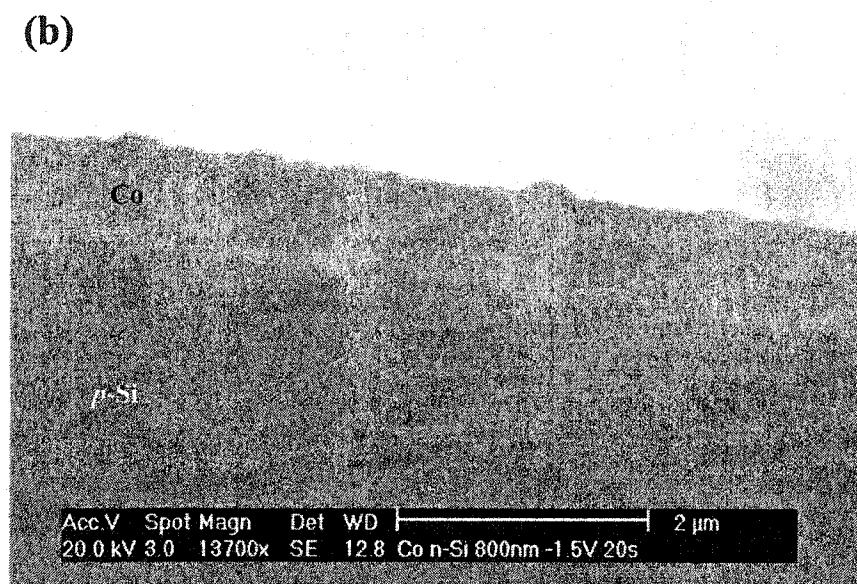
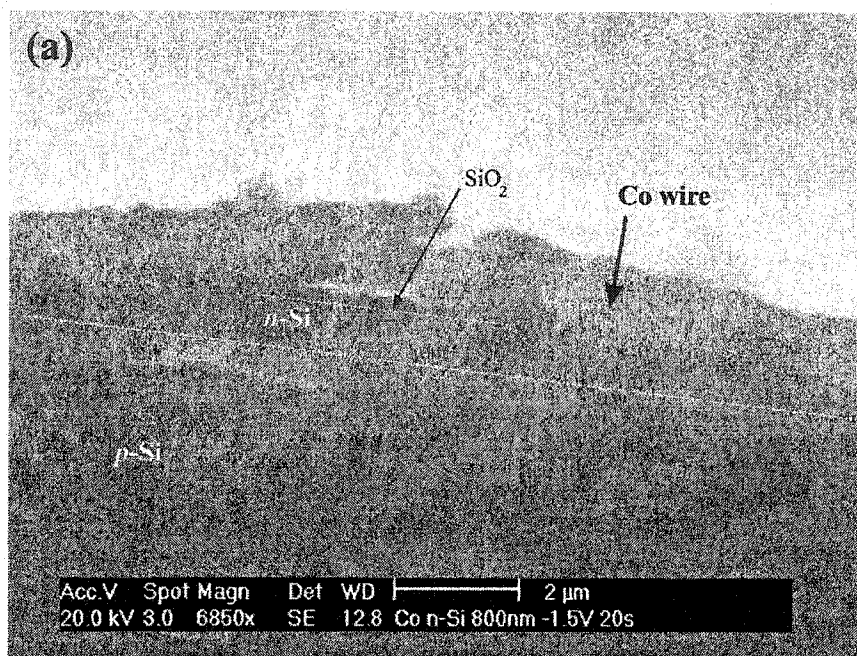


FIG. 129. SEM pictures of a $\sim 1.5 \mu\text{m}$ wide Co wire “electro-sideplated” on a $(200 \text{ nm})\text{SiO}_2/(800 \text{ nm})n\text{-Si}/p\text{-Si}$ substrate. The sample was tilted by 40° with respect to the normal of the wire surface .

As a conclusion, continuous wires are achievable by ECD from standard sulfate solutions on cleaved staked *n/p* SC substrates. This method can be extended to multiple wire deposition leading to pattern nanowires which resolution is controlled by the thickness of the deposited *n*-seed layer. In addition, growth conditions (bias voltage, deposition time) and thickness of the seed layer are crucial parameters to avoid overlapping, over expansion of plated wires and contamination of *p*-regions.

C. Conclusion

In the present work, the photoinduced deposition of Cu dots on *p*-type Si substrates have been studied and the possibility to reduce the lateral dimensions of the deposits by using a reduced laser wavelength or intensity demonstrated. Furthermore, the author has shown how a shorter minority carrier lifetime in the semiconductor substrate induced by ion irradiation may lead to a further reduction of structure dimensions. The smallest dots observed in this study are about 5 μm in diameter for 532 nm radiation wavelength and ion-beam damaged Si substrates. A further reduction is certainly possible through the use of blue laser light or, as demonstrated recently, by illumination using near field techniques.^{37,45}

A size reduction due to a lowered intensity is limited as the deposition process requires the intensity to be above a certain threshold value. This threshold value is related to the Cu/Cu^{2+} redox potential at the Si surface and the electron diffusion and annihilation rates at the surface. The size reduction due to a lower mobility and shorter minority carrier lifetime caused by an increased defect density in the semiconductor might be practical but will also be limited. Too high a defect density at the surface

enables Cu deposition without illumination, as demonstrated by Cu decoration of local ion-beam damage traces³² or, as we found, on amorphous Si layers. Background plating outside the illuminated area has shown to depend on the electrolyte composition. The presence of surfactants is necessary to obtain continuous shiny Cu features while coexisting with spontaneous Cu background in the surrounding area. The surface roughness can be reduced by pulsed deposition techniques.

A promising application is the extension to pattern photoinduced deposition through optical mask with the advantage of leaving the *p*-SC surface free of lithography steps. Electroless pattern photoinduced Cu has been successfully deposited on *p*-Si. On the other hand, the combination of ECD (bias voltage) and laser light excitation is necessary as the deposited material and substrate are replaced. The resolution (i.e. size of the deposited pattern) is controlled through the focus of the laser beam, however deposition parameters (light intensity, bias voltage, electrolyte, etc.) are sensitive and need to be determined according to the material and substrate involved.

Another way to generate selective plating of FM conductive materials (Co, Ni) (i.e. without the use and excitation of laser light), is to use standard ECD technique on a *p/n* doping pattern in a SC (GaAs, Si) surface and take advantage of the different electrochemical response of *p*- or *n*-doped regions under applied bias voltage. The surface *p/n* pattern preparation in the substrate can be achieved by different means (chemical etching of patterned double *p/n* layered SC, ion implantation of patterned *p*-doped SC, etc.) with a limitation though in its resolution due to lithography steps. The method demonstrated here has the advantage to enable direct self assembly of ferromagnetic films on laterally confined regions of semiconductor surfaces, produced by

proven and reliable doping techniques, well known in microelectronic processing. The method can be used to grow contacts for spin injection¹¹⁷ or spin transistor experiments. Electrodeposition has proven to be able to produce high quality epitaxial ferromagnetic layers on GaAs substrates.⁴⁹ Moreover, the low energy deposition process eliminates FM/semiconductor interface intermixing^{28,29} which is essential for preparation of samples suitable for effective spin injection into a semiconductor. The ability to apply this method for direct preparation of contacts to a semiconductor structure depends on the compatibility with the established doping pattern, as the ferromagnetic layer will inevitably plate on the *n*-doped areas. Moreover, the *p*-doped regions should have a sufficiently low doping concentration since plating on a degenerate semiconductor will not be inhibited. Excessive surface damage of semiconductors of poor crystalline quality will generally provide a large density of states in the band gap, which would facilitate electrodeposition independent of doping polarity. The ultimate resolution of this technique will be given by the abruptness of the doping profile and the extension of the depletion region near the boundary between *n*-type and *p*-type regions. The width of the depletion region of this *p/n* junction is given by the Debye length, which is a function of the doping concentrations. On the *p*-doped side of this junction, the depleted region will even more efficiently inhibit the deposition process. The depleted region on the *n*-doped side might as well initially impede the growth; however, with the growth of the metallic film, the electron deficiency in the semiconductor will be filled up and deposition would become possible. In the present work, such transient effects in *p*-doped wafers with a shallow *n*-doped surface layer have been observed. A further limitation to the ultimate

resolution of this technique is the grain size of the deposited metallic structure, which however can be tailored with great precision by the use of appropriate chemistries.¹¹⁸

In addition, flat operating p/n pattern surface can be achieved through ion implantation in a p -doped SC. Unlike chemically etched p/n SC substrate, this irradiation technique allows selective deposition on flat p/n pattern surface however, irradiation conditions (ion dose, beam energy, implantation depth) are very critical to ensure homogenous deposition. In the present work, selective growth of Ni and Co on n -regions is achievable though progressive plating cannot be inhibited.

Along with this technique, modification of the configuration of the ECD procedure and the substrate preparation (i.e. electroplating of material on the cleaved edge of a p/n multilayered SC substrate) can lead to selective deposition of long continuous nanowires, the width of which is controlled by the thickness of the n -layers in the substrate.

IV. CONCLUSION

The proposal to create active spin-electronics three-terminal devices with transistor-like characteristics⁴ triggered great interest in the development of processes for the integration of ferromagnetic materials with semiconductors. Such devices would require electron transfer between a ferromagnet and a semiconductor under conservation of spin polarization which would require a chemically sharp interface, ideally down to the atomic level, with the least possible concentration of defects. One possible way to create a spin-polarized current in these devices is current injection through magnetic films; it is thus important to understand the growth and properties of magnetic thin films on SC. Electrochemical deposition in this respect offers important advantages with respect to UHV techniques; for example, besides being able to grow high-quality epitaxial layers of FM materials onto SC such as Ni, Co or Fe on GaAs,²¹⁻²⁷ it is a low-energy, room-temperature process (i.e. soft landing of the deposited material) which can limit the interdiffusion between the film and the substrate,^{28,29} thus creating well-defined interfaces such as Ni on GaAs. In addition, unlike vacuum growth, the electronic properties of the substrate play an important part in the deposition process and constitute an important experimental variable to manipulate film growth.

Another advantage of this low cost deposition technique is to enable direct self assembly of ferromagnetic films on laterally confined regions of semiconductor surfaces,⁵⁵ produced by proven and reliable doping techniques, well known

in microelectronics processing. For example, ferromagnetic nanowires could be obtained on side-plated multilayered *n/p*-SC substrates such as Ni, Co on Si. Likewise, mask-free selective electrodeposition by local manipulation of the substrate (laser induced deposition of Cu on *p*-Si^{47,48}) or surface defects⁵⁵ (ECD of Co on ion implanted patterned *n/p*-Si) can lead to spatially selective deposition of thin features.

Hence, the ability to perform selective deposition of ferromagnetic films on semiconductors could enable the maskless fabrication of devices based on spin-dependent transport⁵³ such as MRAMs and spin transistors.^{4,54}

Future and prospective work would lead to the selective side-plating deposition of ferromagnetic material onto 2-dimensional electron gas while selective photoinduced electroless spin polarized electrode of Co or Ni onto GaAs would be a hopeful step.

As a conclusion, ECD is a promising, inexpensive, and alternative technique capable of selectively growing epitaxial layers onto SC substrates without significant interface intermixing and might be conceived as a technique in the production of prospective spin-electronics devices.

REFERENCES

- ¹ G. Binasch, P. Grünberg, F. Saurenbach, and W. Zinn, Phys. Rev. B 39, 4828 (1989).
- ² M. N. Baibich, J. M. Broto, A. Fert, F. N. Van Dau, F. Petroff, P. Eitenne, G. Creuzet, A. Friederich, and J. Chazelas, Phys. Rev. Lett. 61, 2472 (1988).
- ³ J. S. Moodera, L. R. Kinder, T. M. Wong, and R. Meservey, Phys. Rev. Lett. 74, 3273 (1995).
- ⁴ Datta, S., and Das, B., *Electronic analog of the electro-optic modulator*, Appl. Phys. Lett. 56, 665 (1990).
- ⁵ Y. B. Xu, D. J. Freeland, E. T. M. Kernohan, W. Y. Lee, M. Tselepi, C. M. Guertler, C. A. F. Vaz, and J. A. C. Bland, S. N. Holmes and N. K. Patel, D. A. Ritchie, J. Appl. Phys. 85, 5369 (1999).
- ⁶ W. Y. Lee, S. Gardelis, B.-C. Choi, Y. B. Xu, C. G. Smith, C. H. W. Barnes, D. A. Ritchie, E. H. Linfield, and J. A. C. Bland, J. Appl. Phys. 85, 6682 (1999).
- ⁷ G. Schmidt, D. Ferrand, L. W. Molenkamp, A. T. Filip, and B. J. van Wees, Phys. Rev. B 62, R4790 (2000).
- ⁸ S.P. Murarka, *Silicides for VLSI Applications*, (Academic Press, New York, 1983).
- ⁹ R. Schad, F. Jentzsch, M. Henzler, J. Vac. Sci. Technol. B 10, 1177 (1992).
- ¹⁰ M. Rubinstein, F.J. Rachford, W.W. Fuller, G.A. Prinz, Phys. Rev. B 37, 8689 (1988).
- ¹¹ B.T. Jonker, J.J. Krebs, G.A. Prinz, J. Appl. Phys. 64, 5340 (1988).
- ¹² J.J. Krebs, B.T. Jonker, G.A. Prinz, J. Appl. Phys. 61, 2596 (1987).
- ¹³ R.F.C. Farrow, S.S.P. Parkin, V.S. Speriosu, J. Appl. Phys. 64, 5315 (1988).
- ¹⁴ Y.B. Xu, E.T. M. Kernohan, D.J. Freeland, A. Ercole, M. Tselepi, and J.A.C. Bland, Phys. Rev. B 58 (2), 890 (1998).
- ¹⁵ M. Zölfl, M. Brockmann, M. Köhler, S. Kreuzer, T. Schweinböck, S. Miethaner, F. Bensch, G. Bayreuther, J. Magn. Magn. Mater. 175 (12), 16 (1997).

- ¹⁶ A. T. Hanbicki and B. T. Jonker, G. Itskos, G. Kioseoglou, and A. Petrou, *Appl. Phys. Lett.* **80**, 1240 (2002).
- ¹⁷ L. Allemand, M. Froment, G. Maurin, E. Souteyrand, *Microsc. Microanal. Microstruct.* **3**, 401 (1992).
- ¹⁸ R. Hart, P. A. Midgley, A. Wilkinson, W. Schwarzacher, *Appl. Phys. Lett.* **67**, 1316 (1995).
- ¹⁹ G. Yi, W. Schwarzacher, *Appl. Phys. Lett.* **74**, 1746 (1999).
- ²⁰ K. Attenborough, J. De Boeck, J.-P. Celis, M. Mizuguchi, H. Akinaga, *IEEE Trans. Magn.* **35**, 2985 (1999).
- ²¹ P. Evans, C. Scheck, R. Schad and G. Zangari, *Electrodeposition of Ferromagnetic thin films on Semiconductor Substrate*, The Electrochem. Soc. Proc. Series, PV 2001-8, Washington, DC, Spring (2001).
- ²² P. Evans, C. Scheck, W. J. M. de Jonge, J. T. Kohlhepp, T. Isaac-Smith, H. Wieldraaijer, J. Williams, R. Schad, and G. Zangari, *IEEE Trans. Magn.* **38**, 2670 (2002).
- ²³ C. Scheck, P. Evans, R. Schad, G. Zangari, J. R. Williams, and T. F. Isaacs-Smith, *J. Phys.: Condensed. Matter* **14**, 12329 (2002).
- ²⁴ C. Scheck, P. Evans, R. Schad, G. Zangari, *J. Magn. Magn. Mater.* **260**, 467 (2003).
- ²⁵ C. Scheck, Y. -K. Liu, P. Evans, R. Schad, G. Zangari, *J. Appl. Phys.* **93**, 7634, (2003).
- ²⁶ Y. -K. Liu, C. Scheck, R. Schad, Y. Ding, C. Alexander, and G. Zangari, *J. Appl. Phys.* **95**, 6546, (2004).
- ²⁷ Y. -K. Liu, C. Scheck, R. Schad, G. Zangari, *Epitaxial growth of Fe films on n-type GaAs by electrodeposition*, *Electrochem. Solid-State Lett.* **7**, D11 (2004).
- ²⁸ C. Scheck, P. Evans, R. Schad, G. Zangari, *Appl. Phys. Lett.* **82**, 2853 (2003).
- ²⁹ C. Scheck, Y. -K. Liu, P. Evans, R. Schad, G. Zangari, *J. Appl. Phys.* **95**, 6549 (2004).
- ³⁰ G. Oskam, J.G. Long, A. Natarajan, and P.C. Searson, *J. Phys. D* **31**, 1927 (1998).
- ³¹ P. Schmuki and L. E. Erickson, *Selective High-Resolution Electrodeposition on Semiconductor Defect Patterns*, *Phys. Rev. Lett.* **85** 2985 (2000).
- ³² L. Santinacci, T. Djenizian, and P. Schmuki, *Appl. Phys. Lett.* **79**, 1882 (2001).

- ³³ R.H. Micheels, A.D. Darrow, and R. David Rauh, *Appl. Phys. Lett.* **39**, 418 (1981).
- ³⁴ W. Kautek, N. Sorg, and W. Paatsch, *Electrochim. Acta* **36**, 1803 (1991).
- ³⁵ T.L. Rose, D.H. Longendorfer, and R.D. Rauh, *Appl. Phys. Lett.* **42**, 193 (1983).
- ³⁶ R.J. von Gutfield, E.E. Tynan, R.L. Meicher, and S.E. Blum, *Appl. Phys. Lett.* **35**, 651 (1979).
- ³⁷ H. Diesinger, A. Bsiesy, and R. Hérino, *J. Appl. Phys.* **90**, 4862 (2001).
- ³⁸ L. Nánai, I. Hevesi, F.V. Bunkin, B.S. Luklyanchuk, M.R. Brook, G.A. Shafeey, D.A. Jelski, Z.C. Wu, and T.F. George, *Appl. Phys. Lett.* **54**, 736 (1989).
- ³⁹ H. Cachet, M. Froment, and E. Souteyrand, *J. Electrochem. Soc.* **139**, 2920 (1992).
- ⁴⁰ J.S. Jeon, S. Raghavan, H.G. Parks, J.K. Lowell, and I. Ali, *J. Electrochem. Soc.* **143**, 2870 (1996).
- ⁴¹ O.M.R. Chyan, J-J. Chen, H.S. Chien, J. Sees, and L. Hall, *J. Electrochem. Soc.* **143**, 92 (1996).
- ⁴² L. Magagnin, R. Maboudian, and C. Carraro, *Electrochem. Solid-State Lett.* **4**, C5 (2001).
- ⁴³ G.J. Norga, M. Platero, K.A. Black, A.J. Reddy, J. Michel, and L.C. Kimerling, *J. Electrochem. Soc.* **144**, 2801 (1997).
- ⁴⁴ R. Memming, *Semiconductor Electrochemistry* (Wiley, New York, 2001), p. 107.
- ⁴⁵ S. Eriksson, P. Carlsson, and B. Holmström, *J. Appl. Phys.* **69**, 2324 (1991).
- ⁴⁶ R.F. Karlicek, V.M. Donnelly, and G.J. Collins, *J. Appl. Phys.* **53**, 1084 (1982).
- ⁴⁷ C. Scheck, Y.-K. Liu, P. Evans, R. Schad, G. Zangari, A. Bowers, J. R. Williams, T. F. Issacs-Smith, *Phys. Rev. B*, **69**, 035334 (2004).
- ⁴⁸ C. Scheck, Y.-K. Liu, P. Evans, R. Schad, A. Bowers, G. Zangari, J. R. Williams, T. F. Issacs-Smith, *J. Vac Soc Technol. A* **22**, 1842 (2004).
- ⁴⁹ G. Fasol, *Nanowires: Small Is Beautiful*, *Science* **280**, 545 (1998).
- ⁵⁰ G. E. Possin, *Forming very small diameter wires*, *Rev. Sci. Instrum.* **41**, 772 (1970).

- ⁵¹ M. Sun, G. Zangari, M. Shamsuzzoha, R. M. Metzger, *Electrodeposition of highly uniform magnetic nanoparticle arrays in ordered alumite*, Appl. Phys. Lett. 78, 2964 (2001).
- ⁵² G. Fasol, K. Runge, *Selective electrodeposition of nanometer scale magnetic wires*, Appl. Phys. Lett. 70 2467 (1997).
- ⁵³ G. A. Prinz, *Magnetoelectronics*, Science 282, 1660 (1998).
- ⁵⁴ S. Sugahara and M. Tanaka, *A spin metal-oxide-semiconductor field-effect transistor using half-metallic-ferromagnet contacts for the source and drain*, Appl. Phys. Lett. 84, 2307 (2004).
- ⁵⁵ C. Scheck, Paul Evans, Rainer Schad, Giovanni Zangari, Lucia Sorba, Giorgio Biasiol, Stefan Heun, *Selective metal electrodeposition through doping modulation of semiconductor surfaces*, Appl. Phys. Lett. (to be submitted).
- ⁵⁶ B.D. Cullity, *Elements of X-ray Diffraction*, 2nd ed., (Addison-Wesley Publishing Company, Philippines, 1978).
- ⁵⁷ Reproduced from: <http://www.vtt.fi/tte/research/tt6/thinfilms/rbs2.htm>, VTT Technical Research Centre of Finland, FIN-02044 VTT.
- ⁵⁸ C. Herring, *Magnetism*, 4, edited by G. T. Rado and H. Suhl (Academic, New York, 1966).
- ⁵⁹ S.M. Jordan, R. Schad, D.J.L. Herrmann, J.F. Lawler, and H. van Kempen, Phys. Rev. B 58, 13133 (1998).
- ⁶⁰ S.K. Sinha, E.B. Sirota, S. Garoff, and H.B. Stanley, Phys. Rev. B 38, 2297 (1988).
- ⁶¹ A. Stierle, P. Boedeker, H. Zabel, Surf. Sci. 327, 9 (1995).
- ⁶² R. Schad, D. Bahr, J. Falta, P. Beliën, Y. Bruynseraede, J. Phys.: Condensed Matter 10, 61 (1998).
- ⁶³ R.S. Saiki, A.P. Kaduwela, J. Osterwalder, C.S. Fadley, C.R. Brundle, Phys. Rev. B 40, 1586 (1989).
- ⁶⁴ F. May, M. Tischer, D. Arvanitis, M. Russo, J. Hunter unn, H. Henneken, H. Wende, R. Chauvistre, N Mårtensson, K. Baberschke, Phys. Rev. B 53, 1076 (1996).
- ⁶⁵ W.-D. Wang, N.J. Wu, P.A. Thiel, J. Chem. Phys. 92, 2025 (1990).
- ⁶⁶ J.C. de Jesus, J. Carrazza, P. Pereira, F. Zaera, Surf. Sci. 397, 34 (1998).

- ⁶⁷ D-M. Smilgies, R. Feidenhans'l, G. Scherb, D.M. Kolb, A. Kazimirov and J. Zegenhagen, *Surf. Sci.* 367, 40 (1996).
- ⁶⁸ J. Zegenhagen, A. Kazimirov, G. Scherb, D. M. Kolb, D-M. Smilgies, and R. Feidenhans'l, *Surf. Sci.* 346,. 352 (1996).
- ⁶⁹ O.I. Kasyutich, W. Schwazacher, V.M. Fedosyuk, P.A. Laskarzhevskiy and A.I. Masliy, *J. Electrochem. Soc.* 147, 2964 (2000).
- ⁷⁰ W.X. Tang, D. Qian, D. Wu, Y.Z. Wu, G.S. Dong, X.F. Jin, S.M. Chen, X.M. Jiang, X.X. Zhang, Z. Zhang, *J. Magn. and Magn. Mater.* 240, 404 (2002).
- ⁷¹ R.M. Bozorth and R.C. Sherwood, *Phys. Rev.* 94, 1439 (1954).
- ⁷² A. J. P. Meyer and G. Asch, *J. Appl. Phys.* 32, 330S (1961).
- ⁷³ A. Ford, J. E. Bonevich, R. D. McMichael, M. Vaudin, and T. P. Moffat, *J. Electrochem. Soc.* 150, C753 (2003).
- ⁷⁴ P.C Riedi, T. Thomson and G. J. Tomka, *Handbook of Magnetic Materials*, 12, edited by K.H.J. Buschow (Elsevier, Amsterdam, 1999), p. 97.
- ⁷⁵ M. Cerisier, K. Attenborough, E. Jedryka, M. Wojcik, S. Nadolski, C. Van Haesendonck and J.P. Celis, *Structural Study of nanometric electrodeposited Co films using 59 Co NMR*, *J. App. Phy.*, 89, 7083 (2001).
- ⁷⁶ E. M. Kneedler, B.T. Jonker, P.M. Thibado, R.J. Wagner, B.V. Shanabrook, L.J. Whitman, *Phys. Rev. B* 56, 8163 (1997).
- ⁷⁷ R. Schad, D. Bahr, J. Falta, P. Beliën, Y. Bruynseraede, *J. Phys.: Condensed Matter* 10, 61 (1998).
- ⁷⁸ M. Dumm, M. Zolfl, R. Moosbuhler, M. Brockmann, T. Schmidt, and G. Bayreuther, *J. Appl. Phys.* 87, 5457 (2000).
- ⁷⁹ A. F. Isakovic, J. Berezovsky, P. A. Crowell, L.C. Chen, D. M. Carr, B. D. Schultz, and C. J. Palmstrom, *J. Appl. Phys.* 89, 6674 (2001).
- ⁸⁰ B. D. Cullity, *Introduction to Magnetic Materials* (Addison-Wesley Publishing Company, New York, 1972), p. 221.
- ⁸¹ B. D. Cullity, *Introduction to Magnetic Materials* (Addison-Wesley Publishing Company, New York, 1972), p. 234.
- ⁸² T. Zhao, H. Fujiwara, K. Zhang, C. Hou, and T. Kai, *Phys. Rev. B* 65, 014431(2002).

- ⁸³ K. J. Miller, Phys. Rev. 32, 689 (1928).
- ⁸⁴ M. Li, G. -C. Wang, J. Magn. Magn. Mater. 217,199 (2000).
- ⁸⁵ H. Meng, C.K. Ong, H.S. Lim, H.C. Fang, Y.P. Feng, J. Magn. Magn. Mater. 213, 37 (2000).
- ⁸⁶ Gabriel Bochi, C. A. Ballentine, H. E. Inglefield, C. V. Thompson, and R. C. O'Handley, J. Appl. Phys. 79, 5845 (1996).
- ⁸⁷ S.A. Haque, A. Matsuo, Y. Yamamoto, H. Hori, J. Magn. Magn. Mater. 247, 117 (2002).
- ⁸⁸ M. Przybylski, S. Chakraborty, J. Kirschner, J. Magn. Magn. Mater. 234, 505 (2001).
- ⁸⁹ C. Uiberacker, J. Zabloudil, and P. Weinberger, L. Szunyogh, C. Sommers, Phys. Rev. Lett. 82, 1289 (1999).
- ⁹⁰ Y. Ding, C. Alexander, Jr., and T. J. Klemmer, J. Appl. Phys. 93, 6674 (2003).
- ⁹¹ R. Bozorth, *Ferromagnetism* (IEEE press, Piscataway, NJ, 1994).
- ⁹² G.W. Anderson, M.C. Hanf, P.R. Norton, M. Kowalewski, K. Myrtle and B. Heinrich, J. Appl. Phys. 79, 4954 (1996).
- ⁹³ Y.B. Xu, E.T. M. Kernohan, D.J. Freeland, A. Ercole, M. Tselepi, and J.A.C. Bland, Phys. Rev. B 58 (2), 890 (1998).
- ⁹⁴ F. Gries, Surface Interface Anal. 24, 38 (1996).
- ⁹⁵ L. J. van der Pauw, Philips Tech. Rev. 26, 220 (1958)
- ⁹⁶ R. M. Bozorth, *Ferromagnetism* (IEEE press, New York, 1978), p.270.
- ⁹⁷ K. Fuchs, Proc. Cambridge Phil. Soc. 34, 100 (1938).
- ⁹⁸ R. Schad, P. Belien, G. Verbanck, C. D. Potter, K. Temst, V. V. Moshchalkov, and Y. Bruynseraede, J. Magn. Magn. Mater. 182, 65 (1998).
- ⁹⁹ Y. Namba, Japn. J. Appl. Phys. 9, 1326 (1970).
- ¹⁰⁰ M. W. Ruckman, J. J. Joyce, and J. H. Weaver, Phys. Rev. B 33, 7029 (1986).
- ¹⁰¹ S. A. Chambers, F. Xu, H. W. Chen, I. M. Vitomirov, S. B. Anderson, and J. H. Weaver, Phys. Rev. B 34, 6605 (1986).

- ¹⁰² S. A. Chambers and V. A. Loebs, *Appl. Phys. Lett.* **60**, 38 (1992).
- ¹⁰³ T.-J. Kim, V. Krishnamoorthy, M. Puga-Lambers, and P. H. Holloway, *J. Appl. Phys.* **85**, 208 (1999).
- ¹⁰⁴ S. M. SZE, *Semiconductor Devices, Physics and Technology*, 2nd ed., (John Wiley&Sons, New York, 2002), p. 232.
- ¹⁰⁵ E. H. Rhoderick and R. H. Williams, *Metal-Semiconductor Contacts* (Clarendon press, Oxford, 1988), p. 106.
- ¹⁰⁶ N. Newman, M. van Schilfgaarde, T. Kendelewicz, M. D. Williams and W. E. Spicer, *Phys. Rev. B* **33**, 1146 (1985b).
- ¹⁰⁷ J. R. Waldrop, *J. Vac. Sci. Technol. B* **2**, 445 (1984).
- ¹⁰⁸ S. M. Sze, *Physics of Semiconductor Devices* (Wiley, New York, 1981).
- ¹⁰⁹ Y. Souche, J.P. Lévy, E. Wagner, A. Liénard, L. Alvarez-Prado, and R.T. Collins, *J. Magn. Mater.* **242**, 578 (2002).
- ¹¹⁰ D.E. Aspnes and A.A. Studna, *Phys. Rev. B* **27**, 985 (1983).
- ¹¹¹ The different optical appearance of the dark and shiny areas is less likely due to a variation in composition (Cu oxides) since individual crystals in the dark regions still appear shiny at higher magnification.
- ¹¹² G.J. Pietsch, M. Henzler, and P.O. Hahn, *Appl. Surf. Sci.* **39**, 457 (1989).
- ¹¹³ H. Davies, *Proc. Inst. Electr. Eng.* **101**, 209 (1954).
- ¹¹⁴ H.E. Bennett and J.O. Porteus, *J. Opt. Soc. Am.* **51**, 123 (1960).
- ¹¹⁵ G. Léron del and R. Romestain, *Appl. Phys. Lett.* **74**, 2740 (1999).
- ¹¹⁶ H. van Kempen, *Een luizenleven: Ontdekkingsreis naar het oppervlak*, retirement speech, Nijmegen, Netherlands 2002 (unpublished).
- ¹¹⁷ for a review see: Jonker, B.T., *Progress Toward Electrical Injection of Spin-Polarized Electrons Into Semiconductors*, *Proc. IEEE* **91**, 727 (2003).
- ¹¹⁸ A. Vicenzo and P. L. Cavallotti, *Growth modes of electrodeposited cobalt*, *Electrochimica Acta*, (to be published).